



University of Canterbury

Department of Chemistry

Designing Graphene Supercapacitor Electrodes

A thesis submitted in partial fulfilment of the requirements for the degree of

Doctor of Philosophy

in the Department of Chemistry

University of Canterbury

Anna K. Farquhar

July 2017

Abstract

Graphene, a two-dimensional material comprised of sp^2 -hybridised carbon atoms, has significant potential in energy storage as an electrode material for supercapacitors. Unfortunately, strong intermolecular forces between the graphene sheets results in aggregation during assembly and use, reducing the accessible surface area and experimentally available capacitance. Prevention of aggregation during electrode assembly and cycling will allow the development of graphene materials with better energy storage capability. In this thesis work, molecular spacers grafted to few-layer graphene (FLG) were investigated as a way of preventing aggregation of the graphene sheets.

Molecular spacers were grafted to FLG using three strategies: the spontaneous reaction with aryldiazonium salts, the Diels Alder reaction of an aryne, and the addition of an amine. The aryldiazonium reaction was studied using five different salts. The results indicated that at least two reaction pathways are operative for the spontaneous reaction, giving a multilayer film with both -C-C- and -N=N- linkages. Furthermore, the experimental protocol allowed the modified FLG to be collected with the film either sandwiched between the FLG and the substrate, or exposed to the electrolyte. In the sandwiched orientation two nitrophenyl reduction peaks were sometimes seen and larger surface concentrations were measured, behaviour that has not been reported previously for films grafted onto carbon materials from aryldiazonium salts. The Diels-Alder reaction, which relied on the generation of an aryne from an anthranilic acid precursor, provided an efficient route to monolayer growth. The amine addition reaction provided an alternative route modifying FLG, though a Michael-like addition or partial intercalation.

Supercapacitor electrodes were assembled from aryldiazonium modified FLG using a layer-by-layer (LBL) strategy. The grafted film could efficiently separate the FLG sheets during assembly and prevent restacking during cycling, with the full surface area remaining accessible even after 20,000 galvanostatic charge discharge cycles. Furthermore, the grafted film did not diminish the total capacitance of the FLG or hinder ion movement to the surface of the sheets. To further enhance the capacitance of the FLG, pseudocapacitive metal hydroxide films were electrochemically deposited

on the FLG sheets prior to LBL assembly, which enhanced the total areal capacitance of the system.

This thesis work successfully developed a novel LBL protocol that allowed electrodes comprised of stacks of FLG to be assembled without diminishing the total accessible surface area and therefore capacitance of each graphene sheet, which is an essential step in the development of energy storage devices from graphene.

Deputy Vice-Chancellor's Office
Postgraduate Office

Co-Authorship Form

This form is to accompany the submission of any thesis that contains research reported in co-authored work that has been published, accepted for publication, or submitted for publication. A copy of this form should be included for each co-authored work that is included in the thesis. Completed forms should be included at the front (after the thesis abstract) of each copy of the thesis submitted for examination and library deposit.

Please indicate the chapter/section/pages of this thesis that are extracted from co-authored work and provide details of the publication or submission from the extract comes:

Chapter 3, Section 3.3

Farquhar, A. K.; Dykstra, H. M.; Waterland, M. R.; Downard, A. J.; Brooksby, P. A.,
Spontaneous modification of free-floating few-layer graphene by aryldiazonium ions:
Electrochemistry, atomic force microscopy, and infrared spectroscopy from grafted films. *J. Phys. Chem. C* **2016**, *120*, 7543-7552

Please detail the nature and extent (%) of contribution by the candidate:

All the experimental work and data analysis covered in this paper was carried out by the candidate (90%), with assistance from Haidee Dkystra and Mark Waterland for Raman spectroscopy, and assistance with writing from Paula Brooksby and Alison Downard.

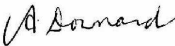
Certification by Co-authors:

If there is more than one co-author then a single co-author can sign on behalf of all

The undersigned certifies that:

The above statement correctly reflects the nature and extent of the PhD candidate's contribution to this co-authored work

In cases where the candidate was the lead author of the co-authored work he or she wrote the text

Name: *Alison Downard* Signature:  Date: 29/06/2017

Deputy Vice-Chancellor's Office
Postgraduate Office

Co-Authorship Form

This form is to accompany the submission of any thesis that contains research reported in co-authored work that has been published, accepted for publication, or submitted for publication. A copy of this form should be included for each co-authored work that is included in the thesis. Completed forms should be included at the front (after the thesis abstract) of each copy of the thesis submitted for examination and library deposit.

Please indicate the chapter/section/pages of this thesis that are extracted from co-authored work and provide details of the publication or submission from the extract comes:

Chapter 4, Section 4.2.1

Farquhar, A. K.; Fitchett, C. M.; Dykstra, H. M.; Waterland, M. R.; Brooksby, P. A.; Downard, A. J., Diels-alder reaction of anthranilic acids: A versatile route to dense monolayers on flat edge and basal plane graphitic carbon substrates. *ACS Appl. Mater. Interfaces* **2016**, *8*, 23389-23395.

Please detail the nature and extent (%) of contribution by the candidate:

All the experimental work and data analysis covered in this paper was carried out by the candidate (90%), with assistance from Haidee Dkystra and Mark Waterland for Raman spectroscopy, and assistance with writing from Paula Brooksby, Chris Fitchett, and Alison Downard.

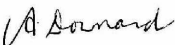
Certification by Co-authors:

If there is more than one co-author then a single co-author can sign on behalf of all

The undersigned certifies that:

The above statement correctly reflects the nature and extent of the PhD candidate's contribution to this co-authored work

In cases where the candidate was the lead author of the co-authored work he or she wrote the text

Name: *Alison Downard* Signature:  Date: 29/06/2017

Deputy Vice-Chancellor's Office
Postgraduate Office

Co-Authorship Form

This form is to accompany the submission of any thesis that contains research reported in co-authored work that has been published, accepted for publication, or submitted for publication. A copy of this form should be included for each co-authored work that is included in the thesis. Completed forms should be included at the front (after the thesis abstract) of each copy of the thesis submitted for examination and library deposit.

Please indicate the chapter/section/pages of this thesis that are extracted from co-authored work and provide details of the publication or submission from the extract comes:

Chapter 6, Section 6.3.1

Farquhar, A. K.; Brooksby, P. A.; Dryfe, R. A.; Downard, A. J., Controlled electrodeposition of gold nanoparticles onto copper-supported few-layer graphene in non-aqueous conditions. *Electrochim. Acta* **2017**, 237, 54-60

Please detail the nature and extent (%) of contribution by the candidate:

All the experimental work and data analysis covered in this paper was carried out by the candidate (90%), with assistance from assistance with writing from Paula Brooksby, Robert Dryfe and Alison Downard.

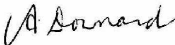
Certification by Co-authors:

If there is more than one co-author then a single co-author can sign on behalf of all

The undersigned certifies that:

The above statement correctly reflects the nature and extent of the PhD candidate's contribution to this co-authored work

In cases where the candidate was the lead author of the co-authored work he or she wrote the text

Name: *Alison Downard* Signature:  Date: 29/06/2017

Acknowledgements

First and foremost, I would like to thank my supervisors Alison Downard and Paula Brooksby. I am exceedingly grateful for their help and guidance over the last three years, and I believe I am exceptionally lucky to have been given the opportunity to work with them both. I would also like to thank Robert Dryfe at the University of Manchester, United Kingdom for hosting me in his research lab in Manchester for three months, which was an extremely rewarding and worthwhile experience.

My thanks to Chris Fitchett for help with various aspects of organic chemistry, especially regarding the Diels-Alder work in this thesis. I would also like to acknowledge Haidee Dykstra and Mark Waterland from Massey University in Palmerston North, for help with Raman spectroscopy, and Robert Stainthorpe and Sally Gaw for their help with the ICPMS analysis. Thanks to Patrick Hill from the University of Manchester and Mike Flaws at the University of Canterbury for SEM imaging. I would also like to thank Colin Doyle at the University of Auckland for XPS analysis. From the Nanolab I would like to acknowledge Helen and Gary for everything they do to keep the Nanolab running. Also thanks to Gill and Laurie from chemical stores. I am very grateful to Danny, Nick, and Wayne in the mechanical workshop, Rob for making and fixing any glassware, and John for fixing my laptop many times. I would also like to thank Bryce Williamson, Sarah Masters, and Matt Polson from the Department of Chemistry for their help and advice over the past three years.

I would like to thank the members of the Downard research group, past and present – Alex, Kalib, Lita, Ting, Joel, Ethan, Luke, Liam, and Prathik – it has been delightful working with you all. I'd also like to thank the members of the Dryfe research group in Manchester, especially Sam and Stephen, for making me feel so welcome during my visit. My thanks to Alana from engineering, both for help with the Hall Effect work and for being an outstanding friend in the Nanolab, and to Nic, Sam, Will, and Rob for their help with any synthetic chemistry and for being great 6th floor company.

I am extremely grateful to my friends and family. To all my wonderful friends, especially Pippa, Lily, Georgie, Anna, and Porsha. Of course, I am forever thankful for Martinique and Andre, two-thirds of the three best friends. Thanks to my sisters Sarah

and Emily, and my brothers in law Jono and Aaron, for their never-ending support, and to the kids, Polly, Ruby, Astro, Tilly, Chester, Henry, Fluff, Scruff, Bailey, Rasta, and Gin. Finally, I cannot begin to express how thankful I am to KJ and Bry, my parents. I couldn't have done any of this without your unconditional love and support. Thanks for being the best parents anyone could hope for - Bry, you can stop asking if I've made a supercapacitor now!

Finally, I would like to thank the University of Canterbury for my doctoral scholarship, and the Royal Society of New Zealand Marsden Fund and the MacDiarmid Institute for Advanced Materials and Nanotechnology for funding.

Table of Contents

| | |
|--|---------------|
| Abstract | iii |
| Acknowledgements | viii |
| Table of Contents | x |
| List of Figures | xv |
| List of Schemes | xxiv |
| List of Tables | xxv |
| List of Abbreviations | xxvii |
| List of Symbols | xxx |
| List of Publications | xxxiii |
| 1 Introduction | 1 |
| 1.1 Graphene | 1 |
| 1.2 Preparation of Graphene | 2 |
| 1.2.1 Methods for Preparing Graphene..... | 2 |
| 1.2.2 Graphene CVD..... | 4 |
| 1.2.3 Transfer of Graphene | 6 |
| 1.3 Molecular Functionalisation of Graphene | 7 |
| 1.3.1 Reactions of Aryldiazonium Salts..... | 7 |
| 1.3.2 Diels-Alder Reactions | 11 |
| 1.3.3 Other Molecular Functionalisation Methods | 15 |
| 1.4 Deposition of Metal Nanoparticles onto Graphene | 15 |
| 1.5 Doping of Graphene | 17 |
| 1.6 Graphene Supercapacitors | 18 |
| 1.6.1 What are Supercapacitors..... | 18 |
| 1.6.2 Quantum Capacitance of Graphene | 22 |
| 1.6.3 Graphene Capacitors in Literature Reports..... | 24 |
| 1.7 Project Aims | 28 |
| 1.8 References | 29 |
| 2 Experimental Methods | 40 |
| 2.1 Chemicals | 40 |
| 2.1.1 Aryldiazonium Tetrafluoroborate Salt Synthesis..... | 40 |
| 2.1.2 2-Aminoterephthalic Acid 4-Methyl Ester Synthesis | 40 |

| | | |
|------------|---|-----------|
| 2.1.3 | Tetraoctylammonium Tetrachloroaurate ((TOA)[AuCl ₄]) Synthesis | 41 |
| 2.2 | Substrate Preparation | 41 |
| 2.2.1 | Pyrolysed Photoresist Film (PPF) preparation..... | 41 |
| 2.2.2 | Au/Epoxy Working Electrode Surfaces..... | 41 |
| 2.3 | Preparation of FLG | 42 |
| 2.3.1 | CVD of FLG | 42 |
| 2.3.2 | Polymer Free Transfer of FLG..... | 42 |
| 2.4 | Modification Methods | 44 |
| 2.4.1 | Aryldiazonium Salt Reaction | 44 |
| 2.4.1.1 | Free-Floating Modification | 44 |
| 2.4.1.2 | On Copper Modification | 44 |
| 2.4.2 | Diels-Alder Reaction of an Anthranilic Acid | 44 |
| 2.4.3 | Primary Amine Addition..... | 44 |
| 2.4.4 | Gold Nanoparticle Deposition | 45 |
| 2.4.5 | Cobalt-Nickel Hydroxide Nanoparticle Deposition..... | 45 |
| 2.5 | Layer by Layer Assembly of Three-Sheet Stacks of Modified and Unmodified FLG | 46 |
| 2.5.1 | Aryldiazonium Modified FLG..... | 46 |
| 2.5.2 | Gold Nanoparticle Decorated FLG | 47 |
| 2.5.3 | Cobalt-Nickel Hydroxide Nanoparticle Decorated FLG | 47 |
| 2.6 | Characterisation Methods | 47 |
| 2.6.1 | Error Analysis | 47 |
| 2.6.2 | Infrared (IR) spectroscopy | 47 |
| 2.6.3 | Ultraviolet (UV)/Visible spectroscopy | 48 |
| 2.6.4 | Raman Spectroscopy..... | 48 |
| 2.6.4.1 | Aryldiazonium and Diels-Alder Modified FLG..... | 48 |
| 2.6.4.2 | Nanoparticle Deposition..... | 49 |
| 2.6.5 | Atomic Force Microscopy (AFM) | 49 |
| 2.6.5.1 | Topographical Measurements | 49 |
| 2.6.6 | AFM Scratch Testing..... | 49 |
| 2.6.7 | Scanning Electron Microscopy (SEM) | 50 |
| 2.6.7.1 | Gold Nanoparticle Decorated FLG (FLG _{Au})..... | 50 |
| 2.6.7.2 | Metal Hydroxide Nanoparticle Decorated FLG..... | 50 |
| 2.6.8 | X-ray Photoelectron Spectroscopy (XPS)..... | 50 |
| 2.6.9 | Electrochemical Surface Concentration Measurements | 51 |
| 2.6.9.1 | Nitrophenyl (NP) Surface Concentration..... | 52 |
| 2.6.9.2 | Anthraquinone Surface Concentration Measurements..... | 53 |

| | | |
|------------|--|------------|
| 2.6.10 | Capacitance of FLG after Aryldiazonium Modification or Gold Nanoparticle Deposition | 53 |
| 2.6.10.1 | Cyclic Voltammetry | 54 |
| 2.6.10.2 | Galvanostatic Charge Discharge Measurements | 54 |
| 2.6.10.3 | Electrochemical Impedance Spectroscopy (EIS) Measurements | 55 |
| 2.6.11 | Capacitance of Metal Hydroxide Modified FLG | 55 |
| 2.6.11.1 | Cyclic Voltammetry | 56 |
| 2.6.11.2 | Galvanostatic Charge Discharge | 56 |
| 2.6.11.3 | Electrochemical Impedance Spectroscopy | 56 |
| 2.6.12 | Four-Point Probe measurements | 56 |
| 2.6.13 | Inductively Coupled Plasma Mass Spectrometry (ICPMS) Measurements .. | 57 |
| 2.7 | References | 58 |
| 3 | Chemical Vapour Deposition of Few-Layer Graphene and Subsequent Modification with Aryldiazonium Salts | 60 |
| 3.1 | Introduction | 60 |
| 3.2 | Experimental Methods | 63 |
| 3.3 | Results and Discussion | 64 |
| 3.3.1 | Preparation and Characterisation of FLG | 64 |
| 3.3.1.1 | Tuning the CVD Parameters | 64 |
| 3.3.1.2 | UV/Visible Spectroscopy | 65 |
| 3.3.1.3 | AFM Imaging | 65 |
| 3.3.1.4 | Raman and IR Spectroscopy | 67 |
| 3.3.2 | Modification with 4-Nitrobenzene Diazonium Salt | 71 |
| 3.3.2.1 | Raman Spectroscopy of FLG _{NP} | 71 |
| 3.3.2.2 | AFM Imaging of FLG Modified with NBD | 74 |
| 3.3.2.3 | IR Spectroscopy of FLG Modified with NBD | 76 |
| 3.3.2.4 | X-ray Photoelectron Spectroscopy (XPS) of FLG Modified with NBD | 80 |
| 3.3.2.5 | Electrochemistry of FLG modified with NBD | 85 |
| 3.3.3 | Modification with Other Aryldiazonium Salts | 90 |
| 3.3.4 | Hall Effect Studies of Aryldiazonium Salt Modification | 95 |
| 3.4 | Conclusion | 98 |
| 3.5 | References | 100 |
| 4 | Other FLG Modification Methods: the Diels-Alder Reaction of an Anthranilic Acid and the Spontaneous Reaction of a Primary Amine | 107 |
| 4.1 | Introduction | 107 |
| 4.1.1 | Diels-Alder Reactions of Anthranilic Acids | 107 |
| 4.1.2 | Reaction of FLG with a Primary Amine | 108 |

| | | |
|------------|--|------------|
| 4.2 | Experimental Methods..... | 110 |
| 4.3 | Results and Discussion | 111 |
| 4.3.1 | Characterisation of FLG Modified via the Diels-Alder Reaction of an Anthranilic Acid | 111 |
| 4.3.1.1 | Raman Spectroscopy | 111 |
| 4.3.1.2 | AFM Imaging..... | 112 |
| 4.3.1.3 | IR Spectroscopy | 113 |
| 4.3.1.4 | XPS Analysis..... | 115 |
| 4.3.1.5 | Electrochemistry..... | 117 |
| 4.3.1.6 | PPF Scratch Testing and Electrochemistry | 119 |
| 4.3.1.7 | Grafting Mechanism..... | 121 |
| 4.3.2 | Characterisation of FLG Modified with a Primary Amine | 122 |
| 4.3.2.1 | Raman Spectroscopy | 122 |
| 4.3.2.2 | AFM Imaging..... | 123 |
| 4.3.2.3 | IR Spectroscopy | 124 |
| 4.3.2.4 | Electrochemistry..... | 126 |
| 4.3.2.5 | Physisorption Studies | 128 |
| 4.4 | Conclusion | 130 |
| 4.5 | References | 132 |
| 5 | Capacitance of Aryldiazonium Modified FLG Electrodes..... | 136 |
| 5.1 | Introduction | 136 |
| 5.2 | Experimental Methods..... | 138 |
| 5.3 | Results and Discussion | 138 |
| 5.3.1 | Capacitance of Unmodified FLG | 138 |
| 5.3.1.1 | CV and CD Testing of Unmodified FLG..... | 138 |
| 5.3.1.2 | EIS of Unmodified FLG..... | 140 |
| 5.3.1.3 | Nyquist Plot Analysis of FLG..... | 145 |
| 5.3.2 | Capacitance of Unmodified FLG Stacks | 148 |
| 5.3.2.1 | CV and CD Testing of Unmodified FLG Stacks | 148 |
| 5.3.2.2 | EIS of Unmodified FLG Stacks | 149 |
| 5.3.3 | Capacitance of NBD Modified FLG Stacks | 150 |
| 5.3.3.1 | EIS of Single Sheet Modified FLG..... | 150 |
| 5.3.3.2 | EIS of Three-Sheet Stacks of Modified FLG..... | 155 |
| 5.3.3.3 | Nyquist Plots for NBD Modified FLG Stacks | 157 |
| 5.3.3.4 | CV and CD Testing of NBD Modified FLG Stacks | 160 |
| 5.3.3.5 | Cycle Stability of NBD Modified FLG Stacks | 164 |
| 5.3.4 | Capacitance of CBD Modified FLG Stacks..... | 165 |
| 5.3.4.1 | EIS of CBD Modified FLG..... | 166 |

| | | |
|------------|--|------------|
| 5.3.4.2 | CV and CD Testing of CBD Modified FLG | 167 |
| 5.3.4.3 | Cycle Stability of CBD Modified Stacks | 170 |
| 5.3.5 | Summary of Capacitance Results | 170 |
| 5.4 | Conclusion | 173 |
| 5.5 | References | 174 |
| 6 | Electrochemical Deposition of Gold Nanoparticles and Cobalt-Nickel Hydroxide Thin Films onto FLG..... | 180 |
| 6.1 | Introduction | 180 |
| 6.1.1 | Gold Nanoparticle Deposition on Graphene | 180 |
| 6.1.2 | Cobalt-Nickel Hydroxide Deposition on Graphene | 181 |
| 6.2 | Experimental Methods..... | 182 |
| 6.3 | Results and Discussion | 182 |
| 6.3.1 | FLG Decorated with Gold Nanoparticles | 182 |
| 6.3.1.1 | Inhibition of Spontaneous Nanoparticle Deposition | 182 |
| 6.3.1.2 | Electrodeposition of Gold Nanoparticles | 183 |
| 6.3.1.3 | Growth in the Absence of an Applied Potential..... | 188 |
| 6.3.1.4 | Doping by Gold Nanoparticles..... | 189 |
| 6.3.1.5 | Capacitance of Gold Nanoparticle Modified FLG | 191 |
| 6.3.2 | Cobalt-Nickel Hydroxide Deposition on FLG..... | 193 |
| 6.3.2.1 | Deposition on FLG/Cu..... | 193 |
| 6.3.2.2 | Deposition on FLG on a Au/Epoxy Substrate..... | 196 |
| 6.3.2.3 | CV and CD of FLG after Cobalt-Nickel Hydroxide Deposition | 200 |
| 6.3.2.4 | EIS of FLG _{Co/Ni} | 204 |
| 6.3.2.5 | Deposition on FLG _{CP} on a Au/Epoxy Substrate..... | 206 |
| 6.3.2.6 | Capacitance of Three-Sheet Stacks | 210 |
| 6.3.3 | Summary of Metal Hydroxide Capacitance | 214 |
| 6.4 | Conclusion | 216 |
| 6.5 | References | 218 |
| 7 | Overall Conclusion and Future Work | 222 |
| 7.1 | Conclusion | 222 |
| 7.2 | Future Work | 227 |
| 7.3 | References | 230 |
| | Appendices..... | 231 |

List of Figures

| | |
|--|----|
| Figure 1.1: Structure of a single sheet of graphene, and illustration of the different graphitic materials derived from graphene: Bucky balls (green), carbon nanotubes (purple), and HOPG (blue). | 1 |
| Figure 1.2: Resonance forms of graphene. | 12 |
| Figure 1.3: Dienes and dienophiles used by Haddon et al. for the Diels-Alder reaction of graphene: (A) tetracyanoethylene; (B) maleic anhydride; (C) 2,3-dimethoxy-1,3-butadiene; (D) 9-methylanthracene. | 12 |
| Figure 1.4: Diels-Alder reaction between graphene (diene) and tetracyanoethylene (dienophile). | 13 |
| Figure 1.5: Diels-Alder reaction between graphene (dienophile) and 2,3-dimethoxy-1,3-butadiene. | 13 |
| Figure 1.6: Different protocols for the generation of an aryne. | 14 |
| Figure 1.7: Ragone plot for common energy storage materials. Reproduced from Liu et al. | 19 |
| Figure 1.8: Models of the double layer: (A) Helmholtz model; (B) Gouy-Chapman model; (C) Stern model; (D) Grahame model, with solvent molecules also shown. Adapted from Conway. | 20 |
| Figure 1.9: Theoretical quantum capacitance vs. potential for graphene, derived from (red) Equation 1.5, and (blue, purple, and orange) Equations 1.6 and 1.7. | 23 |
| Figure 1.10: Variation in minimum capacitance for rGO with different numbers of defects. From Pope & Aksay. | 24 |
| Figure 1.11: Cartoon illustrating the overall aim of this thesis. | 28 |
| Figure 2.1: Au surface with epoxy resin droplet in the centre. | 42 |
| Figure 2.2: Steps for etching copper and collecting FLG onto a substrate: (A) FLG/Cu coupon floating on ammonium persulfate solution; (B) FLG floating on water; (C) & (D) collecting FLG onto a Au/epoxy surface by lifting the surface from below the FLG; (E) FLG on Au/epoxy. In (B), (C), and (D) the FLG has been outlined for clarity. | 43 |
| Figure 2.3: Protocol for collection of FLG on KBr for IR spectroscopy and releasing FLG for further analysis. | 48 |
| Figure 2.4: Box profile across AFM tip scratch on modified PPF. Scale Bar = 3.0 μm | 50 |
| Figure 2.5: Image of FLG collected on HOPG with epoxy defined working electrode area used for ImageJ analysis of working electrode area. Dashed line shows working electrode area. | 51 |
| Figure 2.6: Electrochemical cell used for surface concentration measurements. SCE reference electrode and Au counter electrode shown. | 51 |
| Figure 2.7: Different baselines considered for determining the area under the NP reduction peak. | 52 |
| Figure 2.8: Reduction peak area used in AAQ surface concentration calculation. | 53 |

| | |
|---|----|
| Figure 2.9: Electrochemical cell with Luggin capillary used for capacitance measurements. SCE reference and Au wire counter electrodes shown. | 54 |
| Figure 2.10: CD plot of FLG on Au/epoxy in 1 M HClO ₄ , with discharge time and potential window shown. | 55 |
| Figure 2.11: Left to right: FLG collected onto glass microscope coverslip, with Ti/Au contacts in each corner of the FLG; ECOPIA SPCB-01 spring clip board used for Hall effect measurements..... | 57 |
| Figure 3.1: Structure of (A) NBD; (B) 4-propargyloxybenzene diazonium; (C) 3,5-bis- <i>tert</i> -butylbenzene diazonium; (D) 4-(2-hydroxyethyl)benzene diazonium; (E) 4-docosyloxybenzene diazonium. | 62 |
| Figure 3.2: Aryldiazonium tetrafluoroborate salts used in this work: (A) 4-nitrobenzene diazonium (NBD); (B) 4-nitroazobenzene diazonium (NABD); (C) 4-iodobenzene diazonium (IBD); (D) 4-carboxybenzene diazonium (CBD); (E) 4-methoxybenzene diazonium (MBD). Tetrafluoroborate anion (BF ₄ ⁻) not shown. | 63 |
| Figure 3.3: Different CVD protocols used in this work to grown FLG on copper: (A) 6-7 layer graphene; (B) 3-4 layer graphene. | 64 |
| Figure 3.4: UV/visible spectra from 400 to 800 nm of FLG produced via CVD on a glass microscope cover slip. Each spectrum is an average of four separate FLG samples..... | 65 |
| Figure 3.5: AFM images of as grown, 6-7 layer FLG: (A) and (B) on the copper support; (C) and (D) after transfer to freshly cleaved HOPG..... | 66 |
| Figure 3.6: Raman spectrum of 6-7 layer FLG transferred to a gold substrate. Spectrum is the average from two separate samples, with three spectra taken per sample and normalised to give G-band intensity of 1..... | 68 |
| Figure 3.7: 2D-band of a representative FLG sample on a gold substrate, fitted using Linkfit software with eight different Lorentzian curves. Residual shown in purple. | 68 |
| Figure 3.8: (A) Single beam transmission mode spectra of a new KBr disk (blue), and KBr disk after a ten second immersion in water (red); (B) 1:1 ratio of the single beam spectra given in A..... | 69 |
| Figure 3.9: KBr disk background subtracted IR spectrum of FLG on a KBr disk: (A) 4000 to 750 cm ⁻¹ ; (B) 1800 to 750 cm ⁻¹ . Spectrum recorded in transmission mode and baselined for clarity..... | 70 |
| Figure 3.10: XPS spectra of FLG transferred to a Au wafer. Left to right: C 1s narrow scan and O 1s narrow scan..... | 71 |
| Figure 3.11: Raman spectra of FLG on a gold wafer before and after modification in 20 mM aqueous NBD solution. All samples were washed with methanol prior to spectral acquisition. All spectra were normalised to give G-bands of equal intensity. Spectra are offset for clarity. Spot size ~ 2 μm..... | 72 |
| Figure 3.12: D/G intensity ratio calculated from Raman spectra taken at 0.5 μm intervals across a FLG surface before (blue) and after modification with a 20 mM aqueous NBD solution for 72 hours (green). Spot size ~ 2 μm..... | 73 |

- Figure 3.13: AFM images of FLG_{NP 20 hours} on HOPG: (A) in the sandwiched orientation; (B) in the exposed orientation. Both samples were washed with methanol prior to imaging. Scale bar 2.5 μm 75
- Figure 3.14: KBr disk background subtracted transmission mode IR spectra of FLG collected on a KBr disk before and after modification in 20 mM aqueous NBD: (A) before modification; (B) after 27 hour reaction (no methanol wash); (C) after 24 hour reaction, with a methanol rinse after collection on KBr. (D) ATR spectrum of NBD salt; spectrum scaled $\times 0.08$. Spectra offset for clarity. 76
- Figure 3.15: (A) Transmission mode IR spectrum of empty calcium fluoride solution cell from 4000 to 1250 cm^{-1} ; (B) absorbance (area under the peak at 1356 cm^{-1}) versus concentration of NBD in methanol. Spectra recorded in transmission mode using a calcium fluoride solution cell with a pathlength of 0.013 mm. 79
- Figure 3.16: Plot of NP surface concentration with reaction time, determined from IR spectroscopy. Samples were washed in methanol prior to recording spectra. 80
- Figure 3.17: XPS spectra for FLG on a silicon oxide wafer. Left to right: survey spectrum and C 1s narrow scan, and bottom N 1s narrow scan. 82
- Figure 3.18: XPS spectra for FLG_{NP 72 hours} on a silicon oxide wafer. Sample washed with methanol prior to spectral acquisition. Left to right: survey spectrum and C 1s narrow scan, and bottom N 1s narrow scan. 83
- Figure 3.19: XPS spectra for FLG_{IP 72 hours} on a silicon oxide wafer. Sample washed with methanol prior to spectral acquisition. Left to right: survey spectrum and C 1s narrow scan, and bottom N 1s narrow scan. 84
- Figure 3.20: FLG_{NP} resulting from reaction of FLG with an aqueous solution of NBD. 84
- Figure 3.21: CVs of methanol washed of FLG_{NP} mounted on HOPG in either an exposed orientation (blue, 20 hour reaction) or a sandwiched orientation (red, 66 hour reaction). CVs were recorded in 0.1 M H_2SO_4 at 200 mV s^{-1} 85
- Figure 3.22: CV in 0.1 M H_2SO_4 of methanol washed FLG_{NP} on HOPG after a 20 hour reaction mounted in an exposed orientation, showing the total area used to calculate surface concentration. 88
- Figure 3.23: Plot of surface concentration versus modification time for FLG_{NP} mounted on HOPG in either an exposed orientation (blue) or sandwiched orientation (orange), or on PPF in the sandwiched orientation (red). Green points are for FLG_{NP} films sandwiched between two sheets of FLG. Boxes indicate samples that showed two nitro reduction peaks. Surfaces were washed with methanol prior to analysis. 89
- Figure 3.24: Cartoon illustrating the different electron transfer pathways assumed to be available for the sandwiched and exposed orientations. $\sim\sim\sim$ represents a multilayer film. 90
- Figure 3.25: AFM images of aryldiazonium modified FLG transferred to HOPG in the exposed orientation: (A) and (B) FLG_{NAP 20 hours}; (C) and (D) FLG_{CP 70 hours}. 91
- Figure 3.26: Transmission mode IR spectra on KBr for (A) FLG and (B) FLG_{NAP 20 hours}. (C) ATR spectrum of NABD salt (scaled $\times 0.05$). Spectra are offset for clarity. 92

| | |
|--|-----|
| Figure 3.27: Transmission mode IR spectra on KBr for (A) FLG and (B) FLG _{CP 72hours} . (C) ATR spectrum of CBD salt (scaled $\times 0.05$). Spectra are offset for clarity.... | 94 |
| Figure 3.28: CV in 0.1 M H ₂ SO ₄ of FLG _{NAP 20hours} on HOPG in the exposed orientation. Scan rate = 200 mV s ⁻¹ | 95 |
| Figure 3.29: Plot of sheet resistance for FLG before and after reaction with 20 mM aryldiazonium salt aqueous solutions. Reported values are the average for four applied currents for various sample numbers of FLG: FLG, $n=12$; FLG _{NP 2hours} , $n=3$; FLG _{NP 7hours} , $n=4$; FLG _{MP 7hours} , $n=4$ | 96 |
| Figure 3.30: Plot of carrier concentration of FLG before and after reaction with 20 mM aryldiazonium salt aqueous solutions. Reported values are the average across four applied currents for various sample numbers: FLG, $n=12$; FLG _{NP 2hours} , $n=3$; FLG _{NP 7hours} , $n=4$; FLG _{MP 7hours} , $n=4$ | 97 |
| Figure 3.31: Plot of carrier mobility of FLG before and after reaction with 20 mM aryldiazonium salt aqueous solutions. Reported values are the average across four applied currents for various sample numbers: FLG, $n=12$; FLG _{NP 2hours} , $n=3$; FLG _{NP 7hours} , $n=4$; FLG _{MP 7hours} , $n=4$ | 98 |
| Figure 4.1: Anthranilic acids used in this work: (A) 5-nitroanthranilic acid, and (B) 2-amino-teraphthalic acid 4-methyl ester..... | 110 |
| Figure 4.2: Primary amines used in this work: (A) 4-nitrophenethylamine (NPEA), and (B) 2-aminoanthraquinone (AQQ)..... | 110 |
| Figure 4.3: Raman spectra of FLG on a gold substrate, before (blue) and after (red) a 6 hour reaction with NAA. Spectra normalised to give a G-band intensity of 1. Spectra offset for clarity..... | 111 |
| Figure 4.4: AFM images of FLG after transfer to HOPG: (A) before, and (B) and (C) after a 6 hour reaction with NAA. Line profile across (C) also shown. | 112 |
| Figure 4.5: Transmission mode IR spectra of FLG on a KBr disk before and after modification with NAA: (A) before and (B) after modification for 6 hours. (C) ATR spectrum of solid NAA precursor (scaled $\times 0.1$). Spectra offset for clarity. | 113 |
| Figure 4.6: Transmission mode IR spectra of FLG on a KBr disk before and after modification with ME: (A) before modification, and (B) after modification for 6 hours. (C) ATR spectrum of solid ME precursor (scaled $\times 0.1$). Spectra offset for clarity. | 114 |
| Figure 4.7: XPS spectra for FLG _{ME} after a 6 hour reaction. FLG _{ME} collected on a silicon oxide wafer for analysis. Left to right top: survey spectrum, C 1s narrow scan, and bottom: N 1s narrow scan. | 116 |
| Figure 4.8: CV in 0.1 M H ₂ SO ₄ of FLG _{NAA} on HOPG in the exposed orientation. Scan rate = 200 mV s ⁻¹ | 117 |
| Figure 4.9: Nitrophenyl surface concentration with increasing reaction time for the reaction of FLG with NAA. Red dashed line indicates exponential fit of the data. | 119 |
| Figure 4.10: CV in 0.1 M H ₂ SO ₄ of PPF _{NAA} . Scan rate = 200 mV s ⁻¹ | 119 |

| | |
|--|-----|
| Figure 4.11: AFM tip scratch on PPF _{NAA} after a 2 hour reaction. Scale Bar = 2.0 μm | 120 |
| Figure 4.12: Raman spectra of FLG on a gold wafer, before and after a 20 hour reaction with NPEA. Spectra normalised to give a G band intensity of 1. Spectra offset for clarity. | 123 |
| Figure 4.13: AFM images of FLG on HOPG: (A) and (B) after a 17 hour reaction with NPEA, and subsequent methanol wash; (C) and (D) after a 16 hour reaction with AAQ, and subsequent methanol wash. | 124 |
| Figure 4.14: Transmission mode IR spectra of FLG before (A) and after (B) modification with NPEA, with a subsequent methanol wash. ATR spectrum of NPEA precursor (C) is also shown (scaled $\times 0.02$). Spectra offset for clarity. . | 125 |
| Figure 4.15: Transmission mode IR spectra of FLG before (A) and after (B) modification with AAQ, with a subsequent methanol wash. ATR spectrum of AAQ precursor (C) is also shown (scaled $\times 0.03$). Spectra offset for clarity. | 126 |
| Figure 4.16: CV in 0.1 M H ₂ SO ₄ of FLG _{NPEA} after a 17 hour reaction. Sample collected onto HOPG in the sandwiched orientation and washed with methanol prior to analysis. Scan rate = 200 mV s ⁻¹ | 127 |
| Figure 4.17: CV in 0.5 M H ₂ SO ₄ of FLG _{AAQ} after a 17 hour reaction. Sample collected onto HOPG in the sandwiched orientation and washed with methanol prior to analysis. Scan rate = 200 mV s ⁻¹ | 128 |
| Figure 4.18: Physisorption analogues: (A) nitrotoluene, and (B) anthraquinone-2-sulfonic acid sodium salt. | 129 |
| Figure 4.19: Transmission mode IR spectra recorded on a KBr disk of: (A) FLG _{NPEA} (blue) and FLG _{NT Phys.} (red); (B) FLG _{AAQ} (blue) and FLG _{AS Phys.} (red). Samples washed with methanol prior to acquisition. Spectra offset for clarity. | 129 |
| Figure 4.20: Physisorption CVs: (A) FLG _{NPEA} (blue) and FLG _{NT Phys.} (red) in 0.1 M H ₂ SO ₄ ; (B) FLG _{AAQ} (blue) and FLG _{AS Phys.} (red) in 0.5 M H ₂ SO ₄ . Scan rate = 200 mV s ⁻¹ | 130 |
| Figure 5.1: CV and CD of FLG on Au/epoxy in 1 M HClO ₄ : (A) CV at 200 (blue), 100 (red), 50 (green), 20 (purple), and 5 mV s ⁻¹ (orange); (B) CD at selected current densities. | 139 |
| Figure 5.2: CV of FLG on Au/epoxy in 1 M HClO ₄ before (blue) and after (red) EIS. Scan rate = 200 mV s ⁻¹ | 141 |
| Figure 5.3: Dependence of areal capacitance on frequency at selected potentials for FLG on Au/epoxy, derived from EIS in 1 M HClO ₄ | 141 |
| Figure 5.4: Areal capacitance of FLG on Au/epoxy at different applied potentials derived from EIS in 1 M HClO ₄ at 115 Hz: (A) six different FLG samples (from different CVD batches); (B) average areal capacitance of samples in A, with standard deviation shown. | 143 |
| Figure 5.5: (A) Average total (blue) capacitance for FLG on Au/epoxy, derived from EIS in 1 M HClO ₄ and the quantum capacitance estimated by subtracting 20 $\mu\text{F cm}^{-2}$ (estimated Helmholtz capacitance) from the total capacitance (blue). (B) Quantum capacitance from plot A (blue) and Equation 5.4 (red). | 145 |

| | |
|---|-----|
| Figure 5.6: Data obtained from EIS of FLG on Au/epoxy in 1 M HClO ₄ at 0.1 V: (A) Nyquist plot with inset showing magnified high frequency region; (B) Bode phase angle plot..... | 146 |
| Figure 5.7: (A) Equivalent electrical circuit used to fit FLG EIS data; (B) Nyquist plots for FLG with fit shown in red (inset shows magnified high frequency region). | 148 |
| Figure 5.8: CV and CD results for 3FLG on Au/epoxy in 1 M HClO ₄ : (A) CV at 200 (blue), 100 (red), 50 (green), 20 (purple), and 5 mV s ⁻¹ (orange). Dotted line is the same CV for FLG in Figure 5.1 at 200 mV s ⁻¹ , and given for comparison; (B) CD at selected current densities. | 149 |
| Figure 5.9: Average areal capacitance at different potentials for FLG (blue, <i>n</i> =6) and 3FLG (red, <i>n</i> =3) derived from EIS in 1 M HClO ₄ at 115 Hz. | 149 |
| Figure 5.10: CV of FLG _{AP} on Au/epoxy in 1 M HClO ₄ before and after EIS. Scan rate = 200 mV s ⁻¹ | 151 |
| Figure 5.11: Average areal capacitance derived from EIS in 1 M HClO ₄ at different applied potentials at 115 Hz of: (blue) FLG (<i>n</i> =6); (red) FLG _{AP} after a 7 hour reaction with 20 mM aqueous NBD solution (<i>n</i> =3). | 151 |
| Figure 5.12: Average areal capacitance at different applied potentials derived from EIS in 1 M HClO ₄ at 115 Hz for FLG and FLG _{AP} on Au/epoxy. | 153 |
| Figure 5.13: Dependence of areal capacitance on potential FLG _{NP 1hour} on Au/epoxy derived from EIS in 1 M HClO ₄ at 115 Hz, from 0.3 to -0.5 V, then from -0.5 to 0.3 V (red). FLG plot, starting at 0.3 V shown for comparison (blue). | 154 |
| Figure 5.14: Dependence of areal capacitance on potential of FLG _{AP 1hour} on Au/epoxy derived from EIS at 115 Hz in 1 M HClO ₄ (blue) and 1 M NaClO ₄ (red). | 155 |
| Figure 5.15: Average areal capacitance vs. voltage plots of FLG _{AP} and 3FLG _{AP} derived from EIS in 1 M HClO ₄ at 115 Hz: (A) 1 hour, 1 mM aryldiazonium salt reaction (<i>n</i> =3); (B) 7 hours, 20 mM aryldiazonium salt reaction (<i>n</i> =2); (C) 16 hours, 20 mM aryldiazonium salt reaction (<i>n</i> =2); (D) 72 hours, 20 mM aryldiazonium salt reaction (<i>n</i> =2). | 156 |
| Figure 5.16: EEC used to fit EIS data for aryldiazonium modified FLG one- and three-sheet stacks. Reproduced from Tribollet & Orazem..... | 157 |
| Figure 5.17: EIS data for FLG, FLG _{AP} , and 3FLG _{AP} recorded at 0.1 V in 1 M HClO ₄ : (A) Nyquist plots; (B) Bode phase angle plots; (C) fitted FLG and FLG _{AP} Nyquist plots; (D) fitted FLG _{AP} and 3FLG _{AP} Nyquist plots. | 158 |
| Figure 5.18: CVs in 1 M HClO ₄ of modified FLG at 200 (blue), 100 (red), 50 (green), 20 (purple), and 5 mV s ⁻¹ (orange): (A) FLG _{AP} ; (B) FLG _{NP} ; (C) 3FLG _{AP} ; (D) 3FLG _{NP} . Comparisons of (E) FLG _{AP} and 3FLG _{AP} at 50 mV s ⁻¹ and (F) FLG _{NP} and 3FLG _{NP} at 50 mV s ⁻¹ also shown. | 161 |
| Figure 5.19: CD at selected scan rates in 1 M HClO ₄ of modified FLG: (A) FLG _{AP} ; (B) FLG _{NP} ; (C) 3FLG _{AP} ; (D) 3FLG _{NP} ; (E) comparison of A-D at 10.0 μA cm ⁻² ; (D) areal capacitance at selected current densities. | 162 |
| Figure 5.20: Areal capacitance during charge discharge cycling at 10.0 μA cm ⁻² in 1 M HClO ₄ : (A) FLG _{AP} and 3FLG _{AP} ; (B) FLG _{NP} and 3FLG _{NP} . FLG (blue) shown for comparison. | 164 |

- Figure 5.21: CVs in 1 M HClO₄ before and after 20,000 CD cycles at 10 μA cm⁻²: (A) FLG_{AP} and (B) 3FLG_{AP}. Scan rate = 50 mV s⁻¹. 165
- Figure 5.22: (A) CV of FLG_{CP} before and after EIS in 1 M HClO₄; (B) average areal capacitance versus voltage plots derived from EIS in 1 M HClO₄ at 115 Hz for FLG, FLG_{CP}, and 3FLG_{CP}. 166
- Figure 5.23: EIS data for FLG, FLG_{CP} and 3FLG_{CP} at 0.1 V in 1 M HClO₄: (A) Nyquist plot; (B) Bode phase angle plot; (C) Nyquist plot with fits. 167
- Figure 5.24: CV and CD results in 1 M HClO₄: (A) and (B) FLG_{CP}; (C) and (D) 3FLG_{CP}; (E) CV for FLG_{CP} and 3FLG_{CP} at 50 mV s⁻¹; (F) CD for FLG_{CP} and 3FLG_{CP} at 10 μA cm⁻². CVs recorded at 200 (blue), 100 (red), 50 (green), 20 (purple), and 5 mV s⁻¹(orange). 168
- Figure 5.25: Areal capacitance during charge discharge cycling at 10.0 μA cm⁻² in 1 M HClO₄ of FLG_{CP} and 3FLG_{CP}. 170
- Figure 5.26: Ragone plots for FLG systems shown in colour. Power and energy density calculated at 6.25, 10.0, 12.5, 25.0, and 50.0 μF cm⁻². Literature examples of CVD graphene (1), reduced graphene oxide multilayer film (2), graphene quantum dot micro-supercapacitor (3), layer by layer graphene supercapacitors (4), holey graphene (5), activated reduced graphene oxide (6), pillared graphene paper (7), and reduced graphene oxide hydrogel (8) also shown. 172
- Figure 6.1: AFM images of FLG transferred to a Si wafer before (A) and after (B) a 5 minute immersion on the Cu foil in the DMF gold deposition solution, with no applied potential. Scale bar = 500 nm. 183
- Figure 6.2: CV of FLG/Cu in DMF with: (blue) 0.36 mM (TOA)[AuCl₄] and 0.1 M TBAClO₄ or (red) 0.1 M TBAClO₄. Scan rate = 100 mV s⁻¹. 183
- Figure 6.3: CV of GC in DMF with: (blue) 0.36 mM (TOA)[AuCl₄] and 0.1 M TBAClO₄ or (red) 0.1 M TBAClO₄. Scan rate = 100 mV s⁻¹. 184
- Figure 6.4: Chronoamperometric transients of FLG/Cu in the gold deposition solution at -0.6 (blue) and -0.8 V (red) for 1 minute. 185
- Figure 6.5: AFM images of FLG_{Au} transferred to a silicon wafer after electrodeposition of gold nanoparticles on FLG/Cu for: (A) 5 minutes at -0.4 V; (B) 10 minutes at -0.4 V; (C) 5 minutes at -0.6 V; (D) 10 minutes at -0.6 V; (E) 10 minutes at -0.8 V. Scale bar = 1.25 μm. 186
- Figure 6.6: Dependence of (A) particle density, and (B) particle height on deposition time and applied potential. Error bars show the standard deviation of particle height over a 1 μm × 1 μm area. Hollow and solid symbols of the same colour show results of duplicate experiments under the same conditions. 187
- Figure 6.7: SEM image of FLG_{Au} transferred to a silicon wafer after a 10 minute electrodeposition of gold nanoparticles at -0.8 V on FLG/Cu. Scale bar = 5 μm. 187
- Figure 6.8: Relationship between nanoparticle density and particle height at different applied potentials and deposition times. Hollow and solid symbols of the same colour show results of duplicate experiments under the same conditions. 188

| | |
|---|-----|
| Figure 6.9: AFM image of FLG _{Au} transferred to a silicon wafer after deposition of gold nanoparticles on FLG/Cu for 1 minute at -0.6 V, followed by immersion in the same deposition solution for a further 9 minutes. Scale bar = 1.25 μm | 189 |
| Figure 6.10: Raman spectra of FLG transferred to a silicon wafer before (blue) and after deposition of gold nanoparticles for 5 minutes at -0.6 V on FLG/Cu (red). Spectra normalised to give a G-band intensity of 1. Spectra offset for clarity. | 190 |
| Figure 6.11: Shift in G-band (A) and 2D-band (B) position for FLG decorated with gold nanoparticles. Hollow and solid symbols of the same colour show results of duplicate experiments under the same conditions. | 191 |
| Figure 6.12: (A) CV in 1 M HClO ₄ before and after EIS for FLG _{Au} . Scan rate = 200 mV s^{-1} . (B) Average areal capacitance of FLG on Au/epoxy derived from EIS at 115 Hz in 1 M HClO ₄ before (blue) and after (red) gold deposition at -0.6 V for 10 minutes on FLG/Cu. | 191 |
| Figure 6.13: Average areal capacitance of FLG _{Au} (blue) and 3FLG _{Au} (red) derived from EIS at 115 Hz in 1 M HClO ₄ , after: (A) 10 minute deposition at -0.6 V and (B) 10 minute deposition at -0.8 V. | 193 |
| Figure 6.14: AFM images of a 1 minute Co-Ni hydroxide deposition at -1.0 V: (A) before and (B) after deposition on HOPG; (C) before and (D) after deposition on FLG/Cu. FLG transferred to Au/epoxy substrate for imaging. Scale bar = 1.25 μm | 194 |
| Figure 6.15: CVs of HOPG in 1 M KOH after a 1 minute Co-Ni hydroxide deposition at -1.0 V: (blue) cobalt and nickel hydroxide; (red) cobalt hydroxide only; (green) nickel hydroxide only. Scan rate = 20 mV s^{-1} | 195 |
| Figure 6.16: CV in 1 M KOH of FLG before (blue) and after (red/green) a 1 minute Co-Ni hydroxide deposition at -1.0 V. Scan rate = 20 mV s^{-1} | 196 |
| Figure 6.17: AFM images after Co-Ni hydroxide deposition at -1.0 V on FLG transferred to Au/epoxy for: (A) and (B) 30 seconds; (C) and (D) 1 minute; (E) and (F) 2 minutes. | 197 |
| Figure 6.18: SEM image after cobalt-nickel hydroxide deposition on FLG transferred to a Au/epoxy surface at -1.0 V for 1 minute. Scale bar = 500 nm. | 198 |
| Figure 6.19: XPS narrow scans of FLG _{Co/Ni} after Co-Ni hydroxide deposition on FLG on a Au substrate at -1.0 V for 1 minute. Left to right: O $1s$ narrow scan and Co $2p$ narrow scan; bottom: Ni $2p$ narrow scan. | 200 |
| Figure 6.20: CV in 1 M KOH of FLG _{Co/Ni} after Co-Ni hydroxide deposition at -1.0 V on FLG on a Au/epoxy substrate: (A) CV at 20 mV s^{-1} before and after 30 second, 1 minute, and 2 minute depositions; (B) CV at 50 (blue), 20 (red), 10 (green) 5 (purple), and 2 mV s^{-1} (orange) after a 1 minute deposition. | 201 |
| Figure 6.21: (A) CD at 1.6 mA cm^{-2} in 1 M KOH of FLG _{Co/Ni} after a 30 second, 1 minute, and 2 minute deposition at -1.0 V on FLG on a Au/epoxy substrate; (B) CD at different current densities for a FLG _{Co/Ni} after a 1 minute deposition at -1.0 V; (C) change in areal capacitance with applied current density. | 202 |

| | |
|---|-----|
| Figure 6.22: CV at 20 mV s^{-1} before and after all electrochemical measurements (15 CD cycles at each current density and EIS) of $\text{FLG}_{\text{Co/Ni}}$ in 1 M KOH: (A) 30 second deposition; (B) 1 minute deposition; (C) 2 minute deposition. | 204 |
| Figure 6.23: EIS data for FLG and $\text{FLG}_{\text{Co/Ni}}$ at 0.1 V in 1 M KOH: (A) Nyquist plot with fits and (B) Bode phase angle plot. (C) EEC used to fit data. | 205 |
| Figure 6.24: CV and CD in 1 M KOH of $\text{FLG}_{\text{CP+Co/Ni}}$: (A) CV at 50 (blue), 20 (red), 10 (green) 5 (purple), and 2 mV s^{-1} (orange) after 1 minute deposition on FLG on a Au/epoxy substrate; (B) CV at 20 mV s^{-1} , $\text{FLG}_{\text{Co/Ni}}$ shown for comparison; (C) CD at selected scan rates; (D) CD at 1.6 mA cm^{-2} , $\text{FLG}_{\text{Co/Ni}}$ shown for comparison. | 207 |
| Figure 6.25: AFM images after a 1 minute cobalt-nickel deposition at -1.0 V : (A) $\text{FLG}_{\text{Co/Ni}}$; (B) $\text{FLG}_{\text{CP+Co/Ni}}$ with the metal hydroxide film exposed; (C) $\text{FLG}_{\text{Co/Ni+NP}}$ with the film exposed. Scale bar = $1.25 \text{ }\mu\text{m}$ | 208 |
| Figure 6.26: Chronoamperometric transients for a 1 minute Co-Ni deposition at -1.0 V on FLG and FLG_{CP} | 209 |
| Figure 6.27: LBL deposition protocol to prepare $3\text{FLG}_{\text{Co/Ni}}$ (and $3\text{FLG}_{\text{CP+Co/Ni}}$ if a FLG_{CP} sheet is used rather than FLG). The metal hydroxide has only been drawn on one side of the FLG sheets for clarity. | 210 |
| Figure 6.28: CV in 1 M KOH of three-sheet stacks of $\text{FLG}_{\text{Co/Ni}}$ and $\text{FLG}_{\text{CP+Co/Ni}}$: (A) $3\text{FLG}_{\text{Co/Ni}}$ at 50 (blue), 20 (red), 10 (green), 5 (purple), and 2 mV s^{-1} (orange); (B) $\text{FLG}_{\text{Co/Ni}}$ and $3\text{FLG}_{\text{Co/Ni}}$ at 20 mV s^{-1} ; (C) $3\text{FLG}_{\text{CP+Co/Ni}}$ at 50 (blue), 20 (red), 10 (green), 5 (purple), and 2 mV s^{-1} (orange); (D) $\text{FLG}_{\text{CP+Co/Ni}}$ and $3\text{FLG}_{\text{CP+Co/Ni}}$ at 20 mV s^{-1} | 211 |
| Figure 6.29: Possible electron transport pathways for one- and three-sheet stacks of FLG after cobalt-nickel hydroxide deposition. The metal hydroxide has only been shown on one side of the initial FLG sheet for clarity. | 212 |
| Figure 6.30: CD at selected current densities in 1 M KOH: (A) $3\text{FLG}_{\text{Co/Ni}}$ and (B) $3\text{FLG}_{\text{CP+Co/Ni}}$. (C) Calculated areal capacitance at different current densities for the one- and three-sheet systems. | 213 |
| Figure 6.31: (A) Areal Ragone plot and (B) gravimetric Ragone plot for FLG, $\text{FLG}_{\text{Co/Ni}}$, $3\text{FLG}_{\text{Co/Ni}}$, $\text{FLG}_{\text{CP+Co/Ni}}$, and $3\text{FLG}_{\text{CP+Co/Ni}}$. Literature examples of 3D multilayered graphene foam with $\text{Co}(\text{OH})_2$ flakes (1), reduced graphene oxide with ruthenium nanoparticles (2), 3D graphene/nickel scaffold with MnO_2 nanoflowers (3), Ni-Fe layered double hydroxide/graphene aerogel (4), graphene aerogel with V_2O_5 particles (5), and commercial lead acid batteries, Li-ion batteries, and carbon-based supercapacitors also shown. | 216 |
| Figure 7.1: Metal hydroxide film sandwiched between two sheets of FLG to allow electron transfer from both sides of the film. | 228 |

List of Schemes

| | |
|--|-----|
| Scheme 1.1: Mechanism for the reaction of a carbon surface with an aryldiazonium ion through an aryl radical intermediate. | 8 |
| Scheme 1.2: Mechanism for the reaction of a carbon surface with an aryldiazonium ion through an aryl cation intermediate. | 8 |
| Scheme 1.3: Reaction of aryldiazonium cation directly with a carbon surface. Taken from Belanger et al. | 9 |
| Scheme 1.4: Mechanism explaining the formation of multilayer films through the reaction of aryldiazonium salts with a carbon surface. Adapted from Pinson et al. | 10 |
| Scheme 1.5: Generation of reactive species from aryldiazonium ions after the formation of a diazohydroxide species. | 11 |
| Scheme 3.1: Orienting free-floating and copper supported FLG sheets to give control over the final interface structure, either in a sandwiched or exposed arrangement. | 74 |
| Scheme 3.2: (A) Six proton, six electron reduction process from a NP to an aminophenyl group and (B) four proton, four electron reduction from a NP group to a hydroxylaminophenyl group, and subsequent two proton, two electron process to a nitrosophenyl group. | 86 |
| Scheme 4.1: Diels-Alder reaction between an aryne, generated from an anthranilic acid precursor, and a graphene surface. | 107 |
| Scheme 4.2: Proposed mechanism for the reaction of a primary amine with a carbon surface through a Michael-type addition. | 109 |
| Scheme 4.3: Two proton, two electron redox process of anthraquinone. | 127 |

List of Tables

| | |
|---|-----|
| Table 3.1: G and 2D-band positions, and 2D-band FWHM for FLG, FLG _{NP 2 hours} , and FLG _{NP 72 hours} | 74 |
| Table 3.2: IR peak assignments for the NBD and FLG _{NP} spectra shown in Figure 3.14. | 77 |
| Table 3.3: Atomic % values derived from XPS survey spectra for FLG, FLG _{NP 72hours} , and FLG _{IP 72hours} transferred to a silicon oxide wafer..... | 81 |
| Table 3.4: Narrow scan data for C 1s and N 1s peaks of FLG, FLG _{NP 72hours} , and FLG _{IP 72hours} transferred to a silicon oxide wafer. | 81 |
| Table 3.5: Peak assignments for NABD and FLG _{NAP} | 92 |
| Table 3.6: Peak assignments for CBD and FLG _{CBD 72hours} | 94 |
| Table 4.1: G- and 2D-band positions before and after modification with NAA or ME for six-hours. | 112 |
| Table 4.2: IR peak assignments for NAA and FLG _{NAA} | 114 |
| Table 4.3: IR peak assignments for ME and FLG _{ME} | 115 |
| Table 4.4: Survey spectra data for FLG, and FLG _{ME} | 116 |
| Table 4.5: G and 2D band peak positions for FLG and FLG _{NPEA} after a 20 hour reaction. | 123 |
| Table 4.6: IR peak assignments for NPEA and FLG _{NPEA} | 125 |
| Table 4.7: IR peak assignments for AAQ and FLG _{AAQ} | 126 |
| Table 5.1: Areal capacitance (C_A) of FLG on Au/epoxy in 1 M HClO ₄ calculated via method one (average over the plateau frequency range) or method two (at 115 Hz only), using Equation 5.2 at 0.1 V. | 142 |
| Table 5.2: Reaction conditions, surface concentration, and minimum areal capacitance (C_A) for FLG _{AP} surfaces..... | 152 |
| Table 5.3: Average areal capacitance values and potential drop of FLG, FLG _{AP} , 3FLG _{AP} , FLG _{NP} , and 3FLG _{NP} , calculated at 50 mV s ⁻¹ and at 10.0 μA cm ⁻² . Capacitance values after 20,000 charge discharge cycles (see Section 5.3.3.5) at 10 μF cm ⁻² are also listed. $n=2$ for all samples. | 163 |
| Table 5.4: Average areal capacitance for FLG, FLG _{CP} , and 3FLG _{CP} at 50 mV s ⁻¹ and 10 μA cm ⁻² . Areal capacitance after 20,000 charge discharge cycles at 10 μA cm ⁻² also included. $n=2$ for all samples. | 170 |
| Table 5.5: Average areal capacitance (C_A), gravimetric capacitance (C_G), areal energy density (E_A) and power density (P_A), and gravimetric energy density (E_G) and power density (P_G), calculated from CD at 10 μA cm ⁻² . $n=2$ for all samples... .. | 171 |
| Table 6.1: Atomic % values derived from XPS survey spectra for FLG, and FLG _{Co/Ni} on a gold substrate. | 198 |
| Table 6.2: Narrow scan data for O 1s, Co 2p and Ni 2p peaks of FLG, and FLG _{Co/Ni} on a gold substrate. | 199 |

| | |
|--|-----|
| Table 6.3: Areal capacitance values derived from CV at 20 mV s^{-1} and CD at 1.6 mA cm^{-2} (0.1 mA cm^{-2} for blank) in 1 M KOH before and after Co-Ni hydroxide deposition on FLG on a Au/epoxy substrate. $n=2$ for all samples. | 203 |
| Table 6.4: Capacitance values derived from CV at 20 mV s^{-1} and CD at 1.6 mA cm^{-2} (0.1 mA cm^{-2} for blank), for 1 M KOH after deposition with cobalt-nickel hydroxide nanoparticles onto FLG or FLG_{CP} . $n=2$ for all samples. | 207 |
| Table 6.5: Total mass of cobalt and nickel hydroxide for $\text{FLG}_{\text{Co/Ni}}$ and $\text{FLG}_{\text{CP+Co/Ni}}$ after a 1minute cobalt-nickel hydroxide deposition at -1.0 V on FLG on a Au/epoxy substrate derived from ICPMS analysis. | 210 |
| Table 6.6: Capacitance calculated from CVs at 20 mV s^{-1} and CD at 1.6 mA cm^{-2} for $\text{FLG}_{\text{Co/Ni}}$, $\text{FLG}_{\text{CP+Co/Ni}}$, $3\text{FLG}_{\text{Co/Ni}}$, and $3\text{FLG}_{\text{CP+Co/Ni}}$, and mass of cobalt and nickel hydroxide for each system determined by ICPMS. | 214 |
| Table 6.7: Areal and gravimetric capacitances (calculated using mass derived from ICPMS) for FLG and FLG_{CP} after cobalt-nickel hydroxide deposition, for one- and three-sheet systems (unmodified FLG shown for comparison). Mass of cobalt-nickel hydroxide determined using the area under the CV reduction peak at 20 mV s^{-1} and from ICPMS analysis also shown. | 215 |

List of Abbreviations

| | |
|--------------------------|---|
| $[\text{AuCl}_4]^-$ | Tetrachloroaurate |
| AAQ | 2-aminoanthraquinone |
| AFM | Atomic force microscopy |
| AP | Aminophenyl |
| ATR | Attenuated total reflection |
| CBD | 4-carboxybenzene diazonium tetrafluoroborate |
| CD | Charge discharge |
| CP | Carboxyphenyl |
| CPE | Constant phase element |
| FLG/Cu | Few layer graphene on copper foil |
| CV | Cyclic voltammogram |
| CVD | Chemical vapour deposition |
| DMF | N,N-dimethylformamide |
| DMSO | Dimethylsulfoxide |
| EDS | Energy dispersive X-ray spectroscopy |
| EEC | Electrical equivalent circuit |
| EIS | Electrochemical impedance spectroscopy |
| ESR | Equivalent series resistance |
| Fc | Ferrocene |
| Fc/Fc ⁺ | Ferrocene redox couple |
| FLG | Few layered graphene |
| 3FLG | Three sheet stack of few layer graphene |
| FLG _{AAQ} | Few layer graphene after 2-aminoanthraquinone modification |
| FLG _{AP} | Few layer graphene after nitrobenzene diazonium modification and subsequent reduction to an aminophenyl film |
| 3FLG _{AP} | Three sheet stack of few layer graphene after nitrobenzene diazonium modification and subsequent reduction to an aminophenyl film |
| FLG _{AS Physi.} | Few layer graphene after anthraquinone-2-sulfonic acid sodium salt physisorption |
| FLG _{Au} | Few layer graphene decorated with gold nanoparticles |
| 3FLG _{Au} | Three sheet stack of few layer graphene decorated with gold nanoparticles |
| FLG _{Co/Ni} | Few layer graphene decorated with cobalt-nickel hydroxide nanoparticles |

| | |
|--------------------------|---|
| 3FLG _{Co/Ni} | Three sheet stack of few layer graphene decorated with cobalt-nickel hydroxide nanoparticles |
| FLG _{CP+Co/Ni} | Few layer graphene with carboxyphenyl film, decorated with cobalt-nickel hydroxide nanoparticles |
| 3FLG _{CP+Co/Ni} | Three sheet stack of few layer graphene with carboxyphenyl film, decorated with cobalt-nickel hydroxide nanoparticles |
| FLG _{CP} | Few layer graphene after 4-carboxybenzene diazonium modification |
| 3FLG _{CP} | Three sheet stack of few layer graphene after carboxybenzene diazonium modification |
| FLG _{IP} | Few layer graphene after 4-iodobenzene diazonium modification |
| FLG _{ME} | Few layer graphene after 2-aminoterephthalic acid 4-methyl ester modification |
| FLG _{MP} | Few layer graphene after 4-methoxybenzene diazonium modification |
| FLG _{NAA} | Few layer graphene after 5-nitroanthranilic acid modification |
| FLG _{NAP} | Few layer graphene after 4-nitroazobenzene diazonium modification |
| FLG _{NP} | Few layer graphene after 4-nitrobenzene diazonium modification |
| 3FLG _{NP} | Three sheet stack of few layer graphene after nitrobenzene diazonium modification |
| FLG _{NPEA} | Few layer graphene after 4-nitrophenylethylamine modification |
| FLG _{NT Phys.} | Few layer graphene after nitrotoluene physisorption |
| FWHM | Full width at half maximum |
| GC | Glassy carbon |
| GO | Graphene Oxide |
| HER | Hydrogen evolution reaction |
| Hg/HgO | Mercury/mercury oxide redox couple |
| HOPG | Highly ordered pyrolytic graphite |
| IBD | 4-iodobenzene diazonium tetrafluoroborate |
| ICPMS | Inductively coupled plasma mass spectrometry |
| IP | Iodophenyl |
| IR | Infrared |
| KBr | Potassium Bromide |
| LBL | Layer by layer |
| MBD | 4-methoxybenzene diazonium tetrafluoroborate |
| MCT | Mercury cadmium telluride |
| ME | 2-aminoterephthalic acid 4-methyl ester |
| MP | Methoxyphenyl |
| NAA | 5-nitroanthranilic acid |

| | |
|---------------------------|---|
| NABD | 4-nitroazobenzene diazonium tetrafluoroborate |
| NAP | Nitroazophenyl |
| NBD | 4-nitrobenzene diazonium tetrafluoroborate |
| NP | Nitrophenyl |
| NPEA | 4-nitrophenylethylamine |
| PMMA | Polymethylmethacrylate |
| rGO | Reduced graphene oxide |
| PPF | Pyrolysed photoresist film |
| SCE | Saturated calomel electrode |
| SDS | Sodium dodecylsulfate |
| SEM | Scanning electron microscopy |
| SHE | Standard hydrogen electrode |
| STM | Scanning tunneling microscopy |
| TEM | Transmission electron microscopy |
| TBAClO ₄ | Tetrabutylammonium perchlorate |
| (TOA)[AuCl ₄] | Tetraoctylammonium tetrachloroaurate |
| UV | Ultraviolet |
| XPS | X-ray photoelectron spectroscopy |

List of Symbols

| | |
|------------|--|
| A | Working electrode surface area |
| Abs | Absorbance |
| A_{CV} | Area enclosed by CV |
| B | Magnetic field |
| c | Concentration |
| C_A | Areal capacitance |
| C_{Diff} | Diffuse capacitance |
| C_{DL} | Double layer capacitance |
| C_G | Gravimetric capacitance |
| C_H | Helmholtz capacitance |
| C_Q | Quantum capacitance |
| d | Charge separation distance in electrical double layer |
| db | Doublet |
| e | Electron charge |
| $E_{1/2}$ | Half wave potential |
| E_A | Areal energy density |
| E_G | Gravimetric energy density |
| F | Faraday's constant |
| f | Frequency |
| f_0 | Frequency in Bode phase angle plot where sample transitions from resistive to capacitive behaviour |
| \hbar | Reduced Planck constant |
| I | Current |
| J | Current density |
| k_B | Boltzmann constant |
| l | Pathlength |
| m | Medium intensity IR peak |
| n | Number of electrons involved in reduction or oxidation process |
| N | Number of fringes (IR spectroscopy) |
| n_C | Number of carriers in graphene |
| n_G | Number of carriers caused by potential |
| n_s | Number of carriers caused by charged impurities (holes and electrons) |
| P_A | Areal power density |
| P_G | Gravimetric power density |

| | |
|-----------------|---|
| Q | Charge associated with reduction or oxidation process |
| q | Elementary charge |
| Q_B | Constant phase element due to bulk |
| Q_{DL} | Constant phase element due to double layer |
| Q_L | Constant phase element due to film |
| R | Resistance |
| R_B | Bulk resistance |
| R_{CT} | Charge transfer resistance |
| R_L | Resistance within film |
| R_S | Solution resistance |
| R_{SH} | Sheet resistance |
| s | Strong intensity IR peak |
| T | Temperature |
| t_C | Charge time |
| t_D | Discharge time |
| V_{ch} | Graphene potential |
| V_H | Hall voltage |
| vs | Very strong intensity IR peak |
| w | Weak intensity IR peak |
| W | Warburg impedance |
| Z | Impedance |
| Z' | Real component of impedance |
| Z'' | Imaginary component of impedance |
| ΔV | Potential window |
| Γ | Surface concentration |
| δ | IR bend vibration |
| ε | Molar absorptivity |
| ε_d | Dielectric Constant |
| η | Coulombic efficiency |
| μ | Mobility |
| ν | IR stretch vibration |
| ν_a | IR asymmetric stretch vibration |
| ν_s | IR symmetric stretch vibration |
| $\bar{\nu}$ | Wavenumber |
| v_F | Fermi velocity of the Dirac electron |

| | |
|----------|-------------------------|
| ρ | IR scissoring vibration |
| σ | Conductivity |
| ν | Scan rate |

List of Publications

Results included in this thesis:

1. Farquhar, A. K.; Dykstra, H. M.; Waterland, M. R.; Downard, A. J.; Brooksby, P. A., Spontaneous modification of free-floating few-layer graphene by aryldiazonium ions: Electrochemistry, atomic force microscopy, and infrared spectroscopy from grafted films. *J. Phys. Chem. C* **2016**, *120*, 7543-7552
2. Farquhar, A. K.; Fitchett, C. M.; Dykstra, H. M.; Waterland, M. R.; Brooksby, P. A.; Downard, A. J., Diels-Alder reaction of anthranilic acids: A versatile route to dense monolayers on flat edge and basal plane graphitic carbon substrates. *ACS Appl. Mater. Interfaces* **2016**, *8*, 23389-23395.
3. Farquhar, A. K.; Brooksby, P. A.; Dryfe, R. A.; Downard, A. J., Controlled electrodeposition of gold nanoparticles onto copper-supported few-layer graphene in non-aqueous conditions. *Electrochim. Acta* **2017**, *237*, 54-60.

Others:

4. Brooksby, P. A.; Shields, J. D.; Farquhar, A. K.; Downard, A. J., Reduction of nitrophenyl films in aqueous solutions: How many electrons? *ChemElectroChem* **2016**, *3*, 2021-2026.
5. Brooksby, P. A.; Farquhar, A. K.; Dykstra, H. M.; Waterland, M. R.; Downard, A. J., Quantum capacitance of aryldiazonium modified large area few-layer graphene electrodes. *J. Phys. Chem. C* **2015**, *119*, 25778-25785.
6. Ounnunkad, K.; Patten, H. V.; Velicky, M.; Farquhar, A. K.; Brooksby, P. A.; Downard, A. J.; Dryfe, R. A. W., Electrowetting on conductors: Anatomy of the phenomenon. *Faraday Discuss.* **2017**.

1 Introduction

1.1 Graphene

Graphene is a two-dimensional material consisting of a single sheet of sp^2 -hybridised carbon atoms arranged in a honeycomb lattice.¹⁻³ In 2004, graphene was first isolated by Novoselov and Geim. Using a micromechanical approach involving repeated peeling of highly ordered pyrolytic graphite (HOPG), they successfully prepared single and few layer (2-9 layer) graphene (FLG) sheets.⁴ Graphene is the basic building block for many carbon materials such as carbon nanotubes, fullerenes, and HOPG, illustrated in Figure 1.1.⁵

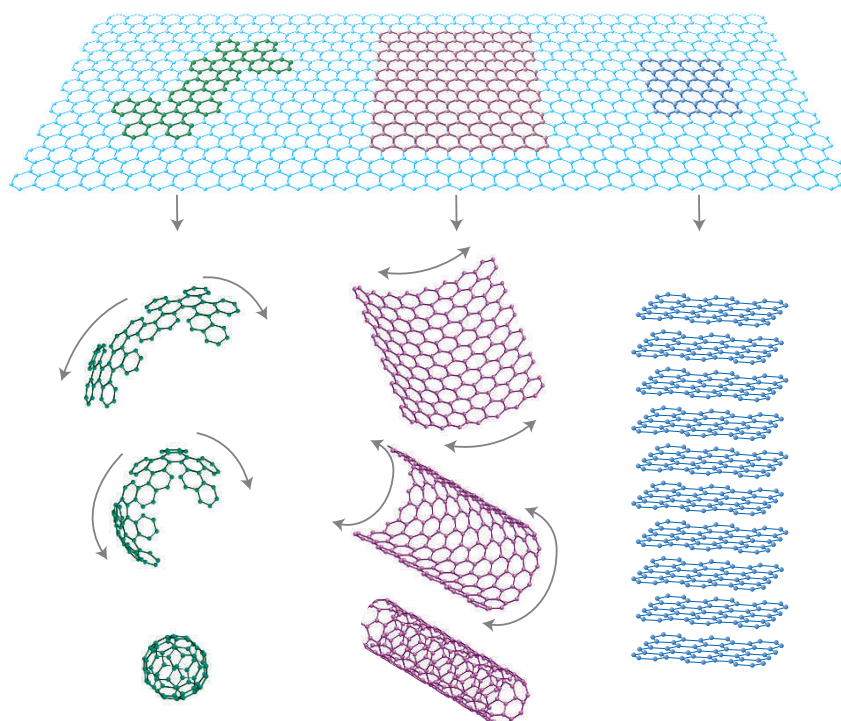


Figure 1.1: Structure of a single sheet of graphene, and illustration of the different graphitic materials derived from graphene: Bucky balls (green), carbon nanotubes (purple), and HOPG (blue).

Since the 2004 discovery of graphene, it has gained much attention due to its wide array of interesting properties. This work focusses on utilising graphene in energy storage materials, specifically supercapacitors. Graphene shows great promise in this area due to its high electrical conductivity and large surface area ($2630 \text{ m}^2 \text{ g}^{-1}$), which is the largest of any carbon material.⁶

1.2 Preparation of Graphene

1.2.1 Methods for Preparing Graphene

The original method for the preparation of graphene was via mechanical exfoliation. This is also known as the “scotch-tape” method, and gives single to FLG that has very few defects so exhibits the high conductivities and mobilities often associated with graphene.⁷ Unfortunately, this process is only able to produce small flakes of graphene and is not particularly scalable.

Several solution-based techniques have been developed for the preparation of graphene dispersions, which can then be collected onto various substrates. The most common method is the reduction of graphene oxide (GO). GO can be formed from the oxidation of graphite, typically via the Hummers method, which involves heating graphite in a mixture of concentrated sulfuric acid, sodium nitrite, and potassium permanganate.⁸ This material can then be readily dispersed in water or other polar solvents due to the presence of various oxygen containing functional groups, to give GO.⁹ Several modified Hummers methods are also available for graphite oxidation, which typically involve changing the oxidising agent.⁹ GO can be reduced via a chemical or thermal reduction process to give reduced graphene oxide (rGO).¹⁰ There are numerous examples of the preparation of GO and rGO in literature reports. Ruoff et al.¹¹ prepared GO using the Hummers method that was then dispersed in water and reduced using hydrazine at elevated temperatures. This procedure resulted in rGO nanoplatelets with improved electrical properties compared to the starting GO. Lu et al.¹² also used hydrazine as a chemical reducing agent. They reported that the addition of stabilising polymers enabled them to prepare rGO sheets with dimensional control due to the incorporation of rGO into the polymer matrix. Alternatively, thermal reduction methods can be used. Chabal et al.¹³ studied the thermal reduction of GO. An aqueous dispersion of GO was drop-cast onto a SiO₂/Si wafer, and then annealed at temperatures up to 850 °C, giving rGO. For all of these examples, the sp²-hybridised carbon network was only partially restored after reduction, which can alter the mechanical, chemical, and electrical properties of the resulting graphene material.¹⁴

Although most dispersion based techniques involve graphite oxidation as the first step, graphite materials can be exfoliated in a limited number of solvents to give dispersions

of graphene. This typically requires an organic solvent and high intensity ultrasonication. For instance, Coleman et al.¹⁵ generated a graphene dispersion of 0.01 mg mL⁻¹ with a monolayer yield of around 1% through exfoliation of graphite powder in N-methyl-pyrrolidone. Tagmatarchis et al.¹⁶ reported that graphene dispersions could also be produced in *o*-dichlorobenzene and the treatment of this dispersion with amphiphilic block copolymers, in acidic conditions, allowed the graphene to be transferred to an aqueous phase. However, the low yields and need for low boiling point organic solvents mean these methods are not suitable in the manufacture of workable devices. More recently, Villar-Rodil et al.¹⁷ described the successful preparation of a graphene dispersion in aqueous conditions. In this work, graphite powder was exfoliated in an aqueous solution of a flavin mononucleotide, which stabilised the graphene sheets, thereby allowing them to be dispersed in water. Hong et al.¹⁸ also prepared graphene dispersions in aqueous conditions by exfoliation of natural graphite flakes in water in the presence of the positively charged stabilising agent, 4-phenylene vinylene. Unfortunately, the addition of stabilising agents in these situations can alter the properties of the resulting graphene.

Electrochemical exfoliation is becoming an increasingly popular method for graphene production. Electrochemical exfoliation can be done at positive or negative potentials, however positive potentials are more common. Usually, a large positive potential (5-10 V) is applied, which causes the generation of hydroxyl radicals that can oxidise the graphite electrode. Intercalation of anions is then possible, causing exfoliation of the graphite electrode. Müllen et al.¹⁹ used this approach, applying a positive voltage (10 V) to a graphite electrode in sulfuric acid electrolyte. They reported that when the voltage was applied, the graphite began to expand, and quickly dissociated generating a graphene dispersion. The dispersion had > 80% of one to three layer graphene flakes, with a C/O ratio of 12.3, determined by X-ray photoelectron spectroscopy (XPS). Further work aimed to decrease oxidation by adding a range of reducing agents to the electrolyte (ascorbic acid, gallic acid, hydrazine monohydrate, sodium borohydride, and hydrogen iodide), to eliminate the hydroxyl radicals formed.²⁰ The C/O ratio was greatly improved (25.3), indicating less oxidation of the graphene. Majumder et al.²¹ used a different approach to eliminate hydroxyl radical production. They utilised shear induced effects to enable the exfoliation process at potentials as low as 1 V. Around 16% of the formed graphene sheets were monolayer, with 75% being less than four

layers. XPS results showed the graphene flakes produced using this method had a very low oxygen content, consistent with high quality graphene flakes.

As an alternative to solution based or “top down” approaches, graphene can be synthesised using “bottom up” approaches such as epitaxial growth and chemical vapour deposition (CVD). The epitaxial method typically involves heating a single crystal silicon carbide substrate above 1000 °C in an ultra-high vacuum chamber. This enables the sublimation of silicon atoms on the surface, and subsequent graphitisation of the carbon, forming a graphene film.²² On the other hand, CVD involves the thermal decomposition of a hydrocarbon precursor over a transition metal catalyst. CVD can produce large area graphene, which is convenient when preparing electrode materials, and so CVD was used as the method of graphene preparation in this project and is described in detail below.

1.2.2 Graphene CVD

The most common transition metal catalyst used in CVD for the preparation of graphene is copper. Copper is used due to the low solubility of carbon in copper: at 900 °C the solubility is only 0.0078%.²³ This means the CVD process is self-limiting because the low solubility results in a negligible amount of dissolved carbon that could contribute to multilayer growth as the substrate cools.²⁴ A typical CVD process involves heating the copper near its melting point (1085 °C) in a reducing atmosphere, typically hydrogen or a hydrogen/argon mixture, and annealing at this temperature for at least thirty minutes. This provides a better substrate for graphene growth as it generates a smooth copper surface, which has been reported to reduce the defect density of the resulting graphene.²⁵ After this, a carbon containing precursor is introduced into the system for a specified growth period.²⁶ During this growth phase a number of steps occur at the surface of the copper. First, the carbon precursor adsorbs to the copper surface and the copper catalyses the partial dehydrogenation of the carbon precursor to active carbon species. These carbon species diffuse across the surface to nucleation or defect sites where they nucleate and grow into a polycrystalline film.^{14, 27-28} After this phase, the carbon precursor is flushed from the system and the system is cooled to room temperature under an inert atmosphere.²⁹ The resulting graphene is a mono- to few-layer polycrystalline graphene sheet, consisting of pristine graphene domains interconnected via grain boundaries composed of aperiodic heptagon and pentagon

carbon ring pairs.²⁹ Grain boundaries can negatively impact the mechanical and electronic properties of the film,³⁰ therefore a film consisting of large domains with fewer grain boundaries is often desired.

Several parameters can be controlled during the CVD process to achieve the desired graphene film structure, including copper pre-treatment, carbon precursor choice, and hydrogen flow rate. Copper pre-treatment influences the size of the resulting graphene domains, and therefore grain boundary density. To grow large graphene domains, the number of defect sites on the copper needs to be minimised to provide fewer nucleation sites.³¹ Several methods have been developed to achieve this. Typically, the copper foil is cleaned prior to the CVD process. Work by Kim et al.²⁴ demonstrated that a nitric acid pre-cleaning step is able to improve the quality of the graphene by removing surface impurities that can act as nucleation sites. An electropolishing step of the copper prior to CVD is further able to decrease surface roughness and therefore nucleation density. Griep et al.³² reported a 99% decrease in copper surface roughness after electropolishing, allowing the formation of graphene with increased domain size and decreased sheet resistance. Many literature reports have utilised liquid or resolidified copper as the growth substrate. Heating the copper above 1085 °C during the annealing phase melts the copper foil, typically on a tungsten support. The copper can then either be resolidified or kept in liquid form for growth, which provides an extremely smooth surface. By using a liquid copper surface, well aligned, monolayer graphene domains of up to 200 µm across have been prepared.^{31, 33} Gu et al.³⁴ used a resolidified copper support as the catalyst; the resulting graphene domains had areas of up to 1 mm², indicating a very low nucleation density. An alternative method for decreasing the number of nucleation sites is through passivation of the copper, for example via oxidation. An oxide surface can suppress nucleation, allowing the synthesis of large domains.³⁵⁻³⁷ The oxide was also shown to accelerate growth rate, and change the growth kinetics to be diffusion limited. Liu et al.³⁸ described a different approach to passivation and utilised melamine to passivate the surface prior to growth. A solid melamine precursor was placed in the growth chamber with the copper foil. Prior to growth, the melamine was heated to the point of sublimation. Argon was then used as a carrier gas to transport the gaseous melamine to the copper, whereby it could passivate the surface. The resulting graphene domains were up to 1 cm across.

Another controlling factor in CVD growth of graphene is the choice of carbon precursor. Graphene has been grown from solid,³⁹ liquid,⁴⁰ and gaseous^{14, 26-27, 41} precursors. Solid precursors include polystyrene and other polymers, whereas liquid precursors can be hexane, benzene, and alcohols. However, gaseous precursors are usually advantageous because they have a higher purity than liquid or solid hydrocarbons, therefore do not dope the resulting graphene.⁴² Use of three different gaseous precursors has been reported: methane, ethylene, and acetylene.⁴¹ Of these, methane is the most popular due to its higher activation temperature. The higher reactivity of acetylene and ethylene means they are more likely to decompose to give amorphous carbon, thus degrading the quality of the resulting graphene. Hydrogen and argon gas are also often added to the system. Hydrogen is often introduced during the annealing stage as it provides a reducing atmosphere to assist in removing contaminants from the copper surface. During the growth phase, hydrogen plays two major roles. First it can catalyse the activation of the adsorbed hydrocarbons thereby encouraging graphene growth.⁴³ Also, it can act as a highly selective etchant to promote the growth of hexagonal graphene domains. The addition of argon to the system during growth dilutes the concentration of methane at the surface, which influences the number of layers of graphene grown.

1.2.3 Transfer of Graphene

After growth, the polycrystalline graphene film is typically removed from the copper support for transfer to a more useful substrate. Usually, the graphene layer is coated with a polymer support, often polymethylmethacrylate (PMMA), to prevent damage during the subsequent etching process.⁴⁴ The copper is then oxidised and completely dissolved by either iron chloride (FeCl_3)⁴⁵ or ammonium persulfate ($(\text{NH}_4)_2\text{S}_2\text{O}_8$)⁴⁶ solution and the graphene transferred to a different substrate. The PMMA layer is removed either by chemical dissolution or thermal annealing.⁴⁶ Unfortunately, both these methods can leave polymeric residues on the graphene surface, which can be detrimental to subsequent applications. Furthermore, graphene transferred this way is often cracked and wrinkled on the substrate. Protocols to improve the transfer procedure have been reported during this thesis work. Cho et al.⁴⁷ recently published a novel transfer method that reduced the formation of cracks and wrinkles in the graphene. The graphene was still spin coated with PMMA prior to the transfer, but before the graphene was collected and dried onto the new substrate, a small amount of

heptane was dropped onto the substrate. This procedure minimised the formation of lamination wrinkles and cracks. It is believed that the high contact angle of the transfer medium (water) trapped between the graphene and the substrate causes these wrinkles, so trapping a low surface tension liquid such as heptane prevents this. In another example, Unwin et al.⁴⁸ demonstrated a novel biphasic transfer method. The graphene/copper coupon is floated on the etchant solution, and a thin layer of hexane is added to the top of the etchant solution. Once the copper is completely etched, the monolayer graphene will sit at the organic/aqueous interface and the etchant is replaced with water. The graphene can then be scooped out with the required substrate. They demonstrated that this technique is applicable to a wide range of substrates including atomic force microscopy (AFM) tips and transmission electron microscopy (TEM) grids. The transfer of monolayer graphene or FLG after CVD onto an appropriate substrate is still problematic, and methods must continue to be developed, both to prevent damage to the graphene and eliminate the need for a polymer support.

1.3 Molecular Functionalisation of Graphene

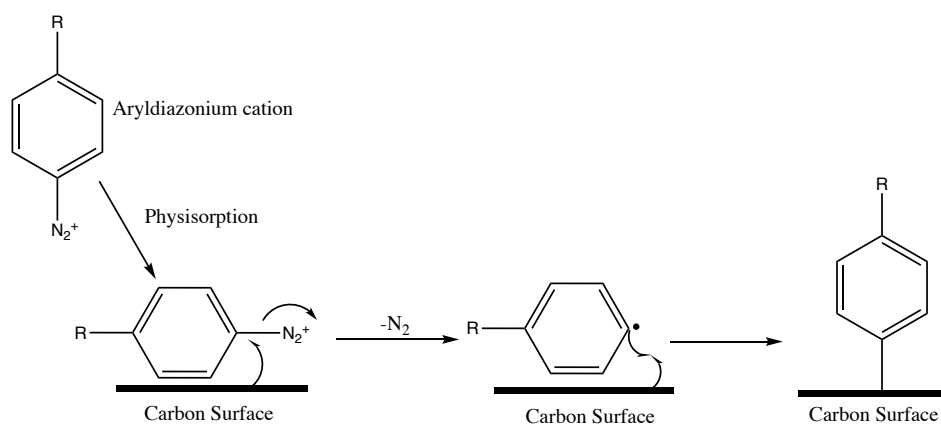
Chemical functionalisation is often used to overcome some of the limitations of graphene including its strong tendency to aggregate,⁴⁹ and limited chemical diversity.⁵⁰ In this work different modification protocols were used to functionalise graphene and these are described below.

1.3.1 Reactions of Aryldiazonium Salts

Aryldiazonium salts have been used to modify a wide variety of carbon surfaces including glassy carbon (GC),⁵¹⁻⁵⁶ HOPG,⁵⁷⁻⁵⁹ carbon powders and fibres,⁶⁰⁻⁶¹ diamond-like carbon,⁶² and graphene.⁶³⁻⁶⁵ The grafting reaction can be electrochemically driven,^{59-60, 66} spontaneous,^{61, 64} or initiated through the addition of a chemical reducing agent such as hypophosphorous acid and typically leads to disordered multilayer films.⁶⁷⁻⁶⁸ The reaction can be carried out in aqueous,^{61, 64, 69} acidic,^{60, 66} non-aqueous,⁵⁵⁻⁵⁶ and high pH solutions.⁷⁰

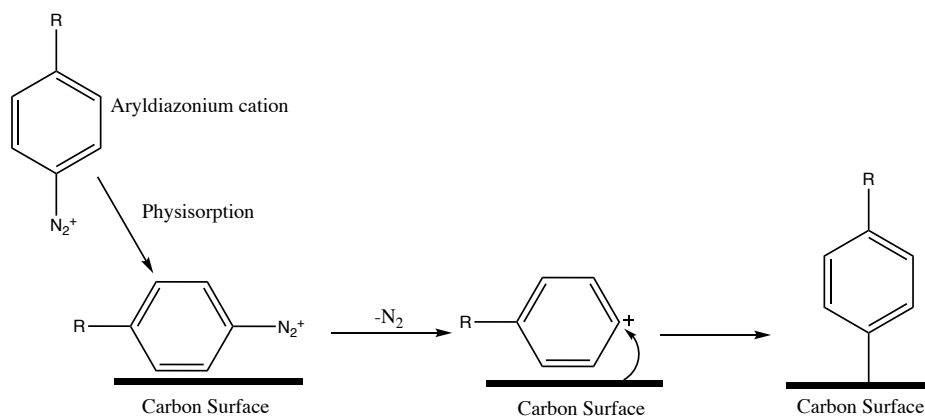
For spontaneous grafting in aqueous conditions the first step is believed to be the physisorption of the aryldiazonium cation at the carbon surface. Work by Colavita et al.⁶¹ and Strano et al.^{69, 71} on amorphous carbon and carbon nanotubes respectively, indicated that spontaneous grafting involved an initial adsorption step, followed by

decomposition into the covalently bonded species. Raman spectroscopy results from Stark et al.⁶³ indicate that this is also true for reactions involving graphene. In aqueous, acidic, and non-aqueous conditions the final reactive species is an aryl radical, an aryl cation, or the diazonium ion itself. The formation of a carbon-carbon bond with the surface via an aryl radical is a well-understood and accepted process. The physisorbed aryldiazonium ion undergoes a one electron reduction via electron transfer from the carbon, resulting in the formation of an aryl radical that can subsequently form a covalent bond with the carbon surface.⁶⁵ This is illustrated in Scheme 1.1; the initial physisorption step is also shown.



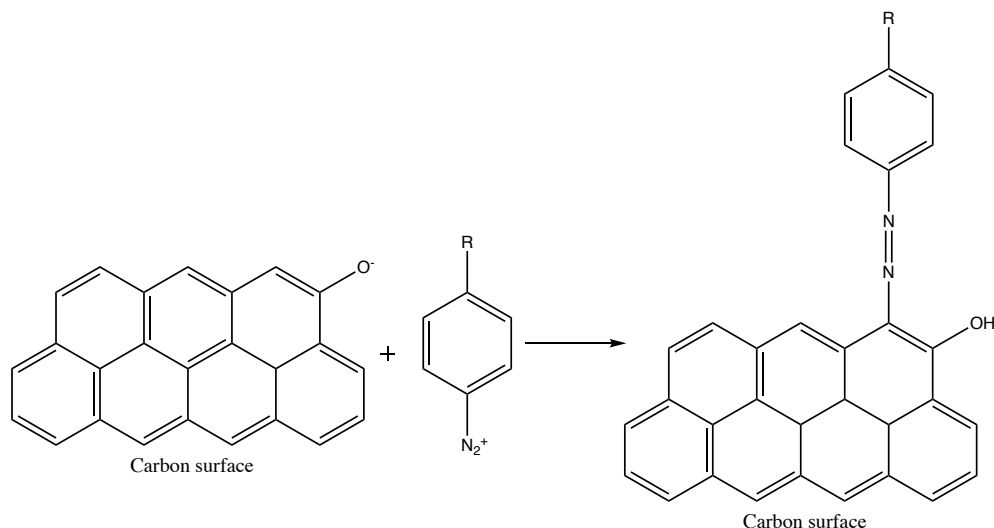
Scheme 1.1: Mechanism for the reaction of a carbon surface with an aryldiazonium ion through an aryl radical intermediate.^{61, 71-72}

An alternative mechanism, leading to grafting via a carbon-carbon bond is through the generation of an aryl cation that results from a heterolytic dediazonation reaction (Scheme 1.2).^{65, 72-73} Unlike the radical mechanism, this pathway does not require an external electron source. The cation mechanism is most favourable in acidic conditions (pH < 4) in the absence of an electron source.^{70, 74}



Scheme 1.2: Mechanism for the reaction of a carbon surface with an aryldiazonium ion through an aryl cation intermediate.⁷²

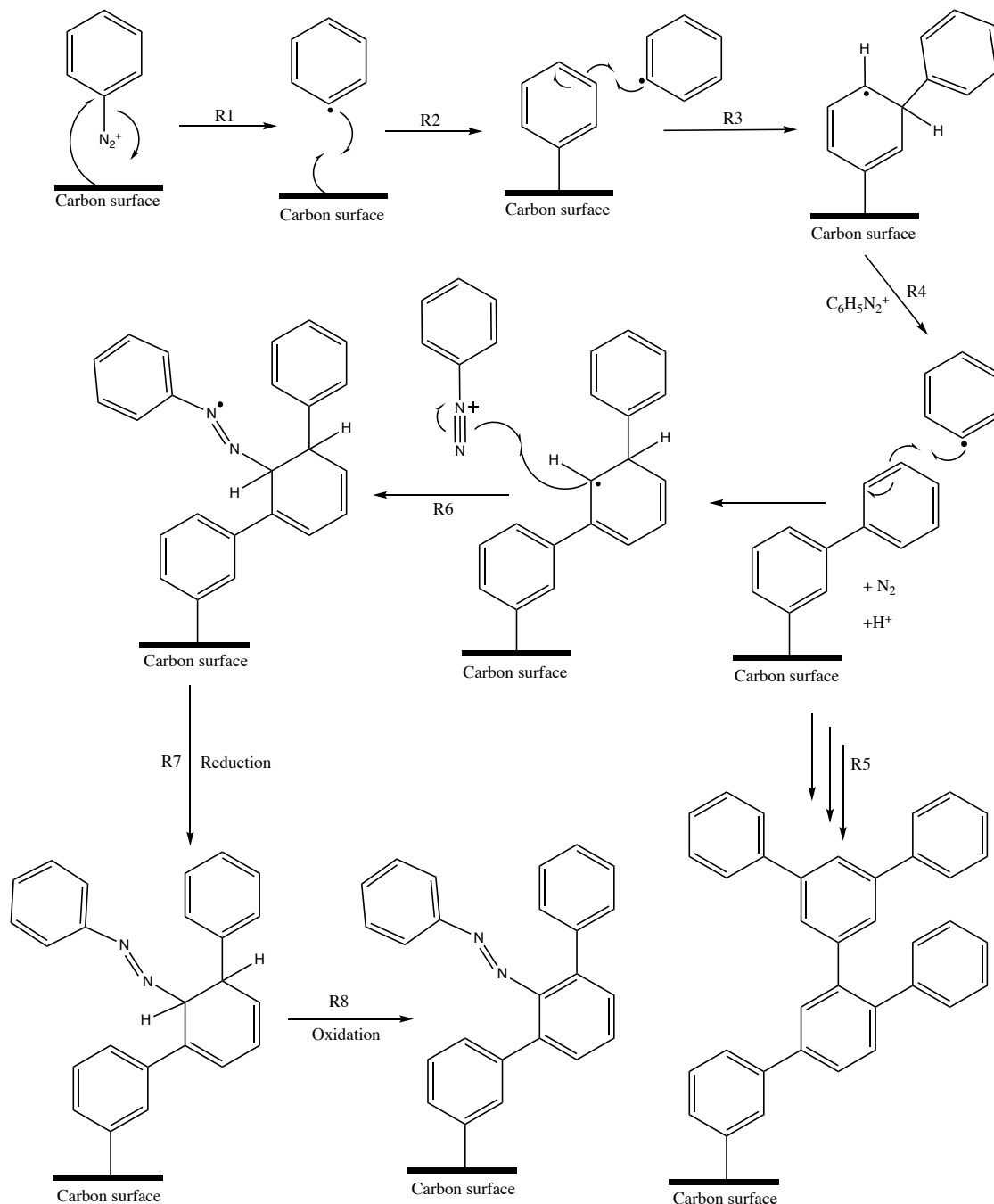
It is also possible to form azo bonds with the carbon surface. Belanger et al.⁷⁵ proposed a mechanism for carbon black modification based on the reaction of β -naphthol with diazonium salts that relies on the presence of an *ortho* phenolic functionality (Scheme 1.3).⁷⁶



Scheme 1.3: Reaction of aryldiazonium cation directly with a carbon surface. Taken from Belanger et al.⁷⁵

Typically, with aryldiazonium salt chemistry, a multilayer is grafted. A mechanism commonly reported in literature and shown in Scheme 1.4, was initially proposed by Pinson et al.⁷⁶ and describes the formation of multilayers on the surface of carbon and other conducting substrates.^{65, 73, 77} This film growth mechanism explains the presence of both carbon-carbon and azo bonds in the film. For simplicity, an unsubstituted aryldiazonium ion has been used, the initial bond to the surface was assumed to be generated via the aryl radical route, and the physisorption step has not been shown. The first step is the single electron reduction of an aryldiazonium ion to give an aryl radical. The aryl radical can then bind to the surface (Scheme 1.1). The generation of a second aryl radical and subsequent reaction with the already grafted group gives a cyclohexadienyl radical (R3). This then opens two possible reaction pathways. The first (R4) involves the generation of a third radical via an electron exchange leading to reoxidation of the cyclohexadienyl radical and reduction of an aryldiazonium ion. This can then form a carbon-carbon bond with the already grafted group. This mechanism has been investigated experimentally on glassy carbon using time of flight-secondary ion mass spectrometry,⁷⁸ as well as on gold using an electrochemical method.⁷⁹ Repetition of this cycle (R5) results in a multilayer phenyl film. The second pathway generates azo linkages. The first step (R6) is the reaction of the diazonium ion with the

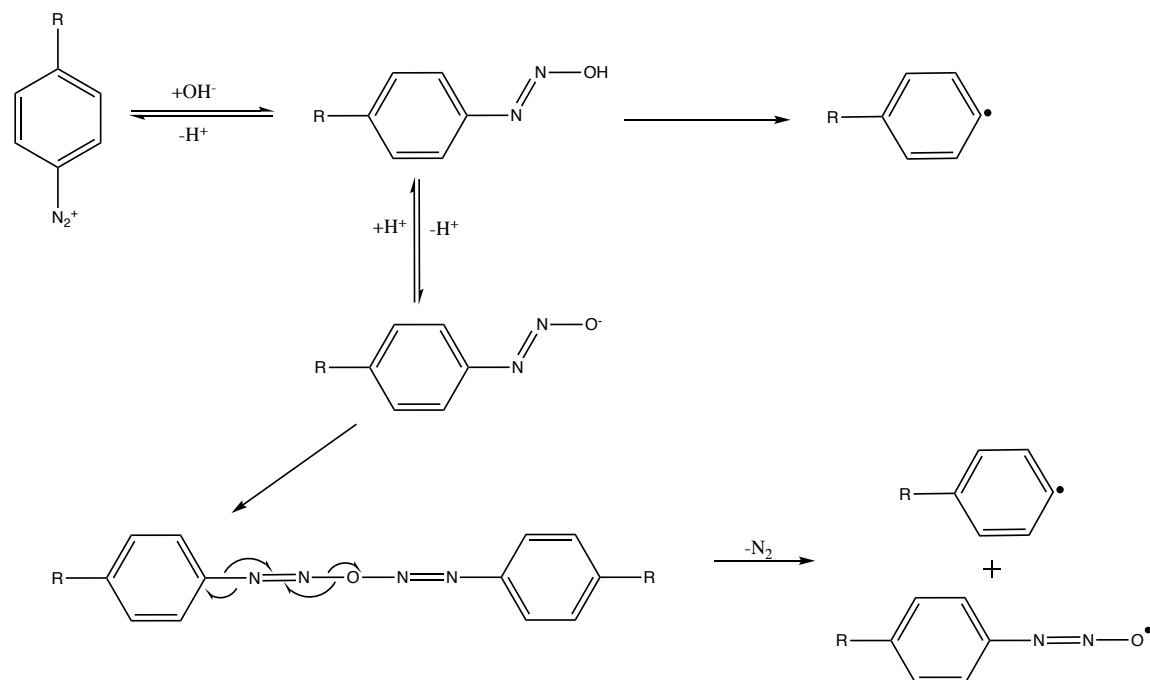
cyclohexadienyl radical, followed by a reduction step (R7). Reoxidation (R8) will then take place to restore aromaticity and conjugation. Both pathways may continue to occur to give multilayer growth. Belanger et al.⁶⁵ suggested both are operative for the modification of graphite and graphene.



Scheme 1.4: Mechanism explaining the formation of multilayer films through the reaction of aryldiazonium salts with a carbon surface. Adapted from Pinson et al.⁷⁶

Alternatively, grafting may involve the formation of a diazohydroxide species, which has been reported in aqueous, weakly acidic, and high pH conditions (Scheme 1.5).⁷⁰ The diazohydroxide can decompose to give an aryl radical that can react with the

surface as illustrated in Scheme 1.1. Furthermore, the diazohydroxide exists in equilibrium with its diazoate form. The diazoate can react with a second aryldiazonium ion forming a diazonium anhydride. Homolytic cleavage of this results in the formation of two radical species, which can both form covalent bonds with the carbon surface.⁸⁰



Scheme 1.5: Generation of reactive species from aryldiazonium ions after the formation of a diazohydroxide species.

1.3.2 Diels-Alder Reactions

Graphene can also be covalently functionalised via a Diels-Alder reaction. This is a [4+2] cycloaddition reaction, between a diene and a dienophile, resulting in a six-membered ring.⁸¹ As graphene is a highly aromatic, chemically stable system, it would not typically be expected to take part in such a reaction, because aromatic molecules do not usually participate in thermal (ground state) reactions. However, the unique electronic structure of graphene means Diels-Alder reactions are possible. Graphene is defined as a zero-band gap semiconductor, meaning that the conduction and valence bands meet at the Dirac point (see Section 1.5).⁸² This absence of an energy gap means graphene can exist in a number of resonance forms, shown in Figure 1.2. This allows graphene to act as either a diene or a dienophile in the Diels-Alder reaction.⁸¹⁻⁸³

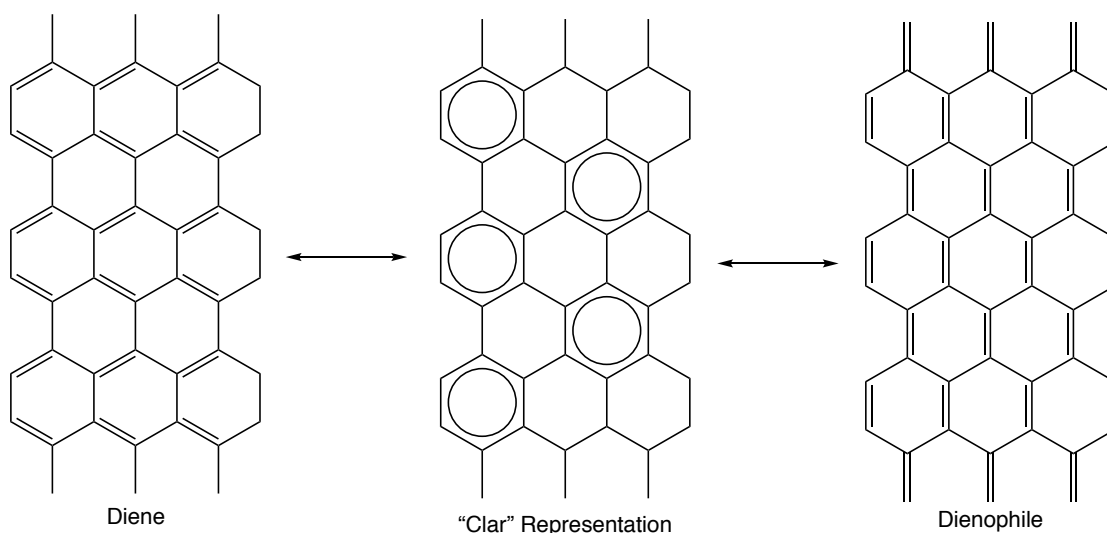


Figure 1.2: Resonance forms of graphene.⁸¹

Haddon et al.⁸² has reported the Diels-Alder reaction of graphene with a variety of modifiers. These are shown in Figure 1.3.

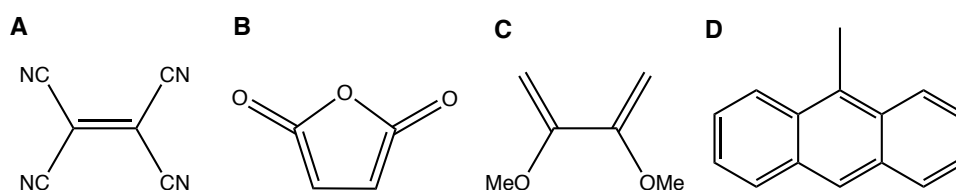


Figure 1.3: Dienes and dienophiles used by Haddon et al. for the Diels-Alder reaction of graphene: (A) tetracyanoethylene; (B) maleic anhydride; (C) 2,3-dimethoxy-1,3-butadiene; (D) 9-methylanthracene.

In Haddon's work, graphene was used as both a diene and a dienophile. As a diene, graphene could be readily functionalised by the highly reactive dienophile tetracyanoethylene (Figure 1.3A) at room temperature. The resulting Raman spectrum showed a high degree of functionalisation, indicated by a very prominent D band. The reaction scheme is shown in Figure 1.4. The dienophile maleic anhydride (Figure 1.3B) was less reactive towards graphene. The reaction required heating to 130 °C for dispersed graphene and 70 °C for epitaxial graphene. For both starting materials, the product underwent a cycloreversion process at 150 °C.

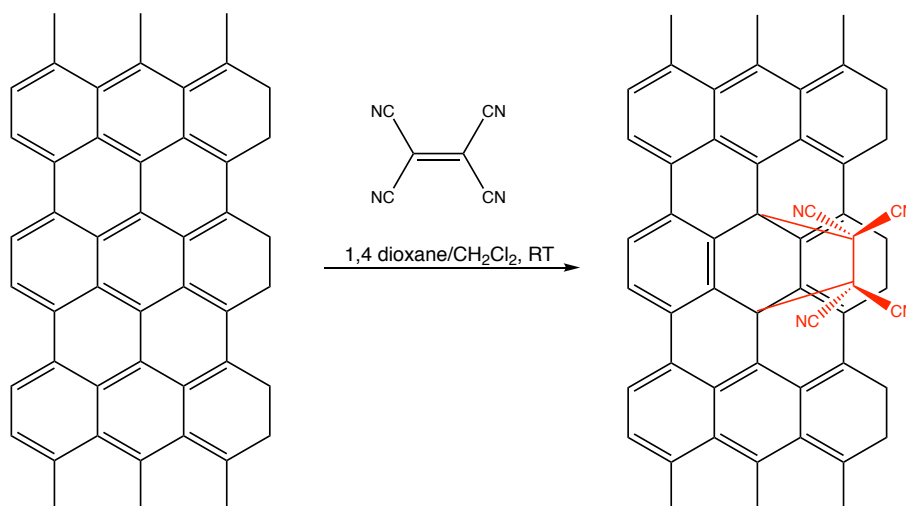


Figure 1.4: Diels-Alder reaction between graphene (diene) and tetracyanoethylene (dienophile).

This work also investigated the use of graphene as a dienophile by investigating the reaction with 9-methylanthracene (Figure 1.3D) and 2,3-dimethoxy-1,3-butadiene (Figure 1.3C). The reaction with 9-methylanthracene required heating to 130 °C, while the optimum temperature for 2,3-dimethoxy-1,3-butadiene was only 50 °C. The reaction scheme for the latter diene is shown in Figure 1.5. The different temperature requirements for the Diels-Alder reaction with each precursor compound indicates that tetracyanoethylene is the most reactive species towards graphene Diels-Alder reactions. This work demonstrates the versatility of the Diels-Alder reaction for graphene functionalisation.

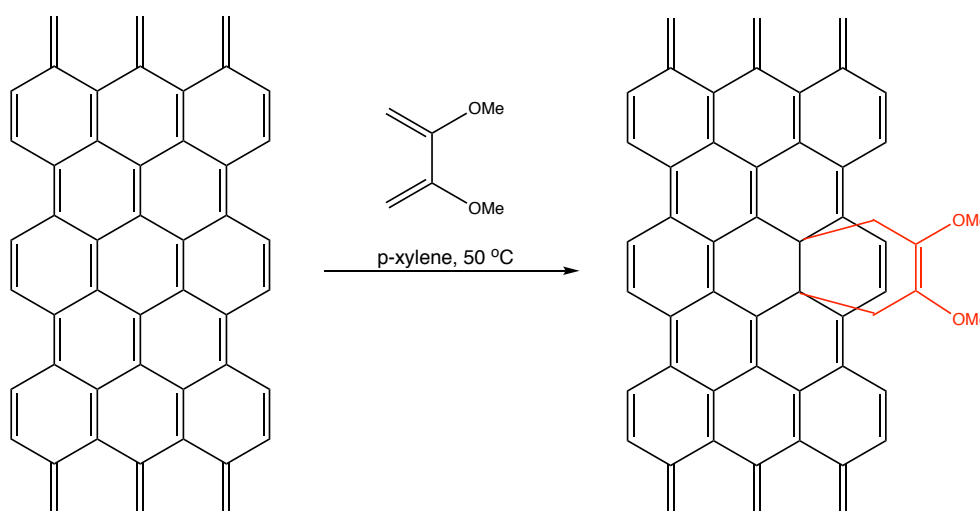


Figure 1.5: Diels-Alder reaction between graphene (dienophile) and 2,3-dimethoxy-1,3-butadiene.

An alternative approach for the Diels-Alder reaction is to use a mechanochemically driven solid-state reaction. Braunschweig et al.⁸⁴ demonstrated this using various

cyclopentadienes with either Raman or electrochemically active tags. These cyclopentadienes were coated onto an elastomeric tip mounted onto an atomic force microscopy cantilever. This could be used to exert a localised force between the cyclopentadiene and the graphene sheet, allowing the Diels-Alder reaction to proceed. The functionalisation was then characterised using either Raman spectroscopy or cyclic voltammetry. This process enabled covalently patterned sheets of graphene to be obtained at ambient temperature and atmospheric pressure. A similar force-accelerated reaction was demonstrated by Baek et al.,⁸⁵ however, here a ball-milling approach was used, where graphite and maleic anhydride or maleimide were crushed together. The resulting product was easily dispersed in various solvents to give functionalised graphene nanoplatelets.

An alternative, and extremely reactive intermediate that can be used as a dienophile in the Diels-Alder reaction is an aryne.⁸⁶ An aryne is a neutral, highly reactive species that is generated from the abstraction of two *ortho* substituents on an arene.⁵⁰ Two common methods exist for the generation of an aryne. Firstly, arynes can be derived from the reaction of 2-trimethylsilylphenyl triflate with caesium fluoride.⁸⁷⁻⁸⁸ Alternatively, the aryne can be generated from an anthranilic acid precursor. Anthranilic acids consist of a benzene ring with a primary amine and carboxylic acid group positioned *ortho* to one another. The treatment of the anthranilic acid with isoamyl nitrite generates a benzenediazonium-2-carboxylate species that will thermally decompose to give an aryne accompanied by the loss of carbon dioxide and nitrogen.⁸⁹ These two protocols are shown in Figure 1.6.

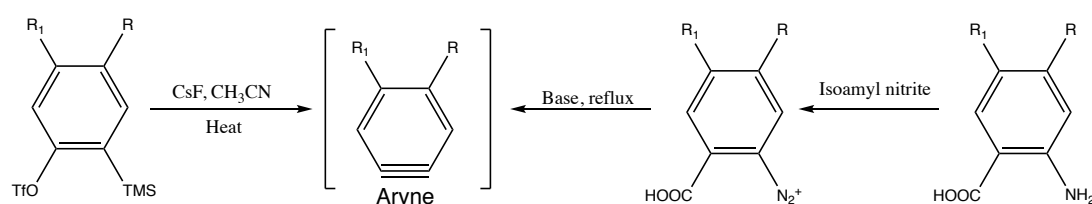


Figure 1.6: Different protocols for the generation of an aryne.

Ma et al.⁸⁷ reported the use of the triflate precursor for reaction with a graphene dispersion. They reported a degree of functionalisation of one group per 17 carbon atoms after a 24 hour reaction at 45 °C. Kalugin et al.⁸⁸ also reported the successful modification of both HOPG and CVD graphene using the triflate precursor. Conversely, Cougnon et al.⁹⁰ utilised an anthranilic acid as the aryne precursor. They

reported that after a 24 hour reaction, a carbon powder could be successfully modified. Interestingly, the application of this reaction to a carbon powder implies it is applicable to both basal plane carbons such as graphene and HOPG, as well as edge plane carbons such as activated carbon.

1.3.3 Other Molecular Functionalisation Methods

Many other reactions have been reported for efficient graphene functionalisation. The 1,3-dipolar cycloaddition reaction is a popular choice for graphene modification. This is a [3+2] cycloaddition reaction between a 1,3-dipole and a dipolarophile (graphene). For graphene, the 1,3-dipole is commonly an unstable azomethine ylid, generated from a decarboxylation reaction between N-methyl-glycine and a carbonyl species.⁹¹ Trapalis et al.⁹² demonstrated this reaction using a graphene dispersion. The thermogravimetric analysis of the resulting product indicated one functional group per 40 carbon atoms, and the functionalised material was readily dispersed in several solvents. Prato et al.⁹³ showed via TEM that this reaction takes place on both the edges and the basal plane. Miranda et al. described a novel way to modify graphene surfaces is using cyanomethyl radicals.⁹⁴ The radicals were generated by electron bombardment of acetonitrile in ultrahigh vacuum. The cyanomethyl radical reacted with the double bonds of graphene forming a C-C single bond. By introducing curvature to the graphene sheet, Miranda and co-workers could dictate the site of functionalisation. A different approach to covalent modification of graphene is through the introduction of single atoms. Hydrogen, fluorine, chlorine, and oxygen atoms have been successfully added to graphene sheets.⁹⁵ For example, graphene can be halogenated by treatment with a halogen based plasma. Although these modification approaches are an ongoing area of research, they are beyond the scope of this thesis work, so will not be discussed further.

1.4 Deposition of Metal Nanoparticles onto Graphene

An alternative way to modify graphene is through the deposition of metal nanoparticles. Metal nanoparticles possess many interesting optical, magnetic, electrical, and chemical properties that are unique from the bulk material. When combined with graphene, the hybrid materials can display the unique properties of graphene and the nanoparticles, as well as novel properties resulting from the synergistic relationship between the two materials.⁹⁶ Of the available metal nanoparticles, gold is the most commonly seen in the literature for graphene/nanoparticle hybrids, although examples

of silver, palladium, and platinum graphene hybrid materials have been reported.⁹⁷⁻⁹⁹ Gold/graphene hybrid materials have been shown to have numerous applications. Work by Vacárcel et al.¹⁰⁰ demonstrated that rGO decorated with gold nanoparticles is a potential substrate for surface-enhanced Raman spectroscopy, and utilised this to detect the antibiotic metronidazole. Gold nanoparticles encapsulated by FLG were shown to be an effective non-enzymatic glucose sensor.¹⁰¹ Zhang et al.¹⁰² used a gold/graphene hybrid material as a field emission device. Finally, Chen and Ju deposited gold nanoparticles onto nitrogen-doped graphene. This material showed high selectivity and sensitivity for the electrochemical detection of hydrogen peroxide.¹⁰³

A range of different preparation methods exist for depositing gold nanoparticles onto graphene. Often a gold film is thermally evaporated onto graphene and subsequent annealing of the film in argon allows nanoparticles to form.¹⁰⁴⁻¹⁰⁶ Work by Kim et al.¹⁰⁵ showed aggregation of these nanoparticles occurred at grain boundaries and wrinkles, and therefore used this technique to visualise these different surface features of graphene. Another option is to make the nanoparticles *ex situ*, typically through the citrate reduction method, and then dropcast them onto graphene.^{100, 107} The distribution of these nanoparticles on graphene is not always uniform. Interestingly, gold nanoparticles can be spontaneously deposited onto graphene grown via CVD. Work by Toth et al.,¹⁰⁸ illustrated that when CVD graphene, on its copper support, is submerged in a tetrachloroaurate aqueous solution, the copper foil is able to reduce the gold salt, causing nanoparticles to deposit at the graphene surface. Substantial nanoparticle growth was reported after only a one minute immersion. This process is possible because the reduction potential of the Cu/Cu²⁺ couple (+0.34 V vs. standard hydrogen electrode (SHE)) is significantly less positive than the reduction potential of the Au/[AuCl₄]⁻ couple (+1.002 V vs. SHE). This means that copper metal can reduce gold salts in aqueous solution. The gold nanoparticles grown ranged from 5 to 10 nm in diameter. Furthermore, it was possible to decorate the other side of the graphene with a second type of metal nanoparticle after removing the copper foil by oxidation. The free-standing graphene/gold nanoparticle sheet was floated, gold side upwards, on an aqueous solution containing either PdCl₄²⁻ or PtCl₄²⁻, and an organic solution containing decamethylferrocene was then added over the graphene/gold sheet. The decamethylferrocene reduced the metal salt at the liquid-liquid interface, resulting in

deposition of the palladium or platinum nanoparticles on the underside of the graphene. Finally, gold nanoparticles can be electrochemically deposited onto graphene. Application of a negative potential reduces the gold salt to Au(0) that can nucleate at the surface as nanoparticles. Benvidi et al.¹⁰⁷ applied a potential of -0.2 V vs. Ag/AgCl to a rGO electrode in a tetrachloroaurate aqueous solution for a fixed time, which allowed nanoparticles to deposit. Yang¹⁰⁹ showed that the electrochemical deposition process enabled the size and shape of the nanoparticles to be efficiently controlled by varying the applied potential and current passed.

Work has also involved depositing metal oxide and metal hydroxide nanoparticles onto graphene. Metal oxide and metal hydroxide nanoparticles can increase the energy storage capability of the system, as will be explained in Section 1.6. Several different metal oxides and hydroxides have been deposited onto graphene for this purpose, including iron oxide, manganese dioxide, cobalt oxide, nickel hydroxide, and cobalt hydroxide. The most common way to prepare the composite materials is through a hydrothermal synthesis. For instance, Gao et al.¹¹⁰ heated a dispersion of GO in an aqueous solution of iron(II) sulfate and hydrazine for 24 hours at 160 °C, in a Teflon lined stainless steel autoclave, resulting in rGO decorated with iron oxide nanocubes. Similarly, Jin et al.¹¹¹ heated a GO dispersion with manganese acetate in an ethanol water mix for 11 hours at 180 °C, to give rGO decorated with 37-50 nm manganese dioxide particles. Alternatively, electrochemical deposition can be used to deposit metal oxide and metal hydroxide nanoparticles. Cobalt hydroxide nanoflakes were deposited onto a graphene foam using cyclic voltammetry (CV) between 0 to -1.2 V vs. Ag/AgCl in cobalt nitrate electrolyte. Reduction of the nitrate results in the generation of hydroxide ions, which forces the precipitation of cobalt hydroxide at the surface.¹¹²

1.5 Doping of Graphene

According to computational tight binding calculations, graphene is a zero-band gap semiconductor or semimetal.¹¹³ This means that the valence and conduction band meet at the Fermi level. The addition of dopants to the graphene can open a band gap, and will increase the carrier concentration. This has important consequences for electronic applications. The influence of carrier concentration on capacitance will be discussed later. Two types of doping have been shown for graphene, namely electrical and

chemical doping. Electrical doping can be gate- or substrate-controlled. Chemical doping is achieved via doping with heteroatoms, or molecular functionalisation, including using the functionalisation methods outlined above. If graphene is functionalised, for example using aryldiazonium chemistry, with an electron-withdrawing group (eg. nitrophenyl), the group will locally remove electrons from the valence band, which will introduce holes and therefore p-dope the graphene. On the other hand, for graphene functionalised with an electron-donating group (eg. methoxyphenyl), the group will donate electrons and therefore n-dope the sample.⁶³ This is analogous to doping in extrinsic semiconductors. Furthermore, doping will shift the Fermi level towards the conduction band in n-doped samples and towards the valence band for p-doped samples, resulting in band gap opening.¹¹⁴

1.6 Graphene Supercapacitors

1.6.1 What are Supercapacitors

Batteries are one of the most well-known energy storage devices. In batteries, energy is stored as chemical potential energy, as an active material in the two electrodes. The energy can be released by connecting a load across the terminals of the electrodes, allowing the electrode materials to react electrochemically, resulting in current generation.¹¹⁵ Unfortunately, batteries have a number of unsatisfactory aspects, including their limited shelf and cycle life, a low charge/discharge rate,¹¹⁶ and their construction from toxic materials such as lead, or scarce metals such as lithium.¹¹⁷ Supercapacitors (also known as ultracapacitors or electrochemical capacitors) are an attractive alternative. Unlike batteries, supercapacitors have a large cycle life, high charge discharge capability, and are typically made from much safer materials, such as carbon,¹¹⁸ however they have a significantly lower energy storage density than batteries, so the technology must be developed.¹¹⁹ The Ragone plot below illustrates the difference in performance between the two devices (Figure 1.7). Batteries have a high energy density but a low power density (the rate at which energy can be supplied), whereas supercapacitors have a high power density, but a low energy density.

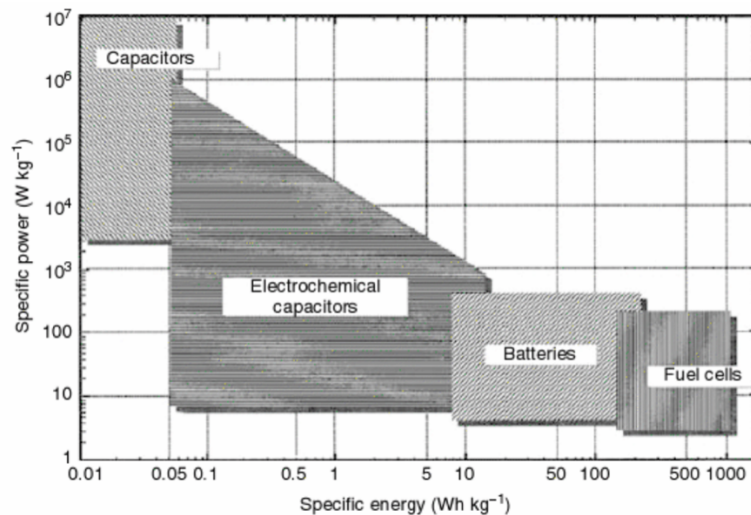


Figure 1.7: Ragone plot for common energy storage materials. Reproduced from Liu et al.¹²⁰

The construction of supercapacitors is similar to batteries in that there are two electrodes submerged in an electrolyte, with a separator between the electrodes.¹¹⁵ There are two modes of energy storage possible in a supercapacitor: electrical double layer capacitance and pseudocapacitance.¹²¹ Electrical double layer capacitance is a result of the double layer formed by accumulation of electrostatic charge at the electrode-electrolyte interface.¹²² Energy storage is a result of charge separation at the interface. It is therefore an electrostatic mode of energy storage, rather than chemical. Figure 1.8 illustrates the development of different models of the electrical double layer. The first model of the electrical double layer was proposed by Helmholtz in 1879, and considered the double layer as a compact layer of equal and opposite charge at the electrode surface. The Helmholtz theory ignored the diffusion or thermal motion of the ions near the electrode and thus oversimplifies the double layer. The Guoy-Chapman model, developed independently from the Helmholtz model, considers the thermal motion of ions near the charged surface. They suggested the electrolyte side of the double layer consisted of a diffuse layer comprised of both anions and cations. The Helmholtz and Guoy-Chapman model both consider the ions to be point charges.

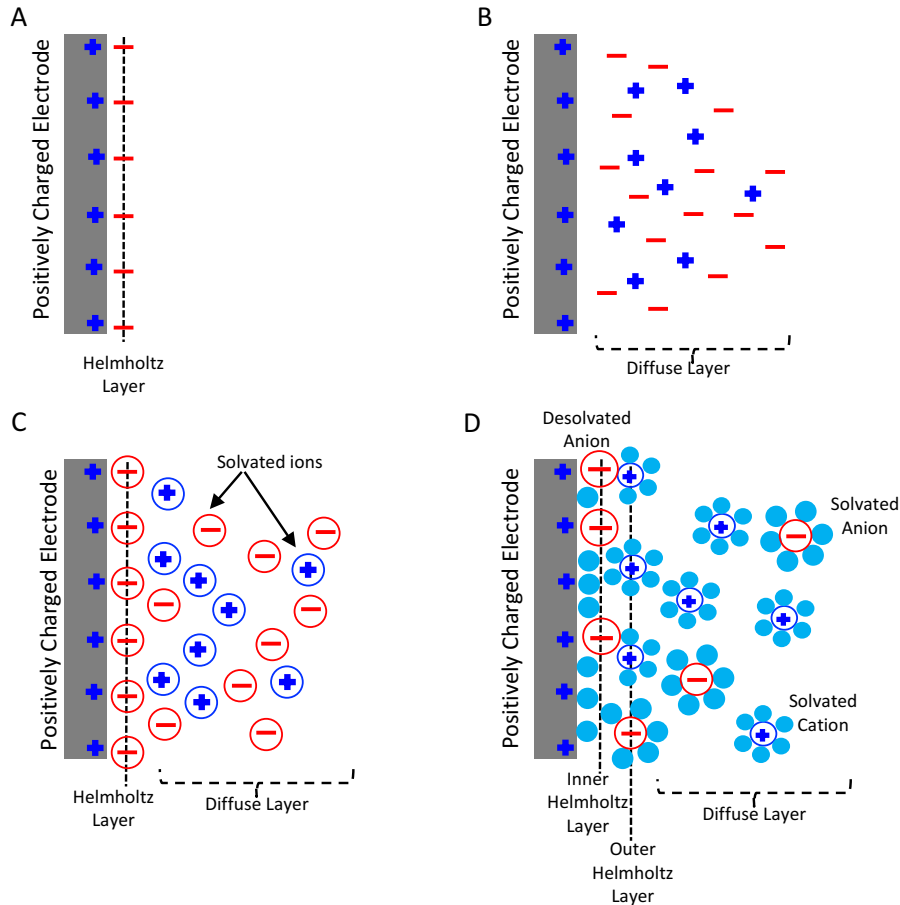


Figure 1.8: Models of the double layer: (A) Helmholtz model; (B) Gouy-Chapman model; (C) Stern model; (D) Grahame model, with solvent molecules also shown. Adapted from Conway.¹²³

In 1924, Stern combined the two models to describe the double layer as a compact layer of ions at the electrode surface (Helmholtz layer) next to a diffuse layer of anions and cations (Gouy-Chapman). Furthermore, Stern considered the solvated ions as having a finite size that dictated the distance of closest approach to the electrode surface. Grahame extended this model to consider ion solvation. Some ions (typically anions) can lose their solvation shell, meaning they have a smaller radius than their solvated counterparts, and so can approach closer to the electrode surface. This means three different regions can be distinguished: the inner Helmholtz layer, consisting of desolvated ions, the outer Helmholtz layer, consisting of solvated ions, and the diffuse layer.¹²³⁻¹²⁵

According to Grahame's model, the electrical double layer capacitance is influenced by both the Helmholtz layer and the diffuse layer. The electrical double layer capacitance (C_{DL}) can therefore be represented by Equation 1.1,

$$\frac{1}{C_{DL}} = \frac{1}{C_H} + \frac{1}{C_{Diff}} \quad (1.1)$$

where C_H is the capacitance arising from the Helmholtz layer, and C_{Diff} is the capacitance arising from the diffuse layer. In concentrated electrolytes, the diffuse capacitance is very large, therefore the double layer capacitance is approximately the same as the Helmholtz capacitance. The electrical double layer capacitance arises at all electrode interfaces, and has values between 15 and 50 $\mu\text{F cm}^{-2}$.¹²⁶ This value can be estimated from Equation 1.2,

$$C_{DL} \approx C_H = \frac{\epsilon_d A}{d} \quad (1.2)$$

where C_{DL} is the double layer capacitance in F, ϵ_d is the dielectric constant for the electrolyte in F m^{-1} , A is the surface area in m^2 , and d is the charge separation distance in m. Electrode materials that exhibit good electrical double layer capacitance are typically high surface area carbon materials including activated carbons, ordered mesoporous carbons, carbon aerogels, and carbon nanomaterials.¹¹⁹

The second method of energy storage is pseudocapacitance, where storage results from Faradaic charge transfer processes.¹²¹ Typically, redox active materials are either chemi- or physisorbed to an electrode material.¹²⁶ Transition metal oxides and conducting polymers are commonly used as pseudocapacitors, as they can undergo fast redox reactions. Pseudocapacitors typically have much higher capacitance values than electrical double layer capacitors, however unlike electrical double layer capacitance, pseudocapacitance is not fully reversible, due to the charge transfer resistance associated with the redox process, hence they suffer from reduced cycle stability compared with electrical double layer capacitors. Electrical double layer capacitors and pseudocapacitors are commonly combined in hybrid electrode materials that benefit from both the superior capacitance of the pseudocapacitor, and the high cyclability and conductivity of the electrical double layer capacitor.

In this project, graphene was used for the construction of an electrical double layer capacitor. Graphene is an ideal material because of its high surface area and good conductivity. Unfortunately, graphene capacitance is often limited due to aggregation of the graphene sheets, which limits the accessibility for electrolyte ions. Furthermore, graphene suffers from an intrinsic property known as the quantum capacitance that limits the total electrode capacitance.

1.6.2 Quantum Capacitance of Graphene

Graphene electrodes have a double layer capacitance that is unusually small ($< 10 \mu\text{F cm}^{-2}$) compared to metallic electrodes ($\sim 20 \mu\text{F cm}^{-2}$).¹²⁷ This is believed to be caused by the quantum capacitance of graphene. Quantum capacitance is widely assumed to be a direct result of the limited density of states near the Fermi level of graphene.¹²⁸ The capacitance of graphene is therefore controlled by three components, and Equation 1.1 can be rewritten to account for this (Equation 1.3),

$$\frac{1}{C_{\text{DL}}} = \frac{1}{C_{\text{Q}}} + \frac{1}{C_{\text{H}}} + \frac{1}{C_{\text{Diff}}} \quad (1.3)$$

where C_{Q} is the quantum capacitance. Tao et al. have studied the quantum capacitance of single layer graphene in detail. An expression for the quantum capacitance of an ideal graphene sheet has been derived based on a two-dimensional, free electron gas model (Equation 1.4),

$$C_{\text{Q}} = \frac{2e^2 k_{\text{B}} T}{\pi(\hbar v_{\text{F}})^2} \ln \left[2 \left(1 + \cosh \frac{eV_{\text{ch}}}{k_{\text{B}} T} \right) \right] \quad (1.4)$$

where \hbar is the reduced Plank constant, e is the electron charge, k_{B} is the Boltzmann constant, v_{F} is the Fermi velocity of the Dirac electron, and V_{ch} is the potential of graphene. When eV_{ch} is significantly larger than kT , the equation can be rewritten as Equation 1.5,

$$C_{\text{Q}} \approx e^2 \frac{2}{\pi} \frac{eV_{\text{ch}}}{(\hbar v_{\text{F}})^2} = \frac{2e^2}{\hbar v_{\text{F}} \sqrt{\pi}} \sqrt{n_{\text{C}}} \quad (1.5)$$

where n_{C} is the number of charge carriers in the graphene. Based on Equation 1.5, a plot of C_{Q} vs. applied potential (V_{ch}) can be drawn, as shown by the red squares in Figure 1.9. This shows a minimum at the Fermi level, which is close to zero. Furthermore, the quantum capacitance increases linearly with potential, with a slope of $23 \mu\text{F cm}^{-2} \text{V}^{-1}$ on both sides of the minimum.

Tao et al. reported that this model was unable to accurately fit experimental data because various impurities and defects exist in graphene, therefore they added an additional term for the carrier concentration induced by charged impurities (holes and electrons) in the graphene, resulting in Equation 1.6,

$$C_{\text{Q}} = \frac{2e^2}{\hbar v_{\text{F}} \sqrt{\pi}} (|n_{\text{G}}| + |n_{\text{s}}|)^{1/2} \quad (1.6)$$

where n_{G} and n_{s} are the carrier concentration caused by the applied potential and charged impurities respectively, and n_{G} can be calculated using Equation 1.7.

$$n_G = \left(\frac{eV_{ch}}{\hbar v_F \sqrt{\pi}} \right)^2 \quad (1.7)$$

If this model is used to plot quantum capacitance against applied potential then Figure 1.9 (blue, purple, and orange points) is obtained.

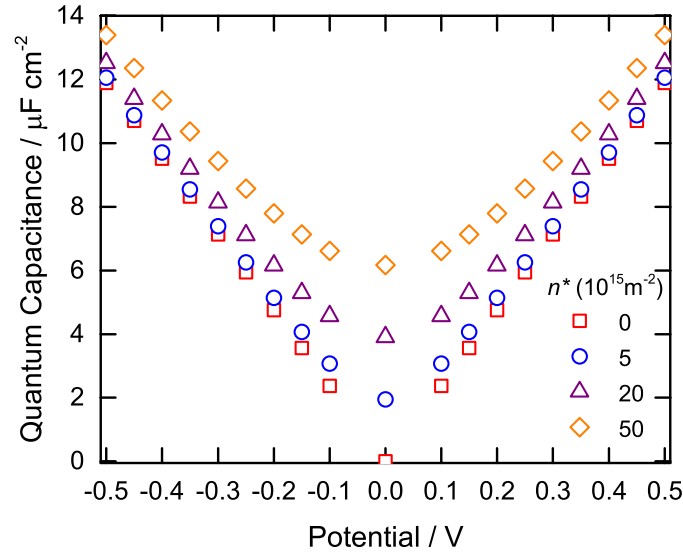


Figure 1.9: Theoretical quantum capacitance vs. potential for graphene, derived from (red) Equation 1.5, and (blue, purple, and orange) Equations 1.6 and 1.7.

Figure 1.9 shows that as the carrier concentration increases, the minimum quantum capacitance increases and the plot becomes increasingly rounder, with the slope on either side of the minimum decreasing with increasing carrier concentration. This model is much more appropriate than Equation 1.5 in explaining experimental results for single layer graphene.^{127, 129-131}

The consequence of this is that increasing the carrier concentration will increase the quantum capacitance and therefore the overall capacitance of the system. This was illustrated by the work of Pope and Aksay.¹³² They controlled the capacitance of graphene by varying the degree of oxidation of rGO, as oxygen containing defects can introduce additional carriers to the system. A plot of defects (expressed as the intensity ratio of the D/G Raman bands) versus minimum capacitance is given in Figure 1.10. Above a certain defect concentration, the number of carriers is sufficiently high that the quantum capacitance is larger than the Helmholtz capacitance, and the system is therefore limited by the Helmholtz capacitance, like a metallic electrode. However, the introduction of defects must be carefully controlled as too many defects may compromise other properties such as conductivity.

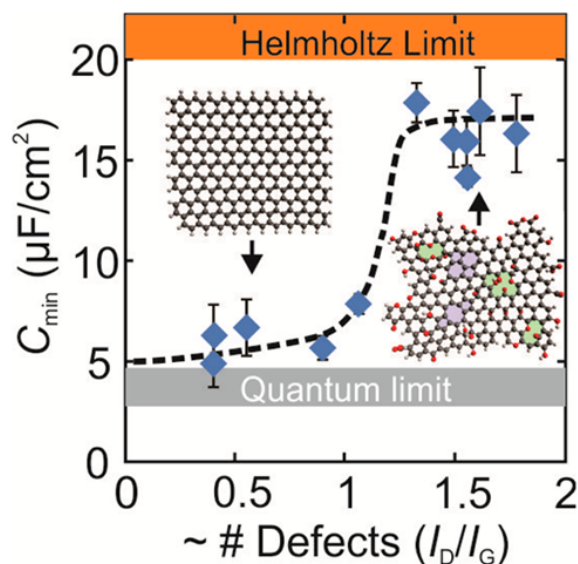


Figure 1.10: Variation in minimum capacitance for rGO with different numbers of defects. From Pope & Aksay.¹³²

Recent studies have also suggested the number of layers of graphene influences the total capacitance. Theoretical predictions indicate that the minimum capacitance increases with increasing layer number in a linear fashion, however, experimentally the capacitance does not increase beyond 3-4 layers.¹³³⁻¹³⁴ Jiang et al.¹³⁴ attempted to rationalise this by introducing a fourth component to Equation 1.3, labelled the dielectric capacitance. This is related to the graphene's ability to screen the electric field, which increases with the number of graphene layers. The exact origin of this layer dependence is still under investigation.

1.6.3 Graphene Capacitors in Literature Reports

Graphene based supercapacitor electrodes are commonly reported in the literature. Much work looks to overcome the limitations of graphene, both in terms of preventing aggregation and minimising the impact of the quantum capacitance component. To determine the capacitance of devices three main techniques are used: cyclic voltammetry (CV), galvanostatic charge discharge testing (CD), and electrochemical impedance spectroscopy (EIS).

The capacitance of CVD graphene has been reported previously. Ajayan et al.¹³⁵ evaluated the capacitance of CVD graphene in a polymer gel electrolyte, using CV and CD. A capacitance of $80 \mu\text{F cm}^{-2}$ was reported at a current density of 281 nA cm^{-2} . Furthermore, the rectangular CV and triangular CD curves indicated good charge propagation and efficient formation of the double layer. The device showed very little

degradation after 1500 cycles. Ruoff et al.¹³¹ also looked at the capacitance of CVD graphene with different layer numbers and minimum capacitances, derived using EIS, of 2-4 $\mu\text{F cm}^{-2}$ was reported for single to five layer graphene.

rGO materials are often used to give porous electrode materials. Various types of activation process can be used to convert rGO films into porous graphene films. Porous graphene films are good for capacitance as they have a high surface area to volume ratio, and the porous structure allows for faster ion transport and better transport pathways for electrolyte ions. For example, Shi et al.¹³⁶ adhered a rGO film to a polymer surface, then used electrochemical activation to prepare a porous material. The electrochemical activation left a porous material because water trapped between the sheets decomposed to a gas, which forced separation of the graphene sheets. The resulting electrode gave a high areal capacitance of 15 mF cm^{-2} , at 0.1 mA cm^{-2} , and had a 94% capacitance retention after 10,000 cycles. Dickerson et al.¹³⁷ deposited a rGO hydrogel onto a nickel foam. This porous material gave a capacitance of 161 F g^{-1} at 1 A g^{-1} , with an 80% retention after 10,000 cycles. Freeze drying rGO films is also an effective way to make porous graphene materials. Costa demonstrated that freeze drying hydrothermally reduced GO gave electrodes with capacitance values up to 441 F g^{-1} at 1 A g^{-1} .¹³⁸ Similarly, Kaner et al.¹³⁹ used freeze drying to give a three-dimensional porous graphene film with a capacitance of 284 F g^{-1} at 1 A g^{-1} . An interesting approach to synthesising graphene electrode materials was reported by Kaner.¹⁴⁰ A GO film was coated on a current collector, and then this was converted to rGO using flash conversion. A flash lamp, like that in a camera, was used to reduce the GO and leave a highly porous graphene film. Capacitances of approximately 64 F g^{-1} at 1 A g^{-1} were reported, which are lower than other methods for forming porous graphene, however this system had a significantly higher power density than previously reported porous graphene.

Porous graphene is one popular option for building graphene capacitors. An alternative is to use holey graphene. This is graphene that has been treated, often through chemically etching the graphene or by air oxidation, leaving holes in the carbon lattice.¹⁴¹ Hu et al.¹⁴¹ reported a holey graphene electrode generated by air oxidation. The holes in the graphene enabled efficient ion transport, as well as increasing the

number of defects within the graphene sheet. A capacitance of 61 F g^{-1} at 0.1 A g^{-1} was reported for this system. This is not significantly higher than the non-hole graphene (59 F g^{-1}), however the system had a much higher rate capability due to increased ion diffusion. Lin et al.¹⁴² also reported the use of holey-graphene in electrodes. They prepared the holey graphene through edge oxidation, and then pressed this into a disk electrode. The measured capacitance was $37\text{-}45 \text{ F g}^{-1}$ at 0.25 A g^{-1} . They also showed an extremely high areal mass loading, meaning the volumetric capacitance was improved compared with a non-hole system.

Pseudocapacitive materials typically have significantly higher specific capacitance values than electrical double layer capacitors. Graphene has been combined with conducting polymers to give electrodes with high specific capacitance. Conducting polymers are famous for their high flexibility, and good capacitive performance resulting from their redox active nature. Conducting polymers perform especially well when dispersed on a conductive, high surface area material such as graphene. Wei et al.¹⁴³ developed a graphene/polyaniline composite that gave a good capacitance of 1046 F g^{-1} at 1 mV/s , compared with 183 and 115 F g^{-1} for the graphene and polyaniline respectively. Furthermore, Liu et al.¹⁴⁴ have reported a rGO/polyaniline/cellulose material. The cellulose frame acts as a support for the graphene/polyaniline architecture. This gave an areal capacitance of 6.15 F cm^{-2} at a current density of 1 mA cm^{-2} . Polypyrrole is also used as a conducting polymer. Zhang et al.¹⁴⁵ reported a rGO/polypyrrole composite with a capacitance of 482 F g^{-1} at 0.5 A g^{-1} .

Metal oxides have very high specific capacitance, but suffer from a low electrical conductivity and cycle stability. Coupling metal oxide nanoparticles with conductive, high surface area materials such as graphene has been shown to overcome these issues, while retaining a high specific capacitance. Various metal oxides have been used for this, including ruthenium oxide, manganese dioxide, nickel oxide, copper oxide, and iron oxide. Roy et al.¹⁴⁶ recently reported a rGO/iron oxide composite material. The oxygen containing groups of the rGO acted as anchor points for the nanoparticles. The capacitance was found to be 576 F g^{-1} at 10 mV s^{-1} , compared with 132 and 60 F g^{-1} for pristine iron oxide and rGO respectively. Moshkalev¹⁴⁷ also synthesised a rGO/iron oxide hybrid material with a maximum capacitance of 455 F g^{-1} at 8 mV s^{-1} . Furthermore, the capacitance retention after 9600 cycles was 91.4% , showing good

stability. Manganese dioxide has also been combined with graphene. Kurungot et al.¹⁴⁸ electrochemically deposited a manganese dioxide nanograss onto a graphene substrate. At 0.5 A g^{-1} , a maximum capacitance of 776 F g^{-1} was recorded. This was shown to rely heavily on metal oxide loading, with a thin film performing best. Li et al.¹⁴⁹ deposited manganese dioxide nanoflowers onto a 3D graphene electrode, supported by a nickel foam. The composite material gave a capacitance of 559.4 F g^{-1} at 0.5 A g^{-1} . Metal hydroxides have also been combined with graphene to give extremely high capacitances. Jun et al.¹¹² used an electrochemical deposition process to grow cobalt hydroxide nanoflakes on a 3D graphene foam. The composite material gave a high specific capacitance of 1030 F g^{-1} at a current density of 9.09 A g^{-1} , with only a 6% decrease in capacitance after 5000 cycles. Zhan et al.¹⁵⁰ electrodeposited nickel hydroxide flakes onto a graphene foam. This gave an extremely high capacitance of 1433 F g^{-1} .

As discussed here, a wide range of methods exist for preparing graphene based supercapacitor electrodes. These can increase the electrical double layer capacitance of graphene, through maximising surface area, or increase the overall capacitance of the system by adding pseudocapacitive groups. In Chapter 5 of this thesis, preventing restacking of graphene sheets to increase the electrical double layer capacitance of the system will be considered. In addition, Chapter 6 will consider depositing cobalt and nickel hydroxide materials onto graphene to increase the total capacitance.

1.7 Project Aims

The overarching goal of this project is to build electrode materials for supercapacitor devices from FLG, with a maximum available surface area. FLG has a strong tendency to aggregate, so molecular spacers will be used to prevent this. This is illustrated in Figure 1.11.

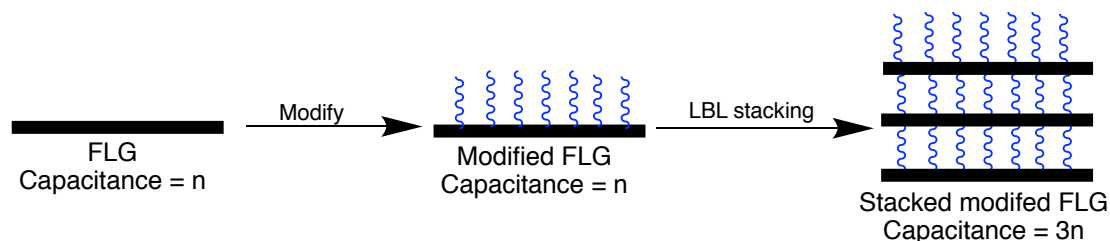


Figure 1.11: Cartoon illustrating the overall aim of this thesis.

If the FLG has a capacitance of n , then it is desired that modified FLG has a capacitance of at least n . Upon stacking the modified FLG, the capacitance of each sheet should be preserved. For example, a stack of three sheets should give a total capacitance of $3n$. This overall goal can be broken down into components, which are addressed in the following chapters:

Chapter 3:

- To successfully synthesis FLG using chemical vapour deposition
- To modify FLG using aryldiazonium chemistry

Chapter 4:

- To modify FLG using the Diels-Alder reaction of an aryne
- To modify FLG via the addition of primary amines

Chapter 5:

- To measure the capacitance of pristine FLG and modified FLG through CV, CD, and EIS
- To develop a LBL protocol for stacking modified FLG and establish the optimum surface concentration of modifiers for complete sheet separation

Chapter 6:

- To increase the overall capacitance of the system by depositing cobalt and nickel hydroxide nanoparticles onto modified and unmodified FLG

1.8 References

1. Loh, K. P.; Bao, Q.; Ang, P. K.; Yang, J., The chemistry of graphene. *J. Mater. Chem.* **2010**, *20*, 2277-2289.
2. Kuila, T.; Bose, S.; Mishra, A. K.; Khanra, P.; Kim, N. H.; Lee, J. H., Chemical functionalization of graphene and its applications. *Prog. Mater. Sci.* **2012**, *57*, 1061-1105.
3. Zhang, Y.; Zhang, L.; Zhou, C., Review of chemical vapor deposition of graphene and related applications. *Acc. Chem. Res.* **2013**, *46*, 2329-2339.
4. Novoselov, K. S.; Geim, A. K.; Morozov, S. V.; Jiang, D.; Zhang, Y.; Dubonos, S. V.; Grigorieva, I. V.; Firsov, A. A., Electric field effect in atomically thin carbon films. *Science* **2004**, *306*, 666-669.
5. Batzill, M., The surface science of graphene: Metal interfaces, CVD synthesis, nanoribbons, chemical modifications, and defects. *Surf. Sci. Rep.* **2012**, *67*, 83-115.
6. Martín, A.; Escarpa, A., Graphene: The cutting-edge interaction between chemistry and electrochemistry. *TrAC, Trends Anal. Chem.* **2014**, *56*, 13-26.
7. Iski, E. V.; Yitamben, E. N.; Gao, L.; Guisinger, N. P., Graphene at the atomic-scale: Synthesis, characterization, and modification. *Adv. Funct. Mater.* **2013**, *23*, 2554-2564.
8. Hummers, W. S.; Offeman, R. E., Preparation of graphitic oxide. *J. Am. Chem. Soc.* **1958**, *80*, 1339-1339.
9. Park, S.; Ruoff, R. S., Chemical methods for the production of graphenes. *Nat. Nano* **2009**, *4*, 217-224.
10. Hamilton, C. E.; Lomeda, J. R.; Sun, Z.; Tour, J. M.; Barron, A. R., High-yield organic dispersions of unfunctionalized graphene. *Nano Lett.* **2009**, *9*, 3460-3462.
11. Stankovich, S.; Dikin, D. A.; Piner, R. D.; Kohlhaas, K. A.; Kleinhammes, A.; Jia, Y.; Wu, Y.; Nguyen, S. T.; Ruoff, R. S., Synthesis of graphene-based nanosheets via chemical reduction of exfoliated graphite oxide. *Carbon* **2007**, *45*, 1558-1565.
12. Chen, Z.; Huang, T.; Jin, B. C.; Hu, J.; Lu, H.; Nutt, S., High yield synthesis of single-layer graphene microsheets with dimensional control. *Carbon* **2014**, *68*, 167-174.
13. Acik, M.; Lee, G.; Mattevi, C.; Chhowalla, M.; Cho, K.; Chabal, Y. J., Unusual infrared-absorption mechanism in thermally reduced graphene oxide. *Nat Mater* **2010**, *9*, 840-845.
14. Yan, Z.; Peng, Z. W.; Tour, J. M., Chemical vapor deposition of graphene single crystals. *Acc. Chem. Res.* **2014**, *47*, 1327-1337.
15. Hernandez, Y.; Nicolosi, V.; Lotya, M.; Blighe, F. M.; Sun, Z.; De, S.; McGovern, I. T.; Holland, B.; Byrne, M.; Gun'Ko, Y. K.; Boland, J. J.; Niraj, P.; Duesberg, G.; Krishnamurthy, S.; Goodhue, R.; Hutchison, J.; Scardaci, V.; Ferrari, A. C.; Coleman, J. N., High-yield production of graphene by liquid-phase exfoliation of graphite. *Nat. Nano* **2008**, *3*, 563-568.

16. Skaltsas, T.; Karousis, N.; Yan, H.-J.; Wang, C.-R.; Pispas, S.; Tagmatarchis, N., Graphene exfoliation in organic solvents and switching solubility in aqueous media with the aid of amphiphilic block copolymers. *J. Mater. Chem.* **2012**, *22*, 21507-21512.
17. Ayán-Varela, M.; Paredes, J. I.; Guardia, L.; Villar-Rodil, S.; Munuera, J. M.; Díaz-González, M.; Fernández-Sánchez, C.; Martínez-Alonso, A.; Tascón, J. M. D., Achieving extremely concentrated aqueous dispersions of graphene flakes and catalytically efficient graphene-metal nanoparticle hybrids with flavin mononucleotide as a high-performance stabilizer. *ACS Appl. Mater. Interfaces* **2015**, *7*, 10293-10307.
18. Wee, B.-H.; Wu, T.-F.; Hong, J.-D., Facile and scalable synthesis method for high-quality few-layer graphene through solution-based exfoliation of graphite. *ACS Appl. Mater. Interfaces* **2017**, *9*, 4548-4557.
19. Parvez, K.; Li, R.; Puniredd, S. R.; Hernandez, Y.; Hinkel, F.; Wang, S.; Feng, X.; Müllen, K., Electrochemically exfoliated graphene as solution-processable, highly conductive electrodes for organic electronics. *ACS Nano* **2013**, *7*, 3598-3606.
20. Yang, S.; Brüller, S.; Wu, Z.-S.; Liu, Z.; Parvez, K.; Dong, R.; Richard, F.; Samori, P.; Feng, X.; Müllen, K., Organic radical-assisted electrochemical exfoliation for the scalable production of high-quality graphene. *J. Am. Chem. Soc.* **2015**, *137*, 13927-13932.
21. Shinde, D. B.; Brenker, J.; Easton, C. D.; Tabor, R. F.; Neild, A.; Majumder, M., Shear assisted electrochemical exfoliation of graphite to graphene. *Langmuir* **2016**, *32*, 3552-3559.
22. Lee, H. C.; Liu, W.-W.; Chai, S.-P.; Mohamed, A. R.; Aziz, A.; Khe, C.-S.; Hidayah, N. M. S.; Hashim, U., Review of the synthesis, transfer, characterization and growth mechanisms of single and multilayer graphene. *RSC Adv.* **2017**, *7*, 15644-15693.
23. Gao, H.; Wang, Y. F.; Liu, Y. X.; Xie, E. Q.; Ajayan, P. M., Synthesis of large-area and monolayer of graphene: Role of transition metal support and growth time by CVD method. In *Emerging focus on advanced materials, pts 1 and 2*, Liu, S. Q.; Zuo, M., Eds. Trans Tech Publications Ltd: Stafa-Zurich, 2011; Vol. 306-307, pp 331-335.
24. Kim, S. M.; Hsu, A.; Lee, Y.-H.; Dresselhaus, M.; Palacios, T.; Kim, K. K.; Kong, J., The effect of copper pre-cleaning on graphene synthesis. *Nanotechnology* **2013**, *24*, 365602.
25. Hsieh, Y.-P.; Chen, D.-R.; Chiang, W.-Y.; Chen, K.-J.; Hofmann, M., Recrystallization of copper at a solid interface for improved CVD graphene growth. *RSC Adv.* **2017**, *7*, 3736-3740.
26. Wu, B.; Geng, D.; Guo, Y.; Huang, L.; Xue, Y.; Zheng, J.; Chen, J.; Yu, G.; Liu, Y.; Jiang, L., Equiangular hexagon-shape-controlled synthesis of graphene on copper surface. *Adv. Mater.* **2011**, *23*, 3522-3525.
27. Li, X.; Magnuson, C. W.; Venugopal, A.; An, J.; Suk, J. W.; Han, B.; Borysiak, M.; Cai, W.; Velamakanni, A.; Zhu, Y.; Fu, L.; Vogel, E. M.; Voelkl, E.; Colombo, L.; Ruoff, R. S., Graphene films with large domain size by a two-step chemical vapor deposition process. *Nano Lett.* **2010**, *10*, 4328-4334.

28. Celebi, K.; Cole, M. T.; Choi, J. W.; Wyczisk, F.; Legagneux, P.; Rupesinghe, N.; Robertson, J.; Teo, K. B. K.; Park, H. G., Evolutionary kinetics of graphene formation on copper. *Nano Lett.* **2013**, *13*, 967-974.
29. Choi, D. S.; Kim, K. S.; Kim, H.; Kim, Y.; Kim, T.; Rhy, S.-h.; Yang, C.-M.; Yoon, D. H.; Yang, W. S., Effect of cooling condition on chemical vapor deposition synthesis of graphene on copper catalyst. *ACS Appl. Mater. Interfaces* **2014**, *6*, 19574-19578.
30. Eres, G.; Regmi, M.; Rouleau, C. M.; Chen, J.; Ivanov, I. N.; Puzos, A. A.; Geoghegan, D. B., Cooperative island growth of large-area single-crystal graphene on copper using chemical vapor deposition. *ACS Nano* **2014**, *8*, 5657-5669.
31. Geng, D. C.; Wu, B.; Guo, Y. L.; Huang, L. P.; Xue, Y. Z.; Chen, J. Y.; Yu, G.; Jiang, L.; Hu, W. P.; Liu, Y. Q., Uniform hexagonal graphene flakes and films grown on liquid copper surface. *Proc. Natl. Acad. Sci. U.S.A.* **2012**, *109*, 7992-7996.
32. Griep, M.; Sandoz-Rosado, E.; Tumlin, T.; Wetzel, E., Enhanced graphene mechanical properties through ultra-smooth copper growth substrates. *Nano Lett.* **2016**.
33. Wu, Y. A.; Fan, Y.; Speller, S.; Creeth, G. L.; Sadowski, J. T.; He, K.; Robertson, A. W.; Allen, C. S.; Warner, J. H., Large single crystals of graphene on melted copper using chemical vapor deposition. *ACS Nano* **2012**, *6*, 5010-5017.
34. Mohsin, A.; Liu, L.; Liu, P. Z.; Deng, W.; Ivanov, I. N.; Li, G. L.; Dyck, O. E.; Duscher, G.; Dunlap, J. R.; Xiao, K.; Gu, G., Synthesis of millimeter-size hexagon-shaped graphene single crystals on resolidified copper. *ACS Nano* **2013**, *7*, 8924-8931.
35. Hao, Y.; Bharathi, M. S.; Wang, L.; Liu, Y.; Chen, H.; Nie, S.; Wang, X.; Chou, H.; Tan, C.; Fallahzad, B.; Ramanarayan, H.; Magnuson, C. W.; Tutuc, E.; Yakobson, B. I.; McCarty, K. F.; Zhang, Y.-W.; Kim, P.; Hone, J.; Colombo, L.; Ruoff, R. S., The role of surface oxygen in the growth of large single-crystal graphene on copper. *Science* **2013**, *342*, 720.
36. Wang, S.; Hibino, H.; Suzuki, S.; Yamamoto, H., Atmospheric pressure chemical vapor deposition growth of millimeter-scale single-crystalline graphene on the copper surface with a native oxide layer. *Chem. Mater.* **2016**, *28*, 4893-4900.
37. Pham, P. H. Q.; Zhou, W.; Quach, N. V.; Li, J.; Zheng, J.-G.; Burke, P. J., Controlling nucleation density while simultaneously promoting edge growth using oxygen-assisted fast synthesis of isolated large-domain graphene. *Chem. Mater.* **2016**, *28*, 6511-6519.
38. Lin, L.; Li, J.; Ren, H.; Koh, A. L.; Kang, N.; Peng, H.; Xu, H. Q.; Liu, Z., Surface engineering of copper foils for growing centimeter-sized single-crystalline graphene. *ACS Nano* **2016**.
39. Wu, T.; Ding, G.; Shen, H.; Wang, H.; Sun, L.; Jiang, D.; Xie, X.; Jiang, M., Triggering the continuous growth of graphene toward millimeter-sized grains. *Adv. Funct. Mater.* **2013**, *23*, 198-203.
40. Campos-Delgado, J.; Botello-Mendez, A. R.; Algara-Siller, G.; Hackens, B.; Pardo, T.; Kaiser, U.; Dresselhaus, M. S.; Charlier, J. C.; Raskin, J. P., Cvd

- synthesis of mono- and few-layer graphene using alcohols at low hydrogen concentration and atmospheric pressure. *Chem. Phys. Lett.* **2013**, *584*, 142-146.
41. Celebi, K.; Choi, J. W.; Cole, M. T.; Altun, A. O.; Teo, K. B. K.; Park, H. G. In *Observation of early to full covering stages of ethylene-based cvd of graphene*, CRC Press: 2012; pp 180-183.
 42. Tsen, A. W.; Brown, L.; Levendorf, M. P.; Ghahari, F.; Huang, P. Y.; Havener, R. W.; Ruiz-Vargas, C. S.; Muller, D. A.; Kim, P.; Park, J., Tailoring electrical transport across grain boundaries in polycrystalline graphene. *Science* **2012**, *336*, 1143-1146.
 43. Zhang, X. F.; Ning, J.; Li, X. L.; Wang, B.; Hao, L.; Liang, M. H.; Jin, M. H.; Zhi, L. J., Hydrogen-induced effects on the CVD growth of high-quality graphene structures. *Nanoscale* **2013**, *5*, 8363-8366.
 44. Liang, X.; Sperling, B. A.; Calizo, I.; Cheng, G.; Hacker, C. A.; Zhang, Q.; Obeng, Y.; Yan, K.; Peng, H.; Li, Q., Toward clean and crackless transfer of graphene. *ACS Nano* **2011**, *5*, 9144-9153.
 45. Lupina, G.; Kitzmann, J.; Costina, I.; Lukosius, M.; Wenger, C.; Wolff, A.; Vaziri, S.; Östling, M.; Pasternak, I.; Krajewska, A.; Strupinski, W.; Kataria, S.; Gahoi, A.; Lemme, M. C.; Ruhl, G.; Zoth, G.; Luxenhofer, O.; Mehr, W., Residual metallic contamination of transferred chemical vapor deposited graphene. *ACS Nano* **2015**, *9*, 4776-4785.
 46. Kim, H. H.; Kang, B.; Suk, J. W.; Li, N.; Kim, K. S.; Ruoff, R. S.; Lee, W. H.; Cho, K., Clean transfer of wafer-scale graphene via liquid phase removal of polycyclic aromatic hydrocarbons. *ACS Nano* **2015**, *9*, 4726-4733.
 47. Kim, H. H.; Lee, S. K.; Lee, S. G.; Lee, E.; Cho, K., Wetting-assisted crack- and wrinkle-free transfer of wafer-scale graphene onto arbitrary substrates over a wide range of surface energies. *Adv. Funct. Mater.* **2016**, *26*, 2070-2077.
 48. Zhang, G.; Güell, A. G.; Kirkman, P. M.; Lazenby, R. A.; Miller, T. S.; Unwin, P. R., Versatile polymer-free graphene transfer method and applications. *ACS Appl. Mater. Interfaces* **2016**, *8*, 8008-8016.
 49. Lillethorup, M.; Kongsfelt, M.; Ceccato, M.; Jensen, B. B. E.; Jorgensen, B.; Pedersen, S. U.; Daasbjerg, K., High- versus low- quality graphene: A mechanistic investigation of electrografted diazonium- based films for growth of polymer brushes. *Small* **2014**, *10*, 922-934.
 50. Park, J.; Yan, M., Covalent functionalization of graphene with reactive intermediates. *Acc. Chem. Res.* **2013**, *46*, 181-189.
 51. Delamar, M.; Hitmi, R.; Pinson, J.; Saveant, J. M., Covalent modification of carbon surfaces by grafting of functionalized aryl radicals produced from electrochemical reduction of diazonium salts. *J. Am. Chem. Soc.* **1992**, *114*, 5883-5884.
 52. Bourdillon, C.; Delamar, M.; Demaille, C.; Hitmi, R.; Moiroux, J.; Pinson, J., Immobilization of glucose oxidase on a carbon surface derivatized by electrochemical reduction of diazonium salts. *J. Electroanal. Chem.* **1992**, *336*, 113-123.

53. Downard, A. J.; Roddick, A. D.; Bond, A. M., Covalent modification of carbon electrodes for voltammetric differentiation of dopamine and ascorbic acid. *Anal. Chim. Acta* **1995**, *317*, 303-310.
54. Liu, S.; Shi, Z.; Dong, S., Preparation of a composite film electrode containing 12-tungstosilicic acid and its electrocatalytic reduction for nitrite. *Electroanal.* **1998**, *10*, 891-896.
55. Kariuki, J. K.; McDermott, M. T., Formation of multilayers on glassy carbon electrodes via the reduction of diazonium salts. *Langmuir* **2001**, *17*, 5947-5951.
56. Liu, G.; Liu, J.; Böcking, T.; Eggers, P. K.; Gooding, J. J., The modification of glassy carbon and gold electrodes with aryl diazonium salt: The impact of the electrode materials on the rate of heterogeneous electron transfer. *Chem. Phys.* **2005**, *319*, 136-146.
57. Liu, Y.-C.; McCreery, R. L., Reactions of organic monolayers on carbon surfaces observed with unenhanced raman spectroscopy. *J. Am. Chem. Soc.* **1995**, *117*, 11254-11259.
58. Kariuki, J. K.; McDermott, M. T., Nucleation and growth of functionalized aryl films on graphite electrodes. *Langmuir* **1999**, *15*, 6534-6540.
59. Allongue, P.; Delamar, M.; Desbat, B.; Fagebaume, O.; Hitmi, R.; Pinson, J.; Savéant, J.-M., Covalent modification of carbon surfaces by aryl radicals generated from the electrochemical reduction of diazonium salts. *J. Am. Chem. Soc.* **1997**, *119*, 201-207.
60. Delamar, M.; Désarmot, G.; Fagebaume, O.; Hitmi, R.; Pinson, J.; Savéant, J. M., Modification of carbon fiber surfaces by electrochemical reduction of aryl diazonium salts: Application to carbon epoxy composites. *Carbon* **1997**, *35*, 801-807.
61. Cullen, R. J.; Jayasundara, D. R.; Soldi, L.; Cheng, J. J.; Dufaure, G.; Colavita, P. E., Spontaneous grafting of nitrophenyl groups on amorphous carbon thin films: A structure-reactivity investigation. *Chem. Mater.* **2012**, *24*, 1031-1040.
62. Kuo, T. C.; McCreery, R. L.; Swain, G. M., Electrochemical modification of boron-doped chemical vapor deposited diamond surfaces with covalently bonded monolayers. *Electrochem. Solid-State Lett.* **1999**, *2*, 288-290.
63. Koehler, F. M.; Jacobsen, A.; Ensslin, K.; Stampfer, C.; Stark, W. J., Selective chemical modification of graphene surfaces: Distinction between single, and bilayer graphene. *Small* **2010**, *6*, 1125-1130.
64. Bekyarova, E.; Sarkar, S.; Niyogi, S.; Itkis, M. E.; Haddon, R. C., Advances in the chemical modification of epitaxial graphene. *J. Phys. D: Appl. Phys.* **2012**, *45*, 154009.
65. Ososon, B. D.; Belanger, D., Functionalization of graphene sheets by the diazonium chemistry during electrochemical exfoliation of graphite. *Carbon* **2017**, *111*, 83-93.
66. Downard, A. J., Electrochemically assisted covalent modification of carbon electrodes. *Electroanal.* **2000**, *12*, 1085-1096.

67. Abiman, P.; Wildgoose, G. G.; Compton, R. G., Investigating the mechanism for the covalent chemical modification of multiwalled carbon nanotubes using aryl diazonium salts. *Int. J. Electrochem. Sci* **2008**, *3*, 104-117.
68. Jayasundara, D. R.; Cullen, R. J.; Colavita, P. E., In situ and real time characterization of spontaneous grafting of aryldiazonium salts at carbon surfaces. *Chem. Mater.* **2013**, *25*, 1144-1152.
69. Usrey, M. L.; Lippmann, E. S.; Strano, M. S., Evidence for a two-step mechanism in electronically selective single-walled carbon nanotube reactions. *J. Am. Chem. Soc.* **2005**, *127*, 16129-16135.
70. Sienkiewicz, A.; Szymula, M.; Narkiewicz-Michalek, J.; Bravo-Diaz, C., Formation of diazohydroxides ArN₂OH in aqueous acid solution: Polarographic determination of the equilibrium constant K_r for the reaction of 4-substituted arenediazonium ions with H₂O⁺. *J. Phys. Org. Chem.* **2014**, *27*, 284-289.
71. Nair, N.; Kim, W.-J.; Usrey, M. L.; Strano, M. S., A structure–reactivity relationship for single walled carbon nanotubes reacting with 4-hydroxybenzene diazonium salt. *J. Am. Chem. Soc.* **2007**, *129*, 3946-3954.
72. Abiman, P.; Wildgoose, G. G.; Compton, R. G., A mechanistic investigation into the covalent chemical derivatisation of graphite and glassy carbon surfaces using aryldiazonium salts. *J. Phys. Org. Chem.* **2008**, *21*, 433-439.
73. Mesnage, A.; Lefèvre, X.; Jégou, P.; Deniau, G.; Palacin, S., Spontaneous grafting of diazonium salts: Chemical mechanism on metallic surfaces. *Langmuir* **2012**, *28*, 11767-11778.
74. Galli, C., Radical reactions of arenediazonium ions: An easy entry into the chemistry of the aryl radical. *Chem. Rev.* **1988**, *88*, 765-792.
75. Toupin, M.; Bélanger, D., Thermal stability study of aryl modified carbon black by in situ generated diazonium salt. *J. Phys. Chem. C* **2007**, *111*, 5394-5401.
76. Doppelt, P.; Hallais, G.; Pinson, J.; Podvorica, F.; Verneyre, S., Surface modification of conducting substrates. Existence of azo bonds in the structure of organic layers obtained from diazonium salts. *Chem. Mater.* **2007**, *19*, 4570-4575.
77. Belanger, D.; Pinson, J., Electrografting: A powerful method for surface modification. *Chem. Soc. Rev.* **2011**, *40*, 3995-4048.
78. Combellas, C.; Kanoufi, F.; Pinson, J.; Podvorica, F. I., Time-of-flight secondary ion mass spectroscopy characterization of the covalent bonding between a carbon surface and aryl groups. *Langmuir* **2005**, *21*, 280-286.
79. Adenier, A.; Combellas, C.; Kanoufi, F.; Pinson, J.; Podvorica, F. I., Formation of polyphenylene films on metal electrodes by electrochemical reduction of benzenediazonium salts. *Chem. Mater.* **2006**, *18*, 2021-2029.
80. Schmidt, G.; Gallon, S.; Esnouf, S.; Bourgoin, J.-P.; Chenevier, P., Mechanism of the coupling of diazonium to single-walled carbon nanotubes and its consequences. *Chem. Eur. J.* **2009**, *15*, 2101-2110.
81. Sarkar, S.; Bekyarova, E.; Haddon, R. C., Chemistry at the dirac point: Diels-Alder reactivity of graphene. *Acc. Chem. Res.* **2012**, *45*, 673-682.

82. Sarkar, S.; Bekyarova, E.; Niyogi, S.; Haddon, R. C., Diels-Alder chemistry of graphite and graphene: Graphene as diene and dienophile. *J. Am. Chem. Soc.* **2011**, *133*, 3324-3327.
83. Zydziak, N.; Yameen, B.; Barner-Kowollik, C., Diels-Alder reactions for carbon material synthesis and surface functionalization. *Polym. Chem.* **2013**, *4*, 4072-4086.
84. Bian, S.; Scott, A. M.; Cao, Y.; Liang, Y.; Osuna, S.; Houk, K. N.; Braunschweig, A. B., Covalently patterned graphene surfaces by a force-accelerated Diels-Alder reaction. *J. Am. Chem. Soc.* **2013**, *135*, 9240-9243.
85. Seo, J. M.; Jeon, I. Y.; Baek, J. B., Mechanochemically driven solid-state Diels-Alder reaction of graphite into graphene nanoplatelets. *Chem. Sci.* **2013**, *4*, 4273-4277.
86. Pellissier, H.; Santelli, M., The use of arynes in organic synthesis. *Tetrahedron* **2003**, *59*, 701-730.
87. Zhong, X.; Jin, J.; Li, S.; Niu, Z.; Hu, W.; Li, R.; Ma, J., Aryne cycloaddition: Highly efficient chemical modification of graphene. *Chem. Commun.* **2010**, *46*, 7340-7342.
88. Magedov, I. V.; Frolova, L. V.; Ovezmyradov, M.; Bethke, D.; Shaner, E. A.; Kalugin, N. G., Benzyne-functionalized graphene and graphite characterized by raman spectroscopy and energy dispersive x-ray analysis. *Carbon* **2013**, *54*, 192-200.
89. Friedman, L.; Logullo, F. M., Arynes via aprotic diazotization of anthranilic acids. *J. Org. Chem.* **1969**, *34*, 3089-3092.
90. Lebègue, E.; Brousse, T.; Gaubicher, J.; Cougnon, C., Chemical functionalization of activated carbon through radical and diradical intermediates. *Electrochem. Commun.* **2013**, *34*, 14-17.
91. Chua, C. K.; Pumera, M., Covalent chemistry on graphene. *Chem. Soc. Rev.* **2013**, *42*, 3222-3233.
92. Georgakilas, V.; Bourlinos, A. B.; Zboril, R.; Steriotis, T. A.; Dallas, P.; Stubos, A. K.; Trapalis, C., Organic functionalisation of graphenes. *Chem. Commun.* **2010**, *46*, 1766-1768.
93. Quintana, M.; Spyrou, K.; Grzelczak, M.; Browne, W. R.; Rudolf, P.; Prato, M., Functionalization of graphene via 1, 3-dipolar cycloaddition. *ACS Nano* **2010**, *4*, 3527-3533.
94. Navarro, J. J.; Leret, S.; Calleja, F.; Stradi, D.; Black, A.; Bernardo-Gavito, R.; Garnica, M.; Granados, D.; Vázquez de Parga, A. L.; Pérez, E. M.; Miranda, R., Organic covalent patterning of nanostructured graphene with selectivity at the atomic level. *Nano Lett.* **2016**, *16*, 355-361.
95. Criado, A.; Melchionna, M.; Marchesan, S.; Prato, M., The covalent functionalization of graphene on substrates. *Angew. Chem. Int. Ed.* **2015**, *54*, 10734-10750.
96. Cui, S.; Mao, S.; Lu, G.; Chen, J., Graphene coupled with nanocrystals: Opportunities and challenges for energy and sensing applications. *J. Phys. Chem. Lett.* **2013**, *4*, 2441-2454.

97. Raj, M. A.; John, S. A., Assembly of gold nanoparticles on graphene film via electroless deposition: Spontaneous reduction of Au³⁺ ions by graphene film. *RSC Adv.* **2015**, *5*, 4964-4971.
98. Bello, A.; Fabiane, M.; Dodoo-Arhin, D.; Ozoemena, K. I.; Manyala, N., Silver nanoparticles decorated on a three-dimensional graphene scaffold for electrochemical applications. *J. Phys. Chem. Solids* **2014**, *75*, 109-114.
99. Bosch-Navarro, C.; Rourke, J. P.; Wilson, N. R., Controlled electrochemical and electroless deposition of noble metal nanoparticles on graphene. *RSC Adv.* **2016**, *6*, 73790-73796.
100. Benitez-Martinez, S.; Inmaculada Lopez-Lorente, A.; Valcarcel, M., Multilayer graphene-gold nanoparticle hybrid substrate for the SERS determination of metronidazole. *Microchem. J.* **2015**, *121*, 6-13.
101. Thanh, T. D.; Balamurugan, J.; Hwang, J. Y.; Kim, N. H.; Lee, J. H., In situ synthesis of graphene-encapsulated gold nanoparticle hybrid electrodes for non-enzymatic glucose sensing. *Carbon* **2016**, *98*, 90-98.
102. Xu, J.; Wang, Q.; Tao, Z.; Qi, Z.; Zhai, Y.; Lei, W.; Zhang, X., Enhanced electron emission of directly transferred few-layer graphene decorated with gold nanoparticles. *RSC Adv.* **2016**, *6*, 78170-78175.
103. Ju, J.; Chen, W., In situ growth of surfactant-free gold nanoparticles on nitrogen-doped graphene quantum dots for electrochemical detection of hydrogen peroxide in biological environments. *Anal. Chem.* **2015**, *87*, 1903-1910.
104. Iyer, G. R. S.; Wang, J.; Wells, G.; Guruvenket, S.; Payne, S.; Bradley, M.; Borondics, F., Large-area, freestanding, single-layer graphene-gold: A hybrid plasmonic nanostructure. *ACS Nano* **2014**, *8*, 6353-6362.
105. Yu, S. U.; Park, B.; Cho, Y.; Hyun, S.; Kim, J. K.; Kim, K. S., Simultaneous visualization of graphene grain boundaries and wrinkles with structural information by gold deposition. *ACS Nano* **2014**, *8*, 8662-8668.
106. Qiu, C.; Zhou, H.; Cao, B.; Sun, L.; Yu, T., Raman spectroscopy of morphology-controlled deposition of Au on graphene. *Carbon* **2013**, *59*, 487-494.
107. Benvidi, A.; Dehghani-Firouzabadi, A.; Mazloum-Ardakani, M.; Mirjalili, B.-B. F.; Zare, R., Electrochemical deposition of gold nanoparticles on reduced graphene oxide modified glassy carbon electrode for simultaneous determination of levodopa, uric acid and folic acid. *J. Electroanal. Chem.* **2015**, *736*, 22-29.
108. Toth, P. S.; Velický, M.; Ramasse, Q. M.; Kepaptsoglou, D. M.; Dryfe, R. A. W., Symmetric and asymmetric decoration of graphene: Bimetal-graphene sandwiches. *Adv. Funct. Mater.* **2015**, *25*, 2899-2909.
109. Wan, Q.; Liu, Y.; Wang, Z.; Wei, W.; Li, B.; Zou, J.; Yang, N., Graphene nanoplatelets supported metal nanoparticles for electrochemical oxidation of hydrazine. *Electrochem. Commun.* **2013**, *29*, 29-32.
110. Yang, S.; Song, X.; Zhang, P.; Sun, J.; Gao, L., Self-assembled α -Fe₂O₃ mesocrystals/graphene nanohybrid for enhanced electrochemical capacitors. *Small* **2014**, *10*, 2270-2279.
111. Wu, Y.; Liu, S.; Wang, H.; Wang, X.; Zhang, X.; Jin, G., A novel solvothermal synthesis of Mn₃O₄/graphene composites for supercapacitors. *Electrochim. Acta* **2013**, *90*, 210-218.

112. Patil, U. M.; Nam, M. S.; Sohn, J. S.; Kulkarni, S. B.; Shin, R.; Kang, S.; Lee, S.; Kim, J. H.; Jun, S. C., Controlled electrochemical growth of Co(OH)₂ flakes on 3D multilayered graphene foam for high performance supercapacitors. *J. Mater. Chem. A* **2014**, *2*, 19075-19083.
113. Lv, R.; Terrones, M., Towards new graphene materials: Doped graphene sheets and nanoribbons. *Mater. Lett.* **2012**, *78*, 209-218.
114. Popvic, R. S., *Hall effect devices, second edition*. Taylor & Francis: 2003.
115. Burke, A., Ultracapacitors: Why, how, and where is the technology. *J. Power Sources* **2000**, *91*, 37-50.
116. Dai, L., Functionalization of graphene for efficient energy conversion and storage. *Acc. Chem. Res.* **2012**, *46*, 31-42.
117. Liu, C.; Yu, Z.; Neff, D.; Zhamu, A.; Jang, B. Z., Graphene-based supercapacitor with an ultrahigh energy density. *Nano Lett.* **2010**, *10*, 4863-4868.
118. Wood, B. C.; Ogitsu, T.; Otani, M.; Biener, J., First-principles-inspired design strategies for graphene-based supercapacitor electrodes. *J. Phys. Chem. C* **2013**, *118*, 4-15.
119. Kim, T.; Jung, G.; Yoo, S.; Suh, K. S.; Ruoff, R. S., Activated graphene-based carbons as supercapacitor electrodes with macro- and mesopores. *ACS Nano* **2013**, *7*, 6899-6905.
120. Liu, R. S.; Zhang, L.; Sun, X.; Liu, H.; Zhang, J., *Electrochemical technologies for energy storage and conversion*. John Wiley & Sons, Inc.: 2011; Vol. 1.
121. Chen, Z.; Yu, D.; Xiong, W.; Liu, P.; Liu, Y.; Dai, L., Graphene-based nanowire supercapacitors. *Langmuir* **2014**, *30*, 3567-3571.
122. Jiang, H.; Lee, P. S.; Li, C., 3D carbon based nanostructures for advanced supercapacitors. *Energ. Environ. Sci* **2013**, *6*, 41-53.
123. Conway, B. E., *Electrochemical supercapacitors: Scientific fundamentals and technological applications*. Kluwer Academic/Plenum Publishers: New York, 1999.
124. Grahame, D. C., The nature of the electrical double layer. *J. Chem. Educ.* **1943**, *20*, 154.
125. Gamburg, Y. D.; Zangari, G., The structure of the metal-solution interface. In *Theory and practice of metal electrodeposition*, Springer: 2011; pp 27-51.
126. Conway, B. E.; Birss, V.; Wojtowicz, J., The role and utilization of pseudocapacitance for energy storage by supercapacitors. *J. Power Sources* **1997**, *66*, 1-14.
127. Zhong, J.-H.; Liu, J.-Y.; Li, Q.; Li, M.-G.; Zeng, Z.-C.; Hu, S.; Wu, D.-Y.; Cai, W.; Ren, B., Interfacial capacitance of graphene: Correlated differential capacitance and in situ electrochemical raman spectroscopy study. *Electrochim. Acta* **2013**, *110*, 754-761.
128. Chang, J.H.; Huzayyin, A.; Lian, K.; Dawson, F., Quantum capacitance of graphene in contact with metal. *Appl. Phys. Lett.* **2015**, *107*, 193902.

129. Brooksby, P. A.; Farquhar, A. K.; Dykstra, H. M.; Waterland, M. R.; Downard, A. J., Quantum capacitance of aryldiazonium modified large area few-layer graphene electrodes. *J. Phys. Chem. C* **2015**, *119*, 25778-25785.
130. Chen, J.; Han, Y.; Kong, X.; Deng, X.; Park, H. J.; Guo, Y.; Jin, S.; Qi, Z.; Lee, Z.; Qiao, Z., The origin of improved electrical double-layer capacitance by inclusion of topological defects and dopants in graphene for supercapacitors. *Angew. Chem. Int. Ed.* **2016**, *55*, 13822-13827.
131. Ji, H.; Zhao, X.; Qiao, Z.; Jung, J.; Zhu, Y.; Lu, Y.; Zhang, L. L.; MacDonald, A. H.; Ruoff, R. S., Capacitance of carbon-based electrical double-layer capacitors. *Nat. Commun.* **2014**, *5*.
132. Pope, M. A.; Aksay, I. A., Four-fold increase in the intrinsic capacitance of graphene through functionalization and lattice disorder. *J. Phys. Chem. C* **2015**, *119*, 20369-20378.
133. Zhan, C.; Jiang, D.E., Contribution of dielectric screening to the total capacitance of few-layer graphene electrodes. *J. Phys. Chem. Lett.* **2016**, *7*, 789-794.
134. Zhan, C.; Neal, J.; Wu, J.; Jiang, D.-e., Quantum effects on the capacitance of graphene-based electrodes. *J. Phys. Chem. C* **2015**, *119*, 22297-22303.
135. Yoo, J. J.; Balakrishnan, K.; Huang, J.; Meunier, V.; Sumpster, B. G.; Srivastava, A.; Conway, M.; Mohana Reddy, A. L.; Yu, J.; Vajtai, R.; Ajayan, P. M., Ultrathin planar graphene supercapacitors. *Nano Lett.* **2011**, *11*, 1423-1427.
136. Wu, M.; Li, Y.; Yao, B.; Chen, J.; Li, C.; Shi, G., A high-performance current collector-free flexible in-plane micro-supercapacitor based on a highly conductive reduced graphene oxide film. *J. Mater. Chem. A* **2016**, *4*, 16213-16218.
137. Pham, V. H.; Dickerson, J. H., Reduced graphene oxide hydrogels deposited in nickel foam for supercapacitor applications: Toward high volumetric capacitance. *J. Phys. Chem. C* **2016**, *120*, 5353-5360.
138. Alazmi, A.; El Tall, O.; Rasul, S.; Hedhili, M. N.; Patole, S. P.; Costa, P. M. F. J., A process to enhance the specific surface area and capacitance of hydrothermally reduced graphene oxide. *Nanoscale* **2016**, *8*, 17782-17787.
139. Shao, Y.; El-Kady, M. F.; Lin, C.-W.; Zhu, G.; Marsh, K. L.; Hwang, J. Y.; Zhang, Q.; Li, Y.; Wang, H.; Kaner, R. B., 3D freeze-casting of cellular graphene films for ultrahigh-power-density supercapacitors. *Adv. Mater.* **2016**, *28*, 6719-6726.
140. Wang, L. J.; El-Kady, M. F.; Dubin, S.; Hwang, J. Y.; Shao, Y.; Marsh, K.; McVerry, B.; Kowal, M. D.; Mousavi, M. F.; Kaner, R. B., Flash converted graphene for ultra-high power supercapacitors. *Adv. Energy Mater.* **2015**, *5*.
141. Lin, Y.; Han, X.; Campbell, C. J.; Kim, J.-W.; Zhao, B.; Luo, W.; Dai, J.; Hu, L.; Connell, J. W., Holey graphene nanomanufacturing: Structure, composition, and electrochemical properties. *Adv. Funct. Mater.* **2015**, *25*, 2920-2927.
142. Walsh, E. D.; Han, X.; Lacey, S. D.; Kim, J.-W.; Connell, J. W.; Hu, L.; Lin, Y., Dry-processed, binder-free holey graphene electrodes for supercapacitors with ultrahigh areal loadings. *ACS Appl. Mater. Interfaces* **2016**, *8*, 29478-29485.

143. Yan, J.; Wei, T.; Shao, B.; Fan, Z.; Qian, W.; Zhang, M.; Wei, F., Preparation of a graphene nanosheet/polyaniline composite with high specific capacitance. *Carbon* **2010**, *48*, 487-493.
144. Wan, C.; Jiao, Y.; Li, J., Flexible, highly conductive, and free-standing reduced graphene oxide/polypyrrole/cellulose hybrid papers for supercapacitor electrodes. *J. Mater. Chem. A* **2017**, *5*, 3819-3831.
145. Zhang, D.; Zhang, X.; Chen, Y.; Yu, P.; Wang, C.; Ma, Y., Enhanced capacitance and rate capability of graphene/polypyrrole composite as electrode material for supercapacitors. *J. Power Sources* **2011**, *196*, 5990-5996.
146. Bhattacharya, G.; Kandasamy, G.; Soin, N.; Upadhyay, R. K.; Deshmukh, S.; Maity, D.; McLaughlin, J.; Roy, S. S., Novel π -conjugated iron oxide/reduced graphene oxide nanocomposites for high performance electrochemical supercapacitors. *RSC Adv.* **2017**, *7*, 327-335.
147. Kumar, R.; Singh, R. K.; Vaz, A. R.; Savu, R.; Moshkalev, S. A., Self-assembled and one-step synthesis of interconnected 3D network of Fe₃O₄/reduced graphene oxide nanosheets hybrid for high-performance supercapacitor electrode. *ACS Appl. Mater. Interfaces* **2017**.
148. Soni, R.; Raveendran, A.; Kurungot, S., Grafoil-scotch tape-derived highly conducting flexible substrate and its application as a supercapacitor electrode. *Nanoscale* **2017**, *9*, 3593-3600.
149. Wu, L.; Hao, L.; Pang, B.; Wang, G.; Zhang, Y.; Li, X., MnO₂ nanoflowers and polyaniline nanoribbons grown on hybrid graphene/Ni 3D scaffolds by in situ electrochemical techniques for high-performance asymmetric supercapacitors. *J. Mater. Chem. A* **2017**, *5*, 4629-4637.
150. Zhang, C.; Chen, Q.; Zhan, H., Supercapacitors based on reduced graphene oxide nanofibers supported Ni(OH)₂ nanoplates with enhanced electrochemical performance. *ACS Appl. Mater. Interfaces* **2016**, *8*, 22977-22987.

2 Experimental Methods

2.1 Chemicals

Unless otherwise stated, all chemicals were purchased from commercial sources and used as received, and all solvents were HPLC grade. The gases used for CVD were purchased from BOC New Zealand. Aqueous solutions were prepared using Milli-Q water (resistivity > 18 M Ω .cm). EPO-TEK 301, two-part epoxy resin was used to fabricate Au/epoxy substrates and to define working electrode areas.

2.1.1 Aryldiazonium Tetrafluoroborate Salt Synthesis

Aryldiazonium salts were synthesised using a standard procedure.¹⁻³ The amine precursors used were 4-nitroaniline, 4-(4-nitrophenylazo)aniline, 4-aminobenzoic acid, 4-iodoaniline, and 4-methoxyaniline. The amine precursor (5 mmol) was dissolved in a solution of water (1 mL) and tetrafluoroboric acid (48%, 1 mL). Sodium nitrite (5 mmol), dissolved in a minimum amount of water, was added dropwise to the amine solution, with stirring. The resulting mixture was cooled for 30 minutes in an ice bath, and filtered. This solid was dissolved in a minimum amount of ice-cold acetonitrile in a 250 mL beaker and ice-cold diethyl ether was subsequently poured slowly down the side of the beaker to precipitate the aryldiazonium tetrafluoroborate salt. This was filtered and washed 3 \times with ice-cold diethyl ether. All aryldiazonium salts were stored at -4 °C in the dark (yield \sim 1 g, 85%).

2.1.2 2-Aminoterephthalic Acid 4-Methyl Ester Synthesis

The synthesis and characterisation of 2-aminoterephthalic acid 4 methyl ester has been described previously.⁴ A mixture of 2-aminoterephthalic acid (2.5 g), sulfuric acid (95%, 2.5 mL), and methanol (25 mL) was stirred at 60 °C for 7 hours. This solution was concentrated to half its volume, poured onto ice, and adjusted to pH 8 using solid sodium carbonate. The solution was washed 3 \times with dichloromethane, acidified to pH 2 with concentrated hydrochloric acid, and the resulting yellow solid filtered. The yellow solid was dissolved in 10% sodium carbonate solution, and this solution was washed 3 \times with dichloromethane, acidified to pH 2 with concentrated hydrochloric acid, and filtered, giving 2-aminoterephthalic acid 4-methyl ester as a yellow solid (yield = 2 g, 75%).

2.1.3 Tetraoctylammonium Tetrachloroaurate ((TOA)[AuCl₄]) Synthesis

A previously reported procedure was used for the synthesis of (TOA)[AuCl₄].⁵ Tetraoctylammonium chloride (2 g) in ethanol (10 mL) and HAuCl₄·3H₂O (1.56 g) in ethanol (10 mL) were mixed. The solution was gently heated to reduce the volume of ethanol, until crystallisation began, then refrigerated for 2 hours and filtered, giving yellow (TOA)[AuCl₄] crystals (yield = 3 g, 87%).

2.2 Substrate Preparation

Potassium bromide (KBr) disks (Sigma Aldrich) were polished prior to use with a LECLOTH pad (LECO) wet with methanol. Highly ordered pyrolytic graphite (HOPG) surfaces (SPI supplies) were freshly cleaved prior to use. Silicon wafer samples were prepared by protecting a larger Si(100) wafer with photoresist, that was then cut into 1 cm × 1 cm pieces, and subsequently sonicated in acetone twice, methanol once, and dried under nitrogen.

2.2.1 Pyrolysed Photoresist Film (PPF) preparation

PPF surfaces were prepared using a previously described method.¹ A small amount of photoresist (2-3 drops of AZ4620 (Clariant)) was spin coated onto a 1 cm × 1 cm pre-cut Si(100) wafer for 30 seconds at 3000 rpm. The photoresist covered wafer was soft-baked for 20 minutes at 95 °C, cooled, and a second layer of photoresist was applied. The wafers were placed in a furnace, within a quartz tube, and heated over 3 hours to 1100 °C in a forming gas (95% nitrogen and 5% hydrogen) atmosphere (flow rate = 1500 sccm). This temperature was maintained for 1 hour, after which the furnace was cooled to room temperature under forming gas flow. The samples were briefly sonicated in successive baths of acetone, methanol and isopropanol, and dried under nitrogen prior to use.

2.2.2 Au/Epoxy Working Electrode Surfaces

Au surfaces were prepared by thermally evaporating 50 nm of Ti, followed by 50 nm of Au onto a large Si(100) wafer. This was then protected using photoresist and cut into approximately 1.5 cm × 1 cm pieces. Once cut, the surfaces were soaked twice in acetone, once in methanol, and dried under nitrogen. A drop (~ 0.1 mL) of an epoxy resin (EPO-TEK 301, two-part resin) was added to the centre of each wafer (diameter ~ 3 mm) and cured to give a Au/epoxy surface (Figure 2.1).

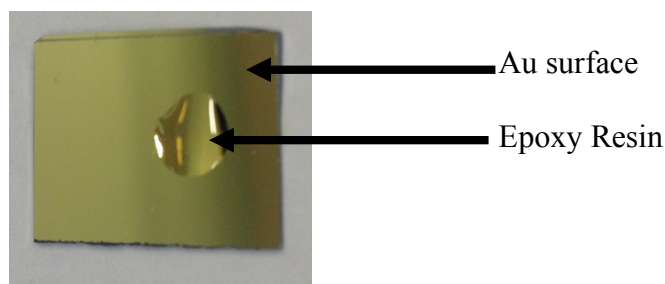


Figure 2.1: Au surface with epoxy resin droplet in the centre.

2.3 Preparation of FLG

2.3.1 CVD of FLG

Protocol A was derived from Wu et al.⁶ Copper foil (99.999%, 25 μm thick, Alfa Aesar) was cleaned in 10% nitric acid, MilliQ water and finally isopropanol, and dried under a stream of nitrogen. The copper foil was cut into 1 cm \times 1 cm pieces and placed in a furnace within a quartz tube. The furnace was heated to 100 $^{\circ}\text{C}$ with 50 sccm H_2 and 400 sccm Ar for 30 minutes, then heated to 1050 $^{\circ}\text{C}$ under 500 sccm H_2 and this temperature was maintained for 30 minutes. Methane (5 sccm) was introduced for 7 minutes, after which the furnace was cooled for 1 hour to approximately 600 $^{\circ}\text{C}$ under 500 sccm H_2 only. The samples were withdrawn from the heating zone of the furnace to cool rapidly to room temperature.

In protocol B, after the 30 minute step at 100 $^{\circ}\text{C}$, the furnace was heated to 1050 $^{\circ}\text{C}$ under 1000 sccm Ar and 300 sccm H_2 , and this temperature was maintained for 30 minutes. The furnace was then heated to 1060 $^{\circ}\text{C}$ and held at this temperature for 30 minutes, after which the Ar flow rate was increased to 1500 sccm, the H_2 decreased to 200 sccm, and methane introduced at 5 sccm for 5 minutes. The furnace was cooled for 1 hour to 600 $^{\circ}\text{C}$, under 1500 sccm Ar and 50 sccm H_2 . The samples were withdrawn from the heating zone of the furnace to cool rapidly to room temperature.

2.3.2 Polymer Free Transfer of FLG

The FLG/Cu coupon prepared via CVD was floated on ammonium persulfate solution (0.5 M) for 15 minutes to remove the FLG from one side. The same coupon was re-floated on fresh ammonium persulfate solution (0.5 M) in a watch glass overnight, leaving a sheet of free-floating FLG on the solution surface. The FLG was washed 5 \times with water by solution replacement. The FLG could either be modified (Section 2.4) or transferred to a desired substrate for analysis by lifting the substrate from below the

FLG, and subsequently drying for 1 hour in air, and 30 minutes in a 60 °C oven. Figure 2.2 shows the different steps of the etching and transfer process. The FLG in Figure 2.2 was collected onto a Au/epoxy surface, however this could be replaced with any of the substrates described in Section 2.2.

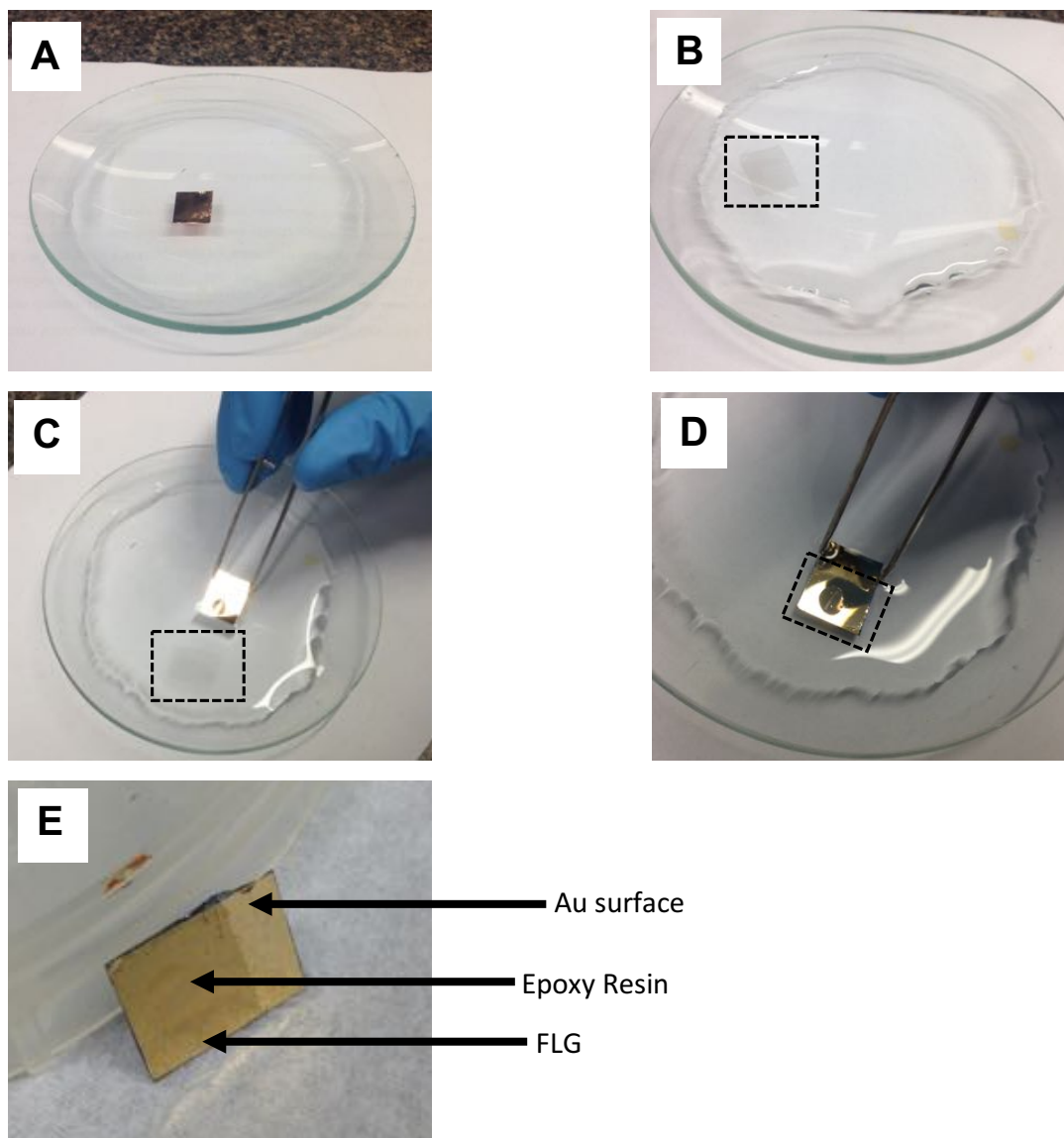


Figure 2.2: Steps for etching copper and collecting FLG onto a substrate: (A) FLG/Cu coupon floating on ammonium persulfate solution; (B) FLG floating on water; (C) & (D) collecting FLG onto a Au/epoxy surface by lifting the surface from below the FLG; (E) FLG on Au/epoxy. In (B), (C), and (D) the FLG has been outlined for clarity.

2.4 Modification Methods

2.4.1 Aryldiazonium Salt Reaction

2.4.1.1 Free-Floating Modification

Free-floating FLG (Figure 2.2B) was transferred to a 5 mL aryldiazonium salt aqueous solution (20 mM, unless otherwise specified) by removing the water and replacing it with modifier solution using a plastic pipette. The FLG was left on the aryldiazonium salt solution for between 1 and 72 hours in the dark, then washed with water 5× via solution replacement. The modified FLG could be collected onto various substrates in the sandwiched orientation (see Chapter 3, Scheme 3.1).

2.4.1.2 On Copper Modification

The FLG/Cu coupon was floated, FLG side down, on a 5 mL aqueous solution of the aryldiazonium salt (20 mM, unless otherwise specified) for 1 to 72 hours in the dark, then rinsed with MilliQ water. The modified FLG was removed from the copper, as described in Section 2.3.2, allowing modified FLG to be collected for analysis in the exposed orientation (see Chapter 3, Scheme 3.1).

2.4.2 Diels-Alder Reaction of an Anthranilic Acid

The FLG/Cu coupon was immersed in a solution of isoamyl nitrite (150 μ L) in 1,2-dichloroethane (10 mL) in a 2-neck round bottom flask. The solution was brought to reflux under a constant flow of nitrogen. The anthranilic acid precursor (5-nitroanthranilic acid or 2-aminoterephthalic acid 4-methyl ester) dispersed in 1,2-dichloroethane (final concentration = 0.14 M) was added slowly to the refluxing solution over a period of 30 minutes. The precursor dissolved once added to the refluxing solution. The solution continued at reflux for between 30 minutes and 6 hours. The coupon was removed from the reaction solution and washed with fresh 1,2-dichloroethane and MilliQ water. The FLG was removed from the copper and collected for analysis, as described in Section 2.3.2. Note that this protocol was only carried out using the FLG/Cu coupon as free-floating graphene was damaged by the reflux process. PPF surfaces were modified using the same protocol.

2.4.3 Primary Amine Addition

Free-floating FLG (Figure 2.2B) was transferred to a 5 mL N,N-dimethylformamide (DMF) solution of diisopropylethylamine (100 μ L) and the primary amine (4-

nitrophenethylamine or 2-aminoanthraquinone, 50 mM) by removing the water and replacing it with modifier solution using a plastic pipette, and left to react for 1 to 25 hours. The FLG was washed 1× with fresh DMF, and 5× with MilliQ water via solution replacement, and collected for analysis.

For physisorption trials, the free-floating FLG (Figure 2.2B) was transferred to a 5 mL DMF solution of diisopropylethylamine (100 μL) and the physisorption analogue (nitrotoluene or anthraquinone-2-sulfonic acid sodium salt, 50 mM) by removing the water and replacing it with modifier solution using a plastic pipette, and left for 20 hours. The FLG was washed 1× with fresh DMF, and 5× with MilliQ water via solution replacement, and collected for analysis.

2.4.4 Gold Nanoparticle Deposition

All electrochemical processes were carried out using an Eco Chemie Autolab PGSTAT302N or PGSTAT302 potentiostat running Nova software. For gold deposition, the working electrode was a 1 cm × 1 cm FLG/Cu coupon, with a copper foil electrical contact. The copper coupon had FLG on both sides, and both sides were exposed to the electrolyte solution. A Pt wire and Pt mesh were used as the pseudo-reference and counter electrodes respectively. Depositions were carried out in a DMF solution of (TOA)[AuCl₄] (0.36 mM) and tetrabutylammonium perchlorate (TBAClO₄, 0.1 M), by applying a fixed potential of -0.4, -0.6, or -0.8 V vs. Fc/Fc⁺ for 30 seconds to 10 minutes. After deposition, the FLG/Cu coupon was rinsed with fresh DMF and MilliQ water, and removed from the copper, as described in Section 2.3.2. To confirm the potential of the [AuCl₄]⁻ reduction, a CV was obtained (scan rate = 100 mV s⁻¹) in the same deposition solution, using a separate Pt wire as the working electrode, with added ferrocene (Fc). The half wave potential ($E_{1/2}$) value for the Fc/Fc⁺ couple was 0.1 V vs. the Pt wire pseudo-reference electrode, and it was assumed that the same $E_{1/2}$ value was applicable to the FLG/Cu working electrode, so this was used to report all potentials vs. Fc/Fc⁺.

2.4.5 Cobalt-Nickel Hydroxide Nanoparticle Deposition

Protocol one: A FLG/Cu coupon was used as the working electrode, with a copper foil electrical contact. There was FLG on both sides of the copper, and both sides were exposed to electrolyte solution. The electrodeposition was carried out in an aqueous

solution of $\text{Co}(\text{NO}_3)_2 \cdot 6\text{H}_2\text{O}$ (0.03 M) and $\text{Ni}(\text{NO}_3)_2 \cdot 6\text{H}_2\text{O}$ (0.1 M), with a Pt mesh counter electrode and a saturated calomel electrode (SCE) reference electrode. A potential of -1.0 V was applied for 1 minute, after which the FLG/Cu was washed with water. The FLG was removed from the copper and collected for analysis, as described in Section 2.3.2.

Protocol two: Free-floating FLG (Figure 2.2B) was collected onto a Au/epoxy surface, and dried. The FLG on the Au/epoxy surface was used as the working electrode, with a copper foil electrical contact. The electrodeposition was carried out in an aqueous solution of $\text{Co}(\text{NO}_3)_2 \cdot 6\text{H}_2\text{O}$ (0.03 M) and $\text{Ni}(\text{NO}_3)_2 \cdot 6\text{H}_2\text{O}$ (0.1 M), with a Pt mesh counter electrode and a SCE reference electrode, by applying a potential of -1.0 V for between 30 seconds and 5 minutes, with the entire Au/epoxy/FLG surface submerged in the deposition solution. The FLG surface was washed with water and dried. This protocol was also carried out with carboxybenzene diazonium modified FLG (FLG_{CP}) that had been modified via the free-floating method (Section 2.4.1.1).

2.5 Layer by Layer Assembly of Three-Sheet Stacks of Modified and Unmodified FLG

2.5.1 Aryldiazonium Modified FLG

A Cu coupon bearing NBD modified FLG with the modifying layer in the exposed orientation (Section 2.4.1.2) was taped to a glass microscope slide. A second, NBD modified FLG sheet (Section 2.4.1.2), that had been modified on copper and removed from its copper support, was collected onto the FLG/Cu surface (with the modifying layer in the exposed orientation), by lifting the substrate from below the floating modified FLG. This was dried at room temperature for 60 minutes, and at 60°C for 30 minutes. Another NBD modified FLG sheet could then be collected onto the FLG/FLG/Cu surface in the same manner, giving a three-sheet stack of NBD modified FLG on copper. The copper was removed, as described in Section 2.3.2, to give a three-sheet stack of modified FLG that could be collected on an appropriate substrate for analysis. This process was also repeated with unmodified FLG, giving a three-sheet stack reference sample.

For CBD modified FLG, the modification was carried out via the free-floating method (Section 2.4.1.1). The modified free-floating FLG was collected onto a Au/epoxy electrode surface in the sandwiched orientation (Section 2.4.1.1) by lifting the substrate from below the free-floating modified FLG and dried first at room temperature for 1 hour, then at 60 °C for 30 minutes. A second and third modified free-floating FLG sheet was collected onto this Au/epoxy/FLG surface in the same manner, giving a three-sheet stack of CBD modified FLG on the Au/epoxy electrode substrate.

2.5.2 Gold Nanoparticle Decorated FLG

Three-sheet stacks of gold nanoparticle decorated FLG were assembled as described in Section 2.5.1, however the NBD modified FLG/Cu was replaced with FLG/Cu decorated with gold nanoparticles (Section 2.4.4).

2.5.3 Cobalt-Nickel Hydroxide Nanoparticle Decorated FLG

A free-floating, unmodified FLG sheet was collected onto a Au/epoxy wafer and dried. Cobalt-nickel hydroxide nanoparticles were deposited onto the FLG as described in Section 2.4.5. A second unmodified FLG sheet was collected on the Au/epoxy/FLG surface, and the deposition process was repeated. A third, unmodified FLG sheet could be collected onto the Au/epoxy/FLG/FLG substrate and the deposition process repeated a final time to give a three-sheet stack of cobalt-nickel hydroxide modified FLG on a Au/epoxy surface. This entire protocol was also carried out using FLG_{CP} sheets rather than unmodified FLG.

2.6 Characterisation Methods

2.6.1 Error Analysis

Throughout this thesis, when the presented results are the average of three or more samples, the reported error/error bars are the standard deviation, and when the results are an average of two samples, the reported error/error bars are the range of values obtained from the two samples.

2.6.2 Infrared (IR) spectroscopy

For IR spectroscopy, the FLG was collected onto a KBr disk. IR spectra were obtained using a Bruker Vertex 70 spectrometer operating OPUS software. All spectra were recorded using 32 scans at 4 cm⁻¹ resolution from 600 to 4000 cm⁻¹ using a liquid nitrogen cooled wide band mercury cadmium telluride (MCT) detector. For KBr/FLG

samples the spectra were measured using transmission mode. A non-transparent cut-out was used to define the sample area. After recording each IR spectrum, the KBr/FLG disk could be resubmerged into a large petri dish containing water. Due to the solubility of KBr in water, the FLG was released from the surface to re-float on the water, so the FLG could be collected onto a second substrate for further analysis (Figure 2.3). For powder samples of the modification precursors, spectra were recorded using a diamond internal reflection element in an attenuated total reflectance arrangement (ATR mode). For ATR mode an air background, and for transmission mode a KBr background, was collected prior to spectral acquisition.

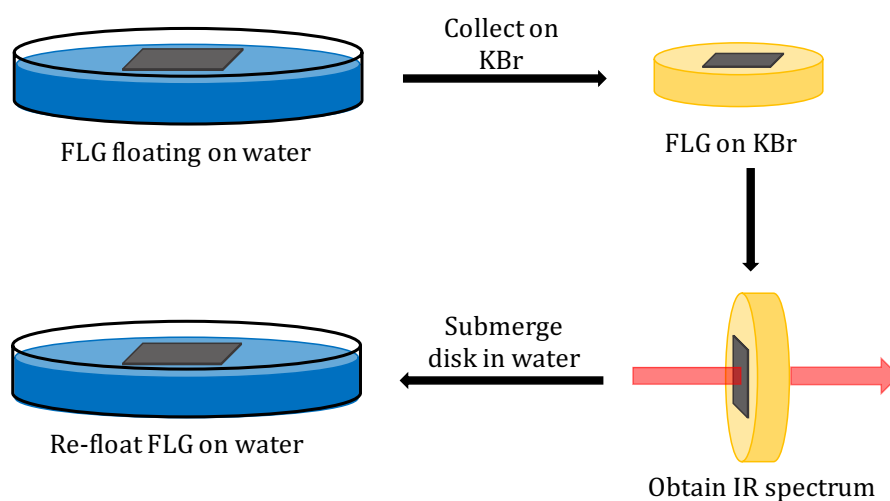


Figure 2.3: Protocol for collection of FLG on KBr for IR spectroscopy and releasing FLG for further analysis.

2.6.3 Ultraviolet (UV)/Visible spectroscopy

For UV spectroscopy, the FLG was collected onto a glass microscope cover slip. The UV spectra were obtained on a Cary 50 UV-visible spectrometer. Spectra were recorded at 600 nm min^{-1} from 800 to 400 nm, with a 1 nm resolution. A clean microscope cover slip background was recorded prior to spectral acquisition.

2.6.4 Raman Spectroscopy

2.6.4.1 Aryldiazonium and Diels-Alder Modified FLG

For Raman spectroscopy of aryldiazonium and Diels-Alder modified FLG, the FLG was collected onto a Au surface with no epoxy resin. The Raman spectra were obtained using a 532 nm (2.33 eV) laser, with 5 mW power in a confocal microscope arrangement with a 40 \times objective lens. The spectra were collected in a backscattering mode using 20 exposures at 5 second exposure times. The spot size was approximately

2 μm . For each sample, three spectra were recorded, and the results presented are the average of these. Spectra were obtained by Ms. Haidee Dykstra at Massey University, New Zealand.

2.6.4.2 Nanoparticle Deposition

For Raman spectroscopy after gold nanoparticle deposition, the modified FLG was collected onto a silicon wafer. The Raman spectra were obtained using a Renishaw RM 264N94 (532 nm laser) spectrometer operating at power < 1 mW. For each sample, three spectra were recorded at three separate points on the surface. The results presented are an average of the 9 spectra from each sample.

2.6.5 Atomic Force Microscopy (AFM)

2.6.5.1 Topographical Measurements

For AFM topographical imaging (Digital Instruments Dimensions 3100) the FLG was transferred to either HOPG or a gold substrate. Images were obtained at 0.65 Hz with a resolution of 512 samples per line in non-contact tapping mode using a silicon cantilever (Tap300A1-G) operating at resonant frequencies of approximately 280 kHz.

For AFM imaging after gold nanoparticle deposition, the FLG was collected onto a silicon wafer. AFM topographical images (Multimode 8 from Bruker, USA) were obtained in peak force quantitative nanomechanical mapping mode with scan assist activated using a silicon cantilever (SNL-10), with 512 samples per line at a scan rate of 0.65 Hz. The particle height and density were measured using Nanoscope analysis software. The particle height was determined by taking a line profile across the nanoparticle, and measuring the height as the vertical distance from immediately before the nanoparticle to the highest point of the nanoparticle. For each sample, the height of 15 nanoparticles was measured, and the presented data is the average of these. To calculate the particle density, the particle analysis tool was used over a $2.5 \mu\text{m} \times 2.5 \mu\text{m}$ area.

2.6.6 AFM Scratch Testing

Depth profiling measurements using scratch testing of modified PPF were performed using a previously described technique.⁷ A chip with three silicon cantilevers of different lengths was used (MikroMasch CSC37/AIBS). The AFM laser was focused on the shortest cantilever while the camera visual system was aligned with the longest.

When the shortest cantilever engaged with the surface, the longest dug into the film. The shortest cantilever was scanned multiple times over a $10\ \mu\text{m} \times 2.5\ \mu\text{m}$ area at a scan rate of 1.0 Hz so the long cantilever could scratch the film from the surface. The chip was replaced with a new single cantilever chip, and imaged as described above. The edge height of the scratch was determined using the box tool on Nanoscope analysis, which averages all the line profiles from within a boxed area. An example of a boxed area, and associated profile is given in Figure 2.4.⁷⁻⁹

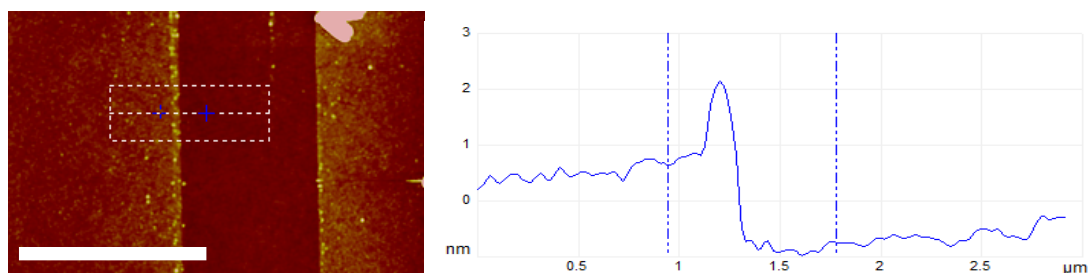


Figure 2.4: Box profile across AFM tip scratch on modified PPF. Scale bar = $3.0\ \mu\text{m}$.

2.6.7 Scanning Electron Microscopy (SEM)

2.6.7.1 Gold Nanoparticle Decorated FLG (FLG_{Au})

The FLG_{Au} sample was collected onto a silicon wafer, and a thin film ($< 1\ \text{nm}$) of Pt was evaporated onto the surface to improve conductivity. The SEM images were obtained using an FEI Quanta 650 ESEM-FEG operating in high vacuum at 20.0 kV. SEM images were obtained by Dr. Patrick Hill at the University of Manchester, United Kingdom.

2.6.7.2 Metal Hydroxide Nanoparticle Decorated FLG

FLG after metal hydroxide nanoparticle deposition on a Au/epoxy surface were imaged using a JEOL 7000F scanning electron microscope with JEOL Ex-2300 energy dispersive X-ray analyser, operating in high vacuum at 15.0 kV. SEM images were obtained by Mr. Mike Flaws at the University of Canterbury, New Zealand.

2.6.8 X-ray Photoelectron Spectroscopy (XPS)

For XPS measurements the FLG was transferred to either a silicon or gold substrate (with no epoxy resin). XPS data were obtained using a Kratos Axis Ultra DLD spectrometer equipped with a monochromatic Al $K\alpha$ source operating at 150 W. The wide scans were recorded with a step size of 1 eV and pass energy of 160 eV. Data were obtained by Dr. Colin Doyle at the University of Auckland, New Zealand.

2.6.9 Electrochemical Surface Concentration Measurements

The modified FLG was collected onto HOPG or PPF and dried, washed with methanol and redried. A circular working electrode area was defined using the two-part epoxy resin. The electrode was photographed and analysed using ImageJ software to establish the working electrode area, as shown in Figure 2.5.

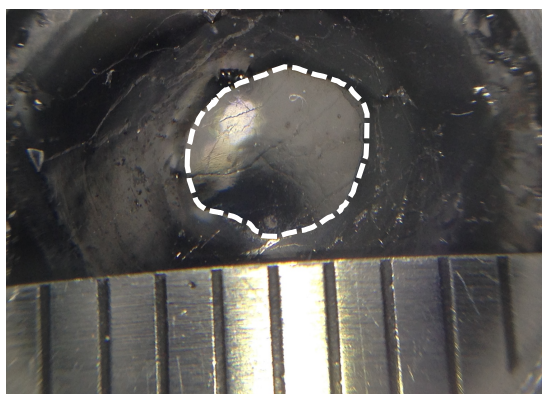


Figure 2.5: Image of FLG collected on HOPG with epoxy defined working electrode area used for ImageJ analysis of working electrode area. Dashed line shows working electrode area.

The cell was assembled with the working electrode placed horizontally between an insulated metal base plate and a glass solution cell with a hole in the base. A copper foil electrical contact was taped to the working electrode. A 0.13 cm² O-ring and four springs from plate to the cell sealed the electrolyte solution above the sample (set up shown in Figure 2.6)

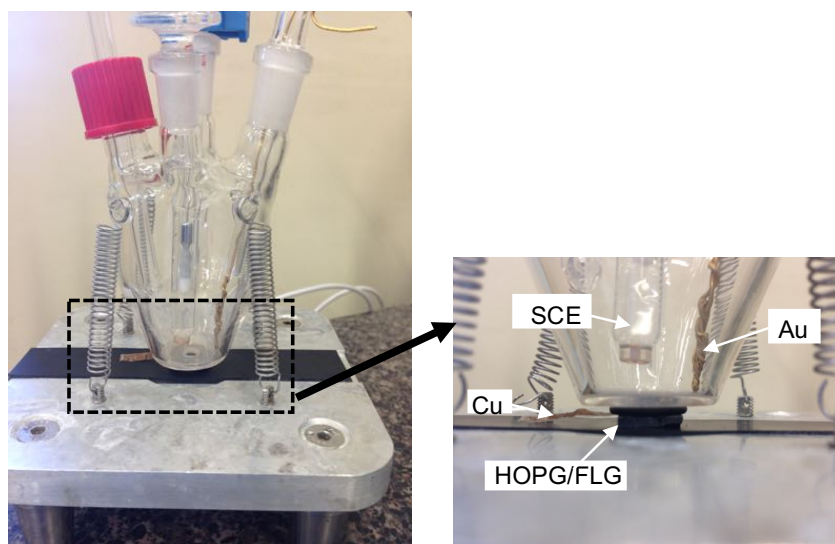


Figure 2.6: Electrochemical cell used for surface concentration measurements. SCE reference electrode and Au counter electrode shown.

2.6.9.1 Nitrophenyl (NP) Surface Concentration

NP reduction measurements were carried out in 0.1 M H₂SO₄ that was sparged for 15 minutes with nitrogen. A large area gold wire was used as the counter electrode and a SCE was used as the reference electrode. CVs were recorded between 0.6 and -1.0 V at 200 mV s⁻¹, starting at 0.6 V. Two cycles were recorded for each reduction measurement. For the PPF modified via the Diels-Alder reaction (Section 2.4.2) the same protocol was used, however no epoxy resin was used and the working electrode area was defined by the O-ring only (0.13 cm²).

The surface concentration of NP groups was calculated based on the charge associated with the reduction of NP groups and the oxidation of hydroxylaminophenyl groups (see Chapter 3, Figure 3.22).¹⁰⁻¹² The reduction and oxidation peak area was calculated using LinkFit software.¹³ To determine the area under the reduction curve, a baseline was fitted. In preliminary work, three different baselines were considered, and these are illustrated in Figure 2.7.

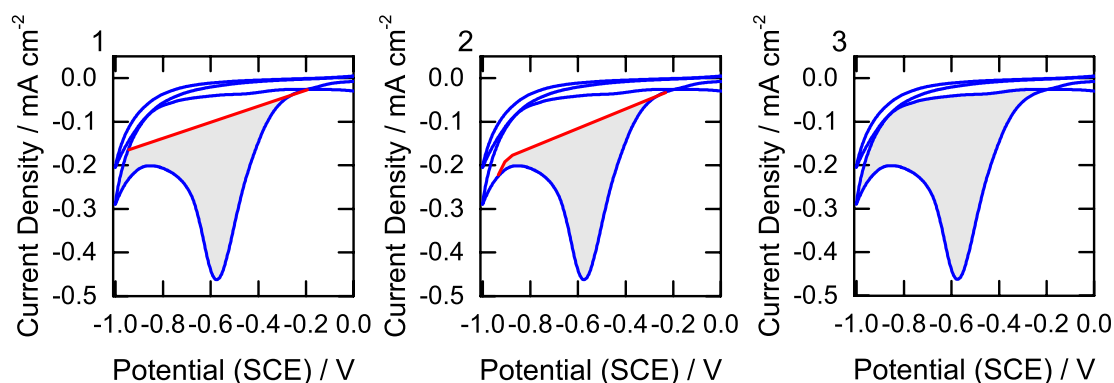


Figure 2.7: Different baselines considered for determining the area under the NP reduction peak.

Option 1 treats the baseline as the linear function of the voltammetric slope prior to the reduction peak. In option 2 the baseline is positioned between the pre and post voltammetric slopes, and option 3 uses the second CV cycle as the baseline. All three options were examined using 18 recorded CVs, and option 2 was chosen as the most appropriate. Option 1 and 3 were both excluded, due to complications from unknown capacitance contributions that may influence the background current. Also, option 1 and 3 appeared to overestimate the area when the reduction peak was small. Equation 2.1 was used to give the surface concentration,

$$\Gamma = \frac{Q}{nFA} \quad (2.1)$$

where Γ is the surface concentration in mol cm⁻², Q is the charge in coulombs (Q is calculated from the area of the NP reduction and hydroxylaminophenyl oxidation peaks), n is the number of electrons involved in the process ($n=6$), F is Faraday's constant, and A is the working electrode area in cm².

2.6.9.2 Anthraquinone Surface Concentration Measurements

Anthraquinone surface concentration measurements were carried out in 0.5 M H₂SO₄ that had been sparged for 15 minutes with nitrogen. A large area gold wire was used as the counter electrode and a SCE was used as the reference electrode. CVs were recorded between 0.5 and -0.7 V, at 200 mV s⁻¹, starting at 0.5 V. The surface concentration of anthraquinone groups was calculated based on the charge associated with the reduction peak (Figure 2.8).¹⁴ Equation 2.1 was used to calculate surface concentration, where $n=2$.

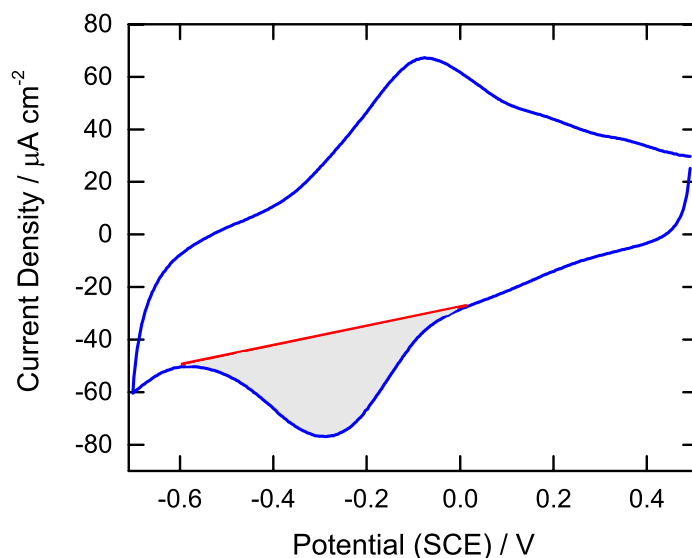


Figure 2.8: Reduction peak area used in AAQ surface concentration calculation.

2.6.10 Capacitance of FLG after Aryldiazonium Modification or Gold Nanoparticle Deposition

The modified FLG and FLG stacks were collected onto a Au/epoxy surface and dried, rinsed with methanol and redried. A circular working electrode area was defined using two-part epoxy resin. The electrode was photographed and analysed using ImageJ software to establish the working electrode area, as described above. The cell was assembled with the working electrode placed horizontally between an insulated metal base plate and a glass solution cell with a hole in the base (Figure 2.9). A copper foil electrical contact was taped to the working electrode. A 0.13 cm² O-ring and four springs from plate to the cell sealed the electrolyte solution above the sample. A large

area gold wire was used as the counter electrode and a SCE, housed in a Luggin capillary, was used as the reference electrode. For capacitance measurements, the electrolyte was 1 M HClO₄, which was sparged with nitrogen for 15 minutes prior to measurement.

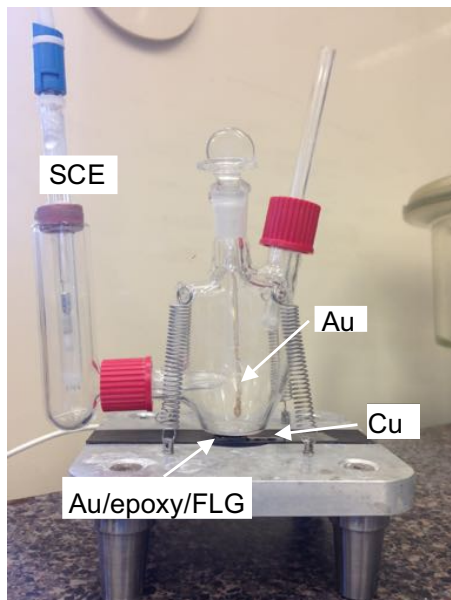


Figure 2.9: Electrochemical cell with Luggin capillary used for capacitance measurements. SCE reference and Au wire counter electrodes shown.

2.6.10.1 Cyclic Voltammetry

CVs were recorded between 0 and 0.4 V, starting at 0 V, at scan rates of 200, 100, 50, 20, 10, 5, and 2 mV s⁻¹, in order of decreasing scan rate. The areal capacitance was calculated based on the area enclosed by the CV plot using Equation 2.2,¹⁵

$$C_A = \frac{A_{CV}}{2\nu\Delta V A} \quad (2.2)$$

where C_A is the capacitance in F cm⁻², A_{CV} is the area enclosed by the CV in AV, ν is the scan rate in V s⁻¹, ΔV is the potential window in V, and A is the working electrode area in cm².

2.6.10.2 Galvanostatic Charge Discharge (CD) Measurements

CD measurements were always recorded after the CVs described in Section 2.6.10.1, from 0 to 0.4 V at current densities of 6.25, 10.0, 12.5, 25.0, and 50.0 $\mu\text{A cm}^{-2}$, in order of increasing current density. The areal capacitance was calculated based on the discharge portion of the plot (Figure 2.10) using Equation 2.3,

$$C_A = \frac{J}{(\Delta V/t_D)} \quad (2.3)$$

where C_A is the capacitance in F cm⁻², J is the current density in A cm⁻², ΔV is the potential window, and t_D is the discharge time. Energy density and power density were

calculated using Equations 2.4 and 2.5 based on the areal capacitance determined via CD testing,¹⁶⁻¹⁷

$$E_A = \frac{0.5C_A(\Delta V)^2}{3.6} \quad (2.4)$$

where E_A is the energy density in mWh cm^{-2} , and C_A is the areal capacitance in F cm^{-2} .

$$P_A = \frac{E_A}{t_D} \times 3600 \quad (2.5)$$

where P_A is the power density in mW cm^{-2} . Equation 2.4 and Equation 2.5 can also be used to give the gravimetric energy density (Wh kg^{-1}) and gravimetric power density (W kg^{-1}), if the areal capacitance is replaced with the gravimetric capacitance (F g^{-1}).

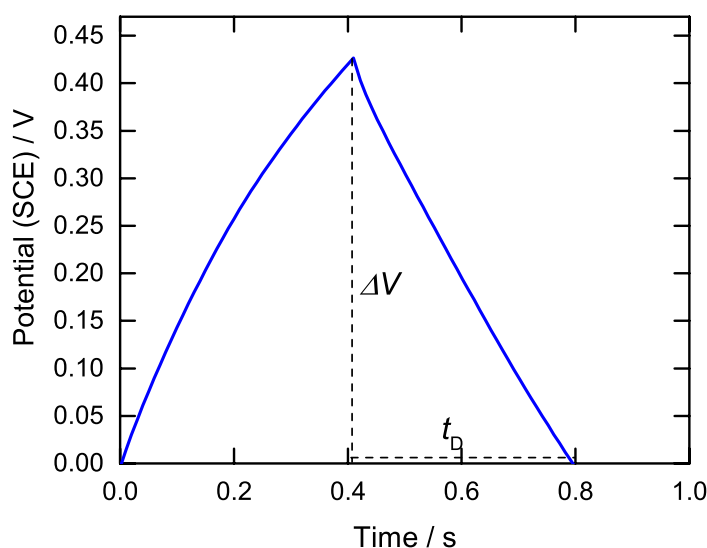


Figure 2.10: CD plot of FLG on Au/epoxy in 1 M HClO_4 , with discharge time and potential window shown.

2.6.10.3 Electrochemical Impedance Spectroscopy (EIS) Measurements

CVs were recorded between -0.6 and 0.3 V, and -0.3 and 0.3 V, at 200 and 20 mV s^{-1} before and after all EIS measurements. EIS data were collected using a perturbation amplitude of 10 mV at 50 frequencies, from 0.1 MHz to 0.1 Hz, between -0.5 and 0.3 V at 50 mV steps. The DC potential was held for two minutes before beginning each measurement to allow the system to achieve a steady state. Unless otherwise stated all EIS measurements were started at the most negative potential and stepped to more positive potentials.

2.6.11 Capacitance of Metal Hydroxide Modified FLG

A circular working electrode area was defined using two-part epoxy resin on the Au/epoxy/FLG surface after metal hydroxide nanoparticle deposition. The electrode was photographed and analysed using ImageJ software to establish the working electrode area, as described earlier. The cell was assembled with the working electrode

placed horizontally between an insulated metal base plate and a glass solution cell with a hole in the base (Figure 2.9). A copper foil electrical contact was taped to the working electrode. A 0.13 cm^2 O-ring and four springs from plate to the cell sealed the electrolyte solution above the sample. A large area gold wire was used as the counter electrode, and a Hg/HgO, 1 M KOH reference electrode was used, housed in a Luggin capillary. For capacitance measurements, the electrolyte was 1 M KOH, which was sparged with nitrogen for 15 minutes prior to measurement.

2.6.11.1 Cyclic Voltammetry

CVs were recorded between -0.2 and 0.65 V at scan rates of 200, 100, 50, 20, 10, 5, and 2 mV s^{-1} , in order of decreasing scan rate. The capacitance was calculated based on the area enclosed by the CV plot, as described by Equation 2.2.

2.6.11.2 Galvanostatic Charge Discharge

CD measurements were always recorded after CVs obtained as described in Section 2.6.11.1. CD curves were recorded from -0.2 to 0.65 V at current densities of 0.8, 1.6, 3.2, and 6.4 mA cm^{-2} , in order of increasing current density. The capacitance was calculated based on Equation 2.3.

2.6.11.3 Electrochemical Impedance Spectroscopy

EIS measurements were carried out as described in Section 2.6.10.3.

2.6.12 Four-Point Probe measurements

The FLG was collected onto a glass microscope cover slip that had been cut into $1 \text{ cm} \times 2.5 \text{ cm}$ pieces. After drying, four ohmic contacts were added to the corners of the FLG sample by thermally evaporating 50 nm of Ti followed by 50 nm of Au. The FLG was masked using aluminium foil, so that only the corners of the FLG were exposed during Ti and Au contact deposition. An ECOPIA SPCB-01 spring clip-board was used to mount the sample. Measurements were made using a EGK Corp. HEM-2000 Hall Effect Measurement System, with a 0.51 T magnet. For each sample, four currents were used, and the voltage output recorded. The choice of current was automated and selected to give a voltage reading close to 200 mV, and therefore was unique for each sample. Figure 2.11 shows a sample collected onto a glass microscope cover slip with ohmic contacts in each corner, and the spring clip-board. Appendix A.2 outlines the calculations required for the four-point probe measurements. The Van der Pauw method

was used to determine sheet resistance, as this method compensates for the geometry dependence of resistivity measurements.

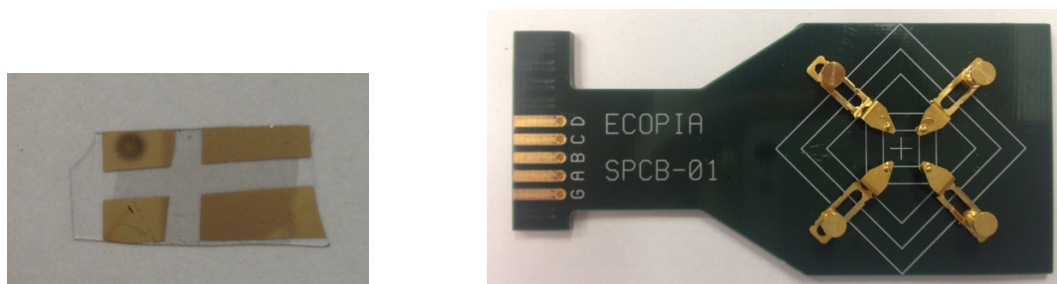


Figure 2.11: Left to right: FLG collected onto glass microscope coverslip, with Ti/Au contacts in each corner of the FLG; ECOPIA SPCB-01 spring clip board used for Hall effect measurements.

2.6.13 Inductively Coupled Plasma Mass Spectrometry (ICPMS) Measurements

For ICPMS measurements, a circular area was defined using two-part epoxy resin on the Au/epoxy/FLG surface after cobalt-nickel nanoparticle deposition. An area was defined prior to immersion so that the measured concentration could be converted into a surface concentration after analysis. This substrate was immersed in 5 mL of 2% ultrapure nitric acid for 24 hours, after which the substrate was removed. The concentration of cobalt and nickel in the solution was determined using an Agilent 7500cx ICPMS with a standard set up, then converted into a surface concentration of cobalt-nickel on the FLG prior to immersion. ICPMS measurements were performed by Mr. Robert Stainthorpe at the University of Canterbury, New Zealand. Standards of 0.1, 1, 10, 100, and 1000 $\mu\text{g L}^{-1}$ were used for calibration prior to analysing samples.

2.7 References

1. Brooksby, P. A.; Downard, A. J., Electrochemical and atomic force microscopy study of carbon surface modification via diazonium reduction in aqueous and acetonitrile solutions. *Langmuir* **2004**, *20*, 5038-5045.
2. K.H., S.; Allen, R. L. M., *Aromatic diazo compounds*, 3rd edn. Edward Arnold: London, 1985.
3. DuVall, S. H.; McCreery, R. L., Self-catalysis by catechols and quinones during heterogeneous electron transfer at carbon electrodes. *J. Am. Chem. Soc.* **2000**, *122*, 6759-6764.
4. Ahmed, S.; Hettwer, S.; Vrijbloed, J. W.; Farina, C.; Allgeier, H. Preparation of acylamino-phthalic acid amides and related compounds as neurotrypsin inhibitors. WO2012059442A2, 2012.
5. Booth, S. G.; Uehara, A.; Chang, S. Y.; Mosselmans, J. F. W.; Schroeder, S. L. M.; Dryfe, R. A. W., Gold deposition at a free-standing liquid/liquid interface: Evidence for the formation of Au(i) by microfocus x-ray spectroscopy (μ XRF and μ XAFS) and cyclic voltammetry. *J. Phys. Chem. C* **2015**, *119*, 16785-16792.
6. Wu, B.; Geng, D.; Guo, Y.; Huang, L.; Xue, Y.; Zheng, J.; Chen, J.; Yu, G.; Liu, Y.; Jiang, L., Equiangular hexagon-shape-controlled synthesis of graphene on copper surface. *Adv. Mater.* **2011**, *23*, 3522-3525.
7. Lee, L.; Gunby, N. R.; Crittenden, D. L.; Downard, A. J., Multifunctional and stable monolayers on carbon: A simple and reliable method for backfilling sparse layers grafted from protected aryldiazonium ions. *Langmuir* **2016**.
8. Lee, L.; Brooksby, P. A.; Leroux, Y. R.; Hapiot, P.; Downard, A. J., Mixed monolayer organic films via sequential electrografting from aryldiazonium ion and arylhydrazine solutions. *Langmuir* **2013**, *29*, 3133-3139.
9. Lee, L.; Leroux, Y. R.; Hapiot, P.; Downard, A. J., Amine-terminated monolayers on carbon: Preparation, characterization, and coupling reactions. *Langmuir* **2015**, *31*, 5071-5077.
10. Ortiz, B.; Saby, C.; Champagne, G. Y.; Bélanger, D., Electrochemical modification of a carbon electrode using aromatic diazonium salts. 2. Electrochemistry of 4-nitrophenyl modified glassy carbon electrodes in aqueous media. *J. Electroanal. Chem.* **1998**, *455*, 75-81.
11. Yu, S. S. C.; Tan, E. S. Q.; Jane, R. T.; Downard, A. J., An electrochemical and XPS study of reduction of nitrophenyl films covalently grafted to planar carbon surfaces. *Langmuir* **2007**, *23*, 11074-11082.
12. Lee, L.; Brooksby, P. A.; Hapiot, P.; Downard, A. J., Electrografting of 4-nitrobenzenediazonium ion at carbon electrodes: Catalyzed and uncatalyzed reduction processes. *Langmuir* **2016**, *32*, 468-476.
13. Loring, J. S., *LinkFit* **2004**.

14. Pognon, G.; Brousse, T.; Demarconnay, L.; Bélanger, D., Performance and stability of electrochemical capacitor based on anthraquinone modified activated carbon. *J. Power Sources* **2011**, *196*, 4117-4122.
15. Stoller, M. D.; Ruoff, R. S., Best practice methods for determining an electrode material's performance for ultracapacitors. *Energy Environ. Sci.* **2010**, *3*, 1294-1301.
16. Shao, Y.; El-Kady, M. F.; Lin, C.-W.; Zhu, G.; Marsh, K. L.; Hwang, J. Y.; Zhang, Q.; Li, Y.; Wang, H.; Kaner, R. B., 3D freeze-casting of cellular graphene films for ultrahigh-power-density supercapacitors. *Adv. Mater.* **2016**, *28*, 6719-6726.
17. Li, H.; Tao, Y.; Zheng, X.; Luo, J.; Kang, F.; Cheng, H.-M.; Yang, Q.-H., Ultra-thick graphene bulk supercapacitor electrodes for compact energy storage. *Energy & Environ. Sci.* **2016**, *9*, 3135-3142.

3 Chemical Vapour Deposition of Few-Layer Graphene and Subsequent Modification with Aryldiazonium Salts

3.1 Introduction

CVD graphene is chemically inert and can be difficult to process due to its tendency to aggregate caused by strong Van der Waals interactions between the sheets. Chemical functionalisation of graphene is a possible way to overcome this. Functionalisation can also add different groups that will be useful to the final application. As explained in Chapter 1, Section 1.7, one aim of this project is to use covalent functionalisation methods to add spacer groups that will prevent aggregation of the FLG sheets during assembly into supercapacitor devices. Covalent modification is a particularly attractive option because covalently bonded groups are unlikely to be removed during assembly and use of the final device. One convenient technique to covalently modify graphene is via reaction with aryldiazonium salts. The mechanism for this reaction was discussed in Chapter 1, Section 1.3.1.

The reaction of aryldiazonium salts with graphene has been explored in various literature reports. Examples of both spontaneous and electrochemical grafting of aryldiazonium salts exist, in both aqueous and non-aqueous conditions. Several different forms of graphene have been modified using aryldiazonium salts. Tour et al.¹⁻² studied the solution phase reaction of rGO. They found that the addition of a surfactant to the reaction mixture enhanced the efficiency of the reaction due to a more concentrated dispersion of rGO. Thermogravimetric analysis indicated there was one functional group per 55 carbon atoms, and functionalisation significantly improved dispersibility in several solvents. Haddon et al.³ studied the spontaneous reaction of epitaxial graphene with aryldiazonium salts. An epitaxial graphene sample was submerged in a non-aqueous, nitrobenzene diazonium (NBD) solution for 20 hours. The modified graphene sample was then analysed by IR spectroscopy, XPS, and resistivity studies. Electrochemistry was used to show a high surface coverage of 1×10^{15} molecules cm^{-2} . Finally, Ago et al.⁴ modified CVD single layer graphene by submerging the graphene, still on the copper, into an aqueous NBD solution. The spontaneous reaction was monitored using Raman spectroscopy.

Studies have shown the reactivity of monolayer, bilayer, and FLG systems are dissimilar.⁵⁻⁷ Monolayer systems are reported to be significantly more reactive than bilayer or FLG, with one literature report highlighting a 10× increase in reactivity for monolayer graphene compared to bilayer graphene.⁵ The suggested reason for this increase in reactivity is that bilayer and FLG have less flexibility to accommodate the local sp³ geometry that results from functionalisation due to the underlying carbon lattice.⁶ For this study, micromechanically prepared graphene was submerged in an aqueous solution of the aryldiazonium salt, and the reaction was observed via Raman spectroscopy. The edges of graphene have also been reported to be more reactive than the basal plane, with one literature report indicating a 2.5× increase in reactivity,⁴ assumed to be due to the presence of defects and dangling bonds, as well as a greater ability to accommodate conversion to sp³-hybridisation.⁷

Strano et al.⁸ demonstrated the influence of the underlying substrate on the functionalisation of graphene with aryldiazonium salts. Four different substrates were chosen to act as supports for CVD graphene, namely silicon oxide, sapphire, hexagonal boron nitride, and a surface coated in an alkyl terminated monolayer. The graphene was then submerged in an aqueous solution of an aryldiazonium salt, in the presence of sodium dodecylsulfate (SDS). The SDS was added to improve the wettability of the graphene. The reactivity of the graphene was determined using the changes in the Raman spectrum for each graphene sample, along with AFM and contact angle measurements. The highest reactivity was achieved with strongly p-doping substrates (silicon oxide and sapphire), while the mildly p-doping substrates, (hexagonal boron nitride), resulted in a reduction in reactivity.

Examples of the different aryldiazonium salts that have been used to functionalise graphene are given in Figure 3.1. De Feyta et al.⁹ modified graphene surfaces using the bulky 3,5-bis-*tert*-butylbenzene diazonium salt, via the electrochemical pathway. The bulkier aryldiazonium salt limited the grafting reaction to a monolayer, rather than the disordered multilayers typically formed from less bulky aryldiazonium salts. Strano et al.¹⁰ modified both CVD and dispersed graphene flakes using an aqueous solution of 4-propargyloxybenzene diazonium salt, which could then be used as a tether molecule to add short chain polyethylene glycol molecules to the graphene surface. Daasbjerg et al.¹¹ also reported using an aryldiazonium grafted film to tether further functionality to

the graphene. First a 4-(2-hydroxyethyl)phenyl film was electrografted from an acetonitrile solution. This was then used to attach polymer brushes to the surface. The ability to tether additional molecules to the phenyl group is advantageous in the development of biosensors and catalysts from graphene systems. Palermo et al.¹² utilised an aryldiazonium salt with a long aliphatic chain as the ‘R’ group (Figure 3.1E). The aryldiazonium salt initially physisorbed onto the CVD graphene into a two-dimensional, ordered pattern, from a non-aqueous solution. Electrochemical reduction then forced the formation of the aryl radical that could covalently bind to the surface. Scanning tunnelling microscopy (STM) images confirmed an ordered pattern of grafted molecules.

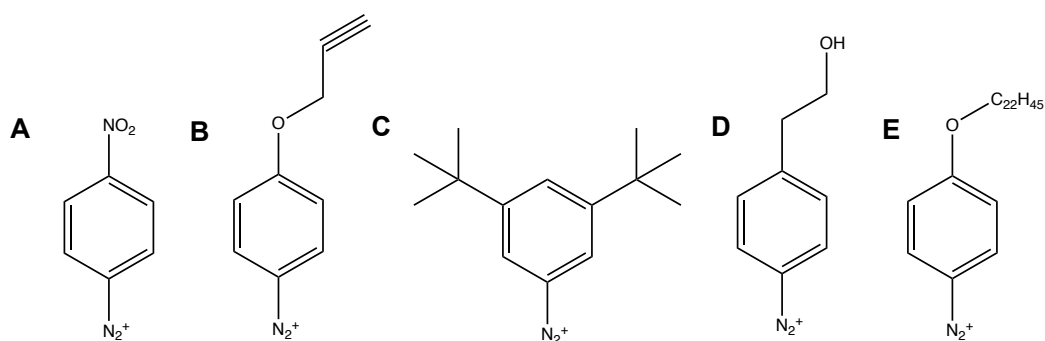


Figure 3.1: Structure of (A) NBD; (B) 4-propargyloxybenzene diazonium; (C) 3,5-bis-*tert*-butylbenzene diazonium; (D) 4-(2-hydroxyethyl)benzene diazonium; (E) 4-docosyloxybenzene diazonium.

Recently, aryldiazonium chemistry and the electrochemical exfoliation of graphite have been coupled to give a dispersion of functionalised few- to multilayer graphene sheets. Dryfe et al.¹³ reported the electrochemical exfoliation of graphite at negative potentials (−4 V vs. Ag wire) in the presence of either NBD or 4-bromobenzene diazonium, to give a functionalised dispersion of graphene sheets. An intercalating agent (CsClO₄/LiClO₄) was also added to the electrolyte to assist the exfoliation process and it was suggested that the generation of nitrogen gas during the diazonium reduction further enhanced exfoliation. Ossoon and Belanger¹⁴ reported the electrochemical exfoliation of graphite and simultaneous grafting of an anthraquinone diazonium derivative. Unlike the work by Dryfe, a positive potential (+10 V) was applied. They suggested that the application of a positive potential facilitated the exfoliation of graphite, and then the aryldiazonium ion could spontaneously react with the freshly cleaved graphene sheets in solution. They reported that this “one-pot” synthesis was faster than a typical two-step process, presumably a result of the enhanced reactivity of the freshly generated graphene sheets.

Thus, the modification of graphene using aryldiazonium salts is an efficient and simple way of adding functionality. Although this reaction has been studied in some detail previously, little is known about the chemical composition of the resulting film, or the reactivity of free-floating graphene. In this work, the modification of FLG, prepared via atmospheric pressure CVD, using five aryldiazonium salts (Figure 3.2), has been studied and spectroscopic analysis gave insight into the types of bonding within the film. Furthermore, the modified FLG was interrogated using electrochemistry and Hall effect measurements.

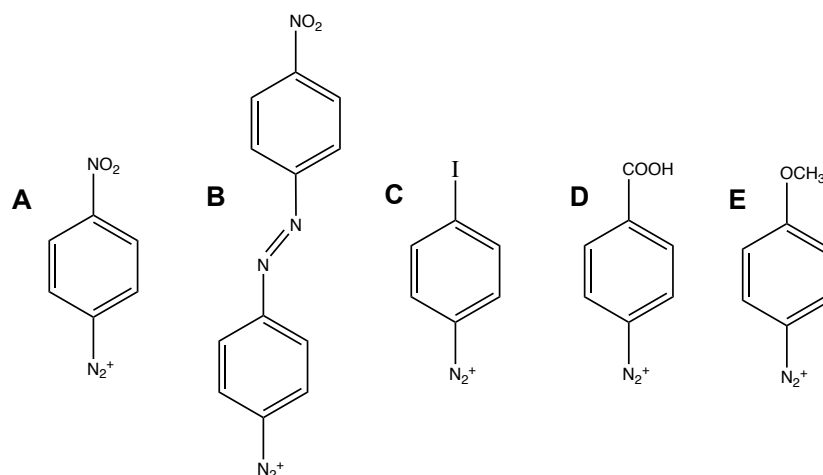


Figure 3.2: Aryldiazonium tetrafluoroborate salts used in this work: (A) 4-nitrobenzene diazonium (NBD); (B) 4-nitroazobenzene diazonium (NABD); (C) 4-iodobenzene diazonium (IBD); (D) 4-carboxybenzene diazonium (CBD); (E) 4-methoxybenzene diazonium (MBD). Tetrafluoroborate anion (BF_4^-) not shown.

3.2 Experimental Methods

The experimental methods have been described in Chapter 2. The CVD growth protocols are given in Section 2.3.1. The synthesis of the five aryldiazonium salts investigated in this chapter is given in Section 2.1.1. The aryldiazonium salt modification strategy and subsequent characterisation techniques are explained in Sections 2.4.1 and 2.6, respectively.

3.3 Results and Discussion

3.3.1 Preparation and Characterisation of FLG

3.3.1.1 Tuning the CVD Parameters

Graphene was grown on copper foils by atmospheric pressure CVD. The two growth protocols are illustrated in Figure 3.3. In this work, the gas flow rates were selected to give the desired graphene domain shape and layer number. As explained by Wu et al.,¹⁵ and others, a high hydrogen flow rate gives hexagonal graphene domains,¹⁶ hence during the 7 minute growth phase the gas parameters were initially set as 500 sccm hydrogen and 5 sccm methane. This gave graphene of 6-7 layers with a hexagonal domain shape. The characterisation of this FLG will be described later in this chapter. For capacitance studies, 3-4 layer graphene was desired. To decrease the number of layers, argon was added to the gas mixture. Diluting the methane concentration at the surface of the copper has been shown to reduce both the number of layers and the nucleation density.¹⁷⁻¹⁹

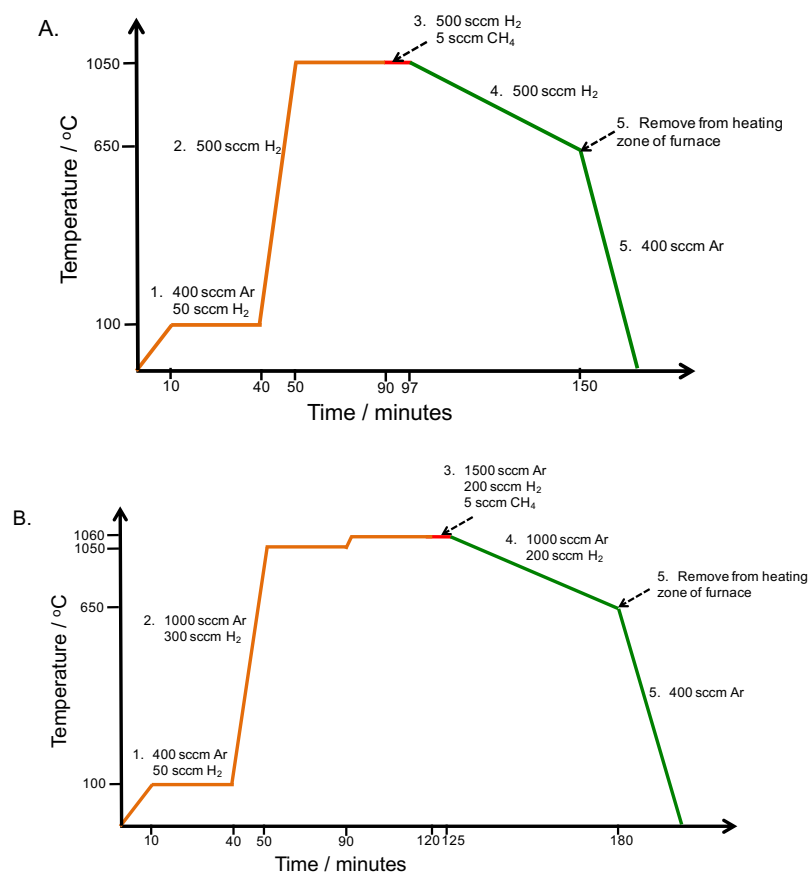


Figure 3.3: Different CVD protocols used in this work to grown FLG on copper: (A) 6-7 layer graphene; (B) 3-4 layer graphene.

3.3.1.2 UV/Visible Spectroscopy

The layer number of a graphene sample can be determined using UV/visible spectroscopy. Work by Geim et al.²⁰ demonstrated that graphene has an opacity of 2.3% that is independent of wavelength over a wide wavelength range (400 to 750 nm), moreover with each additional graphene layer, the transparency decreases by a further 2.3%. Wan et al.²¹ demonstrated the effectiveness of UV/visible spectroscopy in establishing layer number by differentiating between mono-, bi-, and tri-layer graphene. The UV/visible spectra for FLG after transfer to a glass microscope coverslip are given in Figure 3.4.

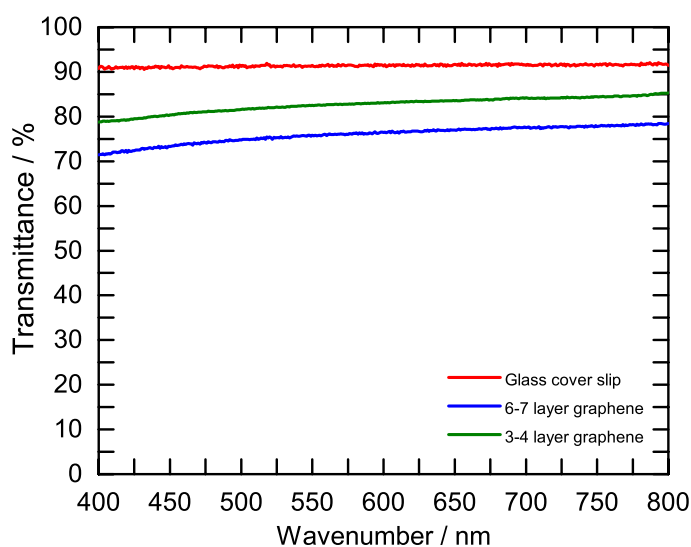


Figure 3.4: UV/visible spectra from 400 to 800 nm of FLG produced via CVD on a glass microscope cover slip. Each spectrum is an average of four separate FLG samples.

The FLG for protocol A gave an average transparency of 76.0% corresponding to 6.9 layers while for protocol B the average transparency was 82.7 % corresponding to 3.9 layers. The FLG samples likely have regions of different layer numbers, due to variations in the copper surface prior to growth. As each spectrum is recorded over the entire 1 cm × 1 cm FLG coupon, it is an average of different layer number regions across the surface and so is not a whole number. This result confirms that manipulating the gas flow rate gives good control over the number of graphene layers. All experiments described in the remainder of this chapter utilised 6-7 layer graphene.

3.3.1.3 AFM Imaging

AFM was used to image the FLG on its copper foil support and after transfer to HOPG. Figure 3.5A and B show as grown FLG on copper foil. In both images, wrinkled, hexagonal graphene domains can be seen, which are interconnected by less well-

defined grain boundaries. The domains are approximately 5 μm across the longest axis. The hexagonal domain shape is typically seen for graphene grown on a Cu(111) surface.²² The CVD process here uses a temperature of 1050 to 1060 $^{\circ}\text{C}$, which is close to the melting point of copper (1085 $^{\circ}\text{C}$). At these high temperatures, the copper atoms can rearrange to give a predominantly Cu(111) surface prior to methane introduction causing hexagonal growth of graphene.²³⁻²⁴

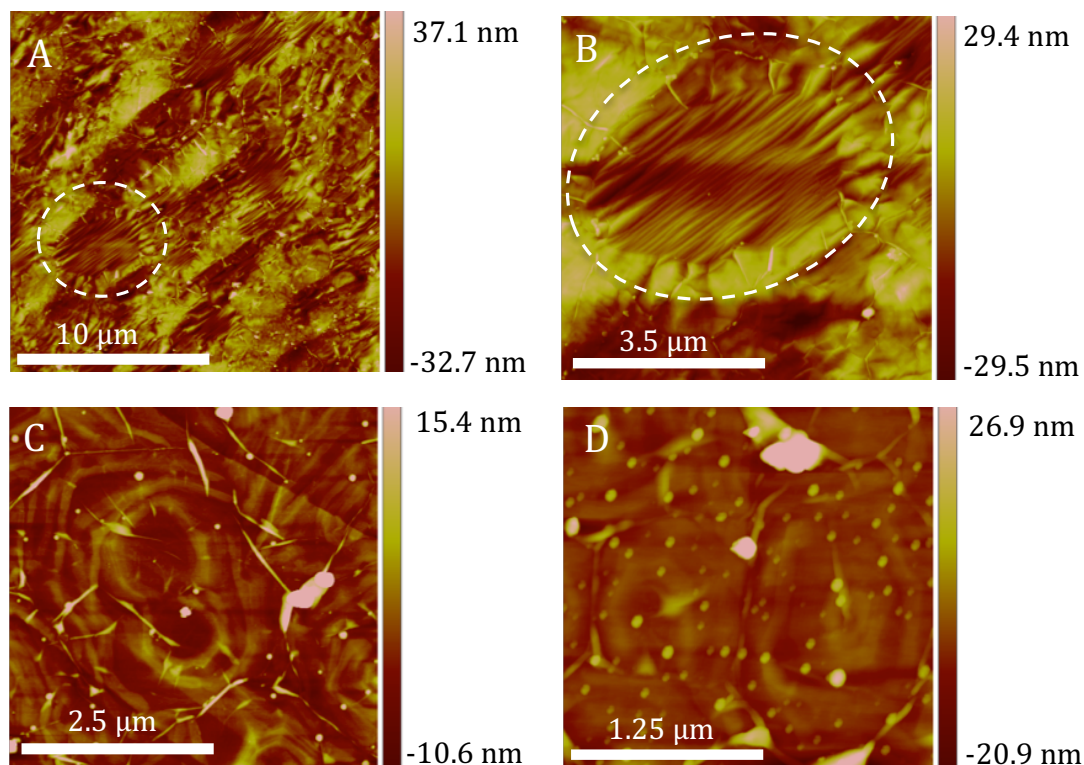


Figure 3.5: AFM images of as grown, 6-7 layer FLG: (A) and (B) on the copper support; (C) and (D) after transfer to freshly cleaved HOPG.

As shown by the UV/visible spectrum (Figure 3.4), the graphene grown is FLG. It is therefore likely that each hexagonal domain is made up of multiple graphene layers. Through carbon isotope labelling, Ruoff et al. have shown that once the first graphene layer has nucleated on copper, a second layer can grow underneath the first.²⁵ This is especially common when methane is used as the carbon precursor.²⁶ It is suggested that active hydrocarbon species can intercalate between the graphene and the substrate, and subsequently decompose to form a new layer of graphene underneath the first. The low methane to hydrogen ratio used in this thesis work results in a Volmer-Weber growth mode,²⁷ in which well faceted, hexagonal domains are typically formed, that stack parallel to give a pyramid shape. The result is easily distinguishable hexagonal domains, as seen in Figure 3.5B. This is also known as AB-stacking. The wrinkles in

the hexagons arise due to the differences in the thermal expansion coefficients for graphene and copper, which cause wrinkles to form during cooling.²⁸⁻²⁹

The topography of FLG after transfer to HOPG is shown in Figure 3.5C and D. The transfer process is polymer-free, as described in Chapter 2, Section 2.3.2. HOPG is a very flat, almost featureless surface, making it an ideal substrate for AFM imaging. The FLG has an undulating appearance and wrinkles that are much larger than those formed during cooling. Work by Park et al.³⁰ and Cho et al.²⁹ has indicated that such wrinkles, commonly seen after transfer of graphene, are a result of water trapped between the FLG and the substrate. Upon drying, evaporation of the trapped water leaves wrinkles and folds. Small circular features on the surface are believed to be residual contaminants that result from the copper etching process.

3.3.1.4 Raman and IR Spectroscopy

Raman spectroscopy is the most common method of characterising graphene. The principles of Raman spectroscopy are outlined in Appendix A, Section A.1. Raman spectroscopy is able to give information on the number of graphene layers, the defect concentration, and the doping type.³¹ There are three predominant bands in the Raman spectrum of graphene: the G-, D-, and 2D-bands, positioned at approximately 1585, 1350, and 2700 cm^{-1} , respectively. The G-band is caused by the high frequency E_{2g} phonon transition and is an in-plane vibrational mode.³² The intensity of the G-band increases almost linearly with the number of layers due to the increase in the number of sp^2 -hybridised carbon atoms. Furthermore, the G-band shifts to lower wavenumbers with an increase in layer number; it can also shift due to doping.³¹ The D-band is due to the breathing modes of the six-carbon rings in graphene and requires a defect (eg. sp^3 -hybridised carbon) for activation. Typically, the intensity ratio of the D- and G-band is used to quantify the number of defects in a graphene sample, with the D-band absent in pristine single-layer graphene. Finally, the 2D-band is an overtone of the D-band, however it does not require a defect for activation. The 2D-band can give information on layer number: for monolayer graphene, the 2D-band can be fitted with a single Lorentzian peak, however, as the number of layers increases, the band begins to split and multiple peaks can be fitted.³¹ The 2D/G band intensity ratio is also indicative of the number of layers, where an intensity ratio greater than one indicates monolayer growth.²¹ The 2D-band, like the G-band, can shift with doping.

The Raman spectrum obtained for 6-7 layer graphene is given in Figure 3.6 and shows the three expected bands, (G-band at 1584.6 cm^{-1} , D-band at 1340.7 cm^{-1} and 2D-band at 2698.0 cm^{-1}) confirming that graphene has been successfully grown. The low D/G band intensity ratio (0.13), indicates a small number of defects. These are most likely due to the grain boundary regions that connect the graphene domains. This D/G band intensity ratio is similar to literature reports, where the intensity ratio ranges from 0 to 0.31 depending on the CVD protocol.^{15-16, 33} The 2D/G band intensity ratio is 0.44 indicating FLG growth.

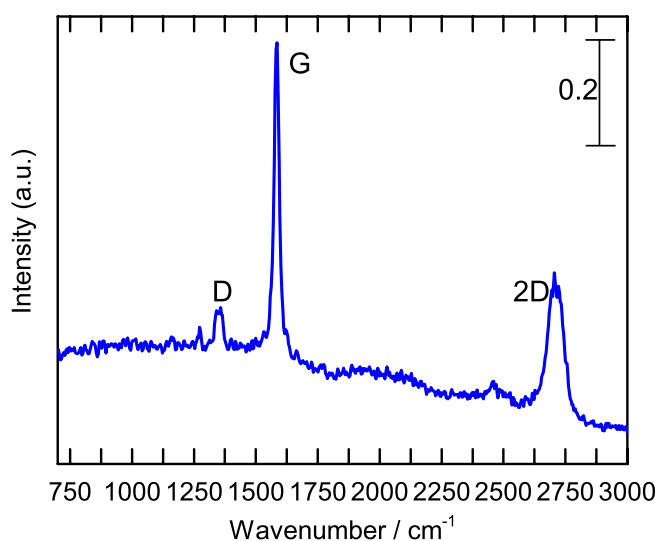


Figure 3.6: Raman spectrum of 6-7 layer FLG transferred to a gold substrate. Spectrum is the average from two separate samples, with three spectra taken per sample and normalised to give G-band intensity of 1.

The curve fitting profile for the 2D-band of a representative Raman spectrum is given in Figure 3.7. More than four Lorentzian components are required to accurately fit this band, verifying that FLG has been grown, which agrees with the UV-visible spectroscopy results.

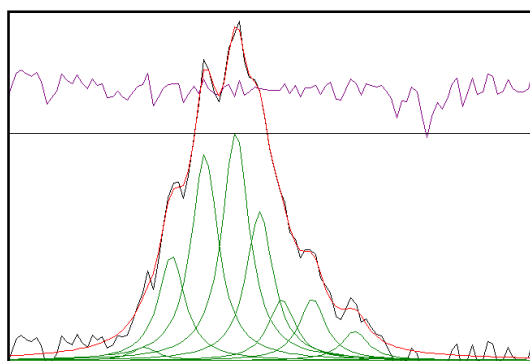


Figure 3.7: 2D-band of a representative FLG sample on a gold substrate, fitted using Linkfit software with eight different Lorentzian curves. Residual shown in purple.

FLG was characterised using IR spectroscopy where the FLG was collected onto a KBr disk, and spectra were collected in transmission mode. KBr is soluble in water therefore after recording the IR spectrum the disk could be resubmerged in a water bath releasing the FLG from the surface and collected on a second substrate for further analysis. Figure 3.8 shows single beam spectra for a new KBr disk (blue) and the same KBr disk after a ten second immersion in water (red). The beam intensity changes after immersion consistent with some dissolution of KBr. A 1:1 ratio of the two single beam spectra (Figure 3.8B) clearly shows features below 1250 cm^{-1} that result from these differences in beam intensity and therefore are not considered as sample vibrational modes when assigning IR spectra throughout this thesis.

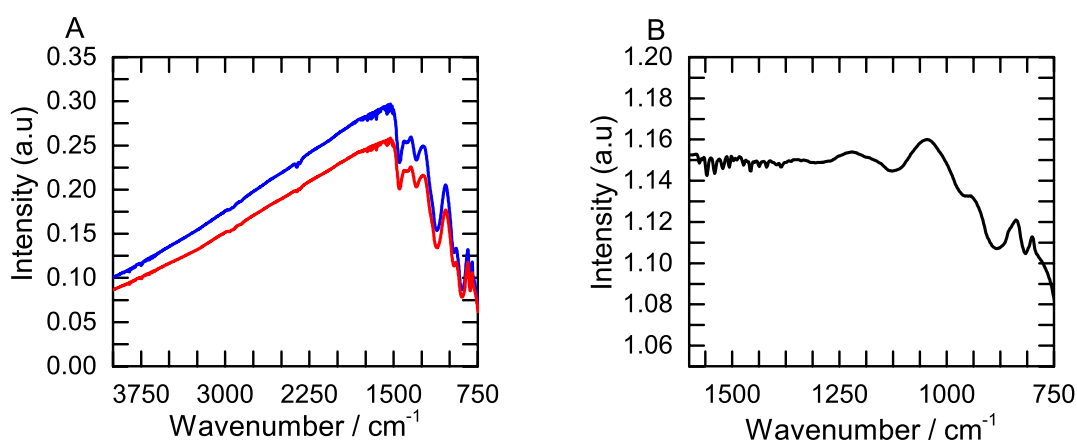


Figure 3.8: (A) Single beam transmission mode spectra of a new KBr disk (blue), and KBr disk after a ten second immersion in water (red); (B) 1:1 ratio of the single beam spectra given in A.

The IR spectrum of FLG is given in Figure 3.9. The oxygen groups of GO have signature peaks at approximately $1750\text{-}1620\text{ cm}^{-1}$ (C=O stretch), $2850\text{-}2970\text{ cm}^{-1}$ (-OH stretch), 1260 cm^{-1} (epoxy breathing), and 1070 cm^{-1} (C-O stretch).³⁴⁻³⁵ None of these peaks are present in the spectrum below, indicating no detectable oxygen groups on the as prepared FLG. There is evidence of a broad band from 3700 and 2700 cm^{-1} that is likely caused by water trapped between the FLG and the KBr disk. There is also a feature at 2919 cm^{-1} , which is the wavenumber associated with the C-H stretch vibration. This is often seen in the spectra obtained using this instrument, and is believed to be due to contaminants. The peak at 2350 cm^{-1} is due to atmospheric carbon dioxide.

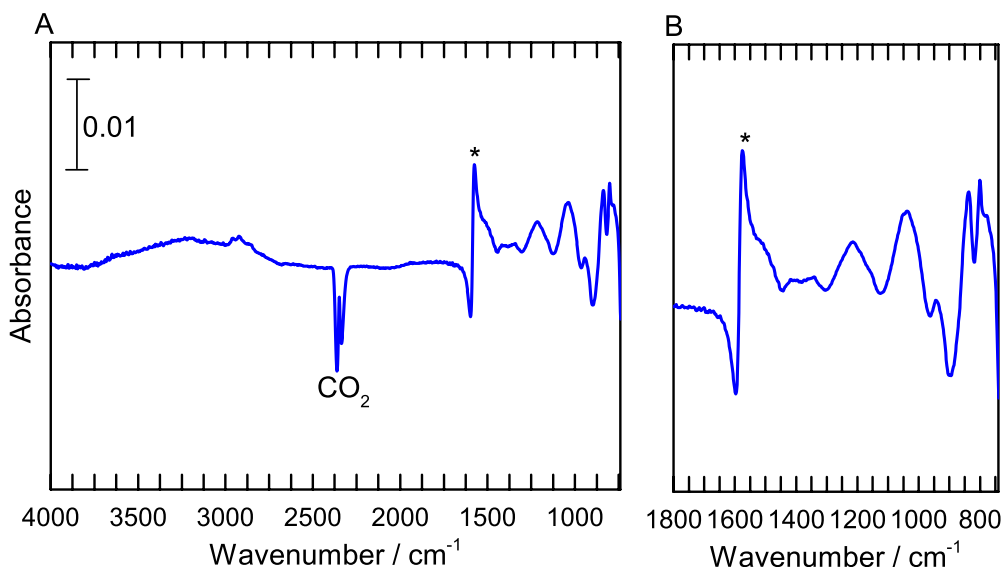


Figure 3.9: KBr disk background subtracted IR spectrum of FLG on a KBr disk: (A) 4000 to 750 cm^{-1} ; (B) 1800 to 750 cm^{-1} . Spectrum recorded in transmission mode and baselined for clarity.

At 1587 cm^{-1} an asymmetric Fano resonance can be clearly seen. The peak position of this resonance is reported as the position of the maximum absorbance (marked with an asterisk in Figure 3.9) throughout this thesis. Fano resonances are a feature of absorption spectra that result from quantum interference between the discrete and continuum states. In other words, it is caused by the interference between two processes, one due to scattering within a continuum of states and the second due to an excitation of a discrete state (vibration).³⁶ A well-known Fano resonance exists for bi- and few-layer graphene, but never monolayer graphene, and is caused by the same in-plane optical phonons as the G-band in the Raman spectrum.³⁷ In bilayer and FLG, the symmetry that exists in monolayer graphene is broken, due to coupling between the layers. Coupling results in a slight inequivalence between the carbon atoms in the graphene unit cell, which causes the E_{2u} mode (an out of phase, asymmetric mode) to become IR active. The E_{2u} mode can interact with the continuum of electronic states that exists for graphene, producing a strong, asymmetric peak at 1587 cm^{-1} . The size and shape of this peak depends on the layer number and stacking order.³⁶⁻³⁸

IR spectroscopy did not provide evidence for oxygen containing groups on the FLG however these may be at a concentration below the detection limit of the measurement, and therefore FLG on a gold substrate was characterised using X-ray photoelectron spectroscopy (XPS). The survey spectrum indicated the FLG surface was comprised of 93.4% carbon, 4.6% oxygen, 0.98% gold, and 1.02% nitrogen. The nitrogen is assumed

to arise from adventitious contaminants. The C 1s spectrum (Figure 3.10) shows the expected peak at 284.4 eV assigned to sp^2 -hybridised carbon atoms of the graphene. Additional peaks at 285.1, 286.2, and 287.5 eV were assigned to sp^3 -hybridised carbon, C-O carbon, and C=O carbon respectively. The O 1s narrow scan gave a peak at 531.9 eV that is assigned to C=O oxygen, and smaller peaks at 532.8 eV and 533.5 eV, which are assigned to C-O oxygen and O-H oxygen respectively.³⁹⁻⁴¹ Thus the XPS indicates that the FLG contains a small amount of carbonyl, hydroxyl, and epoxy functionalities, likely at defect regions.⁴²⁻⁴³

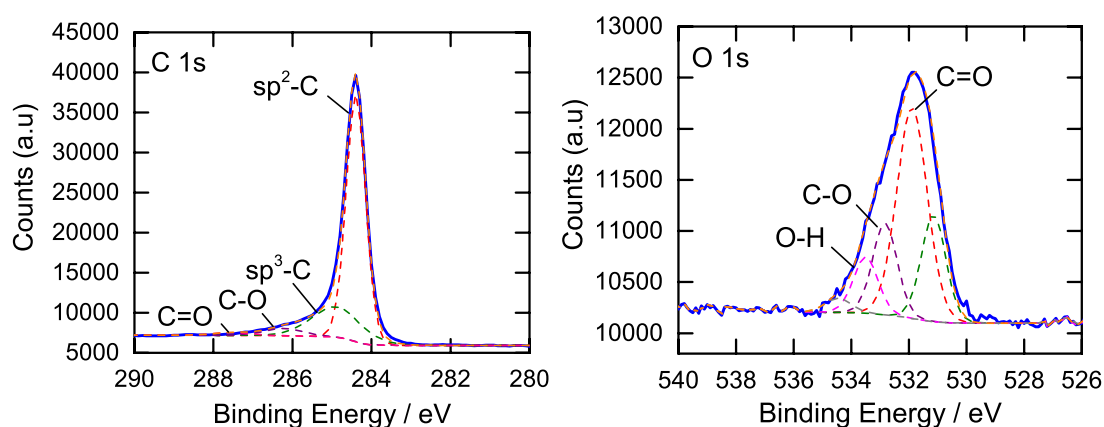


Figure 3.10: XPS spectra of FLG transferred to a Au wafer. Left to right: C 1s narrow scan and O 1s narrow scan.

To summarise, the graphene prepared in this work is few-layer and polycrystalline, with hexagonal domains. Raman spectroscopy confirms it is FLG with a small number of defects, likely to be grain boundaries and point defects. Furthermore, XPS confirmed these defect regions possessed a low concentration of oxygen containing groups.

3.3.2 Modification with 4-Nitrobenzene Diazonium Salt

FLG was modified via reaction with NBD giving a nitrophenyl (NP) film on the FLG surface. The aryldiazonium ion was assumed to react with the FLG surface following the mechanisms outlined in Chapter 1, Section 1.3.1. The resulting surface, hereby represented as FLG_{NP} , was characterised using XPS, IR and Raman spectroscopy, and AFM to gain insight into both the nature of bonding and the morphology of the film.

3.3.2.1 Raman Spectroscopy of FLG_{NP}

Raman spectroscopy is an excellent tool for establishing whether modifiers are attached to a surface via covalent bonds. The D-band in the Raman spectrum is activated by defects, including the formation of sp^3 -hybridised carbons after covalent bond formation between the aryl radical and a carbon atom in the graphene lattice.⁸ Hence

the D/G band intensity ratio can give an indication of the extent of modification. The Raman spectra of as prepared FLG, and FLG_{NP} after reaction in 20 mM NBD aqueous solution for 2 hours (FLG_{NP 2hours}) and 72 hours (FLG_{NP 72hours}) are given in Figure 3.11.

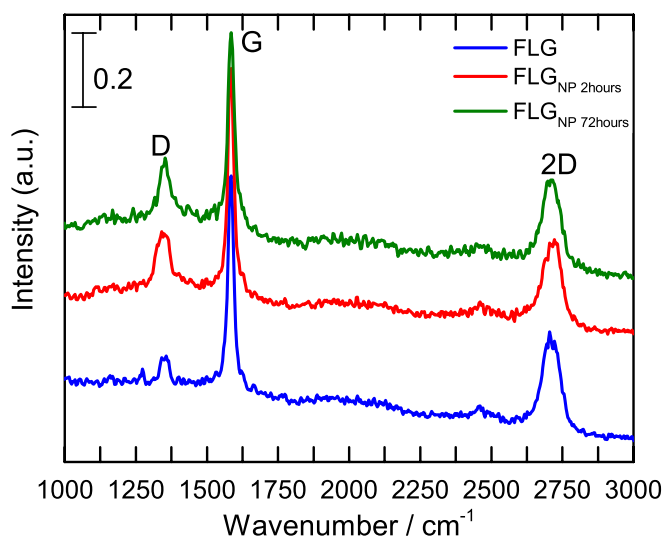


Figure 3.11: Raman spectra of FLG on a gold wafer before and after modification in 20 mM aqueous NBD solution. All samples were washed with methanol prior to spectral acquisition. All spectra were normalised to give G-bands of equal intensity. Spectra are offset for clarity. Spot size $\sim 2 \mu\text{m}$.

The D/G band intensity ratio for FLG, FLG_{NP 2 hours}, and FLG_{NP 72 hours} are 0.13 ± 0.03 , 0.26 ± 0.02 , and 0.26 ± 0.03 respectively. The increase in the D/G band intensity ratio after the reaction confirms that the NP groups are covalently bound to the surface. The D/G band intensity ratio is the same for the 2 and 72 hour reactions, suggesting that after 2 hours, no more NP groups bind directly to the FLG surface. However, as will be shown in Section 3.3.2.5, the amount of film increases with increasing reaction time indicating that although after 2 hours NP groups no longer bind directly to the surface, the film continues to grow. This is due to the aryl radical or aryldiazonium ion reacting with already grafted groups forming a multilayer film.

A Raman spectrum was recorded at $0.5 \mu\text{m}$ intervals across the surface of the FLG_{NP 72hours} sample. A plot of D/G band intensity ratio versus distance across the surface is given in Figure 3.12. The D/G band intensity ratio varies from 0.31 to 0.20 consistent with non-uniform reactivity of FLG towards NBD. The D/G band intensity does not vary to the same extent for the unmodified FLG, indicating this is not a feature of the underlying graphene. The more reactive regions (higher D/G band intensity ratio) may be the edge regions of the hexagonal graphene domains. Strano et al.⁵ studied the difference in reactivity of NBD between graphene edges and the basal plane. After

modification, they found at 2 to 3 \times increase in D-band intensity at the edges compared to the basal plane, indicating a higher degree of functionalisation and therefore reactivity. This enhanced reactivity is attributed to a combination of the disordered atomic structure at the edges (e.g. dangling bonds) and the increased density of states (shown through scanning tunnelling microscopy).^{7, 44} Furthermore, Koehler et al.⁶ suggested that edge regions are more able to accommodate the strain of sp²-hybridised carbon atoms changing to a sp³-hybridisation state, further improving the reactivity of the edge regions.

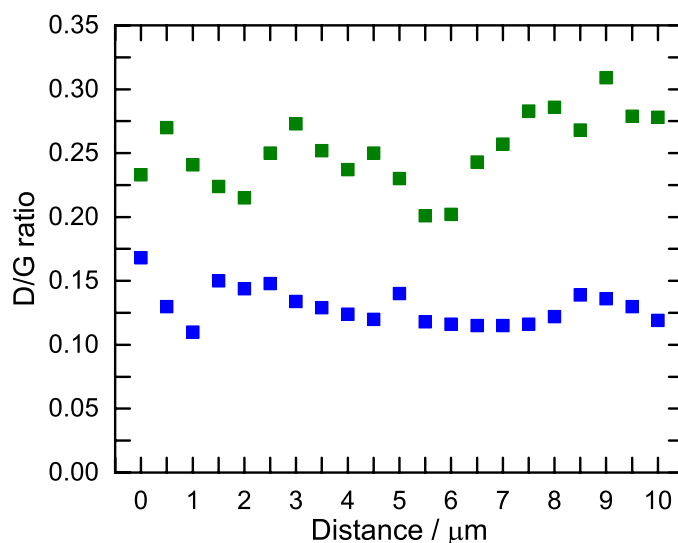


Figure 3.12: D/G intensity ratio calculated from Raman spectra taken at 0.5 μm intervals across a FLG surface before (blue) and after modification with a 20 mM aqueous NBD solution for 72 hours (green). Spot size $\sim 2 \mu\text{m}$.

As explained in Chapter 1, functionalisation has been shown to dope FLG. Raman spectroscopy is often used to determine the type of doping. Graphene can be p-doped (holes) or n-doped (electrons) by chemical functionalisation. Doping causes a shift of the Raman G- and 2D-bands: the G-band shifts to higher wavenumbers for both p- and n-doping, whereas the 2D-band shifts to higher wavenumbers for p-doping and lower wavenumbers for n-doping. The 2D-band shift is more useful as it always shifts regardless of initial doping by the supporting substrate. On the other hand, the G-band shift depends on the initial doping of the FLG, and therefore shifts in the G-band position are much smaller.⁴⁵⁻⁴⁶ Table 3.1 summarises the G- and 2D-band positions for as prepared FLG, FLG_{NP 2 hours}, and FLG_{NP 72 hours}.

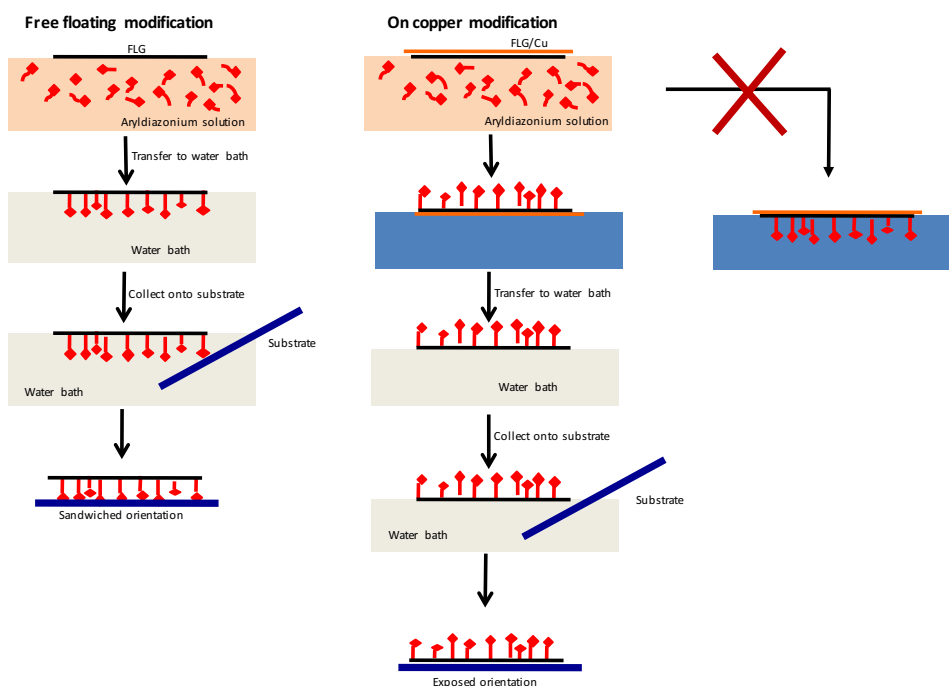
Table 3.1: G and 2D-band positions, and 2D-band FWHM for FLG, FLG_{NP 2 hours}, and FLG_{NP 72 hours}.

| Sample | G-band position / cm ⁻¹ | ΔG / cm ⁻¹ | 2D-band position / cm ⁻¹ | $\Delta 2D$ / cm ⁻¹ | D/G |
|----------------------------|------------------------------------|-------------------------------|-------------------------------------|--------------------------------|-------------|
| FLG | 1584 ± 1 | - | 2711 ± 4 | - | 0.13 ± 0.03 |
| FLG _{NP 2 hours} | 1584 ± 2 | + 0 | 2716 ± 3 | + 5 | 0.26 ± 0.02 |
| FLG _{NP 72 hours} | 1587 ± 1 | + 3 | 2720 ± 1 | + 9 | 0.26 ± 0.03 |

Both the G- and 2D-bands have shifted to a higher wavenumber after modification, indicating p-doping. The shift is especially obvious for the 72-hour sample. Furthermore, the full width at half maximum (FWHM) has increased (68 to 77 cm⁻¹), which is also indicative of doping.⁴⁷ The nitro group is strongly electron withdrawing and is expected to locally remove electrons from the FLG, generating holes and therefore p-doping the FLG surface.⁶

3.3.2.2 AFM Imaging of FLG Modified with NBD

Modified FLG was transferred to HOPG for AFM imaging and electrochemistry. As explained in the Chapter 2, Section 2.4.1, FLG was either modified while free-floating, or while on its copper support. The reactivity of FLG towards NBD is the same in both reaction conditions based on surface concentrations calculated from electrochemistry (see Section 3.3.2.5). When the modified FLG is transferred to a substrate for analysis, the two modification strategies provide two different final film orientations: sandwiched and exposed, as demonstrated by Scheme 3.1.



Scheme 3.1: Orienting free-floating and copper supported FLG sheets to give control over the final interface structure, either in a sandwiched or exposed arrangement.

In the sandwiched orientation, the NP groups sit between the HOPG and the FLG, whereas in the exposed orientation the NP groups point away from the HOPG. AFM images in both orientations for FLG after modification in a 20 mM aqueous NBD solution for 20 hours are given in Figure 3.13.

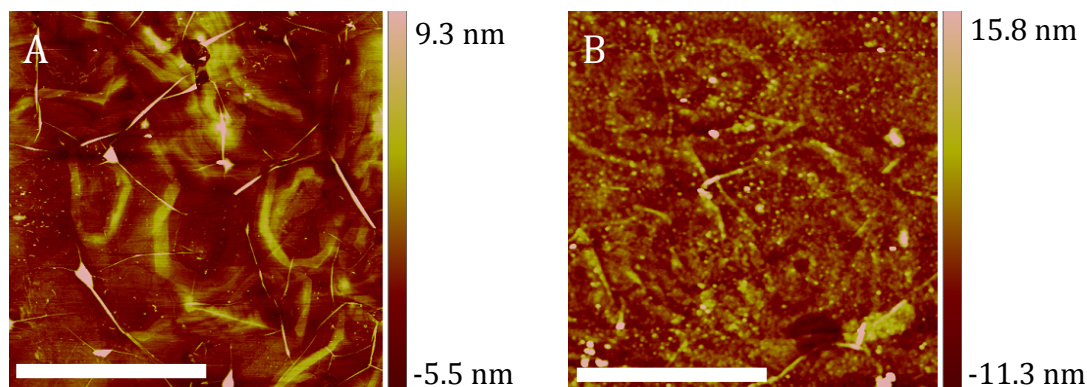


Figure 3.13: AFM images of FLG_{NP 20 hours} on HOPG: (A) in the sandwiched orientation; (B) in the exposed orientation. Both samples were washed with methanol prior to imaging. Scale bar 2.5 μm.

In the sandwiched orientation, the groups sit between the HOPG and the FLG so cannot be seen in the AFM image. On the other hand, in the exposed orientation a film can be seen on the FLG surface with the height of the protrusions approximately 10 ± 3 nm (determined using section tool on Nanoscope Analysis software). Due to the undulating nature of the FLG, this cannot be taken as an exact measure of the film height, however it is likely that the film is multilayered, as the height of a single, vertically oriented NP modifier is 0.68 nm (calculated using Avogadro software). The diameter of the protrusions cannot be determined due to broadening effects from the width of the AFM tip (radius approximately 10 nm). The image in Figure 3.13B shows that the film covers the majority of the surface, indicating that both edge and basal plane modification has occurred, agreeing with the Raman results shown in Figure 3.11 and with literature reports.^{5, 48}

3.3.2.3 IR Spectroscopy of FLG Modified with NBD

Transmission mode IR spectra for FLG, FLG_{NP 27hours} (no methanol wash), and FLG_{NP 24hours} after a brief methanol wash on the KBr disk are given in Figure 3.14. The NP groups are sandwiched between the KBr and FLG. The ATR spectrum of the NBD precursor is also shown.

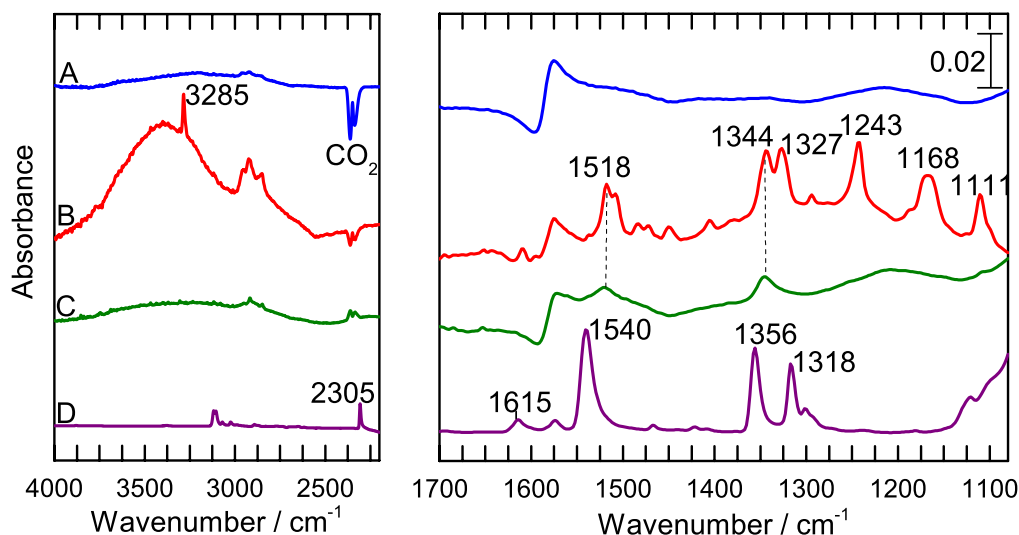


Figure 3.14: KBr disk background subtracted transmission mode IR spectra of FLG collected on a KBr disk before and after modification in 20 mM aqueous NBD: (A) before modification; (B) after 27 hour reaction (no methanol wash); (C) after 24 hour reaction, with a methanol rinse after collection on KBr. (D) ATR spectrum of NBD salt; spectrum scaled $\times 0.08$. Spectra offset for clarity.

Comparison of spectra B and C shows that after washing with methanol some peaks disappear, presumably due to removal of physisorbed material from the surface. However, two strong peaks remain at 1518 and 1344 cm⁻¹, which are assigned to the asymmetric and symmetric NO₂ stretch modes respectively. This confirms, as seen from AFM imaging, that the grafted NP film remains on the FLG surface after washing with methanol. Peak assignments for NBD and FLG_{NP} (washed and unwashed) are given in Table 3.2.⁴⁹⁻⁵⁵ The peaks from the unwashed sample are included because although they disappear after washing, the chemical bonding in the physisorbed material is assumed to give a good indication of the nature of the bonding in the grafted film, and the peaks are more easily distinguishable in the unwashed spectrum.

Table 3.2: IR peak assignments for the NBD and FLG_{NP} spectra shown in Figure 3.14.

| NBD | FLG _{NP} | Assignment |
|--------------|-------------------|--|
| 2305 s | | $\nu(\text{N}_2^+)$ |
| 1615 m | 1610 w | |
| 1574 m | | $\nu(\text{C}=\text{C})$ |
| 1540 vs | 1518, 1508 s, db | $\nu_a(\text{NO}_2)$ |
| 1467 w | 1484, 1472 m, db | Ring def. |
| | 1450 m | $\nu(\text{C}-\text{NN}) + \text{ring def.}$ |
| 1421, 1409 w | 1406 m | Ring def. |
| 1356 s | 1344 s | $\nu_s(\text{NO}_2)$ |
| | 1327 s | $\nu(\text{C}-\text{N})$ |
| 1318 vs | | $\nu_s(\text{NO}_2) + \text{ring def.}$ |
| | 1243 s | $\nu(\text{C}-\text{C})$ |
| | 1168 s, db | $\delta(\text{C}-\text{H})$ |
| | 1126 | $\nu(\text{C}-\text{NN})$ |
| | 1111 | $\nu(\text{C}-\text{NO}_2) + \text{CH wag}$ |

vs, very strong; s, strong; m, medium; w, weak; db, doublet; ν , stretch mode; δ , bend mode

A significant difference between the NBD and the FLG_{NP} spectra is the loss of the peaks at 2308 and 1318 cm^{-1} for the FLG_{NP} sample. The peak at 2308 cm^{-1} is due to the N_2^+ group of the diazonium ion.^{51, 53} Loss of this peak indicates successful reaction of the aryldiazonium ion. The peak at 1318 cm^{-1} in the aryldiazonium precursor is caused by a coupling mode between the NO_2 symmetric stretch and aromatic ring deformations that is only seen in free nitrobenzene molecules.⁵³ The loss of this peak in the FLG_{NP} spectrum supports that the NP groups are grafted to the surface or other parts of the film. The bands at 1540 and 1356 cm^{-1} , and 1518 and 1344 cm^{-1} in the NBD and FLG_{NP} spectra respectively, are due to the stretch modes of the NO_2 group. These stretching vibrations are sensitive to their surrounding environment, so it is not surprising that their position shifts after grafting.⁴⁹⁻⁵⁰ Peaks between 1470 and 1400 cm^{-1} are primarily due to aromatic ring deformation modes. In the spectrum of the unwashed FLG_{NP 27hours} sample, peaks appear at 1450 and 1126 cm^{-1} . These are assigned to the stretch modes of a C-NN group, coupled with an aromatic ring deformation,⁵⁵ suggesting that some NBD modifiers graft via an azo linkage rather than a carbon-carbon bond. The peak at 1243 cm^{-1} is assigned to the CC stretch mode that results from the carbon-carbon bond that forms during the grafting reaction of the aryl radical. However, it is not possible to distinguish between carbon-carbon and azo bonds that form from reaction with the surface or with already grafted NP groups. The strong peaks at 1168 and 1111 cm^{-1} result from the CH bend and C- NO_2 stretch modes respectively.

Figure 3.14 also shows the IR spectra for the same samples from 4000 to 3200 cm^{-1} . The unwashed sample shows a sharp peak at 3285 cm^{-1} ; peaks in this region are often

assigned to NH or free OH (non-hydrogen bonded) modes. One possible origin is C-OH groups formed by oxidation of FLG during reduction of the diazonium ion. In this case, the peak should be unaffected by washing, as it is not part of the physisorbed film, however spectrum C does not show the peak. For the peak to be caused by NH stretching, some nitro groups must be reduced during the grafting process to NHOH or NH₂. NH₂ peaks possess other strong peaks around 1620 cm⁻¹, which are not seen in the unwashed sample spectrum.⁵⁴ NHOH groups are electroactive, so should be seen in the initial electrochemistry reduction scans but they are not (see Section 3.3.2.5), discounting this possibility. The peak at 3285 cm⁻¹ therefore remains unassigned at this time. To summarise, IR spectroscopy confirmed the presence of NP groups on the FLG surface. Although some of the film is washed off with methanol, a NP film remains on the surface. There is evidence for both carbon-carbon and azo linkages within the film. This is explored more thoroughly using XPS (Section 3.3.2.4).

In IR spectroscopy, like all absorption-based techniques, absorbance is proportional to concentration. Hence, the use of IR spectroscopy to estimate the surface concentration of the NP groups on FLG was investigated. The relationship between concentration and absorption is given by the Beer-Lambert law, shown in Equation 3.1,⁵⁶

$$Abs = \epsilon cl \quad (3.1)$$

where *Abs* is the absorbance, *c* is the concentration in mol L⁻¹, and *l* the pathlength in dm. The constant ϵ is the molar absorptivity of the sample, and has units of L mol⁻¹ dm⁻¹. To calculate the concentration of NP groups on the FLG surface, the molar absorptivity of the molecule must be known. To establish a value for NP groups in the film, ϵ was determined for NBD in methanol solution. As NBD, rather than a NP film was used to determine ϵ , this method could only be used to give an estimate of the surface concentration. The area under the symmetric nitro stretch peak (1356 cm⁻¹) of NBD was used as the absorbance and was plotted against the concentration of NBD in methanol. The area under the peak was measured rather than peak height, as peak height is more affected by baseline variations between samples. The symmetric stretch absorbance was used because it is strong and the peak is reasonably isolated from other peaks.⁵⁶

The IR spectrum of the empty solution cell shows a well-known “fringing effect” (Figure 3.15A). This is caused by constructive and destructive interference of the beam

between the parallel calcium fluoride surfaces of the cell.⁵⁷⁻⁵⁸ This effect can be used to calculate the pathlength based on Equation 3.2,

$$l = \frac{10N}{2(\bar{\nu}_1 - \bar{\nu}_2)} \quad (3.2)$$

where l is the pathlength in mm, N is the number of fringes, and $\bar{\nu}_1$ and $\bar{\nu}_2$ are the start and endpoint of the spectral region respectively. In the example shown in Figure 3.15A, N is 5, and $\bar{\nu}_1$ and $\bar{\nu}_2$ are 3635 and 1726 cm^{-1} respectively, giving a pathlength of 0.013 mm.

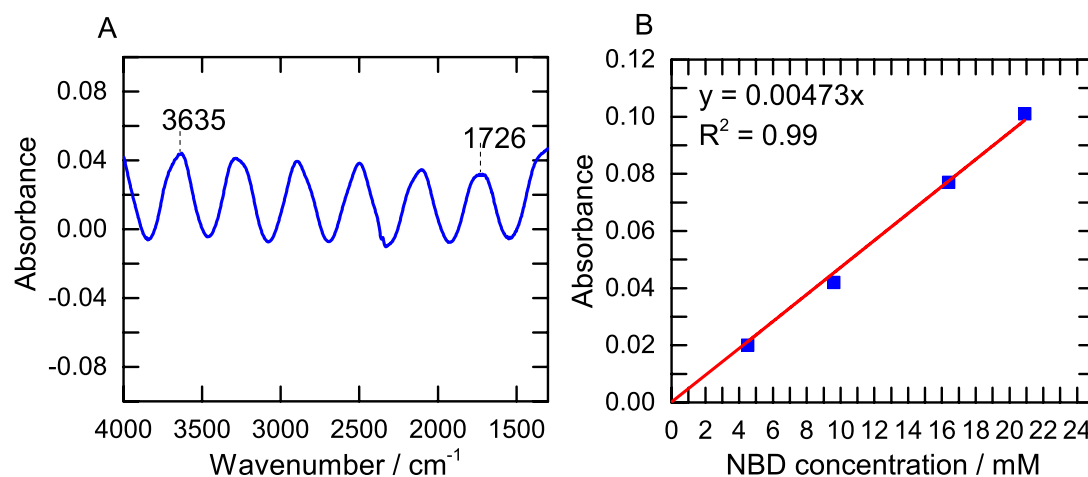


Figure 3.15: (A) Transmission mode IR spectrum of empty calcium fluoride solution cell from 4000 to 1250 cm^{-1} ; (B) absorbance (area under the peak at 1356 cm^{-1}) versus concentration of NBD in methanol. Spectra recorded in transmission mode using a calcium fluoride solution cell with a pathlength of 0.013 mm.

A plot of absorbance of the 1356 cm^{-1} peak versus concentration for the NBD solution is given in Figure 3.15B. The area under each peak was calculated using the integration tool on the OPUS software used to record the spectra. Using the gradient of this plot and the pathlength calculated above, the value for molar absorptivity was calculated as 36,355 $\text{L mol}^{-1} \text{dm}^{-1}$. This value for molar absorptivity was then used to calculate the surface concentration of NP groups on the FLG surface. A detailed description of this calculation and calculated values can be found in Appendix B Sections B.1 and B.2 respectively. Modified samples were washed with methanol prior to recording spectra. The area under the symmetric stretch peak at 1344 cm^{-1} was calculated using the integration tool in the OPUS software. A plot of calculated NP surface concentration (mol cm^{-2}) versus time is given in Figure 3.16.

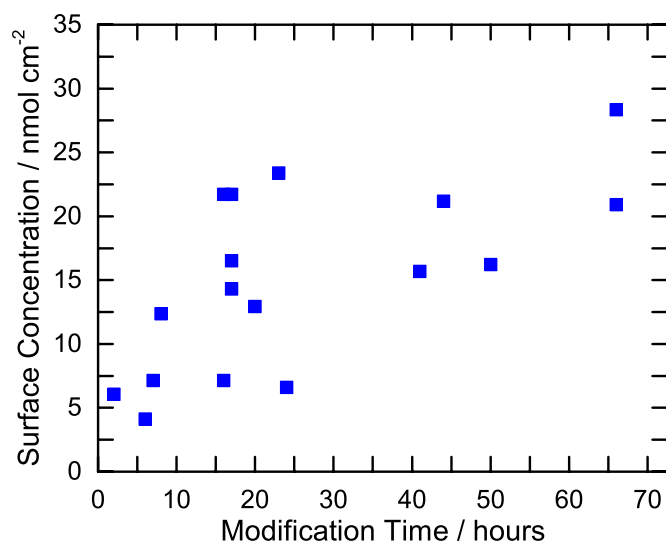


Figure 3.16: Plot of NP surface concentration with reaction time, determined from IR spectroscopy. Samples were washed in methanol prior to recording spectra.

Figure 3.16 shows a trend of increasing concentration with increasing reaction time. The trend is weak, with significant variation between the measured surface concentration values, even at a single time. The source of this variation is currently unknown. Furthermore, the estimated surface concentrations are an order of magnitude higher than those measured using electrochemistry both in this work (Section 3.3.2.5) and in literature reports.^{3, 59-61} This overestimation of surface concentration may be caused by the assumptions made in using the Beer-Lambert law to determine surface concentration. First, the use of NBD to calculate the molar absorptivity may not be appropriate. The diazonium moiety *para* to the nitro group may affect the molar absorptivity; possibly nitrotoluene may be more representative of a NP group bonded to a surface. Further, the Beer-Lambert law describes randomly oriented species such as solutions. A NP film, especially a thin film, is unlikely to be completely random in its orientation, so the Beer-Lambert law may be unsuitable to describe such surfaces. To conclude, IR spectroscopy of NP films is not a suitable technique to estimate the surface concentration, as applied with this method.

3.3.2.4 X-ray Photoelectron Spectroscopy (XPS) of FLG Modified with NBD

XPS was used to gain further insight into the chemical bonding in the FLG_{NP} film. XPS data is summarised in Tables 3.3 and 3.4. FLG was also modified using IBD to give an iodophenyl (IP) film, and this data is also shown in the tables.

Table 3.3: Atomic % values derived from XPS survey spectra for FLG, FLG_{NP 72hours}, and FLG_{IP 72hours} transferred to a silicon oxide wafer.

| Survey Spectra Atomic % | | | | | |
|---------------------------|--------|----------|--------|---------|--------|
| Sample | Carbon | Nitrogen | Oxygen | Silicon | Iodine |
| FLG | 82.6 | 0.6 | 7.9 | 8.9 | - |
| FLG _{NP 72hours} | 71.7 | 8.2 | 17.6 | 2.6 | - |
| FLG _{IP 72hours} | 76 | 8.0 | 8.2 | 0 | 7.8 |

Table 3.4: Narrow scan data for C 1s and N 1s peaks of FLG, FLG_{NP 72hours}, and FLG_{IP 72hours} transferred to a silicon oxide wafer.

| Narrow scan data | | | | |
|---------------------------|---------------------|----------|---------------------|----------|
| Sample | C 1s | | N 1s | |
| | Binding energy / eV | Atomic % | Binding energy / eV | Atomic % |
| FLG | 284.8 | 67.8 | | |
| | 285.3 | 20.4 | | |
| | 286.2 | 6.7 | | |
| | 287.5 | 5.0 | | |
| FLG _{NP 72hours} | 284.8 | 8.74 | 400.4 | 45.9 |
| | 285.4 | 70.6 | 406.3 | 48.1 |
| | 286.6 | 18.3 | 404.4 | 2.3 |
| | 288.6 | 2.4 | | |
| FLG _{IP 72hours} | 285.3 | 74.5 | 400.4 | 97.5 |
| | 286.0 | 25.6 | 404.9 | 2.5 |

Figure 3.17 shows the survey spectrum, and narrow C 1s and N 1s scans for an unmodified FLG sheet. The survey spectrum and data listed in Table 3.3, indicate that the sample is 82.6% carbon. Oxygen (7.9%) and silicon (8.9%) are also detected; their similar content suggests these arise primarily from the silicon wafer support, although some of the oxygen will result from oxygen groups on the FLG as discussed earlier. A negligible amount of nitrogen is present, likely caused by adventitious contaminants. The C 1s narrow scan shows a predominant peak at 284.8 eV due to sp² hybridised carbon. A small peak at 285.3 eV is assigned to sp³-hybridised carbon atoms in the edge and defect regions of the graphene.⁴⁹

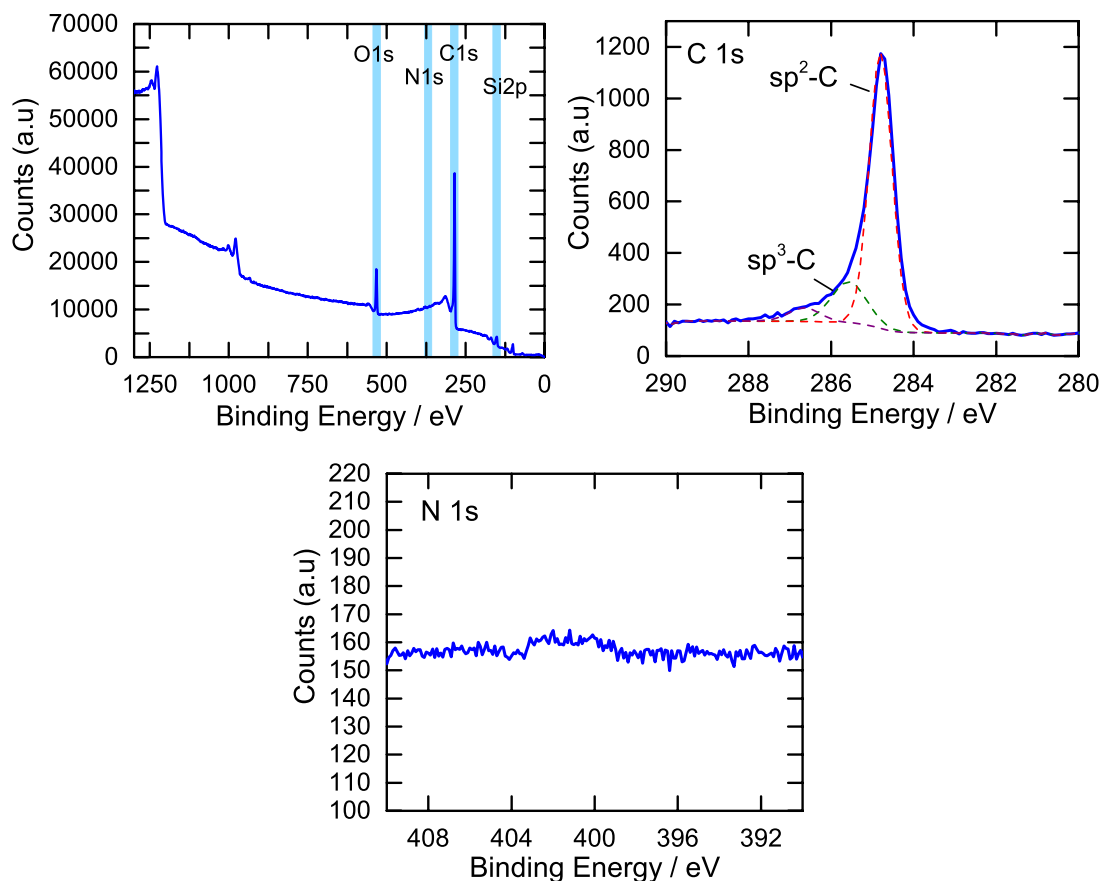


Figure 3.17: XPS spectra for FLG on a silicon oxide wafer. Left to right: survey spectrum and C 1s narrow scan, and bottom N 1s narrow scan.

The XPS spectra for FLG_{NP} on a silicon oxide wafer, after a 72 hour reaction with NBD are given in Figure 3.18. The percentage of nitrogen and oxygen has increased to 8.2% (0.6% in FLG), and 17.7% (7.9% in FLG) respectively (Table 3.3), as expected for a NP film. The C 1s narrow scan spectrum (Figure 3.18) shows an increase in the sp³-hybridised carbon peak at 285.4 eV. This is expected, as functionalisation converts FLG carbon from sp² to sp³ hybridisation.^{3, 9, 62} The N 1s narrow scan shows two peaks at 400.4 and 406.3 eV. The peak at 406.3 eV is commonly assigned to nitro nitrogen. Previously, the 400.4 eV peak has been assigned to either amine nitrogen, resulting from reduction of nitro groups, or azo nitrogen, resulting from the formation of azo bonds during film growth.⁶³⁻⁶⁵

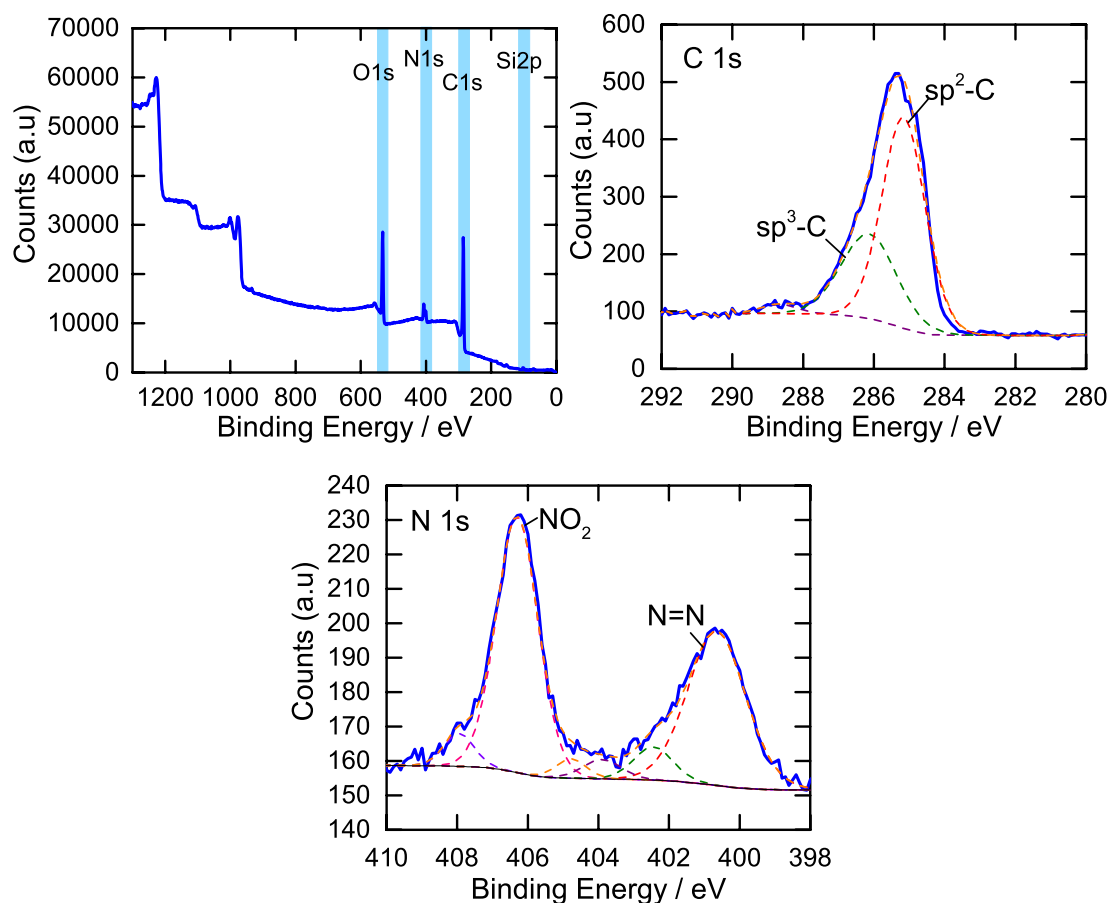


Figure 3.18: XPS spectra for FLG_{NP} 72hours on a silicon oxide wafer. Sample washed with methanol prior to spectral acquisition. Left to right: survey spectrum and C 1s narrow scan, and bottom N 1s narrow scan.

To establish the origin of the 400.4 eV peak, the experiment was repeated using the IBD. Replacing the nitro with an iodo group removes the possibility of amine groups being present. The XPS results for the FLG_{IP} 72hours sample on a silicon oxide wafer, are given in Figure 3.19 and summarised in Table 3.3 and Table 3.4. As expected the C 1s peak shows an increase in the sp³-hybridised carbon content after functionalisation. The N 1s narrow scan shows a single peak at 400.4 eV. As there is no possibility of reduced nitro groups, this peak can be assigned to azo nitrogen, confirming that azo bonds exist in the grafted film. For FLG_{NP} 72hours, the percent of azo to nitro groups is 1:1, and for FLG_{IP} 72hours, the percent of azo to iodo groups is 1:1. This suggests the proportion of azo linkages in the film is the same for both modifiers, so they likely graft via the same mechanistic pathway. Each azo group includes two nitrogen atoms, this means that if the reaction was exclusively through azo bond formation the percent of azo to nitro or iodo would be 2:1. The 1:1 ratio seen here therefore suggests at least two different grafting mechanisms are active, where one gives azo linkages, and the other gives

carbon-carbon bonds. From the IR spectroscopy and XPS results presented, the types of chemical bonding within the film can be discerned, and Figure 3.20 illustrates the types of bonding that exist for the FLG_{NP} surface.

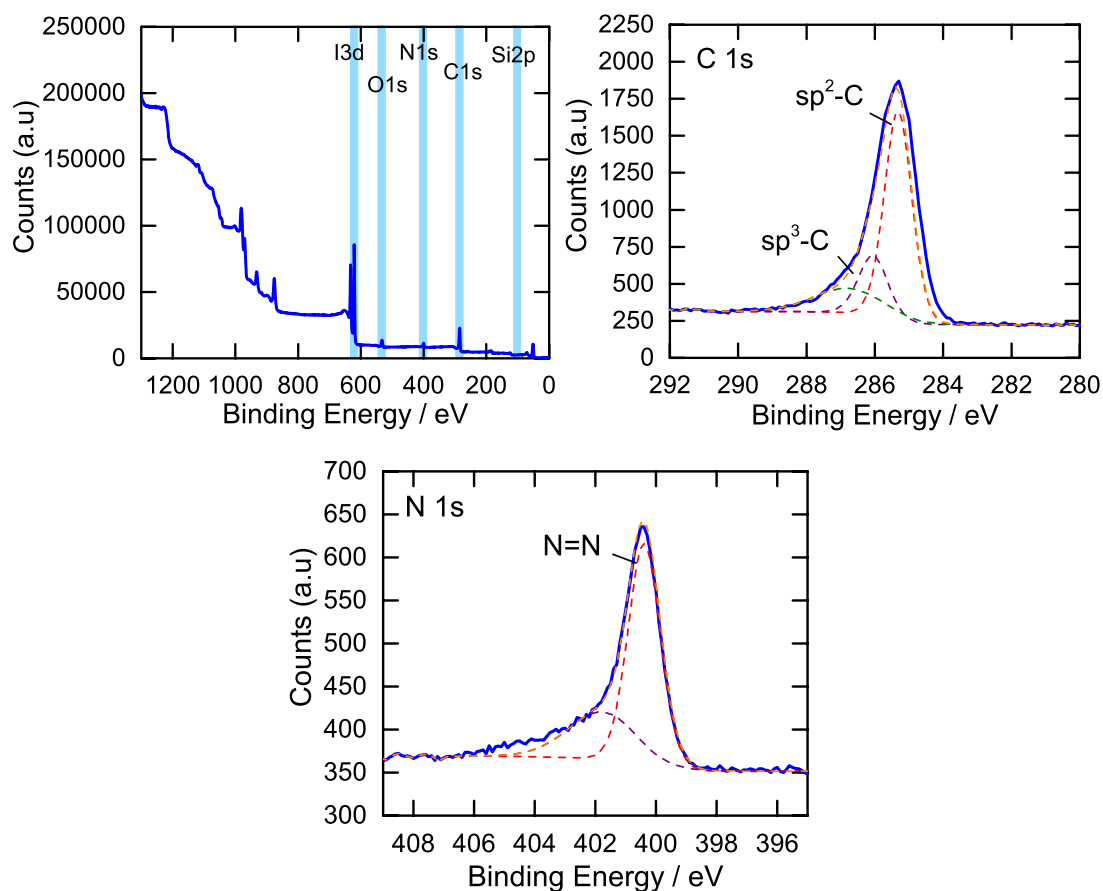


Figure 3.19: XPS spectra for FLG_{IP} 72hours on a silicon oxide wafer. Sample washed with methanol prior to spectral acquisition. Left to right: survey spectrum and C 1s narrow scan, and bottom N 1s narrow scan.

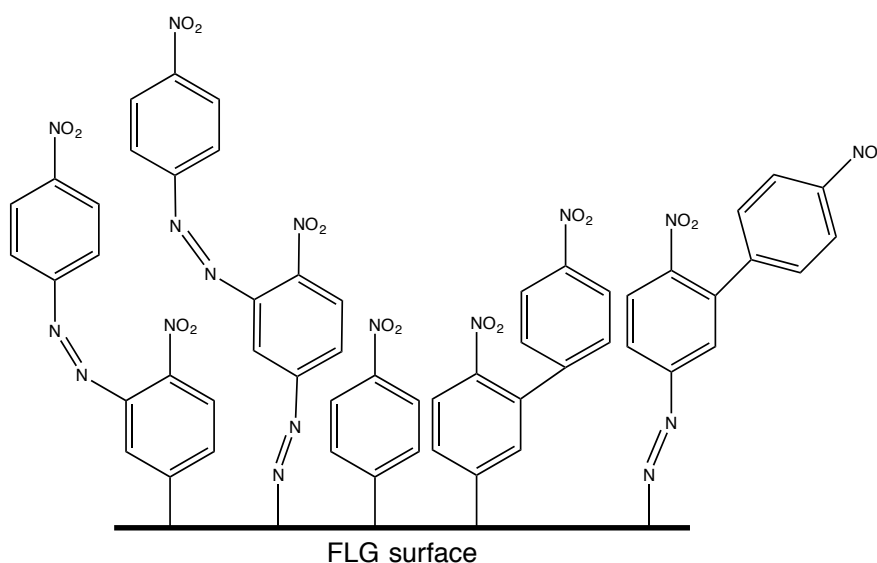


Figure 3.20: FLG_{NP} resulting from reaction of FLG with an aqueous solution of NBD.

3.3.2.5 Electrochemistry of FLG modified with NBD

The NP film can be characterised by electrochemistry via the electroactivity of the NP group. For electrochemistry, the two different film orientations, illustrated in Scheme 3.1, were used: sandwiched, in which the film sits between FLG and the HOPG electrode, and exposed, where the FLG sits on the HOPG with the film exposed to the electrolyte solution. All samples were washed with methanol prior to measurements. CV plots for FLG_{NP} in each orientation are given in Figure 3.21. The observation of a well-defined response for the sandwiched orientation indicates the FLG is permeable to the electrolyte solution, most likely through defect regions.

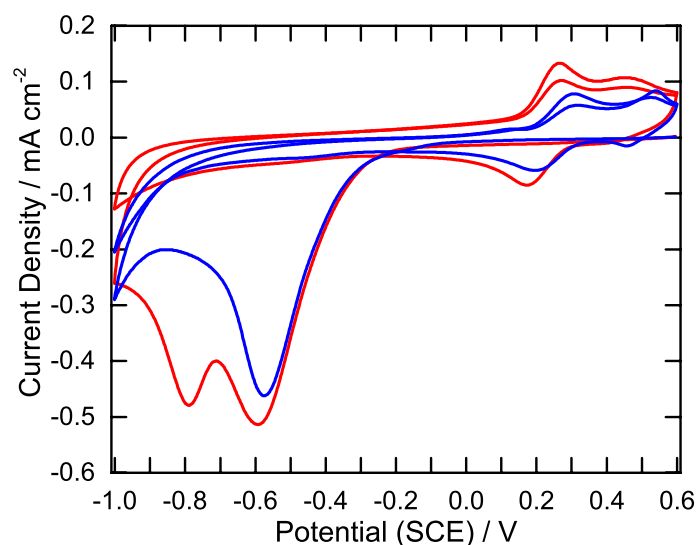
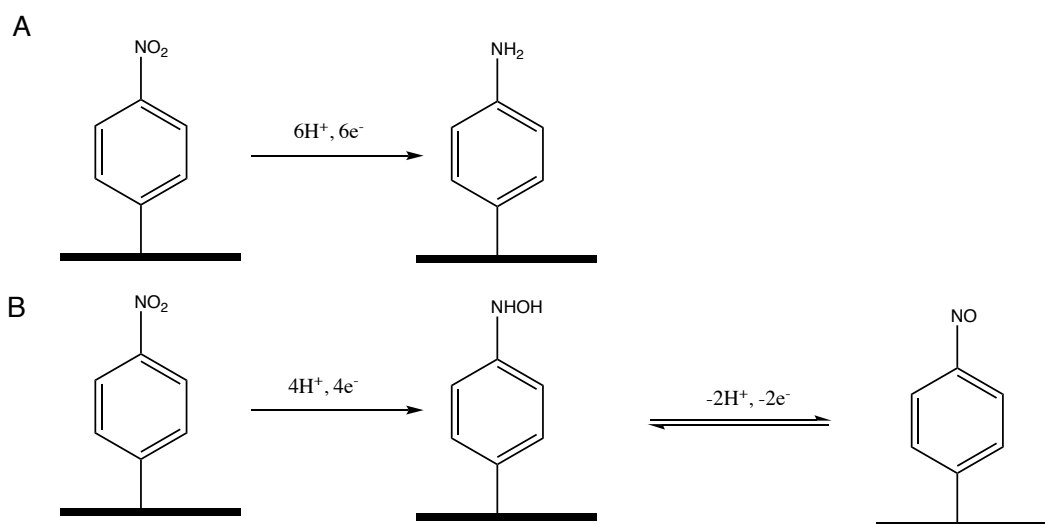


Figure 3.21: CVs of methanol washed of FLG_{NP} mounted on HOPG in either an exposed orientation (blue, 20 hour reaction) or a sandwiched orientation (red, 66 hour reaction). CVs were recorded in 0.1 M H₂SO₄ at 200 mV s⁻¹.

Considering first the exposed orientation (blue) the CV shows two main redox processes. The large irreversible peak centred at -0.57 V caused by a six electron, six proton reduction to an aminophenyl group and a four electron, four proton reduction to a hydroxylaminophenyl group,⁶⁶ and the redox couple at 0.25 V caused by the two electron, two proton reduction of the hydroxylaminophenyl group to a nitrosophenyl group.⁶⁷ These reactions are given in Scheme 3.2.



Scheme 3.2: (A) Six proton, six electron reduction process from a NP to an aminophenyl group and (B) four proton, four electron reduction from a NP group to a hydroxylaminophenyl group, and subsequent two proton, two electron process to a nitrosophenyl group.

The nitrosophenyl/hydroxylaminophenyl system appears as two redox couples. The origin of the two different reduction potentials is unknown, but has been reported previously for NP films on other carbon substrates.^{60, 68} Compton et al.⁶⁹ have suggested that the potential of the hydroxylaminophenyl oxidation is sensitive to the nature of bonding to the surface, therefore hydroxylaminophenyl groups grafted via a carbon-carbon bond may have a different reduction potential to those bonded via an azo linkage, resulting in two oxidation and reduction peaks. Other work has suggested that the film environment, for example hydroxylaminophenyl groups embedded in the film vs. those near the outer surface of the film, can cause the two different potentials for this reaction.⁷⁰

The CV for the sandwiched orientation (red) shows two large reduction peaks for the NP groups at -0.59 and -0.81 V. Two reduction peaks were only seen for films in the sandwiched orientation, and in this orientation two peaks were not always seen (approximately 30% of samples). In the sandwiched orientation, two peaks were sometimes seen for films prepared using long reaction times and occasionally for shorter reaction times. The two peaks are assumed to be both due to the reduction of NP groups. This result has not been reported previously for NP films grafted to graphene or other carbon substrates from aryldiazonium ions. The two peaks cannot arise from the different grafting mechanisms giving NP groups attached to the surface via carbon-carbon bonds and azo linkages, because the same film formation mechanisms are expected at FLG and other carbon substrates. Furthermore, previous

work has shown that the nitro reduction potential for films grown by NABD and NBD are almost identical,⁶⁰ hence this cannot be the origin of these two peaks. The CV was repeated using different substrates to support the FLG. In the sandwiched arrangement, FLG and the base electrode are in electrical contact and hence both function as working electrodes. Only one peak appears for a NP film sandwiched between FLG and GC or two sheets of FLG, even at the longest reaction times. On the other hand, when the NP film is sandwiched between FLG and PPF two reduction peaks are sometimes seen, as observed for HOPG.

This behaviour is suggested to arise from either the difference in electron transfer kinetics for the two working electrodes or from limitations in proton availability within the film. Slower electron transfer kinetics will give a more negative reduction potential. PPF and HOPG may exhibit different electron transfer kinetics to FLG, and so for a thick film, NP groups adjacent to FLG may be reduced at the first peak, and those adjacent to HOPG or PPF at the second peak. Conversely, when the NP groups are sandwiched between two FLG sheets, the electron transfer kinetics are the same, because the two working electrodes are the same, hence only one reduction peak is seen. For GC, fast electron transfer kinetics can be expected, and so only one peak is observed. This behaviour cannot occur in the exposed orientation because electron transfer can only occur from one substrate (FLG). However, in the sandwiched orientation electron transfer is always from both working electrodes, as the total surface area calculated from the NP reduction is the same, irrespective of whether two peaks are seen, (Figure 3.23), therefore this explanation is unlikely as two reduction peaks are not always seen.

A more likely explanation relates to proton availability, as the reduction of each NP group requires six protons (Scheme 3.2). If the diffusion of protons into the film is hindered in the sandwiched orientation, so that the proton concentration decreases during reduction, the reduction potential will become more negative.⁷¹ This could result in the two reduction peaks, the more negative from areas of decreased proton availability. The lack of two peaks for the NP film sandwiched between two FLG sheets, or the FLG sheet and GC suggests these surfaces have greater electrolyte permeability. With the two sheets of FLG, both surfaces have numerous grain boundary regions and defect sites to allow sufficient proton diffusion. For GC, the surface

roughness is much greater than for HOPG and PPF,⁷²⁻⁷³ which may allow for enhanced electrolyte permeability at the GC/NP film interface, and therefore greater proton availability.

CVs can be used to calculate the surface concentration of NP groups in the films by measuring the charge associated with the reduction of NP groups and the oxidation of hydroxylaminophenyl groups (Chapter 2, Section 2.6.9.1). Figure 3.22 shows a CV of FLG_{NP} collected in the exposed orientation with the total area used to calculate surface concentration shown in grey.

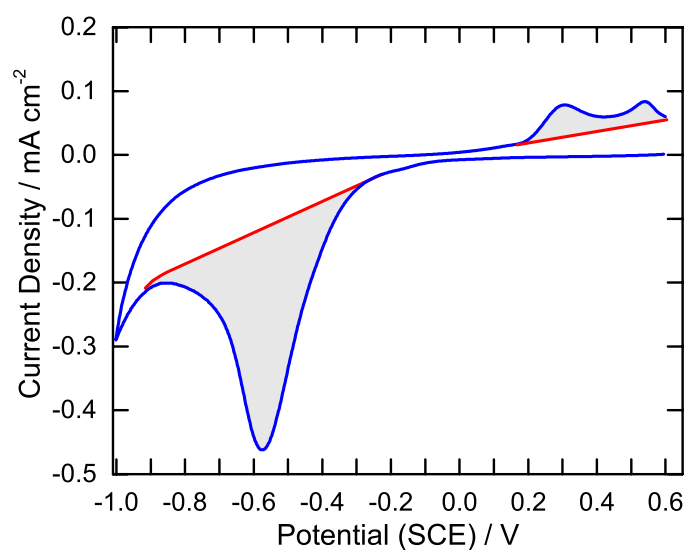


Figure 3.22: CV in 0.1 M H₂SO₄ of methanol washed FLG_{NP} on HOPG after a 20 hour reaction mounted in an exposed orientation, showing the total area used to calculate surface concentration.

Using this area, the surface concentration was calculated for NP films prepared using selected reaction times and orientations. A plot of surface concentration versus modification time is given in Figure 3.23, with data obtained in the exposed orientation with HOPG as the base electrode (blue points), and the sandwiched orientation with PPF (red points) and HOPG (orange points) as the base electrode. The green points are from a NP film sandwiched between two sheets of FLG. For samples that exhibited two NP reduction peaks (indicated by a box), both peaks were included in the surface concentration calculation. Calculated values can be found in Appendix B, Section B.3.

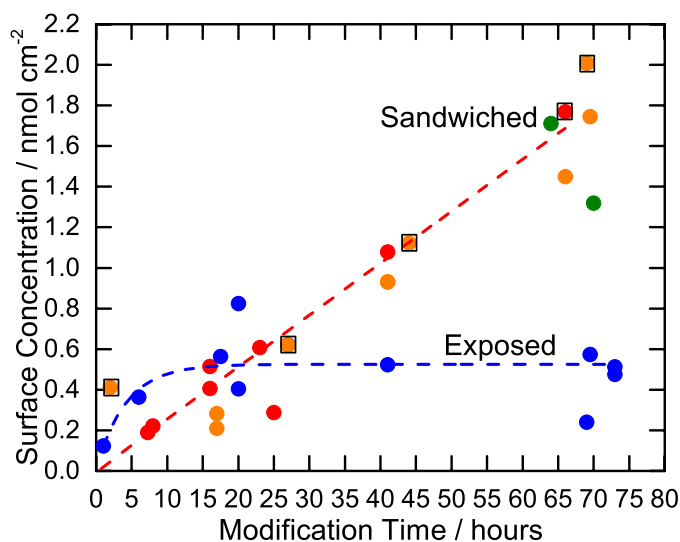


Figure 3.23: Plot of surface concentration versus modification time for FLG_{NP} mounted on HOPG in either an exposed orientation (blue) or sandwiched orientation (orange), or on PPF in the sandwiched orientation (red). Green points are for FLG_{NP} films sandwiched between two sheets of FLG. Boxes indicate samples that showed two nitro reduction peaks. Surfaces were washed with methanol prior to analysis.

For NP films measured in the exposed orientation there was an initial increase in surface concentration with film preparation time, followed by a plateau at approximately 0.5 nmol cm⁻². A limiting measured surface concentration is common for carbon surfaces modified with NP groups.⁶⁰ It has been shown that this behaviour is not caused by the cessation of film growth but instead is due to the electroinactivity of NP groups once the film growth continues beyond a certain thickness. Either electrons can no longer be transferred from the electrode to the outer surface of the film, or the thicker film prevents proton diffusion into the inner regions of the film.⁷¹ This means that although the film continues to grow, it cannot be fully interrogated electrochemically and the measured surface concentration plateaus. In contrast for NP groups in the sandwiched orientation there is a linear relationship between surface concentration and reaction time. This is assumed to be due to reduction of NP groups occurring by electron transfer from both sides of the film. Because electrons can be transferred from the base electrode to the originally outer regions of the film these groups are still electrochemically accessible and full surface concentration measurable, even for the thickest films grown in this study. The two different orientations and their assumed electron transfer pathways are illustrated in Figure 3.24. At a certain film thickness, not reached here, the measured surface concentration in the sandwiched orientation may also reach a plateau, as groups in the middle of the film could become inaccessible. Electrochemistry and IR spectroscopy have both been used to calculate surface

concentration of NP films. The electrochemistry results agree with literature reports involving NBD reactions on carbon surfaces, and are assumed to be a better measure of NP surface concentration than IR measurements (Section 3.3.2.3).^{3, 59-60, 74}

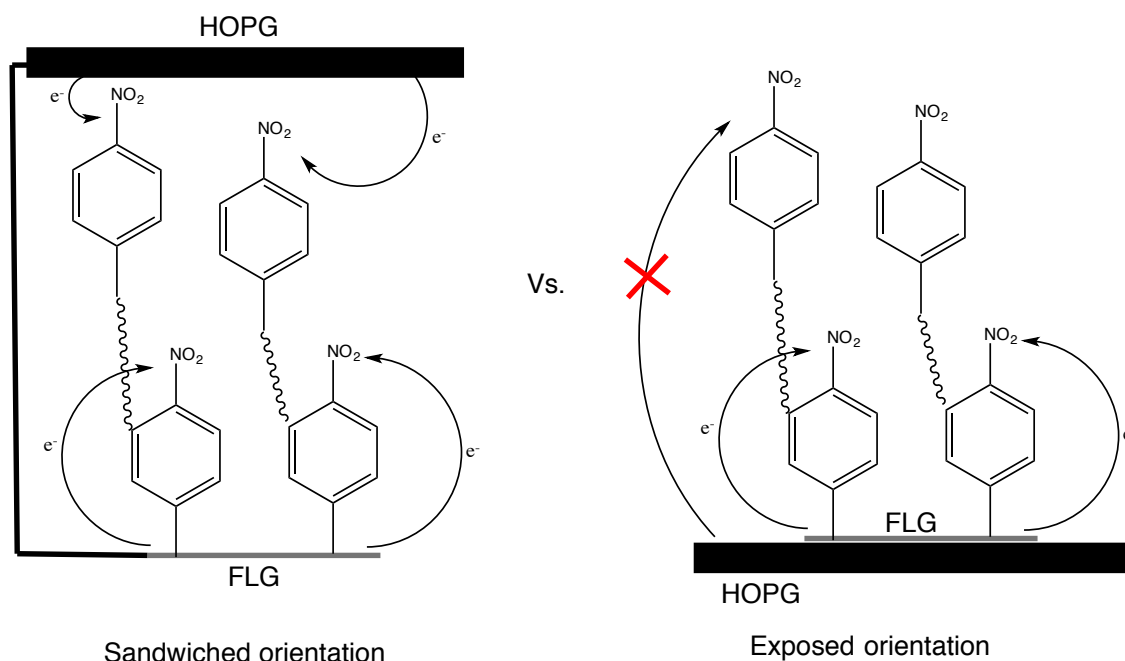


Figure 3.24: Cartoon illustrating the different electron transfer pathways assumed to be available for the sandwiched and exposed orientations. ~~~~ represents a multilayer film.

In summary, FLG sheets have been successfully modified using NBD ions. Film formation involves at least two mechanisms, resulting in two types of linkage (carbon-carbon and azo linkages). Interrogation of the surfaces via electrochemistry has demonstrated the importance of film orientation in accurately measuring surface concentrations of NP groups on FLG surfaces.

3.3.3 Modification with Other Aryldiazonium Salts

The NBD ion is an easily reduced aryldiazonium ion due to the electron withdrawing nature of the nitro group. To ensure modification is applicable to a range of aryldiazonium salts the spontaneous modification of FLG was carried out with NABD and CBD salts. IBD and MBD were also shown to graft successfully (Section 3.3.2.4 and 3.3.4 respectively). The carboxyphenyl (CP) and nitroazophenyl (NAP) films produced from the reaction of FLG with CBD and NABD were analysed by IR spectroscopy, AFM, and in the case of NABD, electrochemistry. All of the films were prepared from a 20 mM aqueous aryldiazonium salt solution and were washed with methanol prior to analysis. AFM images in the exposed orientation for FLG modified with NABD (FLG_{NAP}) and CBD (FLG_{CP}) are given in Figure 3.25. For the CBD

modification, a much longer reaction time was required before a film was seen on the FLG surface. The carboxylic acid group is less electron withdrawing than the nitro group of NBD and NABD, which is assumed to give a decrease in the reactivity of the aryldiazonium salt.

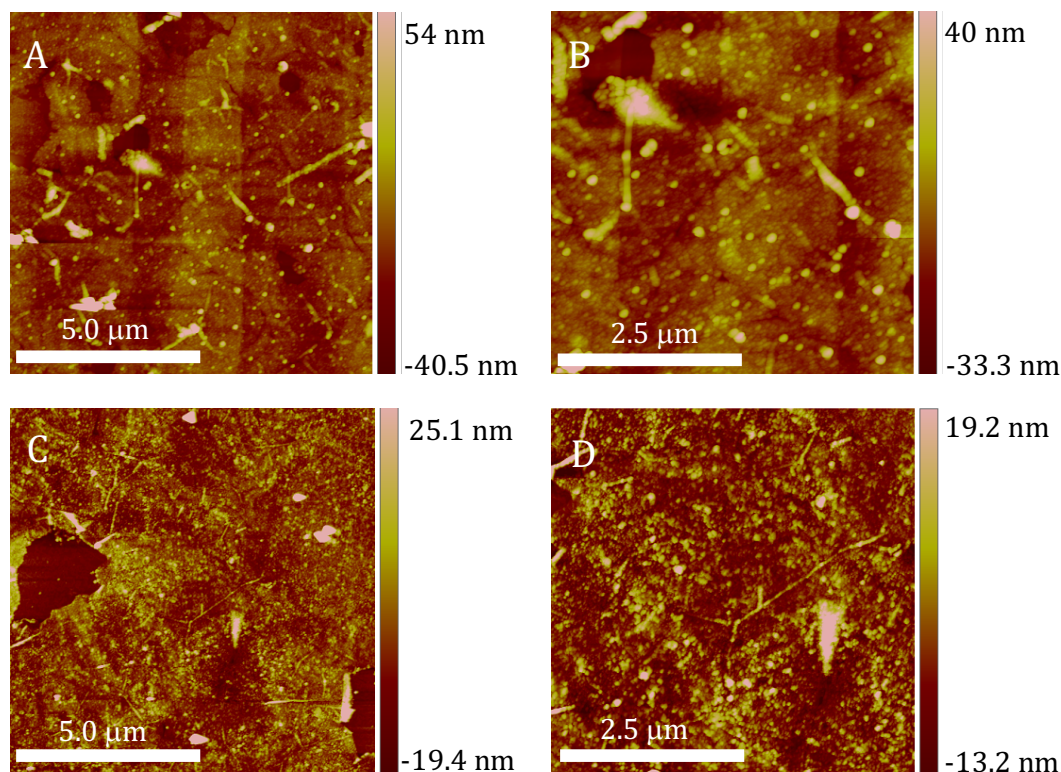


Figure 3.25: AFM images of aryldiazonium modified FLG transferred to HOPG in the exposed orientation: (A) and (B) FLG_{NAP} 20hours; (C) and (D) FLG_{CP} 70hours.

For both the CBD and NABD modification a film can be seen on the surface, even after washing with methanol. This is similar to the NBD modification. Once again, the protrusions are seen across the entire surface indicating the reaction takes place both at the edges and on the basal plane. Protrusions in the NAP film range in height from 4 to 24 nm, and the CP film from 3 to 18 nm. The protrusion heights cannot be taken as an exact measure of film height due to the undulating nature of the underlying FLG, however it is clear that a multilayer film has formed in both instances as the height of an individual group on a carbon surface is 1.27 nm for NAP groups and 0.66 nm for a CP group (calculated using Avogadro software).

The surfaces were characterised by IR spectroscopy, in transmission mode with the FLG supported by a KBr disk. The IR spectra for FLG_{NAP} and the NABD modifier are

given in Figure 3.26. The peak assignments for FLG_{NAP} and NABD were taken from literature and are given in Table 3.5.^{49, 51-52, 63, 75-76}

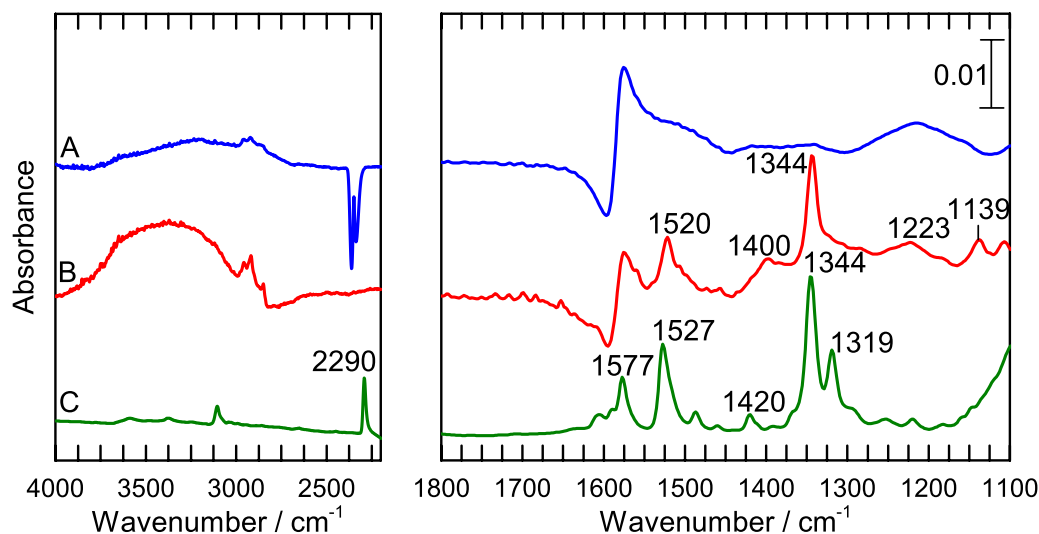


Figure 3.26: Transmission mode IR spectra on KBr for (A) FLG and (B) FLG_{NAP 20hours}. (C) ATR spectrum of NABD salt (scaled $\times 0.05$). Spectra are offset for clarity.

Table 3.5: Peak assignments for NABD and FLG_{NAP}.

| NABD | FLG _{NAP} | Assignment |
|---------|--------------------|--|
| 2290 s | | ν N ₂ ⁺ |
| 1577 s | | ν (C=C) |
| 1527 vs | 1520 vs | ν_a (NO ₂) |
| 1487 m | | Ring def. |
| 1459 w | 1458 w | ν (C-NN) + ring def. |
| 1420 m | 1400 m | Ring def. |
| 1344 vs | 1344 vs | ν_s (NO ₂) |
| 1319 s | | ν_s (NO ₂) + ring def. |
| | 1223 w | ν (C-C) |
| | 1139 m | ν (C-NN) |
| | 1107 m | ν (C-NO ₂) + CH wag |

vs, very strong; s, strong; m, medium; w, weak; ν , stretch mode

FLG_{NP} and FLG_{NAP} show similar peaks. Notably, the peak at 2290 cm⁻¹ in the NABD spectrum is not seen in the FLG_{NAP} spectrum confirming the loss of the diazonium moiety during the reaction.⁵¹ Peaks at 1527 and 1344 cm⁻¹ in the precursor spectrum have shifted to 1520 and 1344 cm⁻¹ in the FLG_{NAP} spectrum, and are assigned to the asymmetric and symmetric NO₂ stretch modes. The shift of these bands is less obvious than for FLG_{NP} surfaces, possibly caused by the different substitution patterns. In NBD, the nitro group is *para* to the diazonium ion. In the NP film, it is *para* to either a carbon-carbon bond or an azo bond. This change in substitution pattern is assumed to cause the shift in the IR peak position for the nitro group in the NP film. In NABD, the nitro group is *para* to the azo linkage, and it remains *para* to the azo linkage in the film. This agrees with work by McCreery et al.⁵² who reported no change in the position of these

two peaks when NABD was reacted with PPF. As observed for NBD, NABD has a peak at 1319 cm^{-1} that is caused by the coupling mode between the symmetric NO_2 stretch and the aromatic ring. This peak is only present in the spectrum of free nitro compounds,⁵³ so as expected is not present in the FLG_{NAP} spectrum. At 1459 cm^{-1} in the NABD spectrum, and 1458 and 1139 cm^{-1} in the FLG_{NAP} spectrum are peaks caused by the stretch modes of the azo linkage.^{52,55} (There is no peak at 1139 cm^{-1} in the NABD spectrum as the tetrafluoroborate counter ion has a very strong absorption peak at 1035 cm^{-1} that envelops all the surrounding peaks.) Similar peaks are seen in Figure 3.14 for the FLG_{NP} surface, and were assigned to azo bonds that form during grafting. For FLG_{NAP} these peaks are also associated with the azo bond between the two benzene rings in the modifier. It is not possible to distinguish between the two types of azo bond using IR spectroscopy. A peak at 1223 cm^{-1} in the FLG_{NAP} spectrum has no complementary peak in the NABD spectrum. This is assigned to the carbon-carbon bonds that form when the aryldiazonium grafts via the aryl radical mechanism to either the FLG surface or an already grafted group.

Figure 3.27 shows the transmission mode IR spectra for CBD and FLG_{CP} . Peak assignments for CBD and FLG_{CP} were taken from literature and are given Table 3.6.⁷⁷⁻⁸⁰ Once again, the peak at 2300 cm^{-1} in the CBD precursor has disappeared in the FLG_{CP} film, which indicates loss of the diazonium moiety during the reaction. The band at 1689 cm^{-1} in the FLG_{CP} spectrum is a combination of a $\text{C}=\text{O}$ stretch and a $-\text{COO}-$ bending vibrational mode. The presence of this peak in the FLG_{CP} spectrum confirms that a CP film resides at the FLG surface. Bands at 1418 and 1290 cm^{-1} are also caused by vibrations associated with the carboxylic acid functional group. The remainder of the bands seen for both the aryldiazonium ion precursor and the modified surface are caused by ring deformation modes. It is not possible to see a peak related to the azo linker at approximately 1135 cm^{-1} : this does not mean that there are no azo linkages present in this film, only that the IR absorbance is not strong enough to be detected. Furthermore, the peak at 1222 cm^{-1} in the FLG_{CP} and CBD spectra is assigned to carbon-carbon bonds, however it is not possible to distinguish between carbon-carbon bonds that result from grafting and carbon-carbon bonds between the aryl ring and the carboxylic acid group.

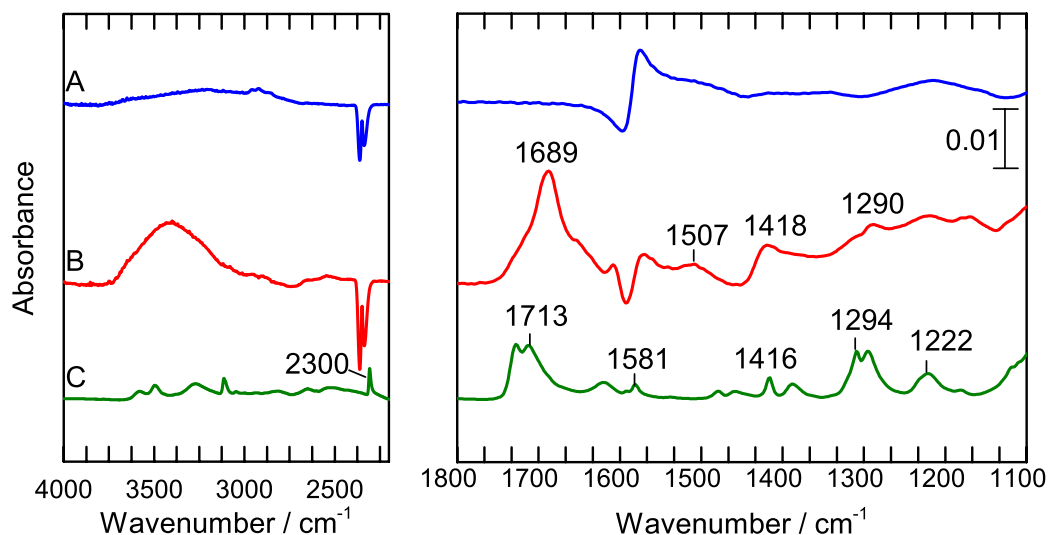


Figure 3.27: Transmission mode IR spectra on KBr for (A) FLG and (B) FLG_{CP 72hours}. (C) ATR spectrum of CBD salt (scaled $\times 0.05$). Spectra are offset for clarity.

Table 3.6: Peak assignments for CBD and FLG_{CBD 72hours}.

| CBD | FLG _{CP} | Assignment |
|-------------------|-------------------|-----------------------------|
| 2300 | | ν (N_2^+) |
| 1727, 1713 vs, db | 1689 vs | ν (CO) + δ (CCO) |
| 1620 s | 1606 w | Ring def. |
| 1581 s | | Ring def. |
| 1480 m | | Ring def. |
| 1459 m | | Ring def. |
| 1416 s | 1418 | ν (OH) |
| 1387 s | | Ring def. |
| 1309, 1294 vs, db | 1290 | ν (CO) + δ (COH) |
| 1222 s | 1222 | ν (C-C) |

vs, very strong; s, strong; m, medium; w, weak; db, doublet; ν , stretch mode; δ , bend mode.

Electrochemistry was also used to characterise the FLG_{NAP} system. A CV for FLG_{NAP} on HOPG in the exposed orientation is given in Figure 3.28. A large peak can be seen for the reduction of NP groups to aminophenyl and hydroxylaminophenyl groups. A small broad redox couple can be seen in the more positive region at $E_{1/2} = 0.48$ V, and is assigned to the hydroxylaminophenyl/nitrosophenyl couple. The double reduction peak that was sometime seen in the FLG_{NP} system was also sometimes seen for the sandwiched FLG_{NAP} system (not shown), and is assumed to have the same origin as for the FLG_{NP} surfaces. For a 20 hour modification time, the sandwiched samples ($n=2$) gave a surface concentration of 1.5 nmol cm^{-2} whereas the exposed sample ($n=2$) gave a surface concentration of 0.7 nmol cm^{-2} . For the exposed configuration, the surface concentration is similar to the maximum value recorded for the analogous FLG_{NP} system. This is surprising, as the NAP film is assumed to be twice the thickness of the NP film, so the limiting surface concentration is expected to be lower. This may be

indicative of an increased density of NAP groups on the surface, however this is not seen in the AFM images. Alternatively, the conductivity through the films may be different, giving different measurable surface concentrations. The surface concentration in the sandwiched orientation is much higher than for the same reaction time for the FLG_{NAP} modification (0.6 nmol cm^{-2}) indicating that either the NABD modifier is more reactive than the NBD salt, there is less physisorption for the NABD modification, or the methanol wash step is not sufficient to remove physisorbed material from the FLG_{NAP} surface. In fact, the latter explanation seems the most reasonable, as when the experiment was repeated without the methanol wash step the surface concentration was 1.2 nmol cm^{-2} , which is similar to that for the washed sample, suggesting methanol washing did not remove physisorbed NAP groups from the surface.

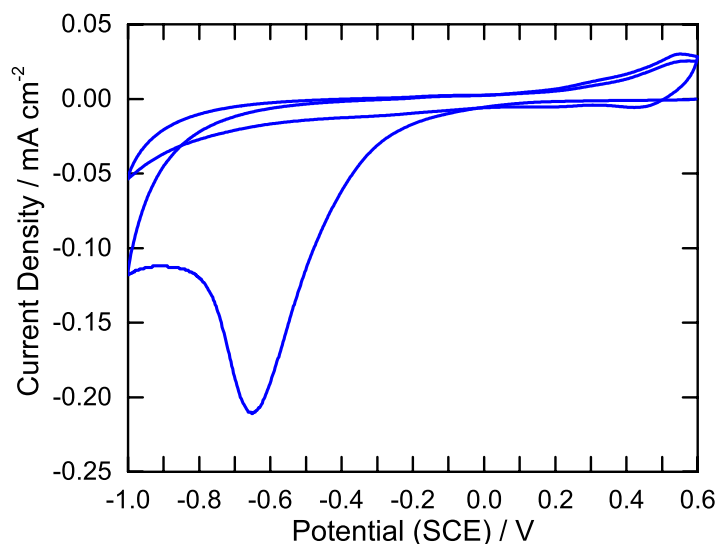


Figure 3.28: CV in 0.1 M H₂SO₄ of FLG_{NAP 20hours} on HOPG in the exposed orientation. Scan rate = 200 mV s⁻¹.

3.3.4 Hall Effect Studies of Aryldiazonium Salt Modification

As explained in Chapter 1, Section 1.5, adding functionality to the graphene can cause doping by adding carriers as either holes or electrons. One possible method to calculate the concentration and type of carriers along with other properties such as sheet resistance and mobility is by using the Hall effect. The principles and practices of Hall effect measurements, and associated calculations are described in Appendix A, Section A.2. Hall effect measurements were performed for FLG and FLG modified with two different aryldiazonium salts: NBD because of its electron-withdrawing nature and MBD because of its electron-donating character. For each measurement, the FLG sample was collected onto a glass microscope cover slip, then Ti/Au contacts were evaporated into the four corners of the sample. Voltages were measured using a Hall

effect measurement apparatus, at four increasingly high currents. The displayed results in Figure 3.29, Figure 3.30, and Figure 3.31 are the average results for at least three samples over the entire current range. The Hall effect measurement was used to calculate sheet resistance, carrier concentration, and mobility for FLG before and after modification.

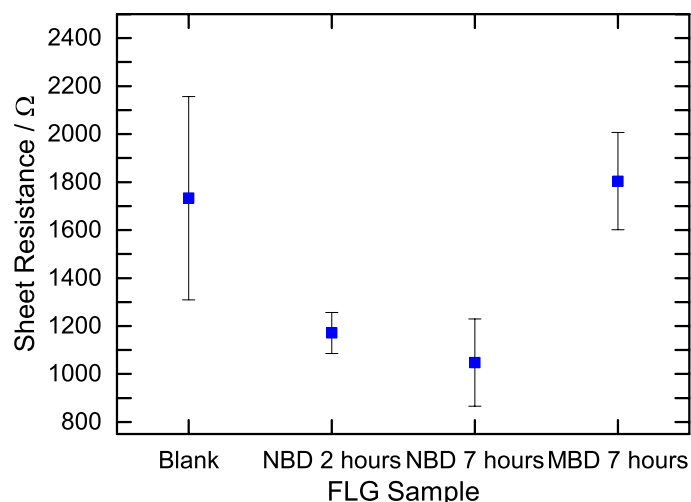


Figure 3.29: Plot of sheet resistance for FLG before and after reaction with 20 mM aryldiazonium salt aqueous solutions. Reported values are the average for four applied currents for various sample numbers of FLG: FLG, $n=12$; FLG_{NP 2hours}, $n=3$; FLG_{NP 7hours}, $n=4$; FLG_{MP 7hours}, $n=4$.

Figure 3.29 shows the sheet resistance after selected modification conditions. The sheet resistance decreases after modification with NP groups, indicating an increase in conductivity. Some studies have shown a decrease in conductivity after covalent functionalisation,^{3, 62} however, work by Gao et al.⁸¹ showed an increase in conductivity, similar to that seen here, after NP functionalisation. The conductivity of the FLG remained constant before and after modification with methoxyphenyl (MP) groups. Note that a change in the mobility after reaction with MBD (see below) confirms that MBD does form a film on FLG. Conductivity (σ) is related to the carrier concentration (n_s) and mobility (μ) by Equation 3.3:

$$\sigma = q\mu n_s \quad (3.3)$$

where q is the elementary charge, μ is the mobility and n_s is the sheet carrier concentration.⁸¹⁻⁸² Carrier concentration, plotted in Figure 3.30, increases after functionalisation for the FLG_{NP} samples, while the significance of the increase for FLG_{MP} is uncertain.

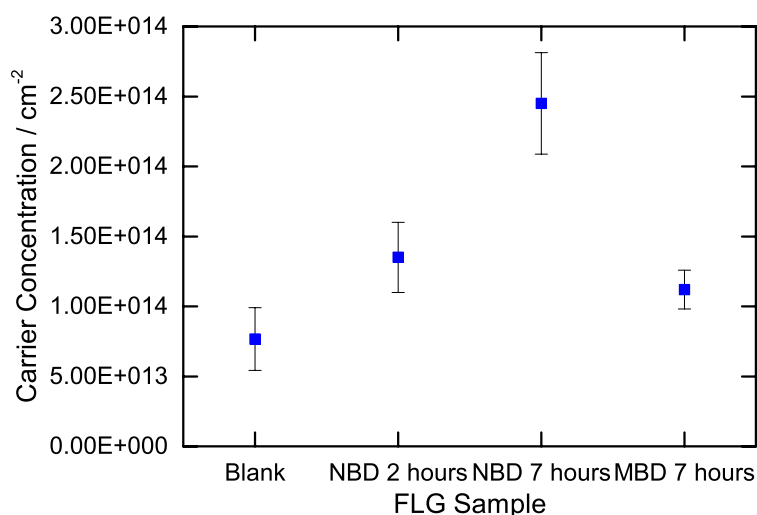


Figure 3.30: Plot of carrier concentration of FLG before and after reaction with 20 mM aryldiazonium salt aqueous solutions. Reported values are the average across four applied currents for various sample numbers: FLG, $n=12$; FLG_{NP 2hours}, $n=3$; FLG_{NP 7hours}, $n=4$; FLG_{MP 7hours}, $n=4$.

For all samples, the Hall coefficient was positive, indicating that the dominant carriers are holes (p-doping). Doping has been shown to increase conductivity due to an increase in the number of charge carriers.⁸³ The FLG is p-doped prior to modification; this is usually attributed to substrate induced doping and other airborne contaminants that can adsorb onto the FLG.⁸⁴ All aryldiazonium ions are expected to p-dope the sample, because the reaction mechanisms for covalent bond formation shown in Chapter 1, Section 1.3.1, require electrons to be removed from the FLG, generating holes.⁸⁵ Doping after functionalisation with NP groups has been reported previously.^{81, 84-85} The NP group is electron withdrawing, so is expected to accept electrons from the FLG generating holes as charge carriers. This is consistent with the increase in carrier concentration with NBD reaction time (Figure 3.30), because the number of NP groups on the surface increases with reaction time. The effect of functionalisation with MP groups on carrier concentration is small. The methoxy group is electron donating, so will donate electron density back into the FLG, countering the inherent p-doping effect of covalent bond formation between MP groups and FLG. The two effects appear to cancel each other out, resulting in a negligible change in the carrier concentration compared to the FLG.

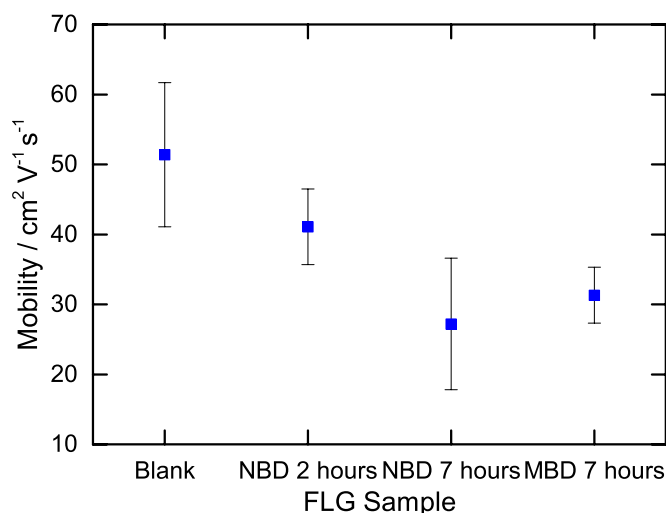


Figure 3.31: Plot of carrier mobility of FLG before and after reaction with 20 mM aryldiazonium salt aqueous solutions. Reported values are the average across four applied currents for various sample numbers: FLG, $n=12$; FLG_{NP 2hours}, $n=3$; FLG_{NP 7hours}, $n=4$; FLG_{MP 7hours}, $n=4$.

Figure 3.31 shows that mobility decreases after functionalisation with both modifiers. The introduction of defects via functionalisation increases scattering within the FLG, which lowers the mean free pathlength, and therefore lowers mobility.⁸¹ Furthermore, functionalisation has been shown to open a bandgap, which also decreases mobility.⁸⁶ Mobility is only influenced by the number of defects, which is independent of whether NP or MP groups are attached, as confirmed by the similar mobility measured for the three samples. Prior to modification, the FLG sample has a lower mobility than often reported for pristine samples,⁸⁷⁻⁸⁹ which is assumed to be caused by defective grain boundary regions, as well as scattering caused by the underlying substrate.

To summarise, for FLG_{NP} the carrier concentration increases, increasing conductivity while mobility decreases, decreasing conductivity. The effect of carrier concentration has overshadowed that of mobility, causing a net increase in conductivity. Gao et al.⁸¹ also reported this outcome when using long reaction times and high aryldiazonium salt concentrations, similar to those used in this work. The conductivity increases with reaction time for the NBD modification because the number of NP groups, and therefore the carrier concentration, increases with reaction time. For the FLG_{MP} there is no change in conductivity attributed to the minimal increase in carrier concentration.

3.4 Conclusion

FLG has been successfully grown using CVD. By altering the gas flow rates, the number of layers can be controlled, as shown by the UV/visible transparency of the

graphene. Both 3-4 and 6-7 layer graphene has been prepared. Raman spectroscopy confirmed the few-layer nature of the graphene, and indicated a small number of defects were present, likely caused by grain boundary regions. The FLG was modified using NBD in both a free-floating manner and on its copper support. This provided two possible orientations for film analysis: sandwiched, and exposed. The modification protocol also allowed additional analysis steps to be performed on a single sheet of FLG after IR spectroscopy on a KBr disk. Raman spectroscopy confirmed that covalent functionalisation occurred, and indicated that the NP groups p-doped the graphene. IR spectroscopy and XPS demonstrated that both carbon-carbon and azo linkages were present in the film. This implies that at least two different grafting mechanisms were active during film growth. Electrochemistry was used to calculate the surface concentration and showed that more of the film could be accessed electrochemically in the sandwiched orientation, as this allowed electron transfer from both sides of the film. Furthermore, the sandwiched orientation sometimes gave two NP reduction peaks, a novel result for carbon surfaces after modification with nitrobenzene diazonium salts. A decrease in the proton concentration during NP reduction is postulated as the cause of these two peaks. The reaction was also carried out with IBD, MBD, NABD and CBD confirming that it is possible to modify FLG with a variety of different aryldiazonium salts.

The electronic properties of the FLG before and after modification with NBD and MBD were established via Hall effect measurements. A significant increase in the carrier concentration after modification with NBD resulted in p-doping and an increase in conductivity. On the other hand, a negligible increase in the carrier concentration with the electron-donating MBD modifier resulted in no change in conductivity. The carrier concentration or density of states plays an important role in determining the quantum capacitance as explained in the introduction. Hence, this will be revisited in Chapter 5 when the capacitance of FLG is discussed.

3.5 References

1. Zhu, Y.; Higginbotham, A. L.; Tour, J. M., Covalent functionalization of surfactant-wrapped graphene nanoribbons. *Chem. Mater.* **2009**, *21*, 5284-5291.
2. Lomeda, J. R.; Doyle, C. D.; Kosynkin, D. V.; Hwang, W.-F.; Tour, J. M., Diazonium functionalization of surfactant-wrapped chemically converted graphene sheets. *J. Am. Chem. Soc.* **2008**, *130*, 16201-16206.
3. Bekyarova, E.; Itkis, M. E.; Ramesh, P.; Berger, C.; Sprinkle, M.; de Heer, W. A.; Haddon, R. C., Chemical modification of epitaxial graphene: Spontaneous grafting of aryl groups. *J. Am. Chem. Soc.* **2009**, *131*, 1336-1337.
4. Bissett, M. A.; Tsuji, M.; Ago, H., Mechanical strain of chemically functionalized chemical vapor deposition grown graphene. *J. Phys. Chem. C* **2013**, *117*, 3152-3159.
5. Sharma, R.; Baik, J. H.; Perera, C. J.; Strano, M. S., Anomalously large reactivity of single graphene layers and edges toward electron transfer chemistries. *Nano Lett.* **2010**, *10*, 398-405.
6. Koehler, F. M.; Jacobsen, A.; Ensslin, K.; Stampfer, C.; Stark, W. J., Selective chemical modification of graphene surfaces: Distinction between single, and bilayer graphene. *Small* **2010**, *6*, 1125-1130.
7. Paulus, G. L. C.; Wang, Q. H.; Strano, M. S., Covalent electron transfer chemistry of graphene with diazonium salts. *Acc. Chem. Res.* **2013**, *46*, 160-170.
8. Wang, Q. H.; Jin, Z.; Kim, K. K.; Hilmer, A. J.; Paulus, G. L. C.; Shih, C.-J.; Ham, M.-H.; Sanchez-Yamagishi, J. D.; Watanabe, K.; Taniguchi, T.; Kong, J.; Jarillo-Herrero, P.; Strano, M. S., Understanding and controlling the substrate effect on graphene electron-transfer chemistry via reactivity imprint lithography. *Nat Chem* **2012**, *4*, 724-732.
9. Greenwood, J.; Phan, T. H.; Fujita, Y.; Li, Z.; Ivasenko, O.; Vanderlinden, W.; Van Gorp, H.; Frederickx, W.; Lu, G.; Tahara, K.; Tobe, Y.; Uji-i, H.; Mertens, S. F. L.; De Feyter, S., Covalent modification of graphene and graphite using diazonium chemistry: Tunable grafting and nanomanipulation. *ACS Nano* **2015**, *9*, 5520-5535.
10. Jin, Z.; McNicholas, T. P.; Shih, C. J.; Wang, Q. H.; Paulus, G. L. C.; Hilmer, A.; Shimizu, S.; Strano, M. S., Click chemistry on solution-dispersed graphene and monolayer CVD graphene. *Chem. Mater.* **2011**, *23*, 3362-3370.
11. Lillethorup, M.; Kongsfelt, M.; Ceccato, M.; Jensen, B. B. E.; Jorgensen, B.; Pedersen, S. U.; Daasbjerg, K., High- versus low- quality graphene: A mechanistic investigation of electrografted diazonium- based films for growth of polymer brushes. *Small* **2014**, *10*, 922-934.
12. Xia, Z.; Leonardi, F.; Gobbi, M.; Liu, Y.; Bellani, V.; Liscio, A.; Kovtun, A.; Li, R.; Feng, X.; Orgiu, E.; Samorì, P.; Treossi, E.; Palermo, V., Electrochemical functionalization of graphene at the nanoscale with self-assembling diazonium salts. *ACS Nano* **2016**, *10*, 7125-7134.
13. Ejigu, A.; Kinloch, I. A.; Dryfe, R. A. W., Single stage simultaneous electrochemical exfoliation and functionalization of graphene. *ACS Appl. Mater. Interfaces* **2017**, *9*, 710-721.

14. Ossonon, B. D.; Belanger, D., Functionalization of graphene sheets by the diazonium chemistry during electrochemical exfoliation of graphite. *Carbon* **2017**, *111*, 83-93.
15. Wu, B.; Geng, D.; Guo, Y.; Huang, L.; Xue, Y.; Zheng, J.; Chen, J.; Yu, G.; Liu, Y.; Jiang, L., Equiangular hexagon-shape-controlled synthesis of graphene on copper surface. *Adv. Mater.* **2011**, *23*, 3522-3525.
16. Zhang, X. F.; Ning, J.; Li, X. L.; Wang, B.; Hao, L.; Liang, M. H.; Jin, M. H.; Zhi, L. J., Hydrogen-induced effects on the CVD growth of high-quality graphene structures. *Nanoscale* **2013**, *5*, 8363-8366.
17. Eres, G.; Regmi, M.; Rouleau, C. M.; Chen, J.; Ivanov, I. N.; Poretzky, A. A.; Geohegan, D. B., Cooperative island growth of large-area single-crystal graphene on copper using chemical vapor deposition. *ACS Nano* **2014**, *8*, 5657-5669.
18. Lin, L.; Li, J.; Ren, H.; Koh, A. L.; Kang, N.; Peng, H.; Xu, H. Q.; Liu, Z., Surface engineering of copper foils for growing centimeter-sized single-crystalline graphene. *ACS Nano* **2016**.
19. Lee, Y.; Bae, S.; Jang, H.; Jang, S.; Zhu, S.-E.; Sim, S. H.; Song, Y. I.; Hong, B. H.; Ahn, J.-H., Wafer-scale synthesis and transfer of graphene films. *Nano Lett.* **2010**, *10*, 490-493.
20. Nair, R. R.; Blake, P.; Grigorenko, A. N.; Novoselov, K. S.; Booth, T. J.; Stauber, T.; Peres, N. M. R.; Geim, A. K., Fine structure constant defines visual transparency of graphene. *Science* **2008**, *320*, 308.
21. Li, J.; Ji, H.; Zhang, X.; Wang, X.; Jin, Z.; Wang, D.; Wan, L.-J., Controllable atmospheric pressure growth of mono-layer, bi-layer and tri-layer graphene. *Chem. Commun.* **2014**, *50*, 11012-11015.
22. Chagas, T.; Cunha, T. H. R.; Matos, M. J. S.; dos Reis, D. D.; Araujo, K. A. S.; Malachias, A.; Mazzoni, M. S. C.; Ferlauto, A. S.; Magalhaes-Paniago, R., Room temperature observation of the correlation between atomic and electronic structure of graphene on Cu(110). *RSC Adv.* **2016**, *6*, 98001-98009.
23. Zhao, L.; Rim, K.; Zhou, H.; He, R.; Heinz, T.; Pinczuk, A.; Flynn, G.; Pasupathy, A., Influence of copper crystal surface on the CVD growth of large area monolayer graphene. *Solid State Commun.* **2011**, *151*, 509-513.
24. Ago, H.; Ohta, Y.; Hibino, H.; Yoshimura, D.; Takizawa, R.; Uchida, Y.; Tsuji, M.; Okajima, T.; Mitani, H.; Mizuno, S., Growth dynamics of single-layer graphene on epitaxial Cu surfaces. *Chem. Mater.* **2015**, *27*, 5377-5385.
25. Li, Q.; Chou, H.; Zhong, J.-H.; Liu, J.-Y.; Dolocan, A.; Zhang, J.; Zhou, Y.; Ruoff, R. S.; Chen, S.; Cai, W., Growth of adlayer graphene on Cu studied by carbon isotope labeling. *Nano Lett.* **2013**, *13*, 486-490.
26. Song, Y.; Zhuang, J.; Song, M.; Yin, S.; Cheng, Y.; Zhang, X.; Wang, M.; Xiang, R.; Xia, Y.; Maruyama, S.; Zhao, P.; Ding, F.; Wang, H., Epitaxial nucleation of CVD bilayer graphene on copper. *Nanoscale* **2016**, *8*, 20001-20007.
27. Ta, H. Q.; Perello, D. J.; Duong, D. L.; Han, G. H.; Gorantla, S.; Nguyen, V. L.; Bachmatiuk, A.; Rotkin, S. V.; Lee, Y. H.; Rummeli, M. H., Stranski–Krastanov and Volmer–Weber CVD growth regimes to control the stacking order in bilayer graphene. *Nano Lett.* **2016**, *16*, 6403-6410.

28. Chen, W.; Gui, X.; Liang, B.; Liu, M.; Lin, Z.; Zhu, Y.; Tang, Z., Controllable fabrication of large-area wrinkled graphene on a solution surface. *ACS Appl. Mater. Interfaces* **2016**.
29. Kim, H. H.; Lee, S. K.; Lee, S. G.; Lee, E.; Cho, K., Wetting-assisted crack- and wrinkle-free transfer of wafer-scale graphene onto arbitrary substrates over a wide range of surface energies. *Adv. Funct. Mater.* **2016**, *26*, 2070-2077.
30. Lee, M. J.; Choi, J. S.; Kim, J. S.; Byun, I. S.; Lee, D. H.; Ryu, S.; Lee, C.; Park, B. H., Characteristics and effects of diffused water between graphene and a SiO₂ substrate. *Nano Res.* **2012**, *5*, 710-717.
31. Tang, B.; Guoxin, H.; Gao, H., Raman spectroscopic characterization of graphene. *Appl. Spectrosc. Rev.* **2010**, *45*, 369-407.
32. Ferrari, A. C.; Basko, D. M., Raman spectroscopy as a versatile tool for studying the properties of graphene. *Nat Nano* **2013**, *8*, 235-246.
33. Tang, B.; Gao, H.; Hu, G., Growth mechanism and influences from kinetic factors on carbon materials with Cu and silica substrates during atmospheric pressure chemical vapor deposition. *J. Phys. Chem. C* **2013**, *117*, 25175-25184.
34. Mangadlao, J. D.; De Leon, A. C. C.; Felipe, M. J. L.; Cao, P.; Advincula, P. A.; Advincula, R. C., Grafted carbazole-assisted electrodeposition of graphene oxide. *ACS Appl. Mater. Interfaces* **2015**, *7*, 10266-10274.
35. Munuera, J. M.; Paredes, J. I.; Villar-Rodil, S.; Ayán-Varela, M.; Pagán, A.; Aznar-Cervantes, S. D.; Cenis, J. L.; Martínez-Alonso, A.; Tascón, J. M. D., High quality, low oxygen content and biocompatible graphene nanosheets obtained by anodic exfoliation of different graphite types. *Carbon* **2015**, *94*, 729-739.
36. Mukhopadhyay, S.; Biswas, R.; Sinha, C., Signature of quantum interference and the Fano resonances in the transmission spectrum of bilayer graphene nanostructure. *J. Appl. Phys.* **2011**, *110*, 7.
37. Cappelluti, E.; Benfatto, L.; Manzardo, M.; Kuzmenko, A. B., Charged-phonon theory and Fano effect in the optical spectroscopy of bilayer graphene. *Phys. Rev. B* **2012**, *86*, 15.
38. Baranowski, J. M.; Mozdzonek, M.; Dabrowski, P.; Grodecki, K.; Osewski, P.; Kozłowski, w.; Kopciuszynski, M.; Jaloehowski, M.; Strupinski, W., Observation of electron-phonon couplings and Fano resonances in epitaxial bilayer graphene. *Graphene* **2013**, *2*, 115-120.
39. Stankovich, S.; Dikin, D. A.; Piner, R. D.; Kohlhaas, K. A.; Kleinhammes, A.; Jia, Y.; Wu, Y.; Nguyen, S. T.; Ruoff, R. S., Synthesis of graphene-based nanosheets via chemical reduction of exfoliated graphite oxide. *Carbon* **2007**, *45*, 1558-1565.
40. Yu, B.; Wang, X.; Qian, X.; Xing, W.; Yang, H.; Ma, L.; Lin, Y.; Jiang, S.; Song, L.; Hu, Y., Functionalized graphene oxide/phosphoramidate oligomer hybrids flame retardant prepared via in situ polymerization for improving the fire safety of polypropylene. *RSC Adv.* **2014**, *4*, 31782-31794.
41. Wei, G.; Yan, M.; Dong, R.; Wang, D.; Zhou, X.; Chen, J.; Hao, J., Covalent modification of reduced graphene oxide by means of diazonium chemistry and use as a drug-delivery system. *Chem. Eur. J.* **2012**, *18*, 14708-14716.

42. Hussain, S.; Iqbal, M. W.; Park, J.; Ahmad, M.; Singh, J.; Eom, J.; Jung, J., Physical and electrical properties of graphene grown under different hydrogen flow in low pressure chemical vapor deposition. *Nano. Res. Lett.* **2014**, *9*, 546.
43. Brownson, D. A. C.; Varey, S. A.; Hussain, F.; Haigh, S. J.; Banks, C. E., Electrochemical properties of CVD grown pristine graphene: Monolayer- vs. Quasi-graphene. *Nanoscale* **2014**, *6*, 1607-1621.
44. Bellunato, A.; Arjmandi Tash, H.; Cesa, Y.; Schneider, G. F., Chemistry at the edge of graphene. *ChemPhysChem* **2016**, *17*, 785-801.
45. Serrano-Espraza, I.; Fan, J.; Michalik, J. M.; Rodriguez, L. A.; Ibarra, M. R.; Maria de Teresa, J., The nature of graphene-metal bonding probed by Raman spectroscopy: The special case of cobalt. *J. Phys. D: Appl. Phys.* **2016**, *49*, 105301-105310.
46. Wu, Y.; Jiang, W.; Ren, Y.; Cai, W.; Lee, W. H.; Li, H.; Piner, R. D.; Pope, C. W.; Hao, Y.; Ji, H.; Kang, J.; Ruoff, R. S., Tuning the doping type and level of graphene with different gold configurations. *Small* **2012**, *8*, 3129-3136.
47. Li, Y., Intrinsic doping dependence of Raman 2D mode in graphene: Signatures of electron–electron interaction. In *Probing the response of two-dimensional crystals by optical spectroscopy*, Springer International Publishing: Cham, 2016; pp 9-18.
48. Bekyarova, E.; Sarkar, S.; Niyogi, S.; Itkis, M. E.; Haddon, R. C., Advances in the chemical modification of epitaxial graphene. *J. Phys. D: Appl. Phys.* **2012**, *45*, 154009.
49. Cullen, R. J.; Jayasundara, D. R.; Soldi, L.; Cheng, J. J.; Dufaure, G.; Colavita, P. E., Spontaneous grafting of nitrophenyl groups on amorphous carbon thin films: A structure-reactivity investigation. *Chem. Mater.* **2012**, *24*, 1031-1040.
50. Murphy, D. M.; Cullen, R. J.; Jayasundara, D. R.; Scanlan, E. M.; Colavita, P. E., Study of the spontaneous attachment of polycyclic aryldiazonium salts onto amorphous carbon substrates. *RSC Adv.* **2012**, *2*, 6527-6534.
51. Pandurangappa, M.; Ramakrishnappa, T.; Compton, R. G., Functionalization of glassy carbon spheres by ball milling of aryl diazonium salts. *Carbon* **2009**, *47*, 2186-2193.
52. Anariba, F.; Viswanathan, U.; Bocian, D. F.; McCreery, R. L., Determination of the structure and orientation of organic molecules tethered to flat graphitic carbon by ATR-FTIR and Raman spectroscopy. *Anal. Chem.* **2006**, *78*, 3104-3112.
53. Toupin, M.; Bélanger, D., Thermal stability study of aryl modified carbon black by *in situ* generated diazonium salt. *J. Phys. Chem. C* **2007**, *111*, 5394-5401.
54. Richner, G.; van Bokhoven, J. A.; Neuhold, Y.-M.; Makosch, M.; Hungerbühler, K., *In situ* infrared monitoring of the solid/liquid catalyst interface during the three-phase hydrogenation of nitrobenzene over nanosized Au on TiO₂. *Phys. Chem. Chem. Phys.* **2011**, *13*, 12463-12471.
55. Tecklenburg, M. M.; Kosnak, D. J.; Bhatnagar, A.; Mohanty, D. K., Vibrational characterization of azobenzenes, azoxybenzenes and azoaromatic and azoxyaromatic polyethers. *J. Raman Spectrosc.* **1997**, *28*, 755-763.
56. Stuart, B. H., *Infrared spectroscopy: Fundamentals and applications*. 1 ed.; John Wiley & Sons, Ltd.: Chichester, England, 2004.

57. Stuart, B.; George, B.; McIntyre, P., *Modern infrared spectroscopy* John Wiley & Sons, Ltd.: 1998.
58. Griffiths, P. R.; De Haseth, J. A., *Fourier transform infrared spectrometry*. John Wiley & Sons, Ltd.: 1986.
59. Lee, L.; Brooksby, P. A.; Hapiot, P.; Downard, A. J., Electrografting of 4-nitrobenzenediazonium ion at carbon electrodes: Catalyzed and uncatalyzed reduction processes. *Langmuir* **2016**, *32*, 468-476.
60. Brooksby, P. A.; Downard, A. J., Electrochemical and atomic force microscopy study of carbon surface modification via diazonium reduction in aqueous and acetonitrile solutions. *Langmuir* **2004**, *20*, 5038-5045.
61. Saby, C.; Ortiz, B.; Champagne, G. Y.; Bélanger, D., Electrochemical modification of glassy carbon electrode using aromatic diazonium salts. 1. Blocking effect of 4-nitrophenyl and 4-carboxyphenyl groups. *Langmuir* **1997**, *13*, 6805-6813.
62. Sinitskii, A.; Dimiev, A.; Corley, D. A.; Fursina, A. A.; Kosynkin, D. V.; Tour, J. M., Kinetics of diazonium functionalization of chemically converted graphene nanoribbons. *Acs Nano* **2010**, *4*, 1949-1954.
63. Jayasundara, D. R.; Cullen, R. J.; Colavita, P. E., In situ and real time characterization of spontaneous grafting of aryl diazonium salts at carbon surfaces. *Chem. Mater.* **2013**, *25*, 1144-1152.
64. Mesnage, A.; Lefèvre, X.; Jégou, P.; Deniau, G.; Palacin, S., Spontaneous grafting of diazonium salts: Chemical mechanism on metallic surfaces. *Langmuir* **2012**, *28*, 11767-11778.
65. Betelu, S.; Tijunelyte, I.; Boubekour-Lecaque, L.; Ignatiadis, I.; Ibrahim, J.; Gaboreau, S.; Berho, C.; Toury, T.; Guenin, E.; Lidgi-Guigui, N.; Félidj, N.; Rinnert, E.; Chapelle, M. L. d. l., Evidence of the grafting mechanisms of diazonium salts on gold nanostructures. *J. Phys. Chem. C* **2016**, *120*, 18158-18166.
66. Brooksby, P. A.; Shields, J. D.; Farquhar, A. K.; Downard, A. J., Reduction of nitrophenyl films in aqueous solutions: How many electrons? *ChemElectroChem* **2016**, *3*, 2021-2026.
67. Masheter, A. T.; Wildgoose, G. G.; Crossley, A.; Jones, J. H.; Compton, R. G., A facile method of modifying graphite powder with aminophenyl groups in bulk quantities. *J. Mater. Chem.* **2007**, *17*, 3008-3014.
68. Lehr, J.; Williamson, B. E.; Downard, A. J., Spontaneous grafting of nitrophenyl groups to planar glassy carbon substrates: Evidence for two mechanisms. *J. Phys. Chem. C* **2011**, *115*, 6629-6634.
69. Abiman, P.; Wildgoose, G. G.; Compton, R. G., Investigating the mechanism for the covalent chemical modification of multiwalled carbon nanotubes using aryl diazonium salts. *Int. J. Electrochem. Sci* **2008**, *3*, 104-117.
70. Yu, S. S. C.; Tan, E. S. Q.; Jane, R. T.; Downard, A. J., An electrochemical and XPS study of reduction of nitrophenyl films covalently grafted to planar carbon surfaces. *Langmuir* **2007**, *23*, 11074-11082.

71. Ceccato, M.; Nielsen, L. T.; Iruthayaraj, J.; Hinge, M.; Pedersen, S. U.; Daasbjerg, K., Nitrophenyl groups in diazonium-generated multilayer films: Which are electrochemically responsive? *Langmuir* **2010**, *26*, 10812-10821.
72. Gross, A. J.; Bucher, C.; Coche-Guerente, L.; Labbé, P.; Downard, A. J.; Moutet, J.-C., Nickel (ii) tetraphenylporphyrin modified surfaces via electrografting of an aryldiazonium salt. *Electrochem. Commun.* **2011**, *13*, 1236-1239.
73. Ranganathan, S.; McCreery, R. L., Electroanalytical performance of carbon films with near-atomic flatness. *Anal. Chem.* **2001**, *73*, 893-900.
74. Ortiz, B.; Saby, C.; Champagne, G. Y.; Bélanger, D., Electrochemical modification of a carbon electrode using aromatic diazonium salts. 2. Electrochemistry of 4-nitrophenyl modified glassy carbon electrodes in aqueous media. *J. Electroanal. Chem.* **1998**, *455*, 75-81.
75. Liu, Y. C.; McCreery, R. L., Raman spectroscopic determination of the structure and orientation of organic monolayers chemisorbed on carbon electrode surfaces. *Anal. Chem.* **1997**, *69*, 2091-7.
76. Chamoulaud, G.; Bélanger, D., Spontaneous derivatization of a copper electrode with in situ generated diazonium cations in aprotic and aqueous media. *J. Phys. Chem. C* **2007**, *111*, 7501-7507.
77. Krishnakumar, V.; Mathammal, R., Density functional and experimental studies on the FTIR and FT-Raman spectra and structure of benzoic acid and 3,5-dichloro salicylic acid. *J. Raman Spectrosc.* **2009**, *40*, 264-271.
78. Chenhimi, M. M.; Lamouri, A.; Picot, M.; Pinson, J., Surface modification of polymers by reduction of diazonium salts: Polymethylmethacrylate as an example. *J. Mater. Chem. C* **2014**, *2*, 356-363.
79. Compton, O. C.; Nguyen, S. T., Graphene oxide, highly reduced graphene oxide, and graphene: Versatile building blocks for carbon,ãbased materials. *Small* **2010**, *6*, 711-723.
80. Bellamy, L. J., *The infra-red spectra of complex molecules*. Methuen & Co Ltd: London, 1958.
81. Huang, P.; Zhu, H.; Jing, L.; Zhao, Y.; Gao, X., Graphene covalently binding aryl groups: Conductivity increases rather than decreases. *ACS Nano* **2011**, *5*, 7945-7949.
82. Popvic, R. S., *Hall effect devices, second edition*. Taylor & Francis: 2003.
83. Kasry, A.; Kuroda, M. A.; Martyna, G. J.; Tulevski, G. S.; Bol, A. A., Chemical doping of large-area stacked graphene films for use as transparent, conducting electrodes. *ACS Nano* **2010**, *4*, 3839-3844.
84. Arnhild, J.; Fabian, M. K.; Wendelin, J. S.; Klaus, E., Towards electron transport measurements in chemically modified graphene: Effect of a solvent. *New J. Phys.* **2010**, *12*, 125007.
85. Farmer, D. B.; Golizadeh-Mojarad, R.; Perebeinos, V.; Lin, Y.-M.; Tulevski, G. S.; Tsang, J. C.; Avouris, P., Chemical doping and electron-hole conduction asymmetry in graphene devices. *Nano Lett.* **2009**, *9*, 388-392.
86. Niyogi, S.; Bekyarova, E.; Itkis, M. E.; Zhang, H.; Shepperd, K.; Hicks, J.; Sprinkle, M.; Berger, C.; Lau, C. N.; deHeer, W. A.; Conrad, E. H.; Haddon, R.

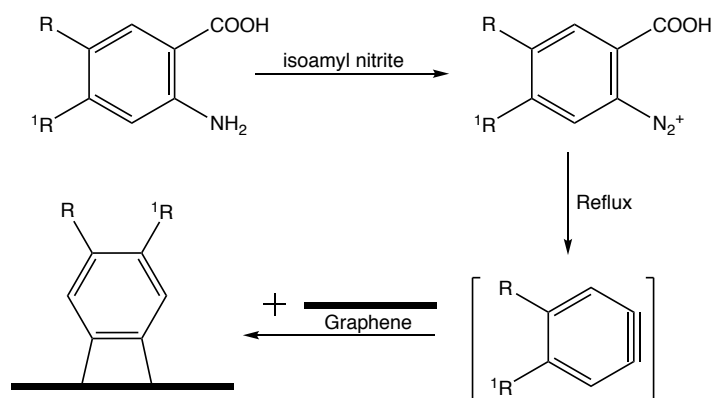
- C., Spectroscopy of covalently functionalized graphene. *Nano Lett.* **2010**, *10*, 4061-4066.
87. Pham, V. P.; Mishra, A.; Yeom, G. Y., The enhancement of hall mobility and conductivity of CVD graphene through radical doping and vacuum annealing. *RSC Adv.* **2017**, *7*, 16104-16108.
88. Bolotin, K. I.; Sikes, K. J.; Jiang, Z.; Klima, M.; Fudenberg, G.; Hone, J.; Kim, P.; Stormer, H. L., Ultrahigh electron mobility in suspended graphene. *Solid State Commun.* **2008**, *146*, 351-355.
89. Morozov, S.; Novoselov, K.; Katsnelson, M.; Schedin, F.; Elias, D.; Jaszczak, J. A.; Geim, A., Giant intrinsic carrier mobilities in graphene and its bilayer. *Phys. Rev. Lett.* **2008**, *100*, 016602.

4 Other FLG Modification Methods: the Diels-Alder Reaction of an Anthranilic Acid and the Spontaneous Reaction of a Primary Amine

4.1 Introduction

4.1.1 Diels-Alder Reactions of Anthranilic Acids

In Chapter 1, Section 1.3.2, Diels-Alder reactions of graphene were discussed. One potential dienophile for these reactions is an aryne. Arynes can be generated through the decomposition of an anthranilic acid precursor, and can then react with graphene, as shown in Scheme 4.1.¹



Scheme 4.1: Diels-Alder reaction between an aryne, generated from an anthranilic acid precursor, and a graphene surface.

Although this reaction has been studied previously for graphene and other carbon substrates,²⁻³ there has been no investigation into the layer thickness of the grafted film. It is often advantageous to have good control over film thickness, and methods for covalently grafting monolayers to graphene are limited. With the aryldiazonium ion reaction discussed in Chapter 3, the film grafted is typically a disordered multilayer. Several methods have been established to limit this growth to a monolayer, but each possesses some disadvantages. Firstly, the use of aryldiazonium derivatives with bulky *meta* substituents has been shown to prevent multilayer growth by inhibiting radical attack at already grafted groups, via steric hindrance.⁴⁻⁵ Unfortunately, the number of suitable derivatives appears limited, so this method has few applications. Using calix[4]-arenediazonium ions, where the aryl groups are protected from attack by a macrocycle also limits film growth to a monolayer,⁶ however this method requires a multistep synthesis prior to film growth. Grafting aryldiazonium ions from ionic liquids

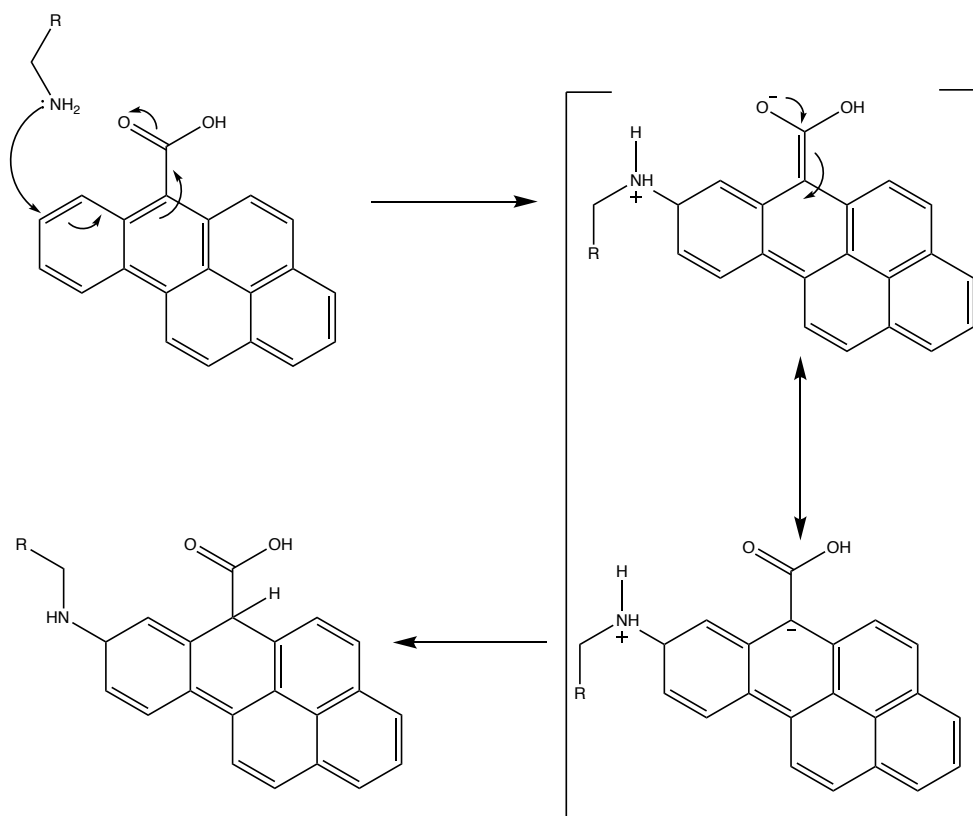
has been used to provide monolayer growth due to a low diffusion rate of the aryldiazonium salt through the ionic liquid.⁷⁻⁸ The addition of a radical scavenger during the aryldiazonium ion reaction can limit film growth to a monolayer, however efficient control of film growth using this approach was reported to be dependent on the *para* substituent. Strict monolayer formation was only obtained when electron withdrawing *para* substituents were used, which limits the applicability of this method.⁹⁻¹¹ Finally, the use of an aryldiazonium salt with a bulky protecting group in the *para* position that can be cleaved after the reaction is a reliable method to give monolayers, but considerable effort is required in the synthesis of protected aryldiazonium salts and the resulting surface concentration is low.¹²

The reaction of an aryne with a carbon surface is expected to give monolayer coverage. The expected mechanism of the cycloaddition reaction means that monolayer formation is favoured. For the Diels-Alder reaction, the aryne must approach perpendicular to the substrate because the reactive orbitals are in the plane of the ring.¹³ This means that the reaction at already grafted groups would require the aryne to approach parallel to the FLG (or other carbon) surface, which would be sterically hindered by both the FLG and the already grafted groups. Furthermore, the reactivity of arynes towards acenes of varying chain lengths has been studied and arynes are much more reactive with larger acenes.¹⁴⁻¹⁵ This suggests the aryne will be more reactive towards the polyaromatic graphitic substrate than the already grafted phenyl rings. The use of an anthranilic acid to provide monolayers is advantageous because a wide range of functionalised anthranilic acid precursors are commercially available, or can be prepared using simple synthetic strategies.

4.1.2 Reaction of FLG with a Primary Amine

In the second part of this chapter, the reaction of FLG with a primary amine is considered. Primary amines have been reported to react with a range of different carbon materials. Gallardo et al.¹⁶ reported the nucleophilic addition of a variety of amines to glassy carbon (GC). This work was further supported by studies on the addition of ferrocene terminated amines to GC.¹⁷ GC is a carbon material known to possess many oxygen containing groups at the surface, and it was suggested that these groups promote a Michael-type addition of the amine, illustrated in Scheme 4.2. XPS results in Chapter

3, Section 3.3.1.4 confirm the presence of some oxygen containing groups at the surface of the FLG, so the reaction mechanism in Scheme 4.2 is plausible.



Scheme 4.2: Proposed mechanism for the reaction of a primary amine with a carbon surface through a Michael-type addition.¹⁶

An alternative way amines can modify FLG is through intercalation. It is well known that small molecules are able to intercalate between the sheets of graphite.¹⁸ Compton et al.¹⁹ have reported the partial intercalation of 4-nitrobenzylamine into both graphite and multiwalled carbon nanotubes at edge and defect sites. Furthermore, they indicated that this process was not available to non-amine derivatives such as nitrotoluene and nitrophenol. They suggest that this is because full or partial electron transfer between the intercalating molecule and the carbon lattices is required, and the electron donating character of the amine enables this. This mechanism is plausible for the FLG used here, as Raman results in Chapter 3, Section 3.3.1.4 indicate that defect sites exist in the FLG where intercalation could occur. Amines could therefore modify FLG through either partial intercalation or a Michael-type addition reaction, most likely at edge and defect regions.

4.2 Experimental Methods

All experimental methods are outlined in Chapter 2. The modification of FLG via the Diels-Alder reaction and the spontaneous addition of a primary amine is described in Sections 2.4.2 and 2.4.3 respectively. For the Diels-Alder reaction, two different anthranilic acids, namely 5-nitroanthranilic acid (NAA) and 2-amino-teraphthalic acid 4-methyl ester (ME), have been used to modify FLG, to give FLG_{NAA} and FLG_{ME} respectively. These are shown in Figure 4.1. The methyl ester precursor is especially useful in further reactions, as the methyl ester functionality can be easily hydrolysed to a carboxylic acid group.

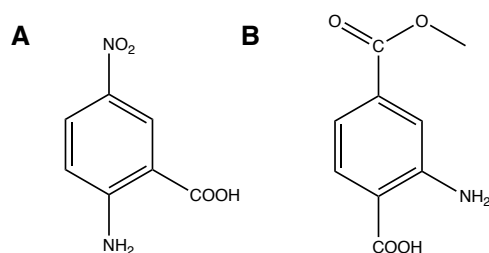


Figure 4.1: Anthranilic acids used in this work: (A) 5-nitroanthranilic acid, and (B) 2-amino-teraphthalic acid 4-methyl ester.

The experimental protocol for the amine addition reaction was based on literature reports for the Michael-like addition of amines to GC surfaces.¹⁶⁻¹⁷ Two different primary amines were studied for the addition reaction, 4-nitrophenethylamine (NPEA) and 2-aminoanthraquinone (AAQ), to give FLG_{NPEA} and FLG_{AAQ} respectively. These are shown in Figure 4.2. The AAQ derivative was selected because like the nitrophenyl group anthraquinones have a well-known electrochemical signature. Subsequent characterisation methods are outlined in Section 2.6.

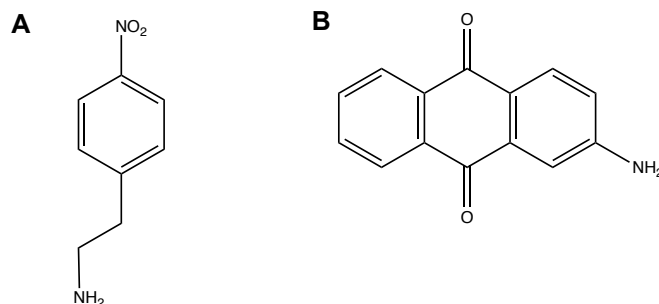


Figure 4.2: Primary amines used in this work: (A) 4-nitrophenethylamine (NPEA), and (B) 2-aminoanthraquinone (AAQ).

4.3 Results and Discussion

4.3.1 Characterisation of FLG Modified via the Diels-Alder Reaction of an Anthranilic Acid

4.3.1.1 Raman Spectroscopy

FLG was initially modified using the NAA precursor. After a 6 hour reaction the FLG_{NAA} was collected onto a gold substrate for Raman spectroscopic analysis. The Raman spectra of FLG and FLG_{NAA} are given in Figure 4.3.

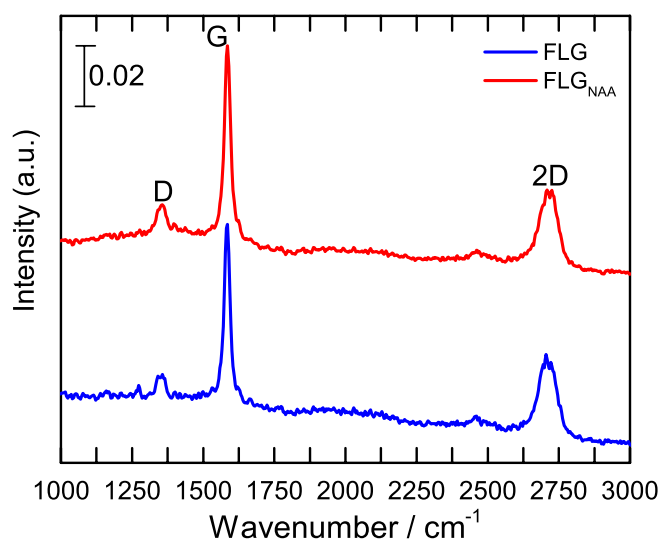


Figure 4.3: Raman spectra of FLG on a gold substrate, before (blue) and after (red) a 6 hour reaction with NAA. Spectra normalised to give a G-band intensity of 1. Spectra offset for clarity.

Peaks at 1585, 2716, and 1348 cm^{-1} can be seen in both spectra, labelled the G-, 2D-, and D-bands respectively.²⁰ The D/G band intensity ratio has increased from 0.13 ± 0.03 in FLG to 0.21 ± 0.03 in FLG_{NAA} . This agrees with other publications that report an increase in the D/G band intensity ratio after reaction with an aryne, both on graphene and carbon nanotubes.^{2, 21-23} This confirms the FLG has been covalently functionalised by the aryne species, as covalent bond formation, as shown in Scheme 4.1, results in the conversion of some carbon atoms in the graphene lattice to sp^3 -hybridisation, which increases the intensity of the D-band. As explained previously, the position of the G- and 2D-bands can shift with doping. The position of the G- and 2D-bands is given in Table 4.1. Both bands have shifted to higher wavenumbers, consistent with p-doping.²⁴ The electron withdrawing nature of the nitro group means p-doping is expected,²⁵ and p-doping was also seen in Chapter 3 for the FLG_{NP} surfaces. Raman spectroscopy was also used to confirm the reaction of FLG with ME. The D/G band intensity ratio increased to 0.24 ± 0.03 after modification, indicating that the Diels-

Alder reaction is also possible with this precursor. The methyl ester functional group is less strongly electron withdrawing than the nitro group, which means the G- and 2D-bands have not shifted significantly after modification.

Table 4.1: G- and 2D-band positions before and after modification with NAA or ME for six-hours.

| Sample | G-band position / cm^{-1} | $\Delta G / \text{cm}^{-1}$ | 2D-band position/ cm^{-1} | $\Delta 2D / \text{cm}^{-1}$ | D/G ratio |
|--------------------|------------------------------------|-----------------------------|------------------------------------|------------------------------|-----------------|
| FLG | 1584 ± 1 | - | 2711 ± 4 | - | 0.13 ± 0.03 |
| FLG _{NAA} | 1585 ± 1 | +1 | 2716 ± 2 | +5 | 0.21 ± 0.06 |
| FLG _{ME} | 1585 ± 1 | 0 | 2710 ± 4 | -1 | 0.24 ± 0.04 |

4.3.1.2 AFM Imaging

AFM images of the FLG before and after a 6 hour NAA modification, and subsequent transfer to HOPG are given in Figure 4.4. The AFM images of FLG_{NAA} show a dense film that covers most the surface.

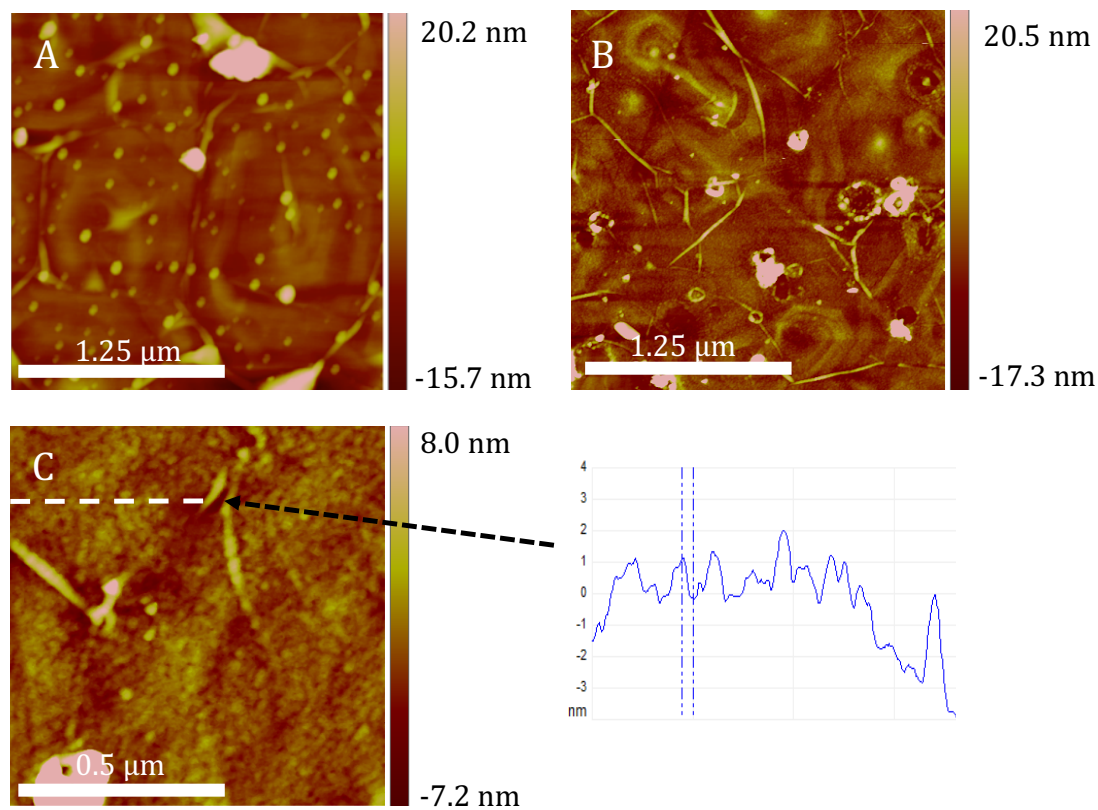


Figure 4.4: AFM images of FLG after transfer to HOPG: (A) before, and (B) and (C) after a 6 hour reaction with NAA. Line profile across (C) also shown.

The line profile across Figure 4.4C indicates the approximate height of each feature is 1 nm. Protrusions caused by residues from the etching process that are seen on the bare sample and the folds caused by trapped water are ignored in these measurements. The measured height is close to that of a single NAA modifier bound to a carbon surface

via two covalent bonds (0.65 nm, calculated using Avogadro software), suggesting monolayer formation. Due to the folded, undulating nature of the FLG on HOPG, this feature height is only approximate. Further, it is not possible to establish if the features are 1 nm higher than the FLG surface, or than a continuous background film and hence scratch testing on modified PPF was used to give a more accurate estimation of film height (see Section 4.3.1.6).

4.3.1.3 IR Spectroscopy

Figure 4.5 shows the IR spectra of FLG on a KBr disk before and after a 6 hour reaction with NAA. The ATR spectrum of NAA is also shown for comparison.

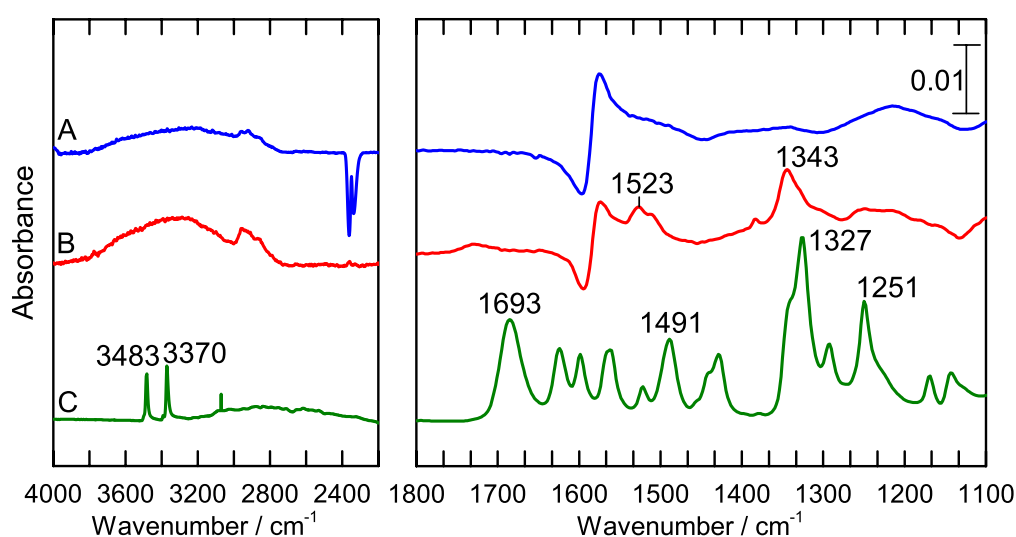


Figure 4.5: Transmission mode IR spectra of FLG on a KBr disk before and after modification with NAA: (A) before and (B) after modification for 6 hours. (C) ATR spectrum of solid NAA precursor (scaled $\times 0.1$). Spectra offset for clarity.

Once again, the FLG shows only the pronounced Fano resonance. After modification, two peaks appear at 1523 and 1343 cm^{-1} , caused by the asymmetric and symmetric stretch modes of the NO_2 group. These peaks have shifted to a higher wavenumber with respect to the NAA precursor. It is assumed this shift is due to the change in substitution pattern.²⁶⁻²⁷ In NAA, the nitro group sits *para* to the amine functionality and *meta* to the carboxylic acid group. However, for the surface bound species, these positions are involved in covalent bonding with the FLG. In the NAA precursor, peaks at 3483 and 3370 cm^{-1} , and 1683 and 1251 cm^{-1} are caused by the amine, and carboxylic acid functionalities respectively. Importantly, these cannot be seen in the FLG_{NAA} spectrum, suggesting that both the amine and carboxylic acid functional groups are lost during the reaction. This supports the mechanism given in Scheme 4.1. Furthermore, no peak attributable to a diazonium functionality can be seen between 2250 and 2350 cm^{-1} ,

which indicates the N_2^+ group formed after treatment of the anthranilic acid with isoamyl nitrite has reacted successfully. The remaining peaks between 1625 and 1100 cm^{-1} in the NAA precursor are believed to be ring deformation modes, and these are too weak to be seen in the FLG_{NAA} spectrum. Full peak assignments for FLG_{NAA} , and NAA were taken from literature reports and are summarised in Table 4.2.

Table 4.2: IR peak assignments for NAA and FLG_{NAA} .²⁸⁻³³

| NAA | FLG_{NAA} | Assignment |
|---------|------------------|--------------------|
| 3483 m | | ν_a (NH) |
| 3370 m | | ν_s (NH) |
| 1683 s | | ν (CO) |
| 1625 s | | Ring deformation |
| 1600 s | | Ring deformation |
| | 1575 s | Fano resonance |
| 1491 s | 1523, 1511 m, db | ν_a (NO_2) |
| 1429 s | | Ring deformation |
| 1327 vs | 1343 s | ν_s (NO_2) |
| 1251 s | | δ (C-OH) |

vs, very strong; s, strong; m, medium; w, weak; db, doublet; ν , stretch mode; δ , bend mode.

Figure 4.6 shows the IR spectra of FLG before and after reaction with ME, as well as the ATR spectrum of the ME precursor.

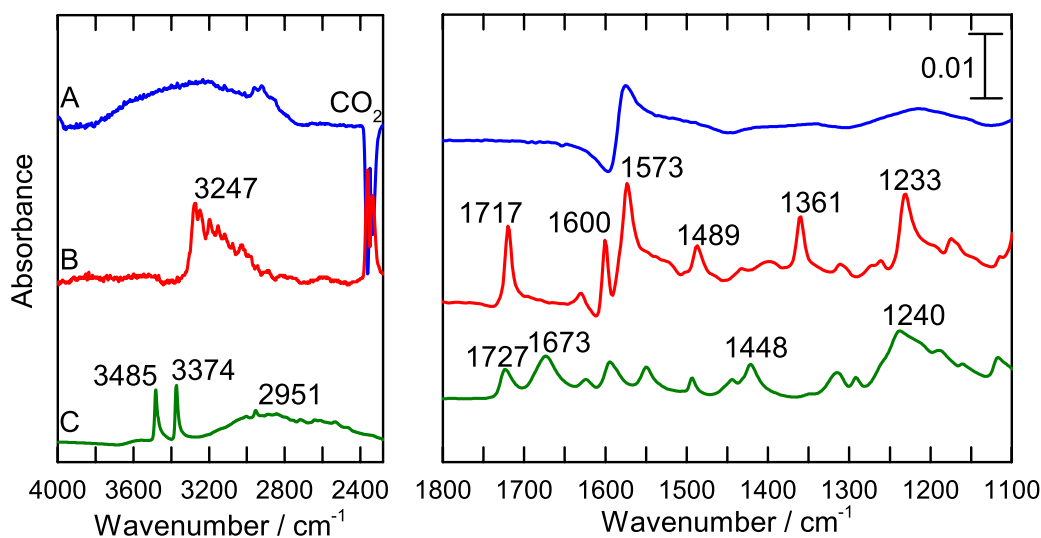


Figure 4.6: Transmission mode IR spectra of FLG on a KBr disk before and after modification with ME: (A) before modification, and (B) after modification for 6 hours. (C) ATR spectrum of solid ME precursor (scaled $\times 0.1$). Spectra offset for clarity.

Like the NAA modifier, in the ME spectrum peaks at 3485 and 3374 cm^{-1} are assigned to the amine group and the strong peak at 1673 cm^{-1} is due to the carboxylic acid functionality. The absence of these in the FLG_{ME} spectrum is strong evidence that the reaction proceeds via the aryne intermediate shown in Scheme 4.1. The lack of any peak associated with the diazonium functionality (2250 to 2350 cm^{-1}) further supports the generation of the aryne intermediate. The strong band at 1727 cm^{-1} in the ME

modifier spectrum, and at 1717 cm^{-1} in the FLG_{ME} spectrum is assigned to the CO group of the methyl ester functionality. The slight shift in position is assumed to be caused by the change in substitution pattern after modification. In the FLG_{ME} spectrum a set of peaks sits around 3247 cm^{-1} . These are assigned to vibrations of the methyl group of the methyl ester functionality. In the ME spectrum, these peaks cannot be seen, possibly because the OH group of the carboxylic acid causes a broad band between 3300 and 2400 cm^{-1} , which envelops any peaks in this region. The remaining peaks are primarily ring deformation modes. The peak assignments for ME and FLG_{ME} were taken from literature and are given in Table 4.3.

Table 4.3: IR peak assignments for ME and FLG_{ME} ^{29-30, 34}

| ME | FLG_{ME} | Assignment |
|------------------|--------------------------|---------------------------------------|
| 3485 m | | ν_{a} (NH) |
| 3374 m | | ν_{s} (NH) |
| | 3247, 3200, 3149 s | CH_3 vibrations |
| 2951 (broad) | | ν (OH) |
| 1727 s | 1717 vs | ν (CO) ester |
| 1673 s | | ν (CO) acid |
| 1596 s | 1600 s | Ring def. + ρ (NH_2) |
| | 1573 vs | Fano resonance |
| 1552 s | | Ring def. + ρ (NH_2) |
| 1495 s | 1489 m | Ring deformation |
| 1448, 1421 m, db | 1438, 1398 w | Ring deformation |
| | 1361 s | Ring deformation |
| 1317 s | | Ring def. + δ (OH) |
| 1290 m | 1300 w | Ring deformation |
| 1240 vs | 1233 vs | Ring def. + ν (C- NH_2) |
| 1115 s | | Ring deformation |

vs, very strong; s, strong; m, medium; w, weak; db, doublet; ν , stretch mode; δ , bend mode, ρ , scissoring mode.

4.3.1.4 XPS Analysis

Although the IR spectroscopy results strongly support the Diels-Alder reaction mechanism outlined in Scheme 4.1, it is important to ensure that grafting is not through the reaction of the aryldiazonium ion. It is possible that the aryldiazonium ion reacts with the FLG surface through the direct attack of the diazonium ion (Chapter 1, Section 1.3.1). In Chapter 3, XPS results indicated that during the reaction of an aryldiazonium salt with FLG, a large concentration of azo nitrogen is generated. Therefore, to determine whether this pathway is operative for the reaction conditions used here, XPS analysis was carried out on the FLG_{ME} surface, to detect any azo nitrogen. Table 4.4 summarises the survey spectra data for FLG, and FLG_{ME} .

Table 4.4: Survey spectra data for FLG, and FLG_{ME}.

| Survey Spectra Atomic % | | | | |
|-------------------------|--------|----------|--------|---------|
| Sample | Carbon | Nitrogen | Oxygen | Silicon |
| FLG | 82.6 | 0.6 | 7.9 | 8.9 |
| FLG _{ME} | 73.2 | 0.6 | 14.5 | 11.7 |

Figure 4.7 shows the survey spectrum, and C 1s and N 1s narrow scans for FLG_{ME}. The equivalent information for FLG is given in Chapter 3, Figure 3.17.

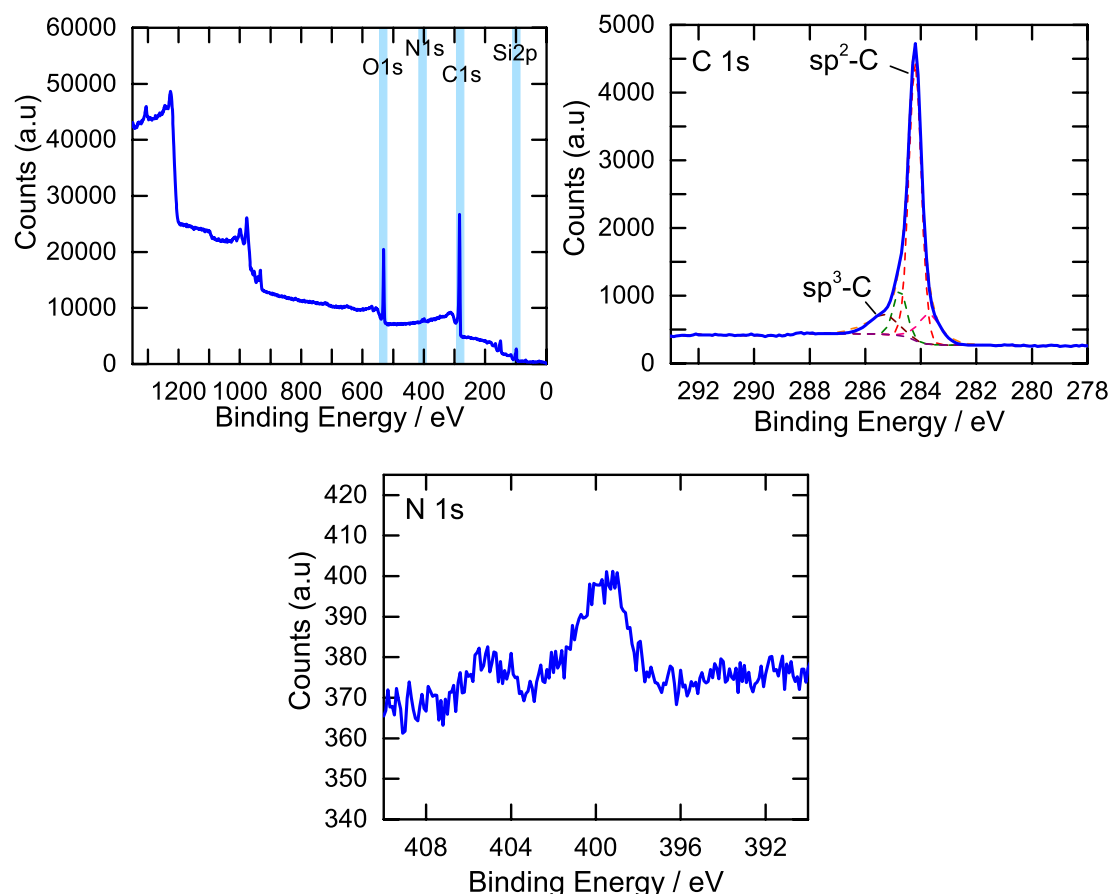


Figure 4.7: XPS spectra for FLG_{ME} after a 6 hour reaction. FLG_{ME} collected on a silicon oxide wafer for analysis. Left to right top: survey spectrum, C 1s narrow scan, and bottom: N 1s narrow scan.

The survey spectrum results indicate that the sample is primarily carbon (73.2%). The small amount of nitrogen (0.6%) seen for both FLG and FLG_{ME} is expected to be caused by adventitious contaminants. The nitrogen content has not changed after modification with ME. This strongly suggests that no azo bonds have formed and hence that the aryldiazonium grafting route is inoperative during this reaction. The C 1s narrow scan shows a strong peak at 284.2 eV. This is caused by the sp²-hybridised carbon of the FLG. A small peak at 285.35 is likely caused by the sp³-hybridised carbon from both defects and carbon atoms involved in grafting. The oxygen content has increased from 7.9% to 14.5% after grafting. Some oxygen will arise from the silicon oxide wafer that

supports the FLG, however the silicon content has only increased by 2.8% after the reaction, suggesting that most of the additional oxygen arises from the methyl ester functionality. These XPS results support the proposed grafting mechanism, as they show no evidence consistent with modification via the aryldiazonium ion intermediate.

4.3.1.5 Electrochemistry

The NAA derivative can be interrogated electrochemically. A typical CV for FLG_{NAA} after a 6 hour reaction is given in Figure 4.8. As described previously (Chapter 3, Section 3.3.2.5), the large peak at -0.51 V is caused by the irreversible reduction of nitrophenyl groups to either aminophenyl or hydroxylaminophenyl groups.³⁵ A second reversible redox couple is at 0.33 V, and is due to the hydroxylaminophenyl /nitrosophenyl system.³⁵ Once again, the surface concentration was calculated using the charge associated with the two redox processes. As the reaction with NAA was always carried out with the FLG supported on copper, the CV was measured with the electroactive groups in the exposed orientation.

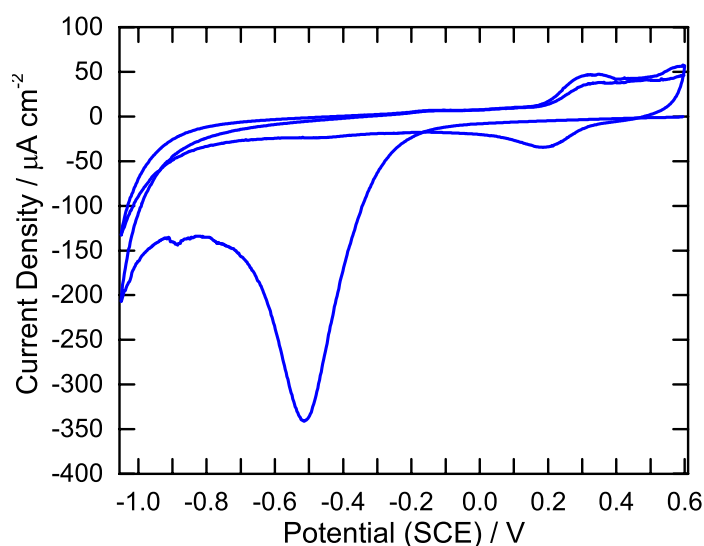


Figure 4.8: CV in 0.1 M H_2SO_4 of FLG_{NAA} on HOPG in the exposed orientation. Scan rate = 200 mV s^{-1} .

The average surface concentration of nitrophenyl groups for the 6 hour reaction was $0.64 \pm 0.12 \text{ nmol cm}^{-2}$ ($n=3$). The surface concentration of a close packed monolayer of nitrophenyl groups on a flat FLG surface is $0.72 \text{ nmol cm}^{-2}$. This was calculated using the molecular footprint of a single nitrophenyl group (0.23 nm^2), assuming free rotation of the nitro group (calculated using Avogadro software).³⁶ Hence, the surface concentration measured for the 6 hour reaction is close to 90% of a closely packed monolayer. The dense film coverage seen via AFM (Figure 4.4) further supports this.

However, the surface concentration of nitrophenyl groups on FLG does not account for any additional surface area resulting from surface roughness. FLG on HOPG has wrinkles and folds, as well as amorphous carbon regions that will increase the surface roughness, and therefore surface area. However, AFM image analysis (using the roughness tool on Nanoscope analysis) of unmodified FLG indicated that the average difference between the geometric working electrode area used for surface concentration calculations and the imaged surface area was $> 1\%$ thus this is not expected to significantly impact the surface concentration calculation.

The surface concentration of nitrophenyl groups on the FLG_{NAA} samples was found to be dependent on reaction time, as illustrated by Figure 4.9 (calculated values given in Appendix B, Section B.3). The surface concentration initially increases with reaction time reaching a plateau around 2 hours. To ensure this plateau is the maximum attainable surface concentration for this reaction and not simply the maximum concentration of electrochemically accessible nitrophenyl groups within the film, the surface concentration was measured for a FLG_{NAA} surface with a second FLG sheet sandwiching the film. The surface concentration found in this orientation was $0.52 \text{ nmol cm}^{-2}$, the same within error of the maximum surface concentration shown in Figure 4.9. It is therefore assumed that when the measured surface concentration reaches a maximum, the nitrophenyl groups have saturated all available bonding sites on the FLG surface.

Computational studies have suggested that the maximum degree of functionalisation for a 4×4 unit cell of graphene is one benzyne group is bonded per 4 carbon atoms,³⁷ however experimentally only a maximum functionalisation of 1 group per 17 carbon atoms has been achieved, measured using thermogravimetric analysis.²² In this work, a degree of functionalisation of 1 group per 14 carbon atoms was calculated, based on the unit cell of graphene and the measured surface concentration, within error of the value calculated by Ma et al.²² This functionalisation limit is suggested to be caused by steric hindrance and bonding interactions.³⁷

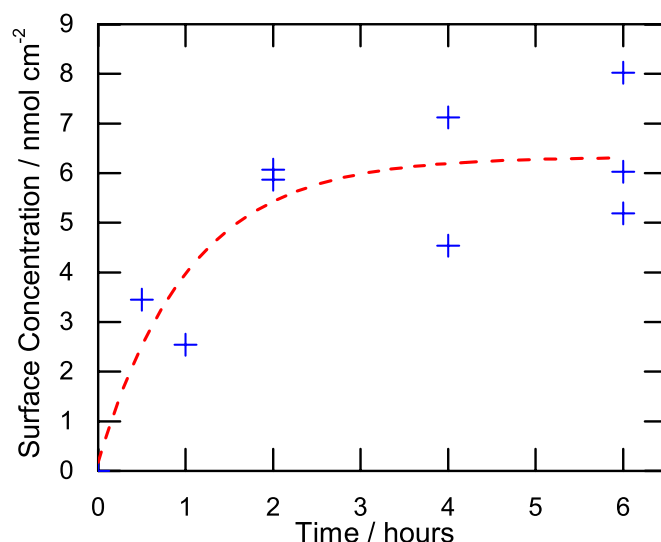


Figure 4.9: Nitrophenyl surface concentration with increasing reaction time for the reaction of FLG with NAA. Red dashed line indicates exponential fit of the data.

4.3.1.6 PPF Scratch Testing and Electrochemistry

The experimental results presented suggest that the modification of FLG with an anthranilic acid is limited to a monolayer. However, the most reliable method for determining whether a mono- or multilayer film has formed is through film thickness measurements. Hence the reaction was repeated on PPF and the film thickness measured using the AFM scratching method. PPF is a predominantly edge plane material and is very flat (roughness < 0.5 nm) and sufficiently hard that it is typically not scratched to any large extent during scratch testing.^{35, 38} PPF was modified in the same manner as FLG using the NAA derivative. A CV for the PPF_{NAA} surface is given in Figure 4.10.

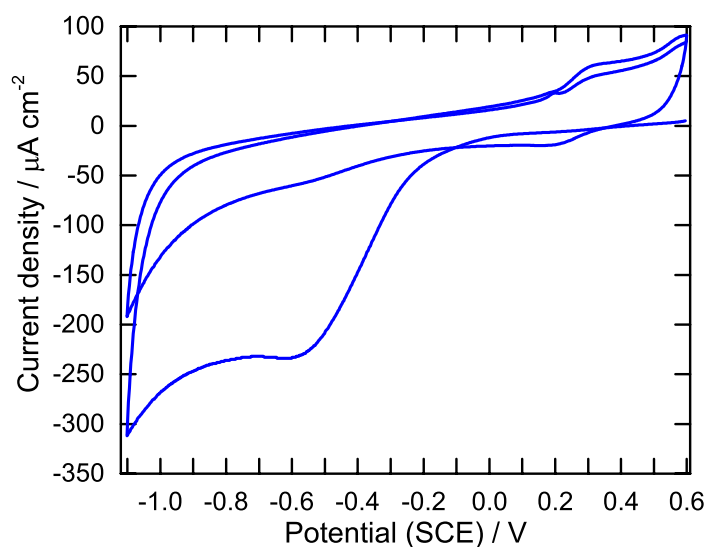


Figure 4.10: CV in 0.1 M H₂SO₄ of PPF_{NAA}. Scan rate = 200 mV s⁻¹.

The presence of the characteristic nitrophenyl redox processes confirms that this reaction can be applied to predominantly edge plane carbon materials such as PPF. The surface concentration of nitrophenyl groups on PPF was $0.55 \pm 0.11 \text{ nmol cm}^{-2}$ ($n=3$) after a 2 hour reaction, which is the same, within experimental uncertainty, as the limiting concentration shown in Figure 4.9. This suggests the mechanism for the reaction is consistent between edge and basal plane graphitic carbons.

AFM tip scratching is a very reliable way to determine film thickness. An AFM image of PPF modified via a 2 hour reaction, with a section of the film scratched away can be seen in Figure 4.11.

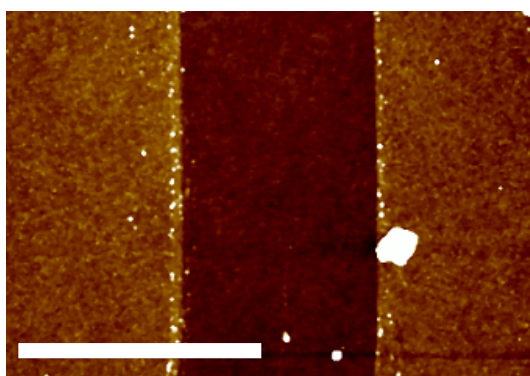


Figure 4.11: AFM tip scratch on PPF_{NAA} after a 2 hour reaction. Scale bar = 2 μm .

The average, blank corrected height was $0.9 \pm 0.4 \text{ nm}$. For this average, twelve box profiles were taken from two different scratches on two PPF_{NAA} samples (Chapter 2, Section 2.6.6). The blank scratch height ($0.6 \pm 0.15 \text{ nm}$) was measured from a PPF surface that was refluxed for 2 hours in 1,2-dichloroethane and isoamyl nitrite only. The height of a single NAA modifier bonded to a carbon surface via two bonds is approximately 0.65 nm (calculated via Avogadro software).³⁶ This means the film height measured here is within monolayer thickness, strongly supporting that the reaction of an anthranilic acid with graphitic carbons gives a monolayer film on the surface.

One interesting feature of this reaction is it provides a densely-packed monolayer on PPF. As explained in Section 4.1.1, several aryldiazonium ion based protocols exist for obtaining monolayer coverage on carbon surfaces, however they typically provide a low surface coverage. For instance, the protection-deprotection strategy described only provides surface concentrations of 0.14 to $0.28 \text{ nmol cm}^{-2}$ on GC,¹² while the radical

scavenger based route is able to give slightly higher surface concentrations of 0.3 to 0.4 nmol cm⁻² on PPF.¹⁰ The highest surface concentration available from the existing diazonium based methods is approximately 0.9 nmol cm⁻², from the ionic liquid approach.⁷ This surface concentration was measured on GC, which is a much rougher substrate than PPF, and a typical roughness correction factor of two can be applied to the GC surface concentration giving a surface concentration of 0.45 nmol cm⁻² on PPF. Furthermore, the preparation of monolayers by this method relied on the low diffusion rates of aryldiazonium ions in ionic liquids, suggesting there is no intrinsic reason for multilayer growth to be prohibited.^{10, 40} This means that the anthranilic acid method presented here can give a more density-packed monolayer film on PPF than previously reported methods, which may be beneficial for some applications.

4.3.1.7 Grafting Mechanism

Both FLG and PPF have been successfully modified using the reaction of an anthranilic acid. The most likely mechanism is that the aryne generated from the anthranilic acid after treatment with isoamyl nitrite undergoes a cycloaddition reaction with the FLG (or PPF). From the IR and XPS results, the aryldiazonium grafting mechanism can be discounted due to the lack of azo bonds in the film structure. Furthermore, AFM and electrochemistry results confirm monolayer formation and aryldiazonium salts are expected to give disordered multilayer films.⁴¹ The inhibition of the diazonium ion reaction pathway was expected due to steric hindrance from the carboxylic acid group. Podvorica et al.⁴² reported that an ethyl group *ortho* to the diazonium functionality completely prevented grafting to the surface, therefore it is assumed that the *ortho* carboxylic acid group will have a similar effect. Aryne intermediates are also able to undergo nucleophilic addition⁴³ and sigma bond insertion reactions, and any oxygen containing groups at the FLG or PPF surface could provide potential sites for these reactions.⁴⁴ As the concentration of oxygen at the surface of both FLG and PPF is low (> 5%), these reactions can be excluded as a major contributor to the surface grafting. The Diels-Alder cycloaddition reaction is a [4+2] cycloaddition reaction, that will give two covalent bonds from the modifier to the FLG surface, forming a six-membered ring. Although this is the pathway assumed to be occurring, computational studies have demonstrated that the [2+2] cycloaddition product (a four membered ring) is also stable for the reaction of graphene with benzyne, whereas a [3+2] cycloaddition is energetically unfavourable.^{37, 45} Furthermore, Simon et al.⁴⁶ used STM to demonstrate that both [4+2] and [2+2] cycloaddition reactions can occur on epitaxial graphene on a

silicon carbide substrate, when using a fluorinated maleimide derivative as the dienophile. The [4+2] and [2+2] cycloaddition mechanism are also possible on edge plane materials such as PPF, and would be most favourable at armchair edges. Both the [4+2] and [2+2] cycloaddition reactions will give two bonds to the carbon surface, which may result in a more strongly adhered film than the aryldiazonium reaction that only gives a single covalent bond to the surface. The presence or absence of two bonds to the FLG or PPF surface will be the subject of further investigation by collaborators, using surface enhanced Raman spectroscopy.

4.3.2 Characterisation of FLG Modified with a Primary Amine

The two reactions considered thus far, grafting from aryldiazonium ions and anthranilic acids, generated dense films that covered the entire surface of the FLG. The amines used were shown in Figure 4.2 and reaction conditions are described in Chapter 2, Section 2.4.3. The non-nucleophilic base, diisopropylethylamine, was added to the reaction mixture, selected based on previous work.¹⁷ This amine is used because it is a good base, but poor nucleophile, due to the tertiary nitrogen atom, so will not take part in amine addition reactions.

4.3.2.1 Raman Spectroscopy

The Raman spectra for FLG and FLG_{NPEA} after a 20 hour reaction are given in Figure 4.12. Once again, the G-, 2D-, and D-bands can be clearly seen. The D/G band intensity ratio for the FLG_{NPEA} is 0.12 ± 0.01 , which is within error of the D/G band intensity ratio of the unmodified FLG (0.13 ± 0.03). The D/G band intensity ratio is related to the number of defects within the FLG lattice, and hence it appears that the number of defects (and specifically sp^3 -hybridised carbons) is not affected by the reaction with NPEA. As explained in Section 4.1.2, two plausible mechanisms exist for this reaction. If the amine precursor is interacting with the FLG via partial intercalation, then no changes are expected in the Raman spectrum as this mechanism does not require covalent bond formation and therefore the introduction of defects. Furthermore, the spontaneous addition reaction is expected to target defective, oxygen containing regions, which may have already activated the D-band in the Raman spectrum.⁴⁷⁻⁴⁸ Hence, it is plausible that covalent modification of these sites will not alter the overall intensity of the D-band.

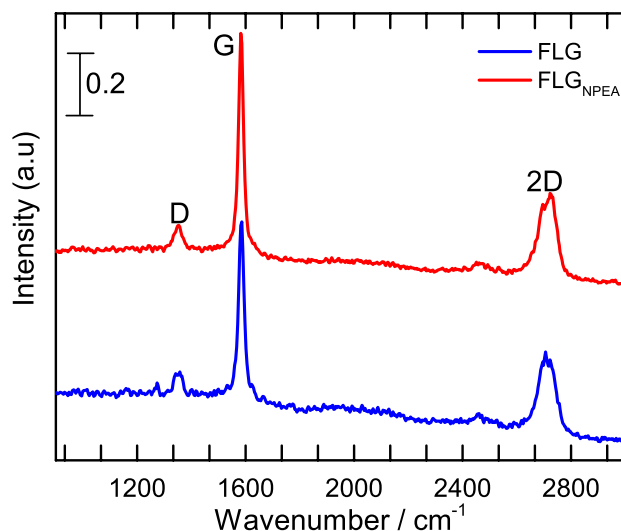


Figure 4.12: Raman spectra of FLG on a gold wafer, before and after a 20 hour reaction with NPEA. Spectra normalised to give a G band intensity of 1. Spectra offset for clarity.

Table 4.5 summarises the G and 2D peak positions for FLG_{NPEA} . The G and 2D bands have not shifted significantly after modification. This suggests that any modifier groups residing at the surface are unable to effectively dope the FLG. As this reaction is expected to be limited to the edges and defects, there may be too few NPEA groups to significantly dope the FLG. Raman spectroscopy was therefore unable to provide evidence for either mechanism, or for modification of FLG, and hence further characterisation was undertaken. Raman spectroscopy was carried out for the NPEA modifier only.

Table 4.5: G and 2D band peak positions for FLG and FLG_{NPEA} after a 20 hour reaction.

| Sample | G-band position / cm^{-1} | $\Delta\text{G} / \text{cm}^{-1}$ | 2D-band position/ cm^{-1} | $\Delta\text{2D} / \text{cm}^{-1}$ | D/G ratio |
|----------------------------|------------------------------------|-----------------------------------|------------------------------------|------------------------------------|-----------------|
| FLG | 1584 ± 1 | - | 2711 ± 1 | - | 0.13 ± 0.03 |
| FLG_{NPEA} | 1583 ± 1 | -2 | 2711 ± 1 | 0 | 0.12 ± 0.01 |

4.3.2.2 AFM Imaging

Figure 4.13 shows selected AFM images of FLG after reaction with NPEA and AAQ. The reaction was done with copper supported FLG, so that the modified FLG could be collected onto HOPG in the exposed orientation for imaging. Figure 4.13A and B show the FLG surface immediately after modification with NPEA and transfer to HOPG. Small protrusions can be seen scattered across the FLG surface, at a much lower density than for the aryldiazonium and Diels-Alder reactions. The approximate height of each group was 1.2 ± 0.6 nm, which is within error of the height of a single group (0.96 nm, calculated using Avogadro software). Figure 4.13C and D show FLG after reaction with AAQ. Protrusions can be seen across the surface, and the height of each is

approximately 2.2 ± 0.7 nm. This is higher than the expected height of a single modifier (1.1 nm, calculated using Avogadro software), which implies each feature represents more than a single AAQ group, however as with previous AFM images, the folded nature of the underlying graphene means these feature heights are only approximate.

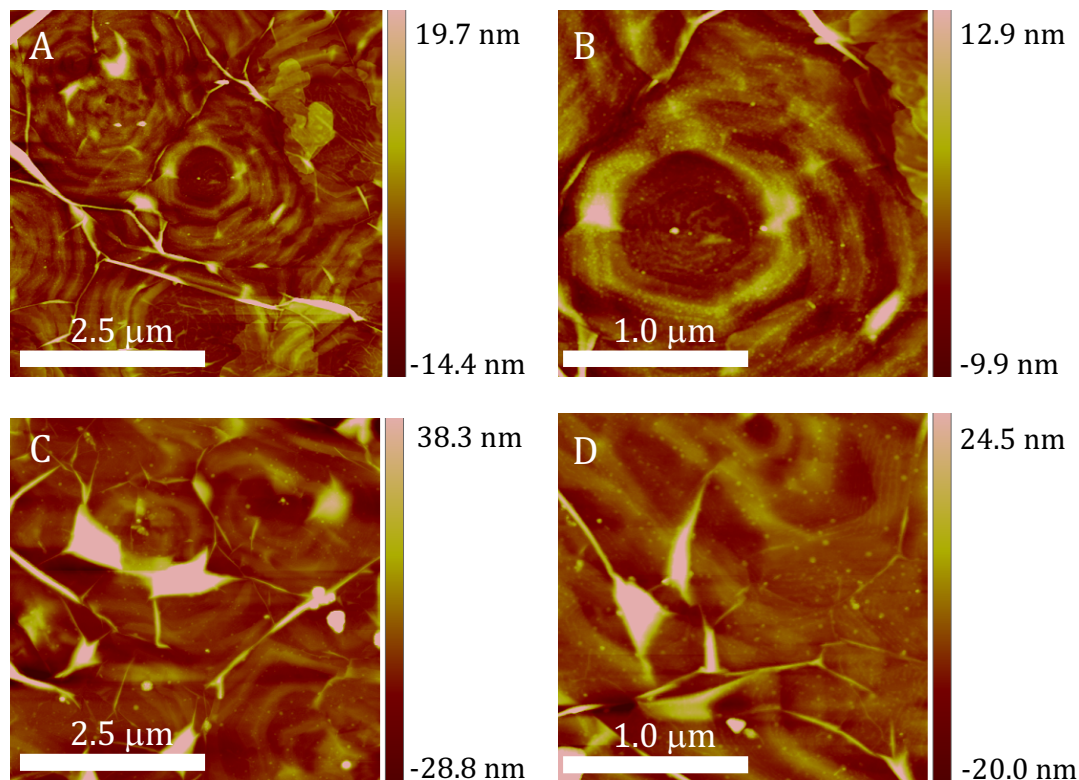


Figure 4.13: AFM images of FLG on HOPG: (A) and (B) after a 17 hour reaction with NPEA, and subsequent methanol wash; (C) and (D) after a 16 hour reaction with AAQ, and subsequent methanol wash.

4.3.2.3 IR Spectroscopy

FLG after modification with NPEA and AAQ was also characterised using IR spectroscopy. The modified FLG_{NPEA} was collected onto a KBr disk for spectral acquisition (Figure 4.14). The spectrum of the precursor, NPEA, is also included for comparison. Peaks at 1520 and 1341 cm^{-1} in the NPEA spectrum, and 1515 cm^{-1} and 1354 cm^{-1} in the FLG_{NPEA} spectra, correspond to the asymmetric and symmetric stretch modes of the NO_2 group. These peaks have shifted slightly upon modification, possibly due to the change in substitution pattern. The weak peak at 1623 cm^{-1} in the NPEA spectrum is caused by a NH_2 bending vibration, this peak is not seen in the FLG_{NPEA} spectrum, however may be obscured by the large Fano resonance. Peaks at 2906 and 2816 cm^{-1} both the NPEA and FLG_{NPEA} spectra are assigned to the CH stretch modes of the ethylamine group. The primary amine NH stretch modes typically result in peaks between 3000 and 3400 cm^{-1} , however no peaks can be seen for either NPEA or

FLG_{NPEA}, and they are possibly enveloped by the CH stretch mode. The peak at 1502 cm⁻¹ in the NPEA spectrum is due to a CH₂ bending vibration of the ethyl chain. A weak broad band at 1506 cm⁻¹ in the FLG_{NPEA} spectra could also be due to this vibration, however a similar weak broad band can be seen at ~1500 cm⁻¹ in the FLG spectrum, so it is not possible to definitively assign this band. Table 4.6 gives the full peak assignments for this modification.^{16, 49-52}

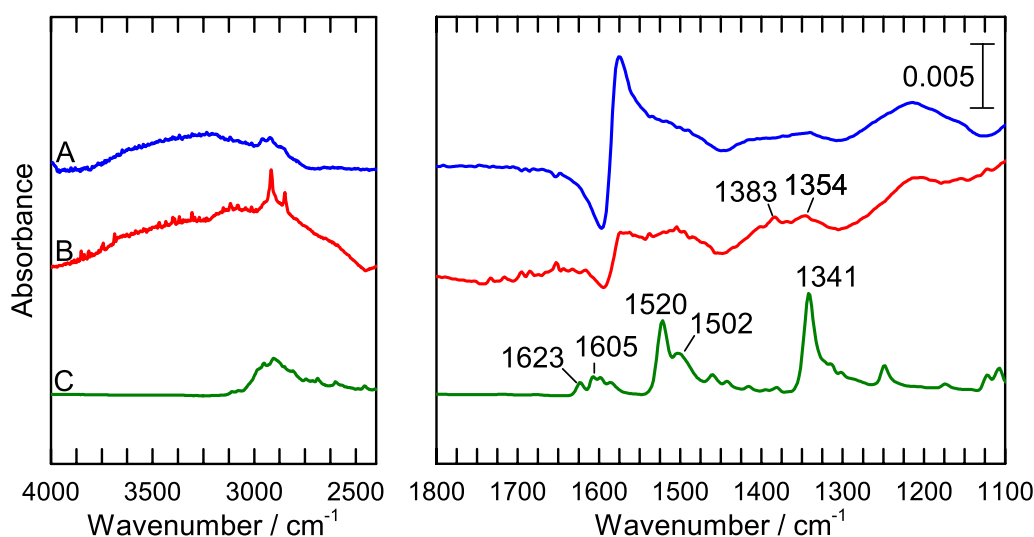


Figure 4.14: Transmission mode IR spectra of FLG before (A) and after (B) modification with NPEA, with a subsequent methanol wash. ATR spectrum of NPEA precursor (C) is also shown (scaled $\times 0.02$). Spectra offset for clarity.

Table 4.6: IR peak assignments for NPEA and FLG_{NPEA}.

| NPEA | FLG _{NPEA} | Assignment |
|--------------|---------------------|-----------------------------|
| 2906, 2816 m | | ν (CH ₂) |
| 1623 w | | δ (NH ₂) |
| 1605 m | | ν (C=C) |
| 1520 vs | 1515 w | ν_a (NO ₂) |
| 1502 s | | δ (CH ₂) |
| 1461 w | | Ring deformation |
| 1441 w | | Ring deformation |
| 1418 w | | Ring deformation |
| 1341 vs | 1354 s | ν_s (NO ₂) |
| 1248 m | | ν (C-C) |

vs, very strong; s, strong; m, medium; w, weak; db, doublet; ν , stretch mode; δ , bend mode.

Figure 4.15 shows the IR spectra for FLG before and after modification with AAQ. A summary of these peak assignments is given in Table 4.7.⁵³⁻⁵⁶ Peaks at 3426 and 3318 cm⁻¹ in the AAQ spectrum are assigned to the NH stretch modes. Equivalent peaks cannot be seen in the FLG_{AAQ} spectrum, but these may be covered by the broad band between 3800 and 2700 cm⁻¹, assumed to be caused by trapped water. A weak peak at 1347 cm⁻¹ can be seen in the FLG_{AAQ} spectra, which is assigned to the CN stretch

vibration that is also seen in the AAQ precursor. The other peaks at 1301 and 1274 cm^{-1} in the precursor are difficult to discern in the FLG_{AAQ} spectra due to the KBr background.

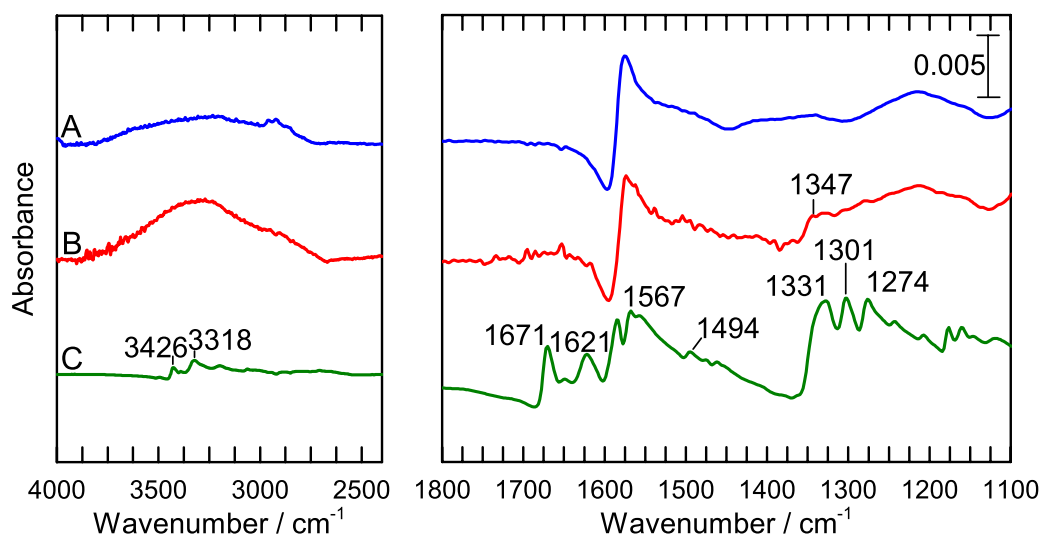


Figure 4.15: Transmission mode IR spectra of FLG before (A) and after (B) modification with AAQ, with a subsequent methanol wash. ATR spectrum of AAQ precursor (C) is also shown (scaled $\times 0.03$). Spectra offset for clarity.

Table 4.7: IR peak assignments for AAQ and FLG_{AAQ} .

| AAQ | FLG_{AAQ} | Assignment |
|--------------|---------------------------|-----------------------------------|
| 3426, 3318 w | | $\nu(\text{NH}_2)$ |
| 1671 s | | $\nu(\text{C}=\text{O})$ |
| 1621 m | | $\delta(\text{NH}_2)$ |
| 1584 m | | Ring deformation |
| 1567 s | | Ring deformation |
| 1494 w | | Ring deformation |
| 1331 vs | 1347 w | $\nu(\text{CN})$ |
| 1301 vs | | $\nu(\text{CO}) + \nu(\text{CC})$ |
| 1274 vs | | $\nu(\text{CO}) + \nu(\text{CC})$ |

vs, very strong; s, strong; m, medium; w, weak; db, doublet; ν , stretch mode; δ , bend mode.

4.3.2.4 Electrochemistry

FLG_{NPEA} and FLG_{AAQ} were interrogated electrochemically. For electrochemistry, the modified FLG was collected onto HOPG in the sandwiched orientation. A typical CV of FLG_{NPEA} is given in Figure 4.16. Once again, the large irreversible reduction peak at -0.61 V corresponds to the six electron, six proton reduction of nitrophenyl groups to aminophenyl groups, and the four electron, four proton reduction of nitrophenyl groups to hydroxylaminophenyl groups. The second broad redox system at approximately 0.3 V corresponds to the hydroxylaminophenyl/nitrosophenyl system.³⁵ Surface concentration values were calculated from the charge associated with these processes.

The surface concentration ranged from 0.11 nmol cm⁻² for a 4 hour reaction to 0.4 nmol cm⁻² for a 25 hour reaction.

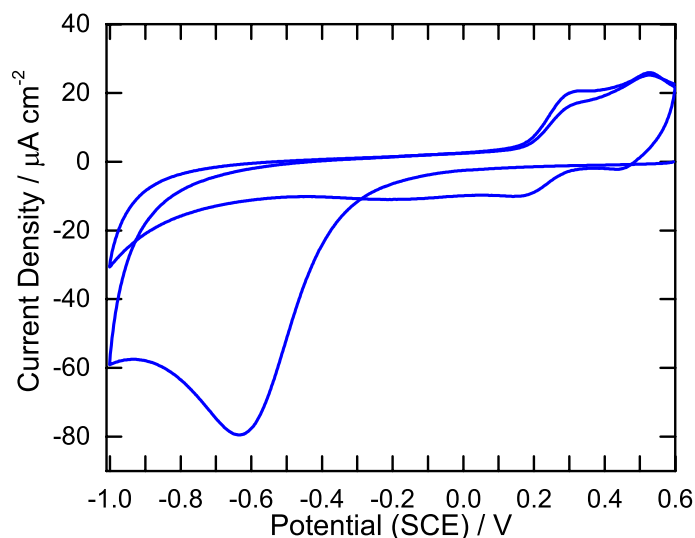
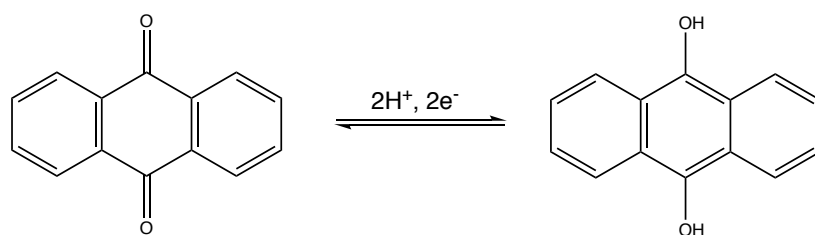


Figure 4.16: CV in 0.1 M H₂SO₄ of FLG_{NPEA} after a 17 hour reaction. Sample collected onto HOPG in the sandwiched orientation and washed with methanol prior to analysis. Scan rate = 200 mV s⁻¹.

Figure 4.17 gives the CV for a FLG_{AAQ} sample on HOPG after a 17 hour reaction. The FLG_{AAQ} CV shows a broad reduction peak and an associated oxidation peak. The reduction peak is due to the two proton, two electron reduction of the anthraquinone to the equivalent anthracenediol, and the oxidation peak is arises from the reverse process (Scheme 4.3).⁵⁷⁻⁵⁹ This response is similar to that reported by Belanger et al. for activated carbon modified with anthraquinone groups; the additional small oxidation peaks that can be seen above 0 V were attributed to anthraquinone molecules whose oxygen functionalities are involved in hydrogen bonding between two closely packed molecules, which would cause the oxidation to occur at slightly higher potentials.⁵⁷



Scheme 4.3: Two proton, two electron redox process of anthraquinone.

Using the charge associated with the reduction peak, the surface concentration of anthraquinone groups was calculated. This ranged from 0.21 nmol cm⁻² for a 4 hour reaction to 0.45 nmol cm⁻² for a 17 hour reaction. The surface concentration for the AAQ reaction is the same, within experimental uncertainty, as the NPEA reaction. This result was unexpected, as alkyl amines are more nucleophilic than aromatic amines,

therefore expected to be more reactive. However, the aromatic 2-aminoanthraquinone molecules would be more susceptible to physisorption to the graphene surface, which may lead to higher than expected surface concentrations.

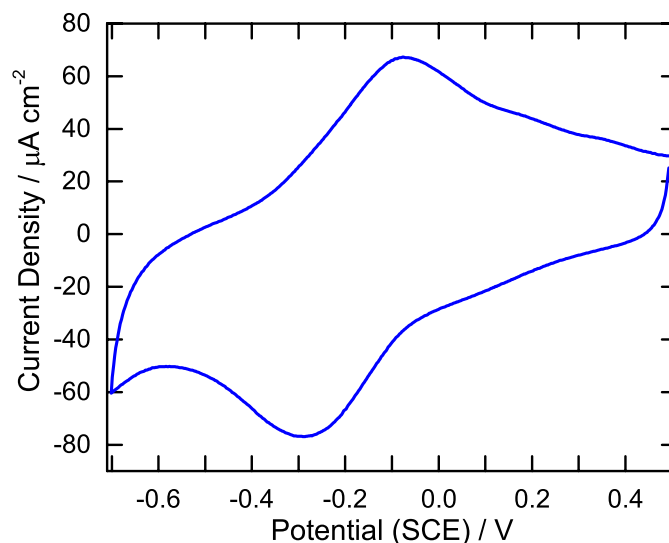


Figure 4.17: CV in 0.5 M H₂SO₄ of FLG_{AAQ} after a 17 hour reaction. Sample collected onto HOPG in the sandwiched orientation and washed with methanol prior to analysis. Scan rate = 200 mV s⁻¹.

4.3.2.5 Physisorption Studies

AFM, IR spectroscopy, and electrochemistry results all suggest the presence of a modifier at the FLG surface after modification with a primary amine, however these methods cannot confirm if the film is simply physisorbed. Typically, Raman spectroscopy is used to confirm covalent bonding to graphene, but results described in Section 4.3.2.1 showed no change in the D/G band intensity ratio for this reaction, which may be due to the edge/defect specific nature of the reaction. To confirm the results are not due to physisorption of the modifier, the protocol was repeated using an analogue of both NPEA and AAQ that did not contain a primary amine functional group. Nitrotoluene was used as a NPEA analogue to give FLG_{NT, Physi.} and anthraquinone-2-sulfonic acid sodium salt was used as an AAQ analogue to give FLG_{AS, Physi.} The structures of these two precursors are given in Figure 4.18. For the physisorption tests, FLG was floated on a 50 mM DMF/diisopropylethylamine solution of each physisorption analogue for 20 hours, then washed in the same manner as the amine modified samples.

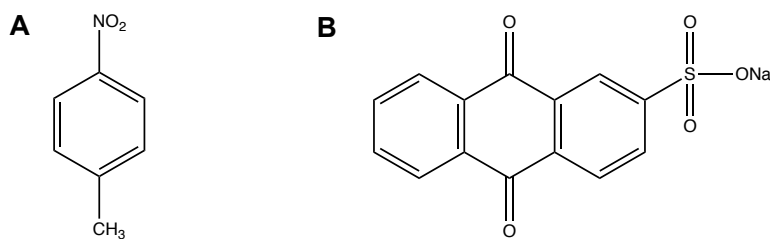


Figure 4.18: Physisorption analogues: (A) nitrotoluene, and (B) anthraquinone-2-sulfonic acid sodium salt.

The IR spectra for FLG_{NPEA} and FLG_{NT, Physi.}, and of FLG_{AAQ} and FLG_{AS Physi.}, are given in Figure 4.19A and B respectively.

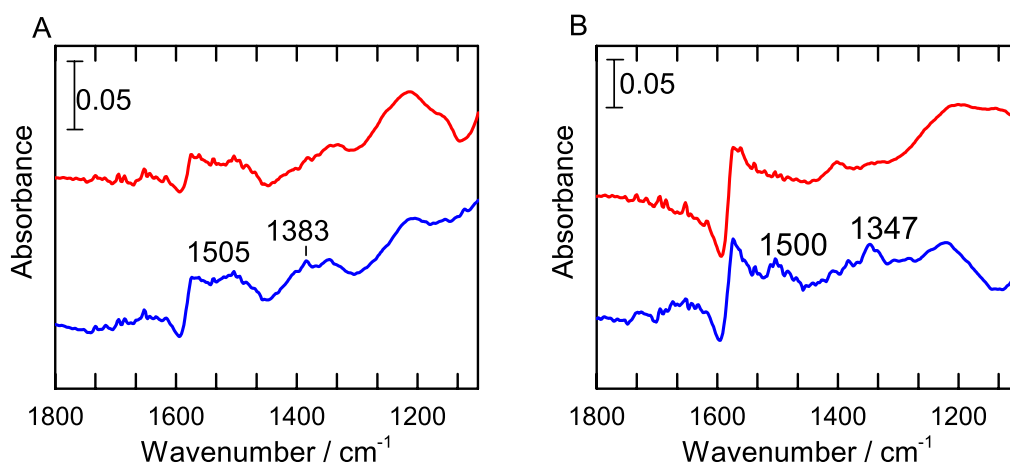


Figure 4.19: Transmission mode IR spectra recorded on a KBr disk of: (A) FLG_{NPEA} (blue) and FLG_{NT Physi.} (red); (B) FLG_{AAQ} (blue) and FLG_{AS Physi.} (red). Samples washed with methanol prior to acquisition. Spectra offset for clarity.

In Figure 4.19A, a small peak corresponding to the symmetric nitro stretch can be seen at 1354 cm⁻¹ in the FLG_{NPEA} spectrum. This peak can also be seen in the FLG_{NPEA Physi.} spectrum, but at a much lower absorbance, suggesting that this peak is not solely a result of physisorption for FLG_{NPEA}. In Figure 4.19B, the absence of the peak at 1347 cm⁻¹ in the physisorption spectrum suggests the appearance of such peaks in the FLG_{AAQ} spectrum is due not due to physisorbed groups.

Figure 4.20A shows CVs for FLG_{NPEA} and FLG_{NT Physi.}, and B shows CVs for FLG_{AAQ} and FLG_{AS Physi.}. Only a very small nitro reduction peak can be seen for the FLG_{NT Physi.} sample, which is significantly smaller than the nitro reduction peak for FLG_{NPEA}. The surface concentration calculated for FLG_{NT Physi.} is 0.007 nmol cm⁻². This indicates that physisorption makes up approximately 2% of the total measured surface concentration. Similarly, only a very small oxidation and reduction peak can be seen for the FLG_{AS Physi.} sample. The surface concentration was 0.06 nmol cm⁻², suggesting

physisorption is responsible for 14% of the total FLG_{AAQ} surface concentration. Physisorption is expected to be more prevalent for the AAQ system as this modifier has multiple aromatic rings that can participate in strong Van der Waals interactions with the graphene. The results from these physisorption studies indicate that the washing steps implemented for this modification method are sufficient to remove most physisorbed material from the surface. This therefore supports the successful modification of FLG with primary amines.

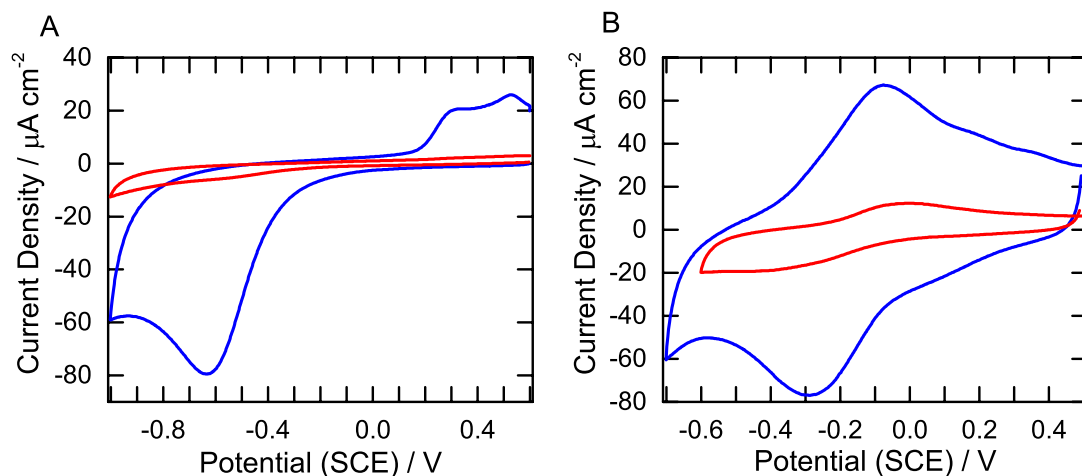


Figure 4.20: Physisorption CVs: (A) FLG_{NPEA} (blue) and FLG_{NT Physi.} (red) in 0.1 M H₂SO₄; (B) FLG_{AAQ} (blue) and FLG_{AS Physi.} (red) in 0.5 M H₂SO₄. Scan rate = 200 mV s⁻¹.

4.4 Conclusion

In summary, FLG has been modified using two alternative methods: the Diels-Alder reaction using an anthranilic acid precursor, and the reaction of a primary amine. The Diels-Alder reaction was successful in providing a dense monolayer film on the surface of both FLG and PPF. Two different precursors were used, indicating this reaction pathway is viable for a range of different modifiers. Based on the reaction mechanism and experimental evidence presented, it is believed this reaction results in each modifier being bound to the surface via two covalent bonds. Confirmation of this bonding mechanism requires further investigation. The two films grafted to the FLG can be used for further surface chemistry. The nitro can be reduced to an amine, while the methyl ester can be hydrolysed to a carboxylic acid, both these groups can then take part in additional coupling reactions such as amide bond formation.

The FLG was also successfully modified using a primary amine. Two possible mechanisms were postulated for this reaction: either partial intercalation of the modifier at edges and defects, or the Michael-type addition at oxygen containing sites.

Physisorption studies confirm that changes to the FLG after the reaction are not simply caused by physisorption of the modifier to the FLG surface. It seems unlikely that the Michael addition reaction is the sole modification mechanism as oxygen groups are required for this reaction. A low concentration of oxygen containing groups was detected on the FLG (4.64%) giving an oxygen to carbon ratio of 0.04. On GC, where the primary modification mechanism is reported to be the Michael addition reaction, a surface concentration of $0.22 \pm 0.02 \text{ nmol cm}^{-2}$ was obtained after a 16 hour reaction in DMF, which is lower than the surface concentration obtained on FLG for a similar reaction time. As GC has a higher oxygen to carbon ratio (0.07), a higher surface concentration would be expected on GC compared with FLG if the Michael addition reaction is the only modification pathway, as there are more oxygen containing sites. Further experimental investigation is required to confirm if partial intercalation of the amine modifier is the primary modification mechanism. One possible option is to use Li^+ ion intercalation electrochemistry studies, like those used by Compton et al.¹⁹ Here, non-aqueous electrochemistry was carried out with either lithium perchlorate or tetrabutylammonium perchlorate as the electrolyte. In lithium perchlorate, the nitrophenyl reduction peaks were well defined, while in tetrabutylammonium perchlorate electrolyte they were not. The lithium perchlorate was suggested to give a better response because the lithium ions can easily intercalate between the graphite sheets, and therefore access the nitrobenzylamine modifier, while the bulky tetrabutylammonium cations are larger therefore cannot intercalate between the sheets and easily access the nitrobenzylamine molecules.

4.5 References

1. Farquhar, A. K.; Fitchett, C. M.; Dykstra, H. M.; Waterland, M. R.; Brooksby, P. A.; Downard, A. J., Diels-alder reaction of anthranilic acids: A versatile route to dense monolayers on flat edge and basal plane graphitic carbon substrates. *ACS Appl. Mater. Interfaces* **2016**, *8*, 23389-23395.
2. Magedov, I. V.; Frolova, L. V.; Ovezmyradov, M.; Bethke, D.; Shaner, E. A.; Kalugin, N. G., Benzyne-functionalized graphene and graphite characterized by raman spectroscopy and energy dispersive x-ray analysis. *Carbon* **2013**, *54*, 192-200.
3. Lebègue, E.; Brousse, T.; Gaubicher, J.; Cougnon, C., Chemical functionalization of activated carbon through radical and diradical intermediates. *Electrochem. Commun.* **2013**, *34*, 14-17.
4. Combellas, C.; Kanoufi, F.; Pinson, J.; Podvorica, F. I., Sterically hindered diazonium salts for the grafting of a monolayer on metals. *J. Am. Chem. Soc.* **2008**, *130*, 8576-8577.
5. Combellas, C.; Jiang, D.-e.; Kanoufi, F.; Pinson, J.; Podvorica, F. I., Steric effects in the reaction of aryl radicals on surfaces. *Langmuir* **2008**, *25*, 286-293.
6. Mattiuzzi, A.; Jabin, I.; Mangeney, C.; Roux, C.; Reinaud, O.; Santos, L.; Bergamini, J.-F.; Hapiot, P.; Lagrost, C., Electrografting of calix [4] arenediazonium salts to form versatile robust platforms for spatially controlled surface functionalization. *Nat. Commun.* **2012**, *3*, 1130.
7. Carvalho Padilha, J.; Noël, J. M.; Bergamini, J. F.; Rault-Berthelot, J.; Lagrost, C., Functionalization of carbon materials by reduction of diazonium cations produced *in situ* in a brønstedt acidic ionic liquid. *ChemElectroChem* **2016**.
8. Ghilane, J.; Martin, P.; Fontaine, O.; Lacroix, J.-C.; Randriamahazaka, H., Modification of carbon electrode in ionic liquid through the reduction of phenyl diazonium salt. Electrochemical evidence in ionic liquid. *Electrochem. Commun.* **2008**, *10*, 1060-1063.
9. Menanteau, T.; Levillain, E.; Breton, T., Electrografting via diazonium chemistry: From multilayer to monolayer using radical scavenger. *Chem. Mater.* **2013**, *25*, 2905-2909.
10. Menanteau, T.; Levillain, E.; Downard, A. J.; Breton, T., Evidence of monolayer formation via diazonium grafting with a radical scavenger: Electrochemical, AFM and XPS monitoring. *Phys. Chem. Chem. Phys.* **2015**, *17*, 13137-13142.
11. Menanteau, T.; Dias, M.; Levillain, E.; Downard, A. J.; Breton, T., Electrografting via diazonium chemistry: The key role of the aryl substituent in the layer growth mechanism. *J. Phys. Chem. C* **2016**, *120*, 4423-4429.
12. Lee, L.; Gunby, N. R.; Crittenden, D. L.; Downard, A. J., Multifunctional and stable monolayers on carbon: A simple and reliable method for backfilling sparse layers grafted from protected aryldiazonium ions. *Langmuir* **2016**.
13. Klanderman, B. H.; Criswell, T. R., Reactivity of benzyne toward anthracene systems. *J. Org. Chem.* **1969**, *34*, 3426-3430.

14. Biermann, D.; Schmidt, W., Diels-alder reactivity of polycyclic aromatic hydrocarbons. 1. Acenes and benzologs. *J. Am. Chem. Soc.* **1980**, *102*, 3163-3173.
15. Zade, S. S.; Bendikov, M., Reactivity of acenes: Mechanisms and dependence on acene length. *J. Phys. Org. Chem.* **2011**, *25*, 452-461.
16. Gallardo, I.; Pinson, J.; Vila, N., Spontaneous attachment of amines to carbon and metallic surfaces. *J. Phys. Chem. B* **2006**, *110*, 19521-19529.
17. Lee, L.; Downard, A., Preparation of ferrocene-terminated layers by direct reaction with glassy carbon: A comparison of methods. *J. Solid State Electrochem.* **2014**, *18*, 3369-3378.
18. Setton, R., The graphite intercalation compounds: Their uses in industry and chemistry. *Synth. Met.* **1988**, *23*, 467-473.
19. Wildgoose, G. G.; Wilkins, S. J.; Williams, G. R.; France, R. R.; Carnahan, D. L.; Jiang, L.; Jones, T. G.; Compton, R. G., Graphite powder and multiwalled carbon nanotubes chemically modified with 4-nitrobenzylamine. *ChemPhysChem* **2005**, *6*, 352-362.
20. Tang, B.; Guoxin, H.; Gao, H., Raman spectroscopic characterization of graphene. *Appl. Spectrosc. Rev.* **2010**, *45*, 369-407.
21. Criado, A.; Gomez-Escalonilla, M. J.; Fierro, J. L. G.; Urbina, A.; Pena, D.; Guitian, E.; Langa, F., Cycloaddition of benzyne to SWCNT: Towards CNT-based paddle wheels. *Chem. Commun.* **2010**, *46*, 7028-7030.
22. Zhong, X.; Jin, J.; Li, S.; Niu, Z.; Hu, W.; Li, R.; Ma, J., Aryne cycloaddition: Highly efficient chemical modification of graphene. *Chem. Commun.* **2010**, *46*, 7340-7342.
23. Chronopoulos, D.; Karousis, N.; Ichihashi, T.; Yudasaka, M.; Iijima, S.; Tagmatarchis, N., Benzyne cycloaddition onto carbon nanohorns. *Nanoscale* **2013**, *5*, 6388-6394.
24. Serrano-Espraza, I.; Fan, J.; Michalik, J. M.; Rodriguez, L. A.; Ibarra, M. R.; Maria de Teresa, J., The nature of graphene-metal bonding probed by raman spectroscopy: The special case of cobalt. *J. Phys. D: Appl. Phys.* **2016**, *49*, 105301-105310.
25. Koehler, F. M.; Jacobsen, A.; Ensslin, K.; Stampfer, C.; Stark, W. J., Selective chemical modification of graphene surfaces: Distinction between single, and bilayer graphene. *Small* **2010**, *6*, 1125-1130.
26. Brown Jr, J. F., The infrared spectra of nitro and other oxidized nitrogen compounds. *J. Am. Chem. Soc.* **1955**, *77*, 6341-6351.
27. Kross, R. D.; Fassel, V. A., The infrared spectra of aromatic compounds. Iv. The nitro valence vibrations in p-disubstituted nitrobenzenes. *J. Am. Chem. Soc.* **1956**, *78*, 4225-4229.
28. Boschetto, D.; Malard, L.; Lui, C. H.; Mak, K. F.; Li, Z.; Yan, H.; Heinz, T. F., Real-time observation of interlayer vibrations in bilayer and few-layer graphene. *Nano Lett.* **2013**, *13*, 4620-4623.

29. Sobolewski, A. L.; Domcke, W., Intramolecular hydrogen bonding in the $s1(\pi\pi^*)$ excited state of anthranilic acid and salicylic acid: TDDFT calculation of excited-state geometries and infrared spectra. *J. Phys. Chem. A* **2004**, *108*, 10917-10922.
30. Karabacak, M.; Cinar, Z.; Kurt, M.; Sudha, S.; Sundaraganesan, N., FTIR, FT-Raman, NMR and UV-vis spectra, vibrational assignments and DFT calculations of 4-butyl benzoic acid. *Spectrochim. Acta, Part A* **2012**, *85*, 179-189.
31. Chehimi, M. M., Ed, *Aryl diazonium salts: New coupling agents and surface science*. John Wiley & Sons: 2012.
32. Chenhimi, M. M.; Lamouri, A.; Picot, M.; Pinson, J., Surface modification of polymers by reduction of diazonium salts: Polymethylmethacrylate as an example. *J. Mater. Chem. C* **2014**, *2*, 356-363.
33. Anariba, F.; Viswanathan, U.; Bocian, D. F.; McCreery, R. L., Determination of the structure and orientation of organic molecules tethered to flat graphitic carbon by ATR-FTIR and Raman spectroscopy. *Anal. Chem.* **2006**, *78*, 3104-3112.
34. Karabacak, M.; Cinar, M.; Unal, Z.; Kurt, M., FT-IR, UV spectroscopic and DFT quantum chemical study on the molecular conformation, vibrational and electronic transitions of 2-aminoterephthalic acid. *J. Mol. Struct.* **2010**, *982*, 22-27.
35. Brooksby, P. A.; Downard, A. J., Electrochemical and atomic force microscopy study of carbon surface modification via diazonium reduction in aqueous and acetonitrile solutions. *Langmuir* **2004**, *20*, 5038-5045.
36. Hanwell, M. D.; Curtis, D. E.; Lonie, D. C.; Vandermeersch, T.; Zurek, E.; Hutchison, G. R., Avogadro: An advanced semantic chemical editor, visualization, and analysis platform. *J. Cheminf.* **2012**, *4*.
37. Denis, P. A.; Iribarne, F., [2 + 2] cycloadditions onto graphene. *J. Mater. Chem.* **2012**, *22*, 5470-5477.
38. Lee, L.; Leroux, Y. R.; Hapiot, P.; Downard, A. J., Amine-terminated monolayers on carbon: Preparation, characterization, and coupling reactions. *Langmuir* **2015**, *31*, 5071-5077.
39. Gross, A. J.; Bucher, C.; Coche-Guerente, L.; Labbé, P.; Downard, A. J.; Moutet, J.-C., Nickel (ii) tetraphenylporphyrin modified surfaces via electrografting of an aryl diazonium salt. *Electrochem. Commun.* **2011**, *13*, 1236-1239.
40. Doppelt, P.; Hallais, G.; Pinson, J.; Podvorica, F.; Verneyre, S., Surface modification of conducting substrates. Existence of azo bonds in the structure of organic layers obtained from diazonium salts. *Chem. Mater.* **2007**, *19*, 4570-4575.
41. Combellas, C.; Jiang, D.-e.; Kanoufi, F.; Pinson, J.; Podvorica, F. I., Steric effects in the reaction of aryl radicals on surfaces. *Langmuir* **2009**, *25*, 286-293.
42. Pellissier, H.; Santelli, M., The use of arynes in organic synthesis. *Tetrahedron* **2003**, *59*, 701-730.
43. Pena, D.; Perezm, D.; Guitian, E., Insertion of arynes into σ bonds. *Angew. Chem.* **2006**, *45*, 3579-3581.

44. Hammouri, M.; Jha, S. K.; Vasiliev, I., First-principles study of graphene and carbon nanotubes functionalized with benzyne. *J. Phys. Chem. C* **2015**, *119*, 18719-18728.
45. Daukiya, L.; Mattioli, C.; Aubel, D.; Hajjar-Garreau, S.; Vonau, F.; Denys, E.; Reiter, G.; Fransson, J.; Perrin, E.; Bocquet, M.-L.; Bena, C.; Gourdon, A.; Simon, L., Covalent functionalization by cycloaddition reactions of pristine defect-free graphene. *ACS Nano* **2017**, *11*, 627-634.
46. Eckmann, A.; Felten, A.; Mishchenko, A.; Britnell, L.; Krupke, R.; Novoselov, K. S.; Casiraghi, C., Probing the nature of defects in graphene by Raman spectroscopy. *Nano Lett.* **2012**, *12*, 3925-3930.
47. Ferrari, A. C.; Basko, D. M., Raman spectroscopy as a versatile tool for studying the properties of graphene. *Nat. Nano* **2013**, *8*, 235-246.
48. Bellamy, L. J., *The infra-red spectra of complex molecules*. Methuen & Co Ltd: London, 1958.
49. Stewart, J. E., Vibrational spectra of primary and secondary aliphatic amines. *J. Phys. Chem* **1959**, *30*, 1259-1265.
50. Ahmed, S.; Hettwer, S.; Vrijbloed, J. W.; Farina, C.; Allgeier, H. Preparation of acylamino-phthalic acid amides and related compounds as neurotrypsin inhibitors. WO2012059442A2, 2012.
51. Krueger, P. J.; Smith, D. W., Amino group stretching vibrations in primary aliphatic amines. *Can. J. Chem.* **1967**, *45*, 1605-1610.
52. Flett, M. S. C., 294. The application of infra-red spectroscopy to structural problems in the anthraquinone field. *J. Chem. Soc.* **1948**, 1441-1448.
53. Bloom, H.; Briggs, L. H.; Cleverley, B., 33. Physical properties of anthraquinone and its derivatives. Part i. Infrared spectra. *J. Chem. Soc.* **1959**, 178-185.
54. Wu, Q.; Sun, Y.; Bai, H.; Shi, G., High-performance supercapacitor electrodes based on graphene hydrogels modified with 2-aminoanthraquinone moieties. *Phys. Chem. Chem. Phys.* **2011**, *13*, 11193-11198.
55. Canamares, M. V.; Garcia-Ramos, J. V.; Domingo, C.; Sanchez-Cortes, S., Surface-enhanced raman scattering study on the adsorption of the anthraquinone pigment alizarin on Ag nanoparticles. *J. Raman Spectrosc.* **2004**, *35*, 921-927.
56. Pognon, G.; Brousse, T.; Demarconnay, L.; Bélanger, D., Performance and stability of electrochemical capacitor based on anthraquinone modified activated carbon. *J. Power Sources* **2011**, *196*, 4117-4122.
57. Qureshi, G. A.; Svehla, G.; Leonard, M. A., Electrochemical studies of strongly chelating anthraquinone derivatives. *Analyst* **1979**, *104*, 705-722.
58. Shamsipur, M.; Salimi, A.; Golabi, S. M.; Sharghi, H.; Mousavi, M. F., Electrochemical properties of modified carbon paste electrodes containing some amino derivatives of 9,10-anthraquinone. *J. Solid State Electrochem.* **2001**, *5*, 68-73.

5 Capacitance of Aryldiazonium Modified FLG Electrodes

5.1 Introduction

Graphene has been theoretically predicted to have a high gravimetric capacitance of approximately 550 F g^{-1} , however, practical capacitances of graphene materials range from 10 to 250 F g^{-1} .¹⁻⁶ Face to face stacking of graphene sheets during assembly and electrochemical cycling is one of the main reasons for this.^{1, 7} Restacking of graphene sheets limits the accessible surface area, so fewer electrolyte ions can accumulate at the electrode surface, thereby decreasing the electrical double layer capacitance. It is therefore essential that practical methods are developed in which the restacking of graphene sheets is prohibited so maximum ion accumulation is possible and higher capacitances are realised.

The separation distance between the graphene sheets is believed to be important in maximising capacitance. It has been suggested that the maximum electrical double layer capacitance is achieved when the pore size matches the diameter of the electrolyte ions.⁸⁻⁹ Amaratunga et al.¹⁰ studied the influence of pore size in detail, using graphene oxide (GO) as the electrode material in a symmetric two-electrode device. The electrolyte was tetraethylammonium tetrafluoroborate (where the radius of the cation is larger than that of the anion), dissolved in propylene carbonate. The propylene carbonate drives the gradual exfoliation of the GO during cycling, which allows electrolyte ion intercalation between the GO sheets. The separation distance was measured using X-ray diffraction. It was reported that when the separation distance is too small, electrolyte ions cannot accumulate between the graphene sheets and so the capacitance is low. As the spacing increases, partially or completely desolvated anions can fit between the sheets and the capacitance increases slightly. As the spacing increases further, both cations and anions can fit between the sheets and so the capacitance reaches a maximum, as both the anode and cathode are completely accessible to their respective solvated ions. The capacitance began to decrease as the interlayer spacing was increased further and it was postulated that this was caused by an increase in the distance between the electrode and the ionic layer. These results suggest that graphene sheets should be separated by a distance close to the diameter of the electrolyte ions to achieve the best possible capacitance.

Layer by layer (LBL) assembly is a popular method to build graphene architectures, which involves sequentially adsorbing two or more macromolecular materials through exploitation of the intermolecular forces between the materials, such as electrostatic interactions or Van der Waals forces.¹¹ The LBL protocol allows good control over film composition and structure.¹² Reduced graphene oxide (rGO) films are often assembled this way, as electrostatic interactions between charged oxygen containing groups on the rGO can be used to control assembly.¹² Ruoff et al.¹³ used a LBL approach to construct graphene electrodes of CVD-grown monolayer graphene. The repeated transfer of PMMA coated graphene onto a single layer of graphene on the copper foil substrate, allowed stacks with different layer numbers of graphene to be built. With each layer added, the electrical double layer capacitance did not double, indicating that electrolyte ions could not fit between the graphene sheets. Separation using appropriate spacers is an effective technique for preventing sheet aggregation,¹⁴ and carbonaceous materials, metal nanoparticles, or pseudocapacitive materials (metal oxides and polymers) have all been trialled as potential spacers. Lian et al.¹⁵ used carbon black powder as a separator for rGO sheets and obtained a specific capacitance of 138 F g^{-1} at 10 mV s^{-1} . The specific capacitance was not improved when the carbon black powder was added, suggesting the carbon black powder did not efficiently separate the graphene sheets and increase the accessible surface area. However, the rate capability improved, suggesting better channels for ion transport. Li et al.¹⁶ utilised carbon nanotubes to separate GO sheets. Once again, the addition of nanotubes did not increase the total capacitance of the system, however the rate performance was improved. Samulski and Si used platinum nanoparticles as spacers for graphene sheets.¹⁷ The platinum/graphene nanocomposite showed a greatly improved surface area compared to the unmodified graphene sheets, increasing from $44 \text{ m}^2 \text{ g}^{-1}$ to $862 \text{ m}^2 \text{ g}^{-1}$, showing the platinum nanoparticles provided sheet separation. The capacitance increased from 14 F g^{-1} for the dried graphene powder to 269 F g^{-1} for the composite, showing an increase in the electrical double layer capacitance, however the nanoparticles possessed additional pseudocapacitance so this increase cannot solely be attributed to the increase in accessible surface area.

In this thesis work molecular spacers, covalently grafted to the graphene, were used to separate the sheets and maximise the total available surface area for electrical double layer formation. Substituted phenyl groups, grafted to FLG via aryldiazonium

chemistry, were investigated as molecular spacers. The modified FLG sheets were assembled using a LBL protocol to give stacks of modified FLG. In addition to providing sheet separation, modification with aryl groups may be expected to increase the total capacitance of the graphene sheets. Computational studies indicated that monovalent functionalisation, like that accomplished via aryldiazonium chemistry, can increase the quantum capacitance of graphene and therefore the total capacitance. This is due to the increase in the density of states after functionalisation, which will increase the quantum capacitance.¹⁸⁻¹⁹

5.2 Experimental Methods

The experimental methods are detailed in Chapter 2. The aryldiazonium salt modification protocol is outlined in Section 2.4.1. The grafted film was on one side of the FLG only for all samples studied. The LBL assembly method is given in Section 2.5.1, and subsequent electrochemical measurements: cyclic voltammetry (CV), galvanostatic charge discharge (CD), and electrochemical impedance spectroscopy (EIS), are given in Section 2.6.10. All calculated capacitance values can be found in Appendix C, Section C.1 and Section C.2, and calculated energy and power density value in Appendix D, Section D.1 and Section D.2.

5.3 Results and Discussion

5.3.1 Capacitance of Unmodified FLG

5.3.1.1 CV and CD Testing of Unmodified FLG

The capacitance of 3-4 layer FLG in 1 M HClO₄ was investigated using CV, CD, and EIS. HClO₄ was selected as the electrolyte for this thesis work. Acid electrolytes are commonly used when studying electrical double layer capacitance as they present higher capacitance values than neutral or organic electrolytes, and exhibit higher ionic conductivities.²⁰ Although H₂SO₄ is more common in literature reports, it was not used in this thesis work to avoid potential complications from sulfate ion adsorption at the electrode surface.²¹ CV and CD give an indication of the integral capacitance of the system, that is the capacitance over the entire potential range, while EIS gives the differential capacitance. Furthermore, EIS gives information on the interfacial properties of the system. As explained in Chapter 1, Section 1.6.2, the total FLG capacitance is controlled by the quantum, Helmholtz, and diffuse capacitance. Within the potential limits used in this work, which were selected based on the potential

window of the electrolyte, the quantum capacitance is expected to be the limiting component.²²⁻²³

The general strategy for investigating the capacitance of all FLG and FLG stacks (modified and unmodified) described in this thesis work was to first record CVs, in order of decreasing scan rate, followed by CD testing. The CD plots shown are the 7th collected at a particular current density. Sets of 15 cycles at each current density were performed in order of increasing current density.

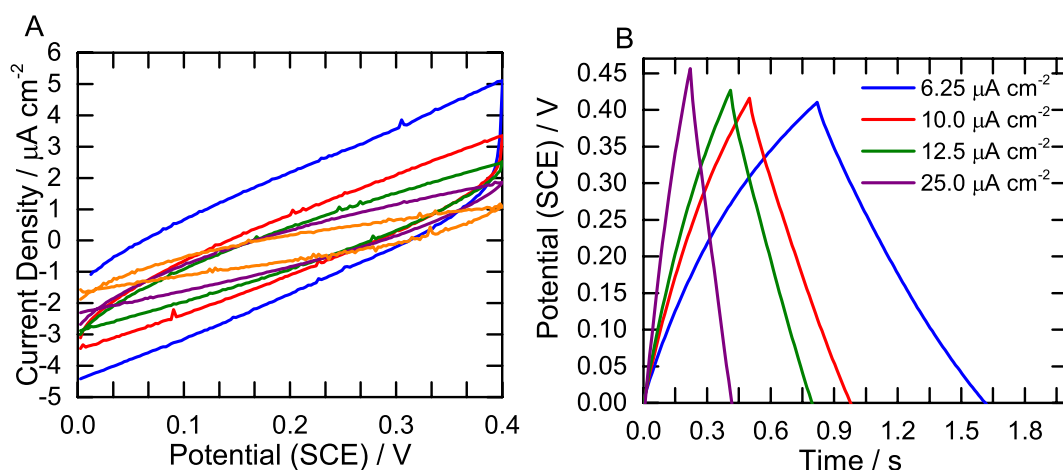


Figure 5.1: CV and CD of FLG on Au/epoxy in 1 M HClO_4 : (A) CV at 200 (blue), 100 (red), 50 (green), 20 (purple), and 5 mV s^{-1} (orange); (B) CD at selected current densities.

In Figure 5.1A, CVs between 0 and 0.4 V are shown for selected scan rates. For an ideal double layer capacitor, the CV is rectangular, resulting from fast double layer formation during charging and discharging.^{4, 8} The CVs shown here give a near rectangular shape, showing that electrical double layer capacitance is the primary method of charge storage. The CVs appear sloped, which indicates some resistance in the system, however the magnitude of the slope appears over exaggerated in the above figure as the y-axis scale is small. The absence of any current peaks confirms that no Faradaic/redox processes are operative.²³ Ideal electrical double layer capacitance is further indicated by the triangular shape of the CD plots (Figure 5.1B).²⁴ Any deviations from this shape are also caused by resistive losses. No abrupt potential drop can be seen at the start of discharging, which suggests the resistance of the FLG sheet is low.²⁵⁻²⁶ As shown in Chapter 3, Section 3.3.2.5, in the working electrode configuration used, protons can access both sides of the FLG sheet through pore and defect regions, so it is possible that the electrical double layer has formed on both sides of the FLG sheet.

The areal capacitance (C_A) was calculated for both sets of data: for areal capacitance calculations of both unmodified and modified FLG throughout this chapter, the geometric working electrode area was used as the electrode area (see Chapter 2, Section 2.6.10 for details), as this approach is often used in literature reports.²⁷⁻²⁹ AFM image analysis of FLG (Chapter 3, Figure 3.5) and aryldiazonium modified FLG (Chapter 3, Figure 3.13) indicated that the average difference between the geometric area and the imaged surface area was $> 1\%$ (calculated using roughness tool on Nanoscope analysis), thus the geometric area was assumed to give a good representation of the working electrode surface area. The areal capacitance for FLG was $10\ \mu\text{F cm}^{-2}$ at $50\ \text{mV s}^{-1}$, and $12.8\ \mu\text{F cm}^{-2}$ at $10.0\ \mu\text{A cm}^{-2}$, which is close to literature reports for FLG ($4\text{-}20\ \mu\text{F cm}^{-2}$).^{19, 24, 30} The CD curve can also be used to calculate the coulombic efficiency (Equation 5.1),

$$\eta = \frac{t_D}{t_C} \times 100\% \quad (5.1)$$

where t_D is the discharging time, and t_C is the charging time.³¹ The coulombic efficiency of the system at all current densities is approximately 100%, suggesting good cyclability and minimal leakage current.³¹

5.3.1.2 EIS of Unmodified FLG

EIS measurements were collected over a wide frequency range (50 frequencies between 0.1 MHz and 0.1 Hz) at 50 mV intervals between -0.5 and $0.3\ \text{V}$. Unless otherwise stated, EIS was started at $-0.5\ \text{V}$. The cell was held at each potential for 2 minutes prior to measurement to ensure a steady state was reached. For all EIS experiments, a Kramers-Kronig analysis was performed, giving values on the order of 10^{-6} , confirming the system was at sufficient steady state for analysis.³² A CV was collected before and after each measurement to ensure the FLG did not change during data acquisition (Figure 5.2). The CV shows no new redox processes after measurement suggesting no chemical changes, such as oxidation of the FLG, occurred. Furthermore, the area of the CV has remained constant, indicating the electrical double layer capacitance did not change during EIS measurement. Below $-0.3\ \text{V}$ for both plots, a redox process begins, which is the hydrogen evolution reaction (HER).³³⁻³⁴

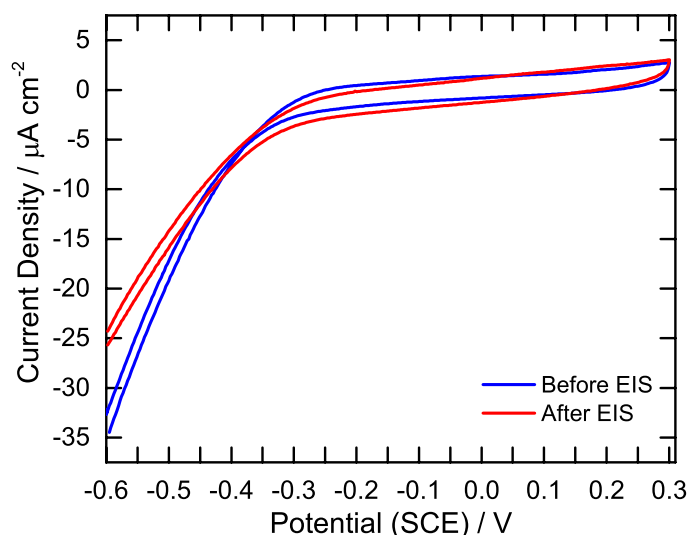


Figure 5.2: CV of FLG on Au/epoxy in 1 M HClO₄ before (blue) and after (red) EIS. Scan rate = 200 mV s⁻¹.

In the absence of any Faradaic processes, a simple model has been developed to calculate the differential capacitance of FLG at different potentials using EIS,^{13, 19, 35} given in Equation 5.2:

$$C = \frac{1}{2\pi f(-Z'')} \quad (5.2)$$

where f is the frequency and Z'' is the imaginary component of the impedance. Below -0.3 V, the HER may mean this model is no longer appropriate, however literature reports utilised this model over the entire potential range, and so the same approach was used in this thesis work.^{19, 35} Figure 5.3 shows the dependence of areal capacitance on frequency at selected potentials.

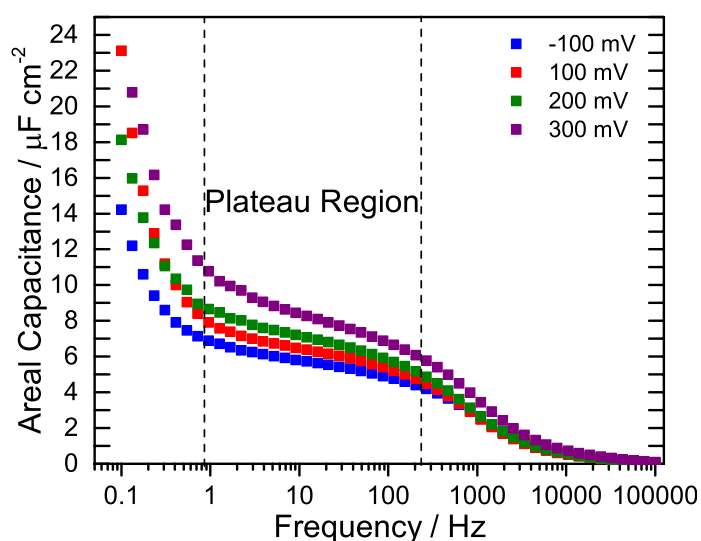


Figure 5.3: Dependence of areal capacitance on frequency at selected potentials for FLG on Au/epoxy, derived from EIS in 1 M HClO₄.

The plot shows a plateau region at mid-frequencies for all applied potentials, and the capacitance in this plateau region increases at more positive applied potentials. There are two approaches reported in literature to determine the best frequency to calculate capacitance: the first, reported by Ruoff, uses the average capacitance of the plateau region¹³ (in this region double layer capacitance and Faradaic effects are most prominent),³⁶⁻³⁷ and the second, reported by Pope and Askay, uses the capacitance at approximately 100 Hz only, as the capacitance does not change greatly within the plateau region, and so the capacitance at approximately 100 Hz is assumed to be an appropriate estimate of the total capacitance.¹⁹ Table 5.1 shows the capacitance calculated using both methods for a selection of FLG surfaces at 0.1 V. Little difference exists between the two methods, with method one always giving a slightly higher value. Both methods are considered valid in literature reports, and so the second approach (capacitance at 115 Hz), was used for the remainder of this work.

Table 5.1: Areal capacitance (C_A) of FLG on Au/epoxy in 1 M HClO₄ calculated via method one (average over the plateau frequency range) or method two (at 115 Hz only), using Equation 5.2 at 0.1 V.

| FLG Sample | C_A from method 1 / $\mu\text{F cm}^{-2}$ | C_A from method 2 / $\mu\text{F cm}^{-2}$ |
|------------|--|--|
| 1 | 6.1 | 5.7 |
| 2 | 4.4 | 4.2 |
| 3 | 4.2 | 3.7 |
| 4 | 3.1 | 2.9 |
| 5 | 3.9 | 3.3 |
| 6 | 4.3 | 3.8 |
| 7 | 5.9 | 5.3 |

Figure 5.4A shows the variation in areal capacitance with potential for a selection of 3-4 layer FLG samples, all from different CVD batches. Figure 5.4B shows the average plot of areal capacitance versus potential (obtained from the data in Figure 5.4A) with the error bars representing the standard deviation.

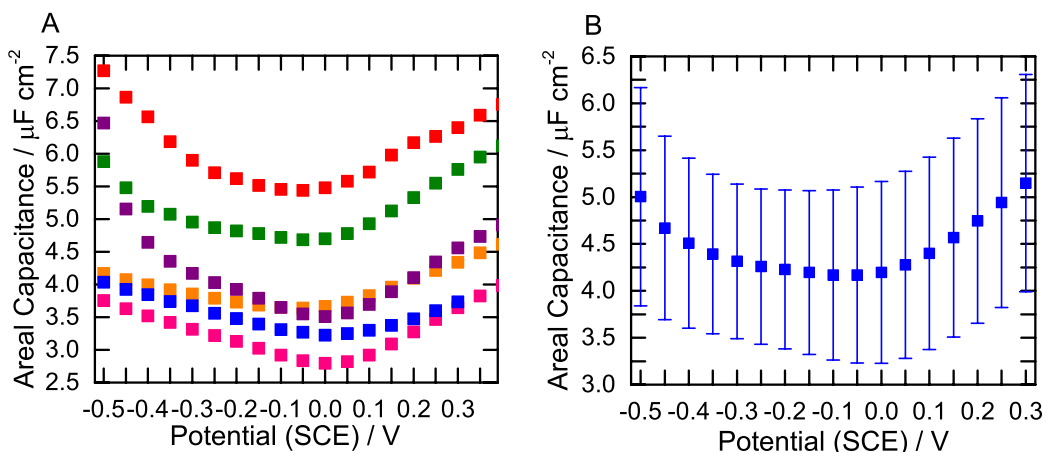


Figure 5.4: Areal capacitance of FLG on Au/epoxy at different applied potentials derived from EIS in 1 M HClO_4 at 115 Hz: (A) six different FLG samples (from different CVD batches); (B) average areal capacitance of samples in A, with standard deviation shown.

The plots in Figure 5.4A are U-shaped with a minimum between 2.8 and 5.6 $\mu\text{F cm}^{-2}$, and the slope either side of this minimum ranges from 2.1 to 6.8 $\mu\text{F cm}^{-2} \text{V}^{-1}$. Some variation exists between different FLG samples, which is assumed to arise from differences in defect concentration and layer number generated during CVD growth of FLG, and from folds and wrinkles caused by transfer of the FLG to the Au/epoxy substrate. This variation was considered when establishing whether differences in capacitance were significant throughout this thesis work.

An average plot for unmodified FLG is given in Figure 5.4B with a minimum at $4.2 \pm 0.9 \mu\text{F cm}^{-2}$. The minimum sits at the Dirac point, and exists because the density of states is lowest at this point.^{13, 38} This minimum agrees with literature reports for FLG, and is close to the minimum found for HOPG.^{13, 19, 35, 38-40} On either side of this minimum, the capacitance increases with an average slope of $3.7 \pm 1.1 \mu\text{F cm}^{-2} \text{V}^{-1}$ for the right arm, and $2.4 \pm 1.3 \mu\text{F cm}^{-2} \text{V}^{-1}$ for the left arm. This increase in capacitance on either side of the Dirac point is caused by an increase in hole and electron doping.¹³ The predicted slope for single layer graphene is $23 \mu\text{F cm}^{-2} \text{V}^{-1}$, however, Ruoff et al. reported a slope of 12.5 and 14 $\mu\text{F cm}^{-2} \text{V}^{-1}$ for the right and left arms respectively, for single layer graphene.¹³ Furthermore, this slope decreased by approximately 74% when the number of layers increased from one to five, and trends towards that of HOPG (approximately $2.5 \mu\text{F cm}^{-2} \text{V}^{-1}$),³⁹⁻⁴⁰ presumably due to the spread of charge into the bulk.¹³ Ruoff et al. reported a slope of approximately $5 \mu\text{F cm}^{-2} \text{V}^{-1}$ for a 4 layer graphene stack. The slopes shown in Figure 5.4A are similar to this, and hence the plot

agrees with previous UV/visible and Raman spectroscopic results that indicate the graphene is 3-4 layers. Unfortunately, this shallow slope means the capacitance remains low over a wider potential window compared to single layer graphene, but the minimum remains higher.

The EIS data can be used to estimate the quantum capacitance of the FLG. As explained in Chapter 1, Section 1.6.2, the total capacitance of a graphene electrical double layer capacitor is comprised of three capacitances, namely the diffuse (C_{Diff}), Helmholtz (C_{H}), and quantum capacitance (C_{Q}), in parallel with one another (Equation 5.3).

$$\frac{1}{C} = \frac{1}{C_{\text{Q}}} + \frac{1}{C_{\text{H}}} + \frac{1}{C_{\text{Diff}}} \quad (5.3)$$

In concentrated electrolyte, like that used here, the diffuse capacitance is significantly larger than the other two components, and can be neglected.³⁸ An approximate value for the Helmholtz capacitance is $20 \mu\text{F cm}^{-2}$, based on the capacitance of a platinum electrode, and so the quantum capacitance can be estimated by subtracting this value from the total capacitance.^{38, 41} Figure 5.5A shows the total and quantum capacitance for the average FLG system.

Equation 5.4 describes the relationship between the quantum capacitance and the number of carriers (see Chapter 1, Section 1.6.2),

$$C_{\text{Q}} = \frac{2e^2}{\hbar v_{\text{F}} \sqrt{\pi}} (|n_{\text{G}}| + |n_{\text{s}}|)^{1/2} \quad (5.4)$$

where

$$n_{\text{G}} = \left(\frac{eV_{\text{ch}}}{\hbar v_{\text{F}} \sqrt{\pi}} \right)^2 \quad (5.5)$$

and \hbar is the reduced Plank constant ($\hbar = h/2\pi$), e is the electron charge, v_{F} is the Fermi velocity of the Dirac electron ($9.99 \times 10^5 \text{ m s}^{-1}$), V_{ch} is the potential of graphene, and n_{s} is the number of carriers caused by charged impurities (holes and electrons). This model can be used to estimate the quantum capacitance for FLG based on the number of carriers determined in Chapter 3, Section 3.3.4 using the Hall effect (n_{s}). Figure 5.5B shows the quantum capacitance estimated using Equation 5.3 (blue) and Equation 5.4 (red). Note the two different y-axis scales.

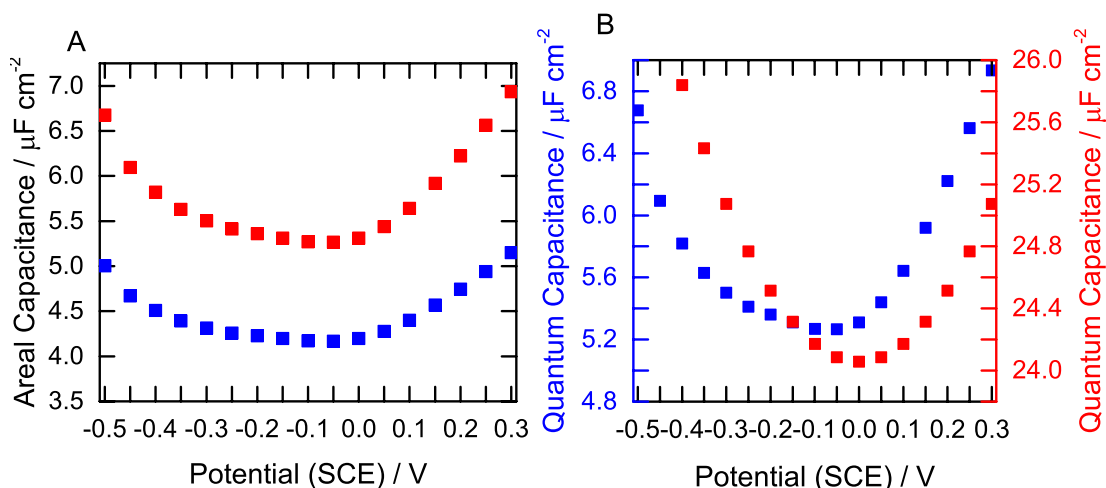


Figure 5.5: (A) Average total (blue) capacitance for FLG on Au/epoxy, derived from EIS in 1 M HClO₄ and the quantum capacitance estimated by subtracting 20 $\mu\text{F cm}^{-2}$ (estimated Helmholtz capacitance) from the total capacitance (blue). (B) Quantum capacitance from plot A (blue) and Equation 5.4 (red).

Examination of Figure 5.5B illustrates that Equation 5.4 is unable to accurately predict the quantum capacitance. The red plot shows a minimum of 24 $\mu\text{F cm}^{-2}$, with a slope of 8.6 $\mu\text{F cm}^{-2} \text{ V}^{-1}$ on either side of the minimum, while the blue plot has a minimum of 5.3 $\mu\text{F cm}^{-2}$, with slopes of 6.0 and 5.0 $\mu\text{F cm}^{-2} \text{ V}^{-1}$ on the right and left sides of the minimum respectively. The difference in the potential of the minimum between the two plots arises from the reference electrode and electrolyte concentration used for EIS.⁴¹ Clearly, the minimum capacitance and slopes calculated using Equation 5.4 are higher than those estimated from Equation 5.3. The discrepancy between the two sets of data is possibly related to the number of graphene layers. The model developed by Tao (Equation 5.4) has been used for single layer systems only.^{38, 41} The number of layers is known to influence the capacitance,^{13, 42-43} so to successfully predict the quantum capacitance for few-layer systems, new models are required. These would need to consider the distribution of carriers and impurities within each layer, screening of impurities, and the possibility of impurities being intercalated between layers. Tao attempted to develop a model for bilayer graphene, but further work is still required to understand the quantum capacitance of such systems. Furthermore, the possibility of a fourth component, the dielectric capacitance, that has been suggested to play an important role in the capacitance of FLG with four layers or more, needs to be considered.⁴²⁻⁴³

5.3.1.3 Nyquist Plot Analysis of FLG

Information on the electrochemical nature of the graphene electrode can also be discerned from EIS using the full range of frequency data. A Nyquist plot is commonly

used to display the real (Z') and imaginary (Z'') components of the total impedance (Z) at each measured frequency. A typical Nyquist plot for a carbon capacitor shows an intercept of the real axis at very high frequency, corresponding to the solution resistance (R_s), which is the electrolyte resistance between the working and reference electrolyte.³ A semicircle follows if Faradaic processes exist for the system, the diameter of which equals the charge transfer resistance. At lower frequencies, mass transport and diffusion related processes tend to dominate. A Bode plot of phase angle vs. frequency can also be used to illustrate impedance data. In EIS measurements, an oscillating potential is applied to the system. If the input and output of this signal are in phase, the phase angle is 0° , characteristic of a resistor, whereas if they are out of phase, with a phase angle of -90° , the system is purely capacitive (a phase angle of $+90^\circ$ indicates inductance, which should not be seen for carbon capacitors.)^{32, 44-48} Figure 5.6 shows the Nyquist and Bode phase angle plots for a representative FLG surface at 0.1 V, which is close to the open circuit potential of the system.

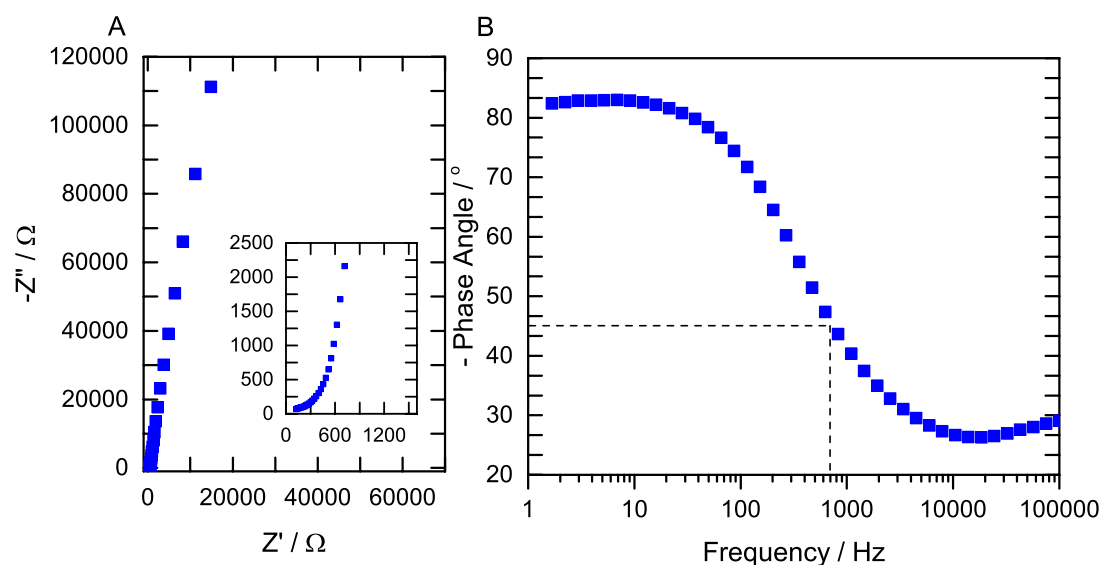


Figure 5.6: Data obtained from EIS of FLG on Au/epoxy in 1 M HClO_4 at 0.1 V: (A) Nyquist plot with inset showing magnified high frequency region; (B) Bode phase angle plot.

The Nyquist plot shows no semicircle in the high frequency region, meaning no interfacial charge transfer resistance exists at the electrode surface. This is expected, as there should only be electrical double layer capacitance at the FLG surface, as no redox processes can be seen in the CV results at 0.1 V (Figure 5.2).^{31, 48-50} A short line, with an angle close to 45° can be seen in the mid-frequency region. The 45° angle is characteristic of a Warburg impedance, caused by obstruction of ion movement at the electrode.^{3, 8, 31, 49, 51} The fact that this portion of the plot is very short suggests good ion diffusion, as expected for planar, FLG capacitors.⁴⁹ At low frequencies, an almost

vertical line can be seen, suggesting the system is showing excellent capacitive behaviour.^{31, 45, 50-51} If this portion of the plot maintained a slope of 45° , the system would be diffusion limited, but this is not the case for the FLG studied here.⁵⁰ The Bode phase angle plot also confirms this good capacitive behaviour at low frequencies, with a phase angle of approximately 85° .⁵² Further, the frequency at -45° on the phase angle plot (f_0) marks the transition point where the system goes from resistive to capacitive behaviour.³ The time constant ($1/f_0$) is 1.2 ms, which is low compared to other carbons (17.8 ms for porous reduced graphene oxide, 26 ms for onion like carbon, and 700 ms for activated carbon),^{3, 53} highlighting the high speed ion diffusion and transport to the surfaces. This is expected because the FLG is a planar electrode, so nothing should block ion movement to the surface, and the electrolyte is highly concentrated so diffusion gradients should not exist.

A common way to analyse EIS data is by using equivalent electrical circuits (EEC) comprised of discrete circuit elements.^{44, 54-55} It is important to select an appropriate circuit to model the data, with components that can be ascribed to actual physical processes occurring for the system. Figure 5.7 shows the circuit used to fit the FLG data, and the fitted Nyquist plot. The circuit is comprised of a R_S in series with two additional components. The capacitance elements of the circuit were modelled as constant phase elements (CPE), as this compensates for any deviations from ideality resulting from surface roughness and any inhomogeneities caused by defect and grain boundary regions.⁵⁶ The CPE (Q_{DL}) in parallel with a Warburg impedance (W) relates to the formation of the double layer at the electrode interface. Typically, a charge transfer resistance is also in parallel with this CPE, however the best fit for the FLG data is obtained when the charge transfer resistance is zero, further confirming the lack of a charge transfer resistance for this system.⁴⁹ The second part of the circuit, consisting of a CPE in parallel with a resistance, corresponds to the bulk capacitance (Q_B) and associated resistance (R_B).³ It is typically best to discuss quantitative parameters for each circuit element when comparing similar interface structures, therefore numerical values for the EEC will be discussed in Section 5.3.3.3, when FLG is compared with modified FLG surfaces, to establish the effect of modification on the electrode/electrolyte interface.⁴⁷

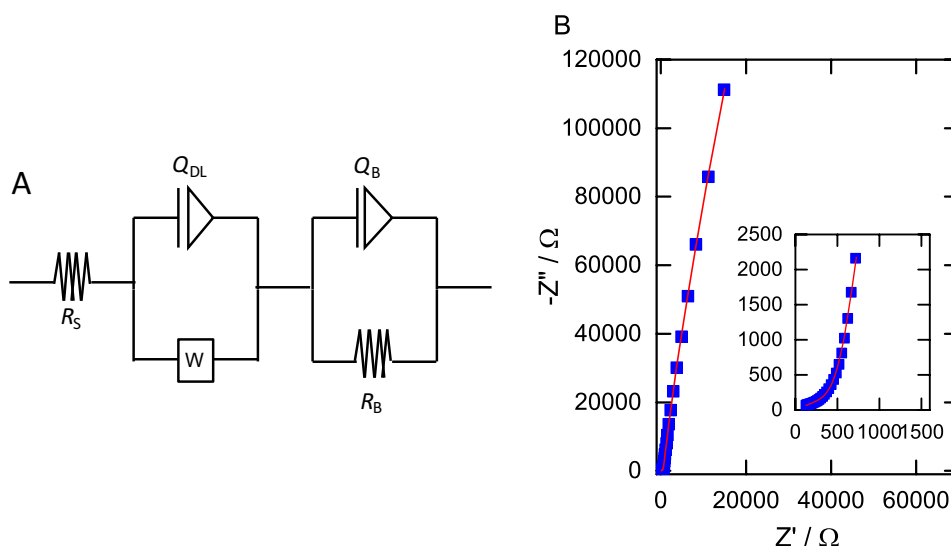


Figure 5.7: (A) Equivalent electrical circuit used to fit FLG EIS data; (B) Nyquist plots for FLG with fit shown in red (inset shows magnified high frequency region).

5.3.2 Capacitance of Unmodified FLG Stacks

5.3.2.1 CV and CD Testing of Unmodified FLG Stacks

The goal of this project is to increase the total capacitance by stacking FLG sheets, using a LBL protocol. The free-floating FLG sheets were successively collected and dried on a FLG/Cu coupon from a water bath. The full experimental details can be found in Chapter 2, Section 2.5.1. The stacked FLG working electrodes consisted of three sheets of FLG (3FLG); the stacks were limited to three sheets of FLG because there was sufficient difference between a one- and three-sheet stack to establish if the sheets were completely separated.

In initial experiments, the capacitance of three-sheet stacks of unmodified (as prepared) FLG was examined. Figure 5.8 shows the CV and CD profiles for 3FLG, which look like those for a single FLG sheet (Figure 5.1) suggesting the 3FLG also behaves as an electrical double layer capacitor, with no Faradaic reactions contributing to the total capacitance. The calculated areal capacitance was $7.1 \mu\text{F cm}^{-2}$ at 50 mV s^{-1} , and $10.3 \mu\text{F cm}^{-2}$ at $10.0 \mu\text{A cm}^{-2}$, values that are slightly lower than for a single sheet. The capacitance indicates that the stacked FLG sheets behave more as a single 9-12 layer sheet rather than 3 individual sheets.

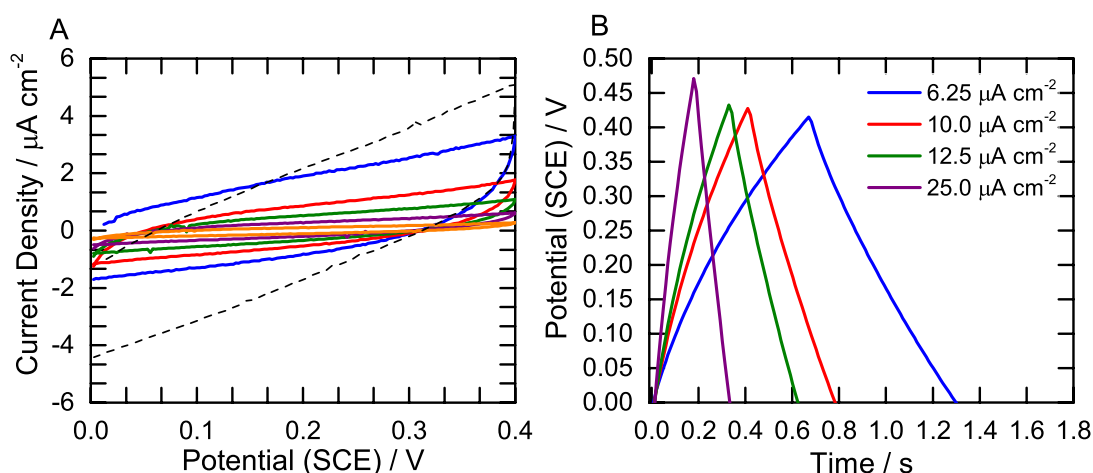


Figure 5.8: CV and CD results for 3FLG on Au/epoxy in 1 M HClO₄: (A) CV at 200 (blue), 100 (red), 50 (green), 20 (purple), and 5 mV s⁻¹ (orange). Dotted line is the same CV for FLG in Figure 5.1 at 200 mV s⁻¹, and given for comparison; (B) CD at selected current densities.

5.3.2.2 EIS of Unmodified FLG Stacks

The capacitance versus voltage plot for 3FLG derived from EIS is given in Figure 5.9 with the FLG plot (from Figure 5.4B) shown for comparison.

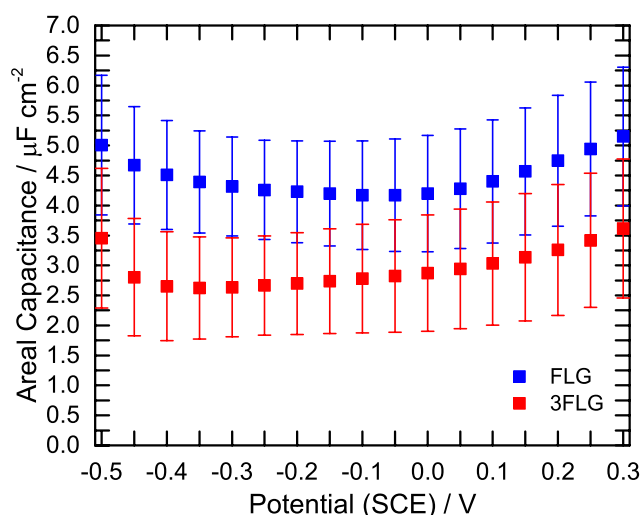


Figure 5.9: Average areal capacitance at different potentials for FLG (blue, $n=6$) and 3FLG (red, $n=3$) derived from EIS in 1 M HClO₄ at 115 Hz.

The average minimum areal capacitance for 3FLG ($2.8 \mu\text{F cm}^{-2}$) is lower than FLG ($4.2 \mu\text{F cm}^{-2}$). Also, the slope of the left and right arms of the FLG plot decreased to 0.7 and $2.4 \mu\text{F cm}^{-2} \text{ V}^{-1}$ respectively. There are two possible explanations for the decrease in capacitance seen for CV, CD, and EIS. Firstly, having three sheets of FLG stacked together may hinder ion and solvent transport through the graphene layers, preventing efficient double layer formation on both sides of the stack. As shown in Chapter 3, Section 3.3.2.5, electrolyte can access both sides of the single FLG sheets in the working electrode configuration used. Secondly, the decrease in capacitance could be related to the increase in the number of layers. From a FLG sheet to 3FLG, the total

number of graphene layers increases from 3-4 to 9-12. Ruoff et al.¹³ showed that increasing the number of layers decreases the minimum capacitance and the slope of the capacitance versus voltage plot. At 9-12 layers, the system would resemble HOPG, and indeed the minimum capacitance for Figure 5.9 is close to that for HOPG ($2\text{-}3\ \mu\text{F cm}^{-2}$).³⁹⁻⁴⁰ Furthermore, the slope for the left and right arm for 3FLG is similar to that for HOPG ($1.0\text{-}2.5\ \mu\text{F cm}^{-2}$) with the left arm typically having a smaller slope.³⁹⁻⁴⁰ This decrease in slope implies the integral capacitance over a wide potential range (-0.5 to $0.3\ \text{V}$ for EIS) would decrease, and so a lower capacitance is also seen from CV and CD results. Hence, stacking the FLG sheets has most likely resulted in an HOPG-like electrode, with decreased capacitance over the $0.4\ \text{V}$ potential window used in CV and CD testing. Thus, spacer groups became essential in building stacks of FLG to keep the sheets sufficiently separated for the double layer to form at each FLG surface.

5.3.3 Capacitance of NBD Modified FLG Stacks

5.3.3.1 EIS of Single Sheet Modified FLG

Spacer groups were added to the FLG using nitrobenzene diazonium (NBD) and the capacitance of the resulting surface was analysed using EIS to determine the most appropriate reactions conditions. The EIS measurements started at $-0.5\ \text{V}$, which meant the NP film was initially reduced to an aminophenyl (AP) film (Chapter 3, Section 3.3.2.5) to give FLG_{AP} . The reaction was carried out on copper, so the FLG_{AP} is collected on the Au/epoxy substrate in the exposed orientation, and the FLG_{AP} was washed with methanol prior to EIS measurement. Figure 5.10 gives the CV response between -0.5 and $0.3\ \text{V}$ for the FLG_{AP} sample before and after EIS. Similar to FLG, no current peaks can be seen within this potential window, indicating no Faradaic processes are active, thus Equation 5.2 can be used to extract the capacitance from the data. Furthermore, the CV shape and area does not change after the measurement, suggesting good stability.

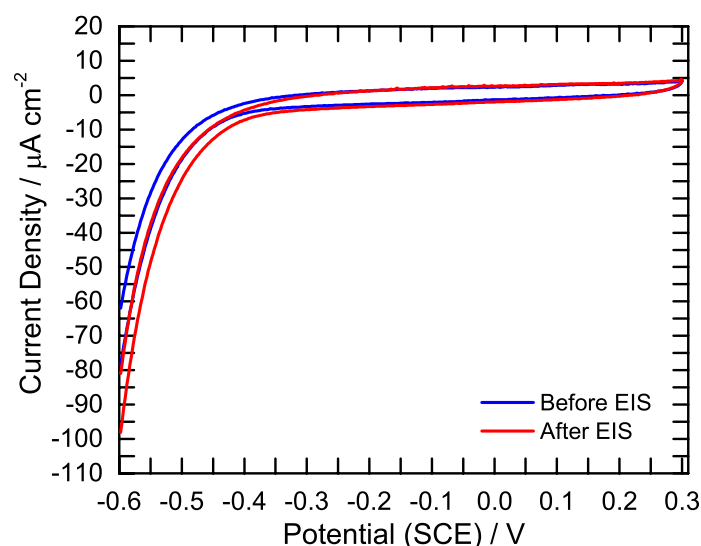


Figure 5.10: CV of FLG_{AP} on Au/epoxy in 1 M HClO₄ before and after EIS. Scan rate = 200 mV s⁻¹.

Figure 5.11 shows the dependence of areal capacitance on potential for FLG_{AP} after a 7 hour reaction.

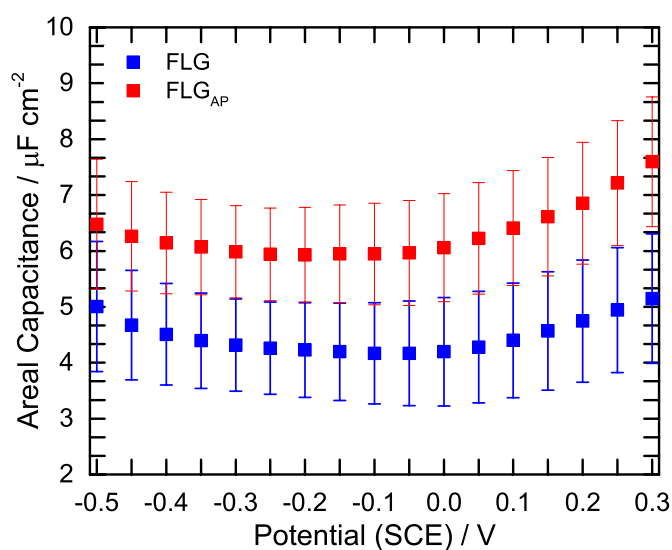


Figure 5.11: Average areal capacitance derived from EIS in 1 M HClO₄ at different applied potentials at 115 Hz of: (blue) FLG ($n=6$); (red) FLG_{AP} after a 7 hour reaction with 20 mM aqueous NBD solution ($n=3$).

The FLG_{AP 7hours} gives the same U-shaped plot, and the average minimum capacitance increased after functionalisation to 5.6 $\mu\text{F cm}^{-2}$, however the minimum is within the expected experimental error. Consequently, it is not possible to say whether this increase is due to functionalisation, or is simply a result of variation between different batches of FLG and certainly it is not significant. The functionalisation does increase the carrier concentration ($n_s=2.4 \times 10^{14} \text{ cm}^{-2}$, Chapter 3, Section 3.3.4), which was expected to increase the quantum capacitance and hence the total capacitance. Pope and

Askay showed that above a certain defect concentration the quantum capacitance is no longer the limiting capacitance component, rather the Helmholtz capacitance controls the total capacitance, and the total capacitance is approximately $20 \mu\text{F cm}^{-2}$.¹⁹ This is not the case for $\text{FLG}_{\text{AP } 7\text{hours}}$, hence the increase in carrier concentration must not be sufficient to increase the quantum capacitance above the Helmholtz capacitance. Importantly, although the capacitance may not increase significantly after modification, it is unlikely to decrease, indicating that the functionalisation process is not detrimental to the areal capacitance of the system.

The areal capacitance was also measured for four other NP surface concentrations, by varying the modification time and aryldiazonium salt solution concentration. Table 5.2 gives the experimental parameters, resulting surface concentration, and minimum capacitance values for each condition, and Figure 5.12 shows the areal capacitance versus potential plots. Surface concentration was measured by carrying out a NP reduction CV (Chapter 2, Section 2.6.9.1) prior to EIS measurements, and the surface concentration calculated based on the charge associated with the NP reduction and hydroxylaminophenyl oxidation peaks.

Table 5.2: Reaction conditions, surface concentration, and minimum areal capacitance (C_A) for FLG_{AP} surfaces.

| Sample | Reaction Conditions | Surface Concentration / nmol cm^{-2} | Minimum C_A / $\mu\text{F cm}^{-2}$ |
|--|---------------------|--|--|
| FLG ($n=6$) | - | - | 4.2 ± 0.9 |
| $\text{FLG}_{\text{AP } 1\text{hour}}$ ($n=5$) | 1 hour, 1 mM | 0.12 ± 0.04 | 3.9 ± 1.1 |
| $\text{FLG}_{\text{AP } 7\text{hours}}$ ($n=3$) | 7 hours, 20 mM | 0.21 ± 0.02 | 5.6 ± 1.3 |
| $\text{FLG}_{\text{AP } 16\text{hours}}$ ($n=2$) | 16 hours, 20 mM | 0.47 ± 0.06 | 4.4 ± 0.2 |
| $\text{FLG}_{\text{AP } 72\text{hours}}$ ($n=2$) | 72 hours, 20 mM | 1.92 ± 0.13 | 5.8 ± 0.2 |

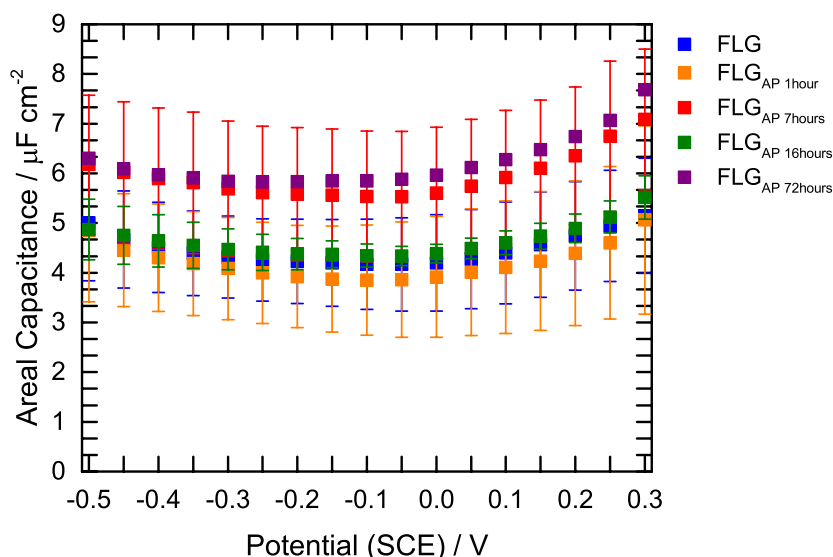


Figure 5.12: Average areal capacitance at different applied potentials derived from EIS in 1 M HClO_4 at 115 Hz for FLG and FLG_{AP} on Au/epoxy.

There is no obvious trend between surface concentration and the minimum areal capacitance, and the measured capacitance values are within the maximum experimental variation seen between samples. This suggests that regardless of the surface concentration, the increase in the carrier concentration induced by modification is not sufficient to significantly increase the total capacitance of the system. This may be a consequence of using FLG, as the increase in capacitance with the number of carriers has only been predicted for single layer graphene, and it is unknown how FLG should behave. Further the functionalisation is only on the top layer of the graphene, with the underlying sheets remaining unmodified.

A comparison of the capacitance for FLG modified with NP and AP groups was undertaken by starting the EIS measurement at 0.3 V, and moving towards more negative potentials. The plot in Figure 5.13 shows the dependence of capacitance on voltage, first for an $\text{FLG}_{\text{NP 1hour}}$ surface going from 0.3 to -0.5 V and then the same surface from -0.5 to 0.3 V (red). Initially, the capacitance of the FLG_{NP} surface is lower than the unmodified FLG. At approximately -0.2 V, the capacitance increases by around $1 \mu\text{F cm}^{-2}$. This occurs at a similar potential to the onset of the nitro reduction peak (Chapter 3, Figure 3.21), indicating that the increasing capacitance is likely related to the reduction of NP groups to AP groups. The capacitance remains high on the return scan, with the capacitance being $2.1 \mu\text{F cm}^{-2}$ higher at the end potential than the starting potential, suggesting this change is irreversible, as expected for the electrochemical

reduction of a NP film. The same experiment was repeated for a FLG surface (not shown) and no change in the capacitance was seen at -0.2 V.

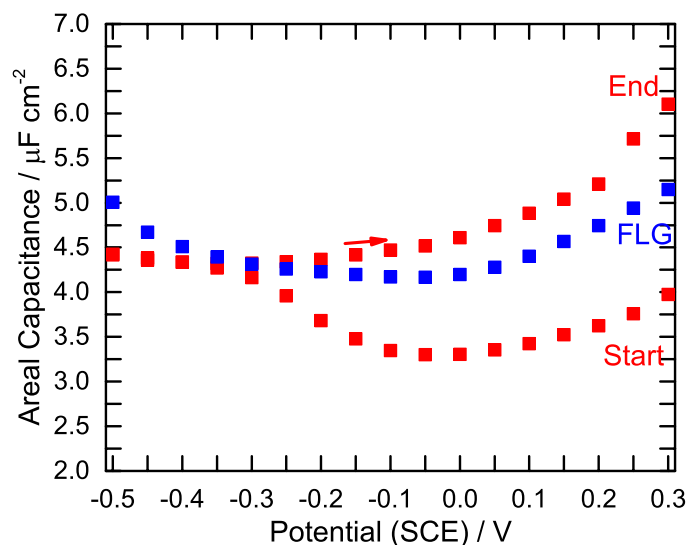


Figure 5.13: Dependence of areal capacitance on potential $\text{FLG}_{\text{NP 1hour}}$ on Au/epoxy derived from EIS in 1 M HClO_4 at 115 Hz, from 0.3 to -0.5 V, then from -0.5 to 0.3 V (red). FLG plot, starting at 0.3 V shown for comparison (blue).

The AP groups are expected to be protonated in the acidic solution conditions, and therefore charged, which may influence the capacitance as the NP group would be neutral. To test this hypothesis, a $\text{FLG}_{\text{AP 1hour}}$ surface was analysed in both perchloric acid and sodium perchlorate ($\text{pH} \sim 6$). The pK_a of aniline is 4.6, therefore the AP groups will be largely deprotonated in sodium perchlorate. The capacitance against voltage plot for the $\text{FLG}_{\text{AP 1hour}}$ surface in both electrolytes is given in Figure 5.14. No difference can be seen between the two plots, which strongly suggests that the increase in capacitance is not caused by the charged nature of the AP film in perchloric acid. Daasbjerg et al.⁵⁷ reported a potential-induced desorption process that lead to voids in an organic layer grafted from an aryldiazonium salt. This means that reduction of the NP film to an AP film may generate a more porous grafted layer leading to more efficient formation of the double layer at the FLG surface. This may explain why the initial capacitance of FLG_{NP} is lower than that of unmodified FLG, as the film could block access of electrolyte ions to the FLG surface thereby hindering double layer formation. After reduction, the film becomes more porous leading to more space on the FLG surface for double layer formation. Additionally, Targholi and Mousavi-Khoshdel¹⁸ predicted, based on computational studies, that graphene functionalised with AP groups gives a higher quantum capacitance than graphene functionalised with NP groups or simply a phenyl ring, due to an increased density of states for AP

functionalisation, and an increase in quantum capacitance is expected to increase the total capacitance. The main consequence for this work is that reduction of the NP film increases the capacitance, albeit within the variation seen between different batches of FLG, and so is expected to be better for designing supercapacitor electrodes.

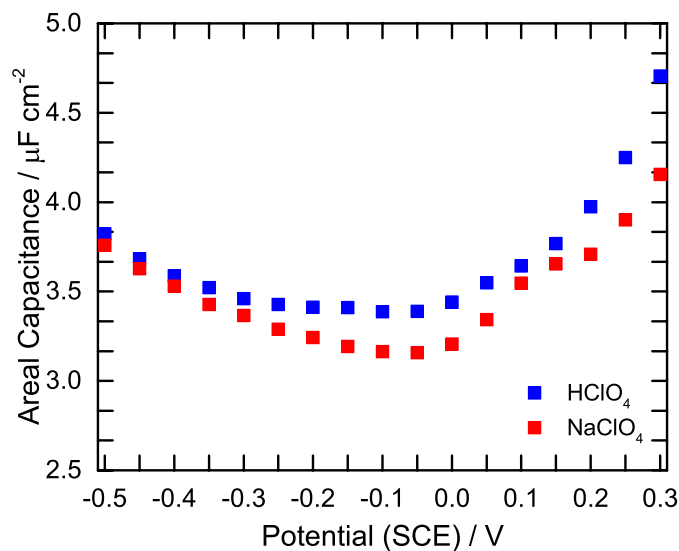


Figure 5.14: Dependence of areal capacitance on potential of $\text{FLG}_{\text{AP } 1\text{hour}}$ on Au/epoxy derived from EIS at 115 Hz in 1 M HClO_4 (blue) and 1 M NaClO_4 (red).

5.3.3.2 EIS of Three-Sheet Stacks of Modified FLG

The FLG_{NP} sheets were assembled into three-sheet stacks using the LBL approach described in Chapter 2, Section 2.5.1. FLG_{NP} sheets with four different surface concentrations (Table 5.2) were stacked in this manner to give 3FLG_{NP} systems, and then analysed using EIS. Based on the project goals outlined in Chapter 1, Section 1.7, the experimental protocol must be optimised so that the stack has $3\times$ the areal capacitance of a single sheet of FLG, as this confirms each FLG sheet is totally accessible to the electrolyte ions. Once again, EIS measurements started at -0.5 V, so the 3FLG_{NP} was converted to 3FLG_{AP} prior to data collection. The areal capacitance versus voltage plots for the four different surface concentrations of NP groups are given in Figure 5.15. Using $\text{FLG}_{\text{AP } 1\text{hour}}$, with the lowest surface concentration of modifiers, the stack only gives an average $2.2\times$ increase in the minimum capacitance, suggesting this surface concentration is insufficient to separate the FLG_{AP} sheets. On the other hand, the 7 hour modification time gave an average increase of approximately $3\times$ for the $3\text{FLG}_{\text{AP } 7\text{hour}}$ stacks compared to $\text{FLG}_{\text{AP } 7\text{hour}}$ single sheet, indicating that a reaction time of 7 hours is sufficient to give a surface concentration high enough to separate the sheets.

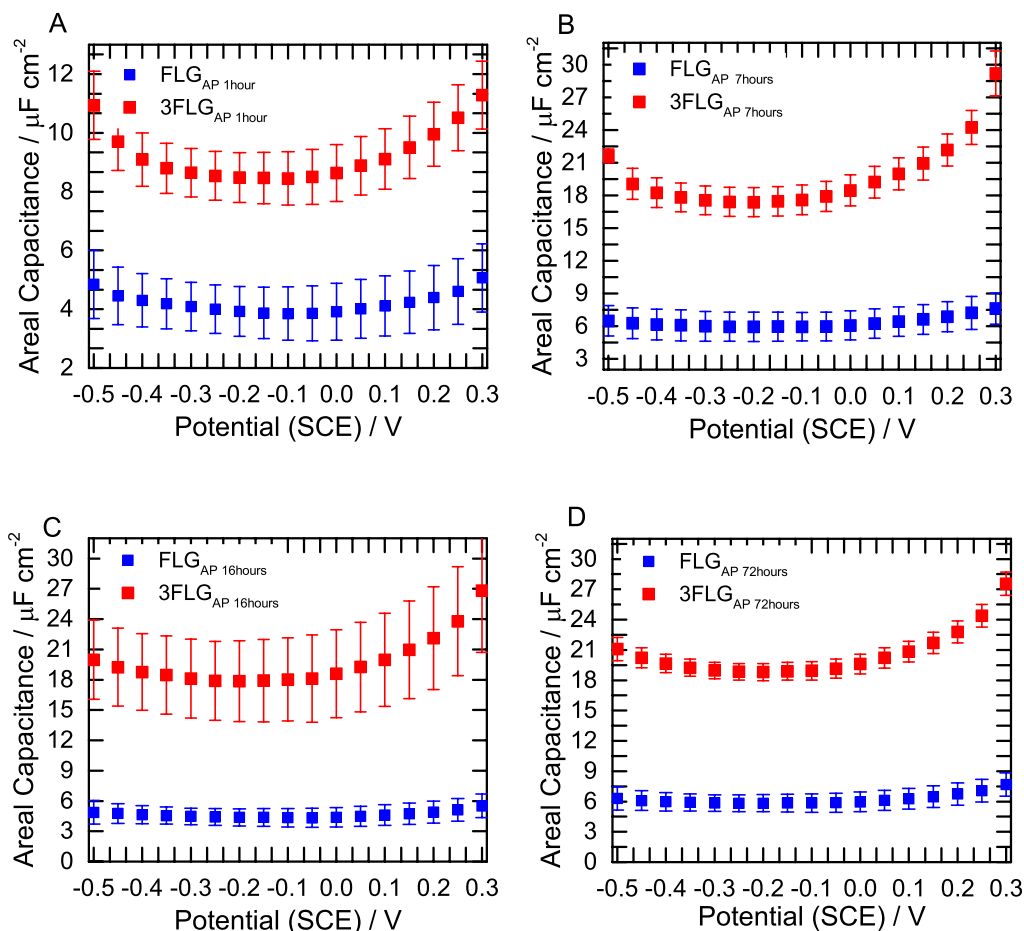


Figure 5.15: Average areal capacitance vs. voltage plots of FLG_{AP} and 3FLG_{AP} derived from EIS in 1 M HClO_4 at 115 Hz: (A) 1 hour, 1 mM aryldiazonium salt reaction ($n=3$); (B) 7 hours, 20 mM aryldiazonium salt reaction ($n=2$); (C) 16 hours, 20 mM aryldiazonium salt reaction ($n=2$); (D) 72 hours, 20 mM aryldiazonium salt reaction ($n=2$).

Somewhat surprisingly, the minimum capacitance remained $3\times$ higher for the highest surface concentrations. This suggests that for even the thickest films, access of electrolyte ions between the FLG sheets is not significantly hindered by the grafted layer. In Section 5.1, it was explained that a pore size approximately the same as the diameter of the electrolyte ions is expected to give the highest capacitance. This effect is not seen here, as even the lowest surface concentration of AP groups is expected to provide a film height of 0.4 nm,⁵⁸ which is approximately the same as the ionic radius of the solvated and unsolvated perchlorate ion (0.37 and 0.24 nm respectively).⁵⁹ Furthermore, the capacitance does not decrease as the film thickness increases (the 72 hour reaction is predicted to give a film of 6 nm).⁵⁸ It is possible that film density may be responsible for this behaviour. For the $\text{FLG}_{\text{AP 1hour}}$ reaction, the surface concentration is $0.12 \text{ nmol cm}^{-2}$, which is only 10% of an ideal close packed monolayer of NP groups (1.2 nmol cm^{-2}).⁶⁰ This means that approximately 90% of the FLG surface does not

contain modifier groups, and so in these regions the FLG_{AP} sheets may be in contact, preventing electrolyte ions from accessing these areas and therefore limiting double layer formation. As the surface concentration increases, the film becomes thicker and so the FLG_{AP} sheets are further apart and can therefore no longer contact one another in the unmodified regions of the surface. The remainder of work in this chapter focusses on FLG after a 7 hour, 20 mM reaction with NBD, as this surface concentration is able to fully separate the sheets. Hence, $FLG_{AP/NP}$ and $3FLG_{AP/NP}$ for the remainder of this chapter will refer to FLG modified via a 7 hour reaction in 20 mM aqueous NBD solution.

5.3.3.3 Nyquist Plots for NBD Modified FLG Stacks

The Nyquist plots for the one- and three-sheet FLG_{AP} systems were also analysed. To accurately fit the FLG_{AP} and $3FLG_{AP}$ data, additional circuit elements were required to account for the film. An appropriate EEC was taken from literature reports, with the film modelled as an inert porous layer, with the electrical double layer forming at the FLG surface at the base of the film.^{44, 52} Figure 5.10 indicated that Faradaic processes are not operative at 0.1 V for FLG_{AP} , and so the film could be considered as inert. Figure 5.16 shows assumed structure of the FLG_{AP} electrode surface, with different circuit elements to account for the porous layer. The R_L circuit element corresponds to the electrolyte resistance within the pore or grafted layer, and the film is modelled as a CPE (Q_L), whose magnitude relates to the permittivity and thickness of the film. This circuit was used to fit all aryldiazonium modified one- and three-sheet stacks of FLG.

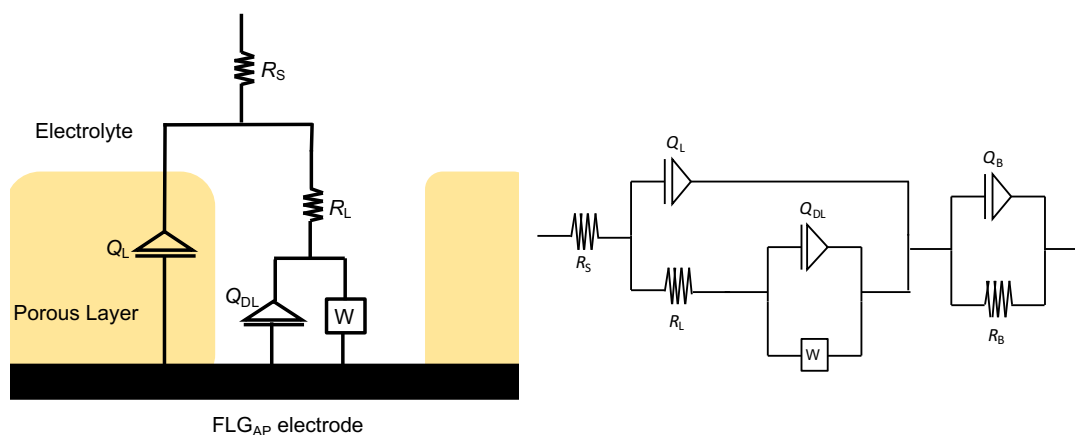


Figure 5.16: EEC used to fit EIS data for aryldiazonium modified FLG one- and three-sheet stacks. Reproduced from Tribollet & Orazem.⁴⁴

The Nyquist and Bode phase angle plots for FLG_{AP} and $3FLG_{AP}$ are given in Figure 5.17. The fitted Nyquist plots are also shown, with the FLG included for comparison.

All values calculated from the EEC are given in Appendix E, Section E.1, and selected values will be discussed further.

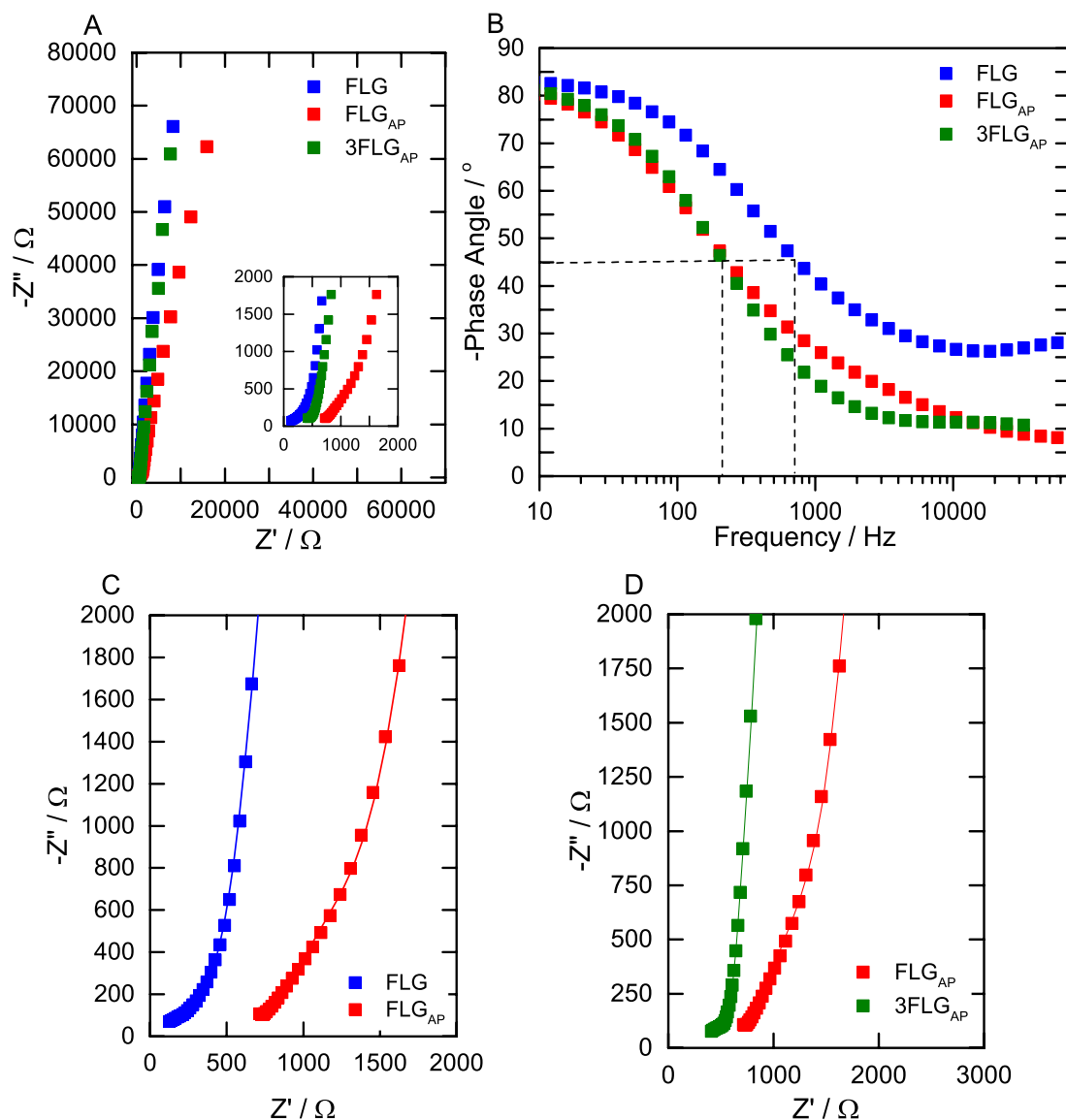


Figure 5.17: EIS data for FLG, FLG_{AP}, and 3FLG_{AP} recorded at 0.1 V in 1 M HClO₄: (A) Nyquist plots; (B) Bode phase angle plots; (C) fitted FLG and FLG_{AP} Nyquist plots; (D) fitted FLG_{AP} and 3FLG_{AP} Nyquist plots.

The most obvious difference between the FLG and FLG_{AP} Nyquist plots is the increase in R_s from 6.8 Ω for FLG to 27.4 Ω for FLG_{AP}. This is responsible for the shift of the plot along the Z' axis. The exact origin for this increase is unknown at this time. The R_s value corresponds to the solution resistance between the working electrode and the reference electrode, and depends on the electrolyte concentration and the position of the reference electrode with respect to the working electrode. The electrolyte is 1 M HClO₄ for both FLG and FLG_{AP}, furthermore the use of the Luggin capillary to house the reference electrode ensures the separation between the two electrodes remains constant. The AP film is protonated, therefore the positive charge of the film could

interact with electrolyte ions and alter R_S , however when the experiment was repeated with a FLG_{NP} surface, which would not be protonated, a similar increase in the R_S value (22.4 Ω) was observed, indicating the charge of the film is not the sole cause of this increase. Surprisingly, the R_S value for 3 FLG_{AP} (6.3 Ω) has not increased compared to the FLG and this behaviour is consistent for all samples regardless of film type. This unusual behaviour for the solution resistance requires further investigation to establish the exact cause of the increase for FLG_{AP} (and FLG_{NP}).

Similar to FLG, no charge transfer resistance was required to fit the data for both FLG_{AP} and 3 FLG_{AP} , which is expected as there are no Faradaic processes occurring at 0.1 V (Figure 5.10). In addition, both FLG_{AP} and 3 FLG_{AP} required the additional R_L component, suggesting an additional resistance caused by the film. The R_L value was higher for 3 FLG_{AP} (40.0 $k\Omega\text{ cm}^{-2}$) than FLG_{AP} (12.2 $k\Omega\text{ cm}^{-2}$), indicating the stacking of the sheets increases the electrolyte resistance within the porous layer. At low frequencies, both FLG_{AP} and 3 FLG_{AP} behave similarly to FLG, with a vertical tail, corresponding to the low frequency capacitive behaviour of the system. The slope is smaller for the modified surfaces possibly due to reduced ion accessibility to the surface.³¹ In Figure 5.13 it was shown that FLG_{AP} gives a higher capacitance than FLG_{NP} , and it was postulated that this is caused by removal of some film during reduction, giving a more porous film. The Nyquist plot results support this hypothesis, as the FLG_{NP} surface presents a higher R_L value (36.7 vs. 12.2 $k\Omega\text{ cm}^{-2}$) and a higher Warburg impedance (3.1 vs. 1.7 $\mu S\text{ cm}^{-2}$) than FLG_{AP} , which suggests the FLG_{NP} impedes ion diffusion to the FLG surface.

On the Bode plot, the frequency at which the electrode transitions from diffusion limited to capacitive behaviour is lower for FLG_{AP} and 3 FLG_{AP} than FLG, giving a higher time constant (FLG = 1.2 ms; FLG_{AP} = 3 FLG_{AP} = 4.9 ms. FLG_{AP} and 3 FLG_{AP} gave the same time constant). This suggests the film decreases the speed of ion transport to the surface.³ This increase in time constant is consistent for all samples studied. An important observation is that even with the small increase, the time constant is much lower than other porous graphene and carbon systems (17.8 ms for porous reduced graphene oxide, 26 ms for onion-like carbon, and 700 ms for activated carbon).^{3,53} The time constant is the minimum time needed to discharge all the energy from the electrical double layer capacitor, with an efficiency of at least 50% of the maximum available

capacitance. It is important to maintain a low time constant when increasing the total capacitance of electrical double layer capacitors, as this ensures the device can be charged and discharged rapidly, and therefore the power density remains high.⁶¹

5.3.3.4 CV and CD Testing of NBD Modified FLG Stacks

The modified FLG surfaces were analysed via CV and CD testing. For these measurements, the NBD modified FLG was analysed both before (FLG_{NP}) and after (FLG_{AP}) reduction, as both a single sheet and a three-sheet stack. The CVs between 0 and 0.4 V of FLG_{AP}, 3FLG_{AP}, FLG_{NP}, and 3FLG_{NP} are given in Figure 5.18. The most notable difference between the FLG_{NP} and FLG_{AP} CVs is the appearance of a set of redox peaks at approximately 0.3 V for FLG_{AP}, while the FLG_{NP} CVs show the rectangular shape typical of electrical double layer capacitors. The redox peaks are seen outside the potential window used in EIS studies. As explained in Chapter 3, Section 3.3.2.5, some NP groups will be reduced to give hydroxylaminophenyl groups, and these can undergo a second, reversible redox reaction, which may cause the peaks seen in Figure 5.18A and B. In Figure 5.18E and F, CVs obtained at 50 mV s⁻¹ are shown for the one- and three-sheet systems for FLG_{AP} and FLG_{NP}. For both modifiers, the area enclosed by the CV increases for 3FLG_{AP/NP}, as there are more FLG surfaces available for electrical double layer formation. Table 5.3 summarises the areal capacitance values for each system, calculated at 50 mV s⁻¹, with FLG included for comparison. Both FLG_{AP} and 3FLG_{AP} show higher areal capacitances than their FLG_{NP} counterparts, due to the additional pseudocapacitance provided by the hydroxylaminophenyl group.

Figure 5.19 shows the CD plots for FLG_{AP}, 3FLG_{AP}, FLG_{NP}, and 3FLG_{NP} at various current densities. The CD plots for the FLG_{AP} and 3FLG_{AP} samples show a bell-shaped curve. The deviation from an ideal triangular shape is indicative of a material possessing both electrical double layer capacitance and pseudocapacitance, as expected for these surfaces that contain the redox active hydroxylaminophenyl group.⁴⁸ The pseudocapacitance causes a longer discharge time between 0.4 and 0.3 V, as discharge time is proportional to capacitance. This agrees with the CV results given in Figure 5.18A and B, as the redox peaks are seen between 0.3 to 0.4 V. Conversely, the FLG_{NP} and 3FLG_{NP} plots show a triangular shape, indicating only electrical double layer capacitance is operative.⁶²

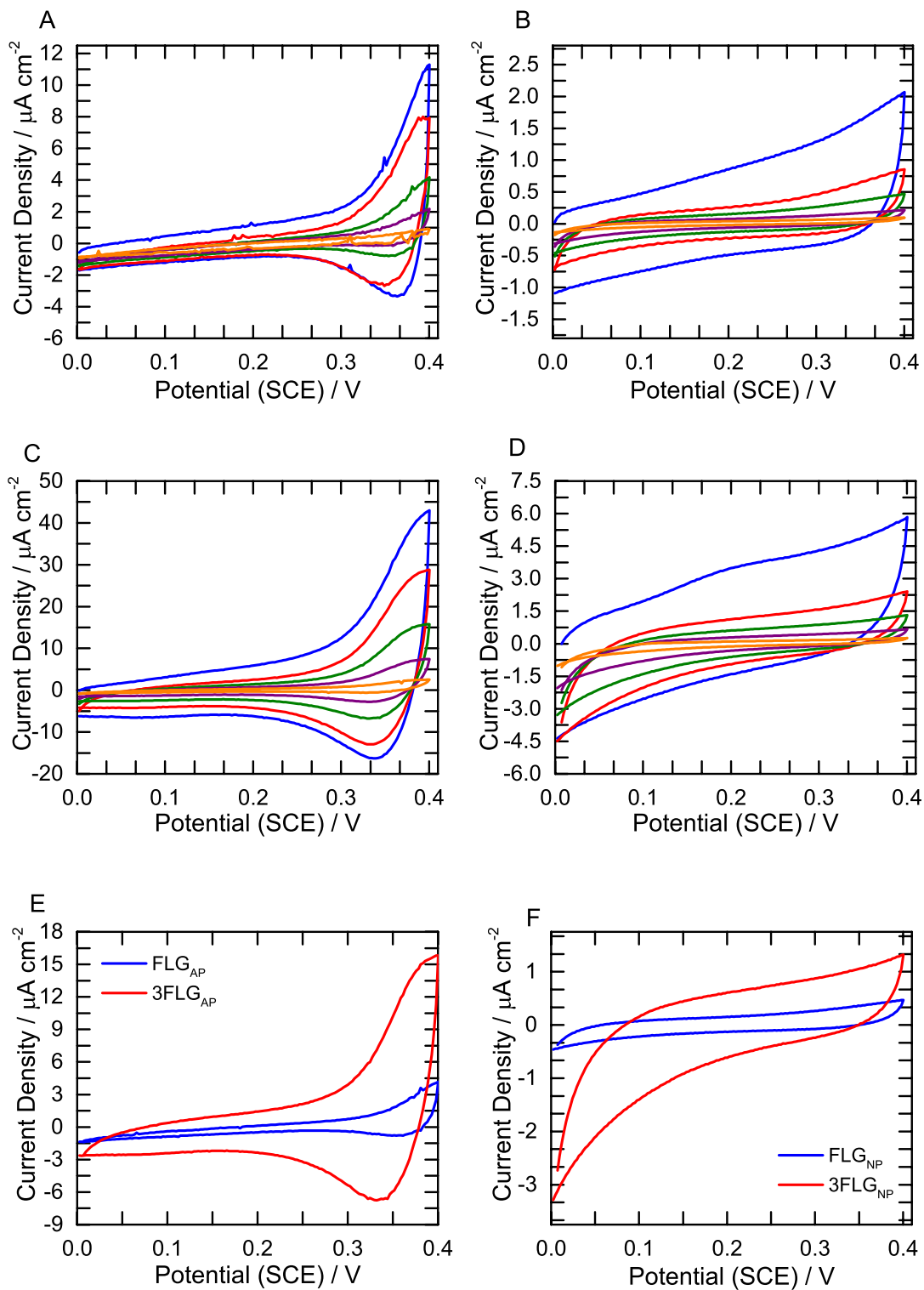


Figure 5.18: CVs in 1 M HClO₄ of modified FLG at 200 (blue), 100 (red), 50 (green), 20 (purple), and 5 mV s⁻¹(orange): (A) FLG_{AP}; (B) FLG_{NP}; (C) 3FLG_{AP}; (D) 3FLG_{NP}. Comparisons of (E) FLG_{AP} and 3FLG_{AP} at 50 mV s⁻¹ and (F) FLG_{NP} and 3FLG_{NP} at 50 mV s⁻¹ also shown.

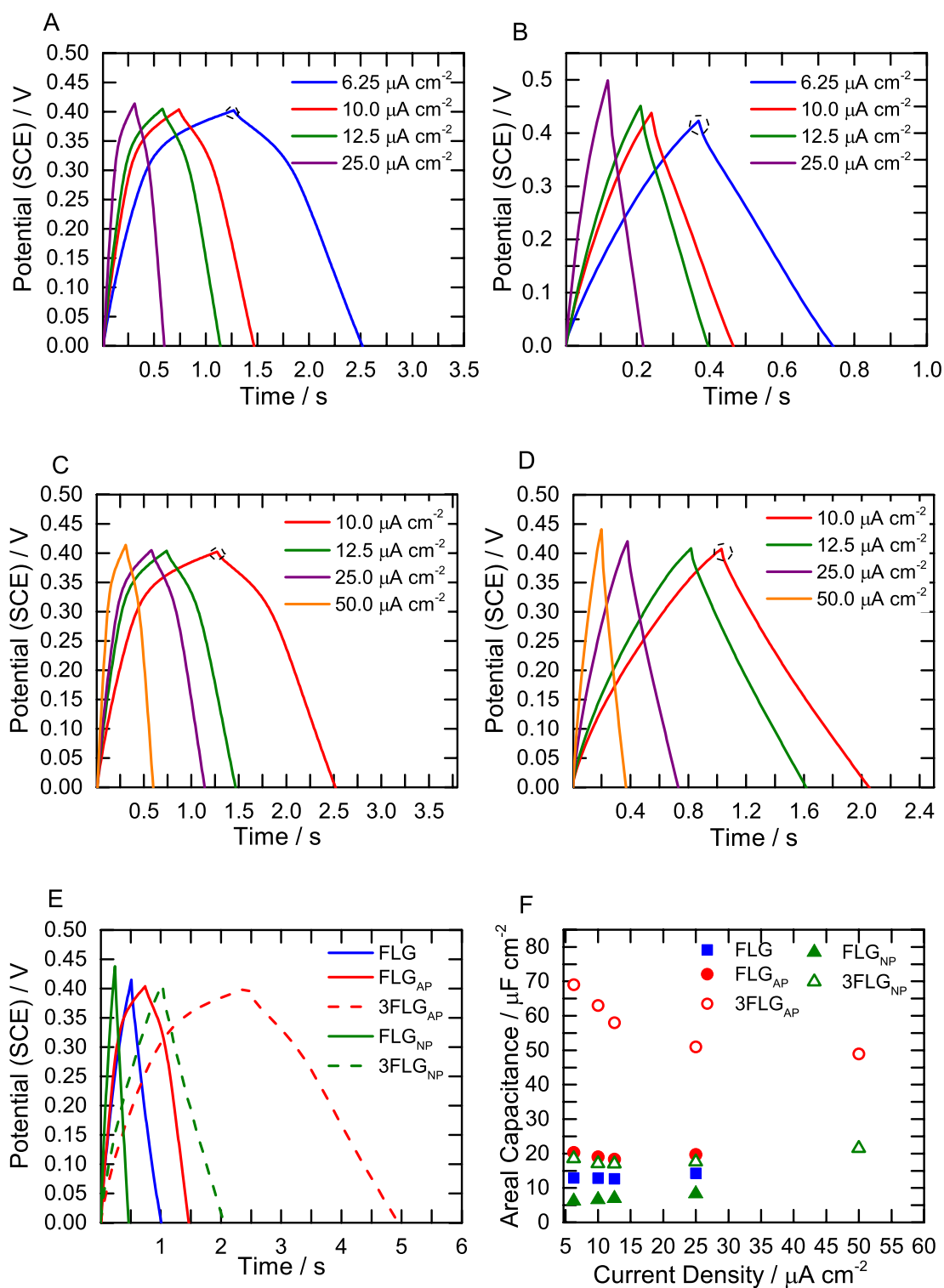


Figure 5.19: CD at selected scan rates in 1 M HClO₄ of modified FLG: (A) FLG_{AP}; (B) FLG_{NP}; (C) 3FLG_{AP}; (D) 3FLG_{NP}; (E) comparison of A-D at 10.0 μA cm⁻²; (F) areal capacitance at selected current densities.

Table 5.3 summarises the areal capacitance values derived from the discharge portion of the plot for each surface at $10.0 \mu\text{A cm}^{-2}$. As expected, the areal capacitance increases approximately $3\times$ from FLG_{NP} to the three-sheet counterpart. For the FLG_{AP} system the areal capacitance increases by slightly more than $3\times$ after stacking. IR spectroscopy results in Chapter 3, Section 3.3.2.3, showed that washing the surface with methanol removes a large amount of physisorbed material from the surface, and therefore this methanol wash step has been used for all samples analysed for capacitance. However, the three-sheet systems were washed after stacking, so material trapped between the sheets may not be removed, therefore additional physisorbed material may be present for the three-sheet stacks, which would increase the total capacitance as more pseudocapacitive groups are present. Both the 3FLG_{AP} and 3FLG_{NP} surfaces show a higher areal capacitance than the 3FLG with no phenyl groups, confirming the modifier groups are needed to separate the sheets and improve energy storage capability. The FLG_{NP} surface shows a slight decrease in areal capacitance compared with the FLG surface, possibly due to the blocking nature of the film, which may limit double layer formation, as discussed earlier.

Table 5.3: Average areal capacitance values and potential drop of FLG, FLG_{AP} , 3FLG_{AP} , FLG_{NP} , and 3FLG_{NP} , calculated at 50 mV s^{-1} and at $10.0 \mu\text{A cm}^{-2}$. Capacitance values after 20,000 charge discharge cycles (see Section 5.3.3.5) at $10 \mu\text{F cm}^{-2}$ are also listed. $n=2$ for all samples.

| Sample | C_A (CV) / $\mu\text{F cm}^{-2}$ | C_A (CV) after cycling / $\mu\text{F cm}^{-2}$ | C_A (CD) / $\mu\text{F cm}^{-2}$ | C_A (CD) after cycling / $\mu\text{F cm}^{-2}$ | Potential drop / V |
|---------------------------|------------------------------------|--|------------------------------------|--|--------------------|
| FLG | 11.5 | 9.0 | 15.6 | 15.2 | 0 |
| 3FLG | 7.1 | 9.0 | 10.3 | 9.8 | 0 |
| FLG_{AP} | 14.9 | 7.0 | 15.9 | 11.8 | 0.01 |
| 3FLG_{AP} | 71.9 | 21.7 | 85.7 | 44.0 | 0.02 |
| FLG_{NP} | 2.9 | 5.2 | 6.4 | 10.4 | 0.01 |
| 3FLG_{NP} | 15.6 | 18.4 | 19.1 | 30.3 | 0.01 |

The plot in Figure 5.19F shows the variation in areal capacitance with current density. All surfaces except 3FLG_{AP} show approximately the same areal capacitance for the highest and lowest current densities, suggesting a very good rate capability.^{3, 63-64} The capacitance of the 3FLG_{AP} sample decreases with increasing current density, although the percent retention is still high (77% of the capacitance at $6.25 \mu\text{A cm}^{-2}$ is retained at $50 \mu\text{A cm}^{-2}$, so only 23% of the total capacitance is lost at the fastest scan rate studied). This may be a result of restricted proton diffusion, enhanced at higher current densities, which could limit the pseudocapacitance as the hydroxylaminophenyl/nitrosophenyl

redox process (Chapter 3, Scheme 3.2) is a two electron, two proton process. Unfortunately, it was not possible to analyse the one-sheet systems at the highest current density because the discharge time was too fast to accurately calculate capacitance. A small potential drop at the start of the discharge portion of the plot (circled in Figure 5.19A, B, C, and D) can be seen for the modified FLG systems of approximately 0.01 to 0.02 V, which indicates the modified FLG possess a small internal resistance, agreeing with EIS results that show an additional solution resistance within the pores for the modified surfaces.

5.3.3.5 Cycle Stability of NBD Modified FLG Stacks

The FLG and modified FLG, one- and three-sheet systems, were cycled at $10.0 \mu\text{A cm}^{-2}$ for 20,000 cycles to confirm stability (Figure 5.20). The plots below show a single sample for each condition, however each experiment was repeated twice to confirm trends were reproducible, and the values presented in Table 5.3 represent the average capacitance.

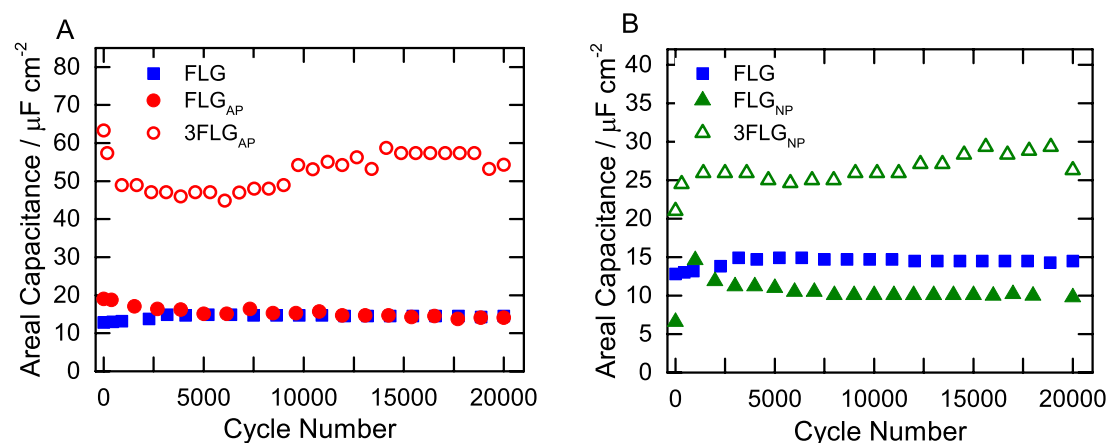


Figure 5.20: Areal capacitance during charge discharge cycling at $10.0 \mu\text{A cm}^{-2}$ in 1 M HClO_4 : (A) FLG_{AP} and 3FLG_{AP} ; (B) FLG_{NP} and 3FLG_{NP} . FLG (blue) shown for comparison.

In both plots, the blue squares show the stability of the unmodified FLG. After an initial conditioning or activation period (~ 3000 cycles)⁶⁵⁻⁶⁶ the capacitance of the FLG is stable, with the final capacitance being 98% of the capacitance at 3000 cycles. Similarly, the FLG_{NP} and 3FLG_{NP} show good cycle stability after the initial conditioning period, with a capacitance retention of 87% and 100% for the one- and three-sheet systems respectively.^{4, 67} The FLG_{AP} and the 3FLG_{AP} show a drop of up to 50% during the initial activation period (as a comparison, the capacitance of FLG increases by approximately 10%). After the initial drop, the capacitance remains stable for the additional 15,000 cycles. Furthermore, even with the initial capacitance drop for FLG_{AP} and 3FLG_{AP} , 3FLG_{AP} maintains a capacitance $3\times$ higher FLG_{AP} after 20,000

cycles (Table 5.3), indicating that the film is still able to effectively separate the FLG sheets after charge discharge cycling. The same is true for FLG_{NP} and 3FLG_{NP} .

The decrease in areal capacitance for the FLG_{AP} and 3FLG_{AP} surfaces is believed to be caused by a loss of pseudocapacitance. Figure 5.21 gives the CV responses at 50 mV s^{-1} , for the FLG_{AP} one- and three-sheet systems, before and after cycling. Clearly, the redox peaks disappear after cycling, and the system shows electrical double layer capacitance only, as evidenced by the rectangular shape of the CV. The areal capacitance of the 3FLG_{AP} is still $3\times$ the capacitance of FLG_{AP} after the cycling period (Table 5.3) which suggests the molecular spacers remain grafted to the FLG surface. The results indicate that the pseudocapacitive hydroxylaminophenyl/nitrosophenyl groups of the FLG_{AP} samples likely underwent a transformation during cycling to a non-redox active group (for example an aminophenyl group). This is not unexpected, as molecular redox reactions can suffer from poor cyclability that leads to degradation of the active material in the initial cycles.⁴

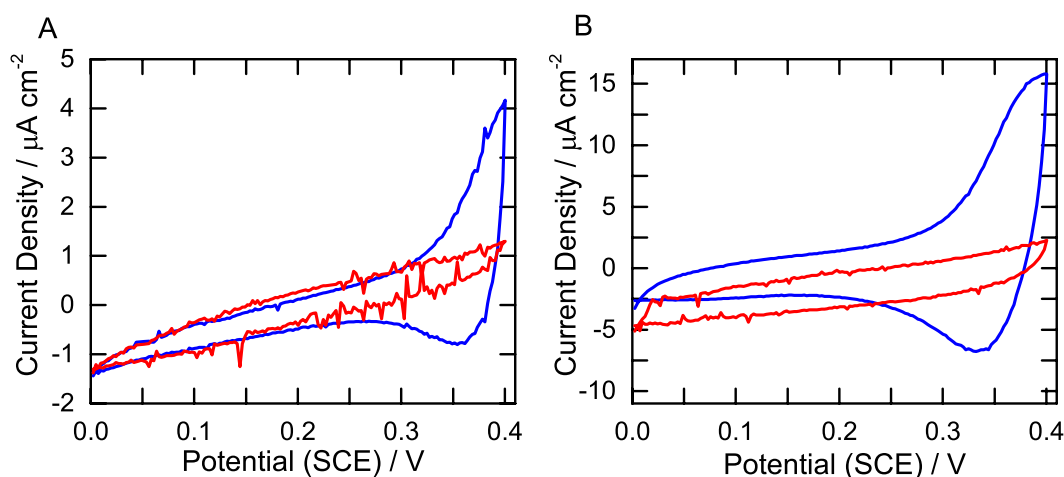


Figure 5.21: CVs in 1 M HClO_4 before and after 20,000 CD cycles at $10 \mu\text{A cm}^{-2}$: (A) FLG_{AP} and (B) 3FLG_{AP} . Scan rate = 50 mV s^{-1} .

5.3.4 Capacitance of CBD Modified FLG Stacks

The FLG was also modified with carboxybenzene diazonium (CBD) and stacked into a three-sheet system. The NP/AP film was replaced with the CP film to improve the stability of the one- and three-sheet stacks. The CP film is not expected to undergo Faradaic processes so will not exhibit pseudocapacitance, and therefore should provide electrodes with better cyclic stability. Unlike the NBD modification, the CBD modification was via the free-floating protocol, so the working electrodes are in the sandwiched orientation.

5.3.4.1 EIS of CBD Modified FLG

EIS was used to calculate the capacitance at different potentials to establish whether the CP film could separate the sheets of FLG. Figure 5.22A gives the CV response of FLG_{CP} before and after EIS. Once more, the CV shows no current peaks within the potential window studied, indicating Equation 5.2 can be used to calculate the capacitance. Furthermore, no obvious changes can be seen after completion of the EIS measurement, confirming the system is stable.

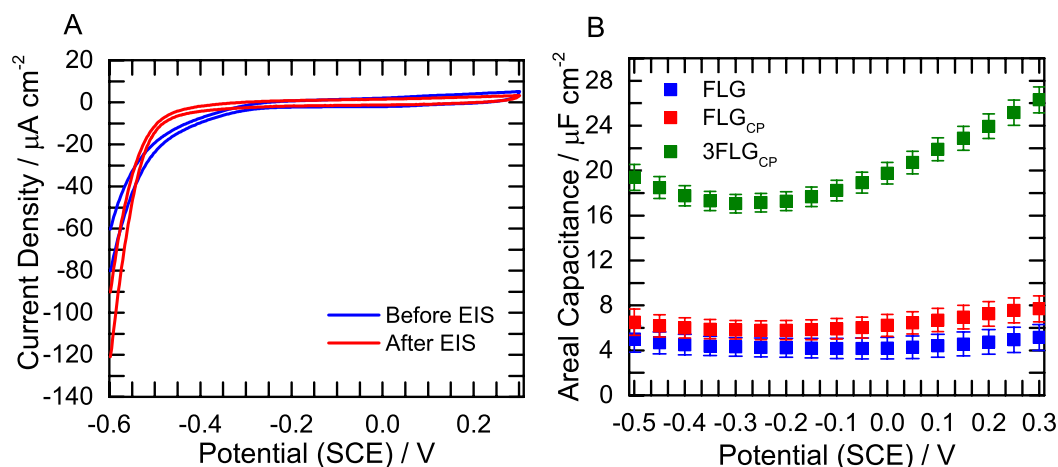


Figure 5.22: (A) CV of FLG_{CP} before and after EIS in 1 M HClO_4 ; (B) average areal capacitance versus voltage plots derived from EIS in 1 M HClO_4 at 115 Hz for FLG, FLG_{CP} , and 3FLG_{CP} .

Figure 5.22B shows the average areal capacitance against voltage plots for FLG, FLG_{CP} , and 3FLG_{CP} . All the plots show a U-shaped dependence on potential, with the FLG_{CP} having the same areal capacitance as FLG, within experimental error. After stacking, the minimum areal capacitance of the system increases from 5.8 to 17.2 $\mu\text{F cm}^{-2}$, an approximate 3 \times increase, confirming all sheets are sufficiently separated by the CP film.

Figure 5.23 gives the Nyquist and Bode phase angle plots for FLG_{CP} and 3FLG_{CP} with the fits shown. The EEC used to fit the FLG_{AP} surfaces was used again for the CP modified surfaces (Figure 5.16). As before, the R_{S} value for FLG_{CP} has increased slightly after modification from 6.8 to 9.1 Ω . The 3FLG_{CP} and FLG_{CP} samples required the additional R_{L} component to fit the data, highlighting the increase in resistance caused by the film. The R_{L} value is once again higher for 3FLG_{CP} compared to FLG_{CP} (60.0 vs. 18.7 $\text{k}\Omega \text{ cm}^{-2}$). In the low frequency region, the plots show the expected capacitive behaviour. The calculated time constant from the Bode plots is 8.9 ms for both the one- and three-sheet systems, showing stacking does not decrease the rate of

ion diffusion to the surface. Furthermore, like the FLG_{AP} samples the time constant is low indicating a fast charge and discharge rate compared with other porous carbons.

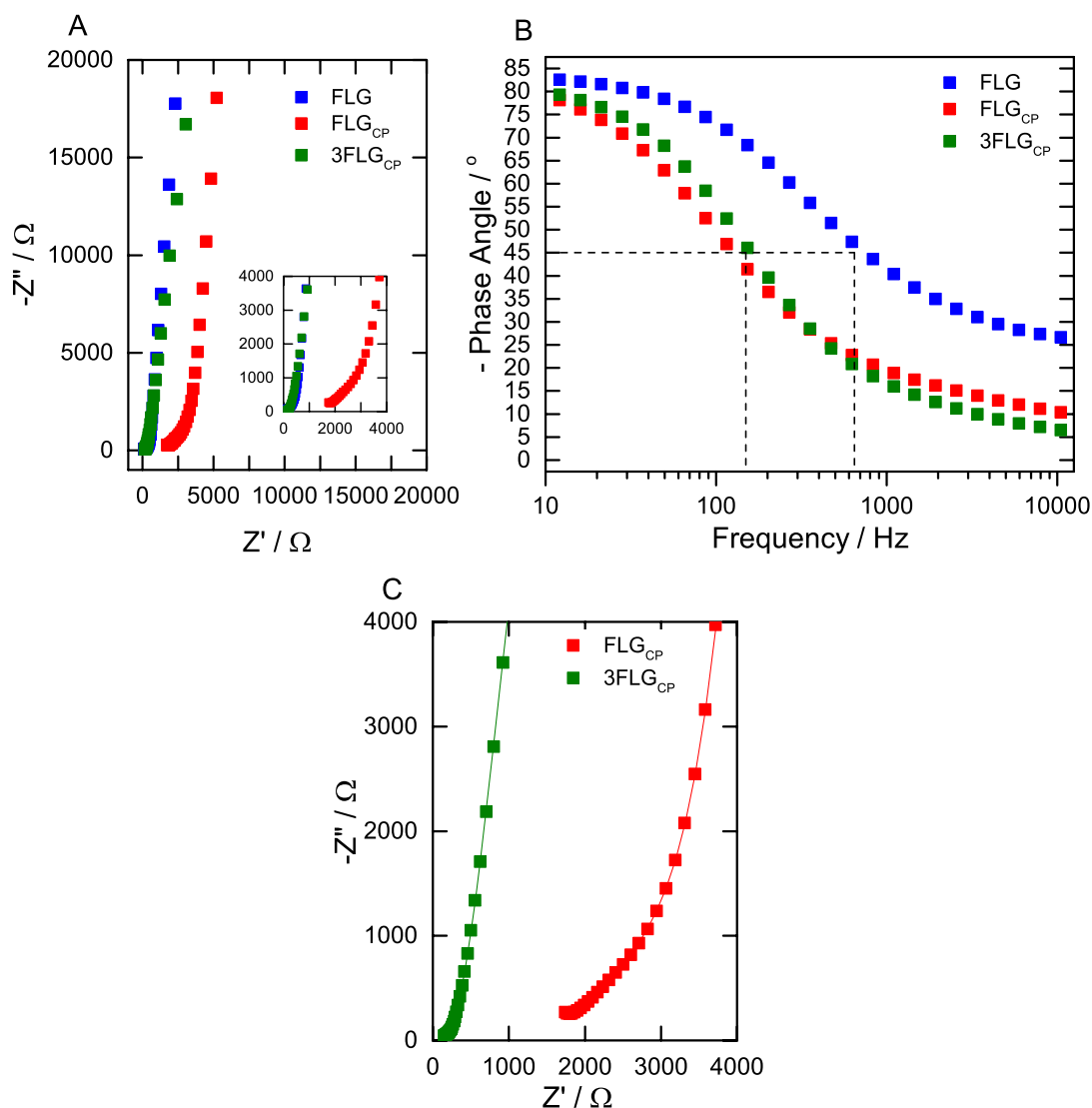


Figure 5.23: EIS data for FLG, FLG_{CP} and $3FLG_{CP}$ at 0.1 V in 1 M $HClO_4$: (A) Nyquist plot; (B) Bode phase angle plot; (C) Nyquist plot with fits.

5.3.4.2 CV and CD Testing of CBD Modified FLG

CV and CD were used to characterise the FLG_{CP} and $3FLG_{CP}$ electrodes. Figure 5.24 shows the CV and CD profiles of the two sample types, with Figure 5.24E and F comparing the one- and three-sheet systems. The CV plots for the one- and three-sheet systems both show a rectangular shape, confirming electrical double layer capacitance.⁶⁸ For the three-sheet system, some deviation from ideality can be seen around 0.2 V, suggesting a small amount of pseudocapacitance exists, albeit a minor contribution to the total area of the CV. The CD profiles show the expected triangular shape characteristic of electrical double layer capacitors,⁶⁸ with a slight deviation from ideal behaviour for the $3FLG_{CP}$ sample, expected to have the same origin as the small

peaks in the CV. As evidenced by Figure 5.24E and F, the areal capacitance increases from the one- to three-sheet systems as expected.

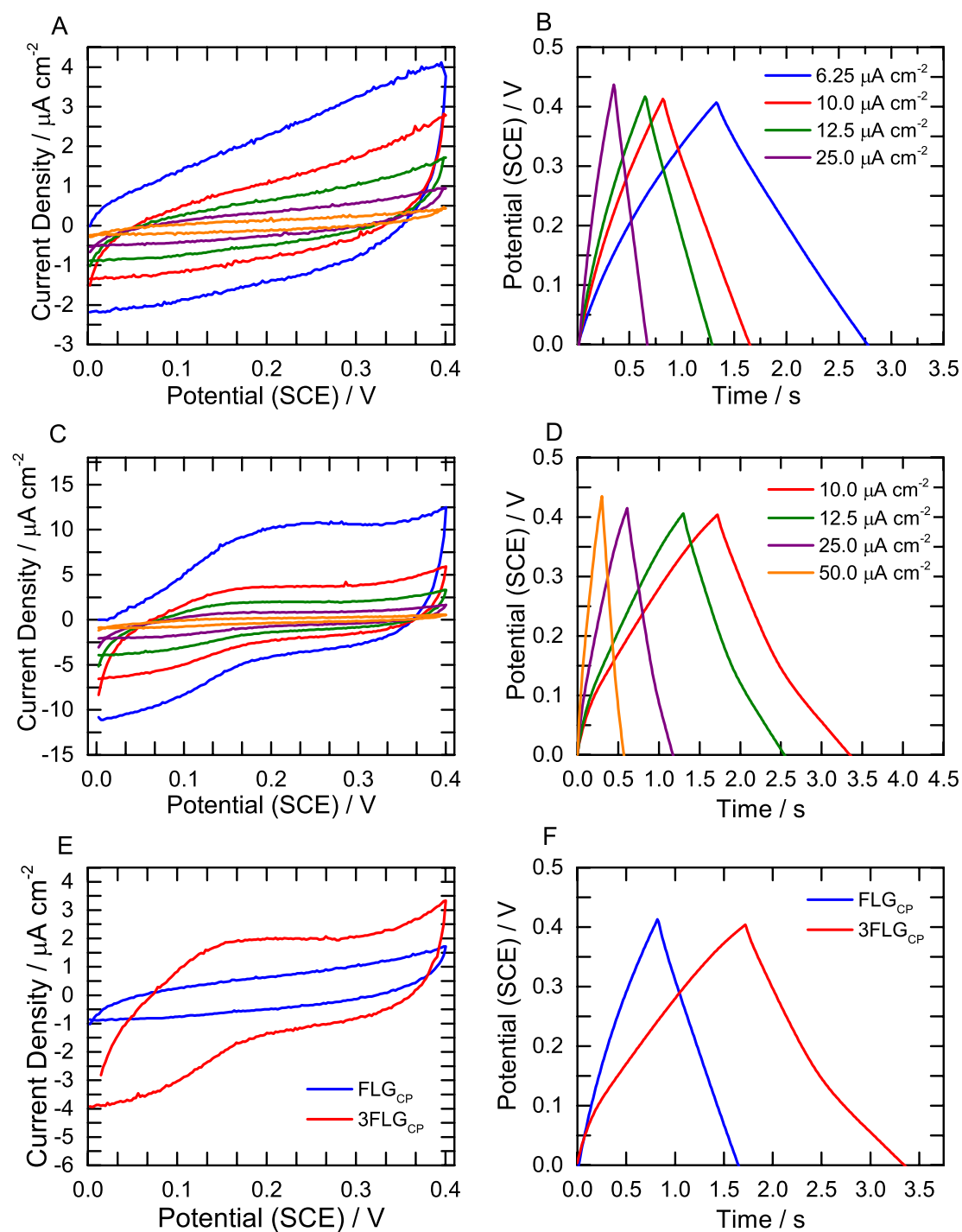
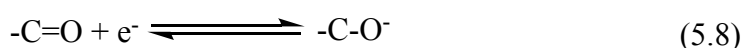
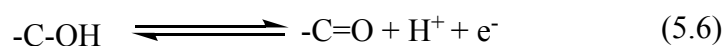


Figure 5.24: CV and CD results in 1 M HClO_4 : (A) and (B) FLG_{CP} ; (C) and (D) 3FLG_{CP} ; (E) CV for FLG_{CP} and 3FLG_{CP} at 50 mV s^{-1} ; (F) CD for FLG_{CP} and 3FLG_{CP} at $10 \mu\text{A cm}^{-2}$. CVs recorded at 200 (blue), 100 (red), 50 (green), 20 (purple), and 5 mV s^{-1} (orange).

The redox peaks for the 3FLG_{CP} sample were unexpected. Literature reports have suggested carboxylic acid groups on carbon nanotubes can take part in Faradaic reactions, for example those shown in Equations 5.6, 5.7, and 5.8.⁶⁹⁻⁷⁰



However, the exact mechanism for these Faradaic processes is controversial, and there is no experimental evidence presented in literature reports. Nevertheless, current peaks are seen for the 3FLG_{CP} samples studied in this thesis work, and are often reported for rGO electrodes, although other oxygen containing functionalities (for example epoxy and hydroxyl groups) may contribute to redox processes for rGO.⁷¹ The only difference between the FLG and FLG_{CP} samples is the CP film, therefore it is reasonable to assume the redox peaks seen in Figure 5.24 are a result of the carboxylic acid moiety. Interestingly, the redox peaks can only be seen for the three-sheet stack. This may mean the peaks are caused by excess physisorbed material that remains between the modified FLG sheets in the stacked sample after the methanol wash.

Table 5.4 summarises the areal capacitance values for the two systems, with the FLG results given for comparison. The areal capacitance increases 3× for the three-sheet system, agreeing with the EIS results, and is much higher than for the 3FLG system, confirming the CP film can also effectively prevent restacking of the FLG sheets. The areal capacitance of the FLG_{CP} and FLG are similar, suggesting the CP film does not diminish the total capacitance of the FLG sheets, unlike the NP film. The small potential drop at the start of the discharge portion of the CD plots suggests a small internal resistance for the modified surfaces, which agrees with EIS analysis, where the FLG_{CP} surfaces possess an additional resistance caused by the film. The three-sheet system retains approximately 90% of its areal capacitance when increasing the current density from 10 to 50 μA cm⁻², while the one sheet system maintains 95% capacitance when increasing the current density from 6.25 to 25 μA cm⁻², indicating the good rate capability of both systems.⁷²

Table 5.4: Average areal capacitance for FLG, FLG_{CP}, and 3FLG_{CP} at 50 mV s⁻¹ and 10 μ A cm⁻². Areal capacitance after 20,000 charge discharge cycles at 10 μ A cm⁻² also included. $n=2$ for all samples.

| Sample | C_A (CV) / μ F cm ⁻² | C_A (CV) after cycling / μ F cm ⁻² | C_A (CD) / μ F cm ⁻² | C_A (CD) after cycling / μ F cm ⁻² | Potential drop / V |
|--------------------|---------------------------------------|---|---------------------------------------|---|--------------------|
| FLG | 11.5 | 9.0 | 15.6 | 15.2 | 0 |
| 3FLG | 7.1 | 9.0 | 10.3 | 9.8 | 0 |
| FLG _{CP} | 6.4 | 5.7 | 15.3 | 14.3 | 0.01 |
| 3FLG _{CP} | 29.6 | 30.7 | 52.4 | 60.7 | 0.01 |

5.3.4.3 Cycle Stability of CBD Modified Stacks

The FLG_{CP} and 3FLG_{CP} samples were cycled at 10.0 μ A cm⁻² for 20,000 cycles to evaluate stability (Figure 5.25). The plot below shows a single sample for each surface type, however the experiments were repeated at least twice to confirm reproducibility and the values presented in Table 5.4 are the average for all samples. The capacitance shows very good stability over the 20,000 cycles, with no loss in areal capacitance, unlike the FLG_{AP} surfaces. These results suggest that the CP layer can efficiently separate the FLG sheets, and the resulting devices do not degrade over time, which is ideal for supercapacitor applications.

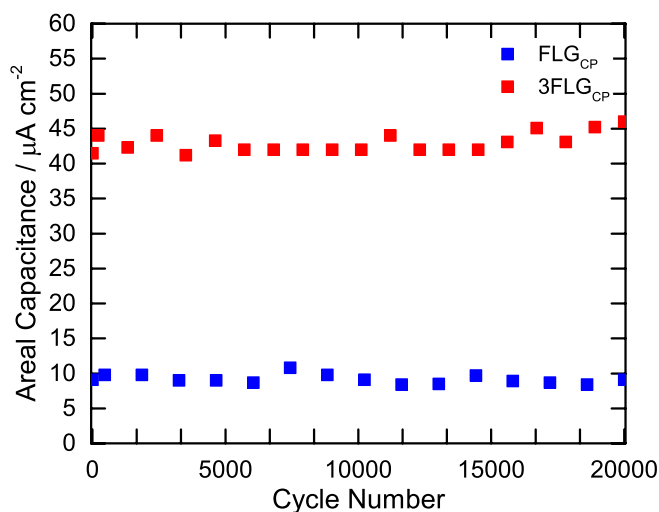


Figure 5.25: Areal capacitance during charge discharge cycling at 10.0 μ A cm⁻² in 1 M HClO₄ of FLG_{CP} and 3FLG_{CP}.

5.3.5 Summary of Capacitance Results

Three different aryldiazonium modified surfaces were considered as supercapacitor electrodes, with the grafted film on one side of the FLG. Table 5.5 summarises the areal capacitances of each system determined using CD at 10 μ A cm⁻². The areal capacitance of each sample type (AP, NP, and CP), increased 3 \times upon stacking into a three-sheet system, confirming the film is able to completely separate the sheets, while when no film is present, there is no increase in the areal capacitance upon stacking, as the

graphene surfaces aggregate. The areal capacitance was converted into a gravimetric capacitance using the calculated weight of each working electrode. To calculate the electrode weight, the theoretical surface area of graphene ($2630 \text{ m}^2 \text{ g}^{-1}$)⁷³ and an average layer number of 3.9 (Chapter 3, Section 3.3.1.2) was used, and the films were assumed to have a surface concentration of $0.21 \text{ nmol cm}^{-2}$, based on the surface concentration of a NP film after a 7 hour reaction. The gravimetric capacitance (C_G) drops significantly between the FLG and 3FLG samples, because the sheets are not separated during stacking, so the total capacitance remains approximately the same, but the total mass increases 3 \times , resulting in a net decrease in the gravimetric capacitance. The C_G for FLG_{AP} and FLG_{CP} is similar to FLG, indicating the additional weight of the grafted film does not diminish the total gravimetric capacitance. For the FLG_{NP} film the C_G is lower due to the decrease in the areal capacitance possibly caused by the film blocking electrolyte access to the surface. Upon stacking of the FLG_{CP} and FLG_{NP} surfaces, the gravimetric capacitance remains relatively constant, indicating that increasing the total mass of the system does not diminish the capacitance, further confirming efficient sheet separation by the film. The 3FLG_{AP} system has a higher gravimetric capacitance than its one sheet counterpart, possibly due to physisorbed material that remains between the sheets after the methanol wash, which will increase the total capacitance through Faradaic reactions. It is difficult to account for the additional mass of the trapped physisorbed material when calculating the electrode mass, so the gravimetric capacitance may be overestimated.

Table 5.5: Average areal capacitance (C_A), gravimetric capacitance (C_G), areal energy density (E_A) and power density (P_A), and gravimetric energy density (E_G) and power density (P_G), calculated from CD at $10 \mu\text{A cm}^{-2}$. $n=2$ for all samples.

| Sample | $C_A / \mu\text{F cm}^{-2}$ | $C_G / \text{F g}^{-1}$ | $E_A \times 10^{-6} / \text{mWh cm}^{-2}$ | $E_G / \text{Wh kg}^{-1}$ | $P_A / \text{mW cm}^{-2}$ | $P_G \times 10^3 / \text{W kg}^{-1}$ |
|--------------------|-----------------------------|-------------------------|---|---------------------------|---------------------------|--------------------------------------|
| FLG | 15.6 | 52.3 | 0.35 | 1.2 | 0.0020 | 6.8 |
| 3FLG | 10.3 | 11.6 | 0.23 | 0.3 | 0.0020 | 2.2 |
| FLG _{AP} | 15.9 | 52.4 | 0.32 | 1.1 | 0.0018 | 5.9 |
| 3FLG _{AP} | 85.7 | 90.4 | 1.7 | 1.8 | 0.0018 | 1.9 |
| FLG _{NP} | 6.4 | 19.0 | 0.13 | 0.4 | 0.0019 | 5.7 |
| 3FLG _{NP} | 19.1 | 19.7 | 0.40 | 0.4 | 0.0019 | 2.0 |
| FLG _{CP} | 15.3 | 47.6 | 0.32 | 1.0 | 0.0019 | 5.9 |
| 3FLG _{CP} | 52.4 | 54.1 | 1.0 | 1.1 | 0.0024 | 2.0 |

From the capacitance values, the energy and power density of each system can be calculated. The energy and power densities at $10 \mu\text{A cm}^{-2}$ are given in Table 5.5, and the calculated values for the other three current densities can be found in Appendix D,

Sections D.1 and D.2. Figure 5.26 uses this information in an areal and gravimetric Ragone plot, with literature examples of other graphene based systems shown for comparison. There are four points for each sample on the Ragone plots, each corresponding to a single applied current density. The areal Ragone plot shows the areal energy density increases with increasing layer number for the modified FLG, as expected with the areal capacitance increasing $3\times$ for the three-sheet systems. The gravimetric energy density remains constant for the one- and three-sheet systems because the gravimetric capacitance remains constant, as explained earlier. The energy density of all systems is lower than most other systems based on reduced graphene oxide and various porous graphene materials, however the areal energy density is similar to CVD graphene and rGO multilayer films assembled via a LBL protocol. The areal capacitance for this literature report was also calculated based on the geometric working electrode area of the CVD graphene or rGO,²⁴ so can be directly compared with this thesis work. The systems show an excellent power density compared with the other graphene based devices, indicating the electrodes can be charged and discharged very quickly due to rapid formation of the double layer and good ion diffusion to each FLG surface.³ The power density remains high in the three-sheet systems, suggesting stacking the sheets does not compromise the speed at which the system can operate, within the current densities examined in this thesis.

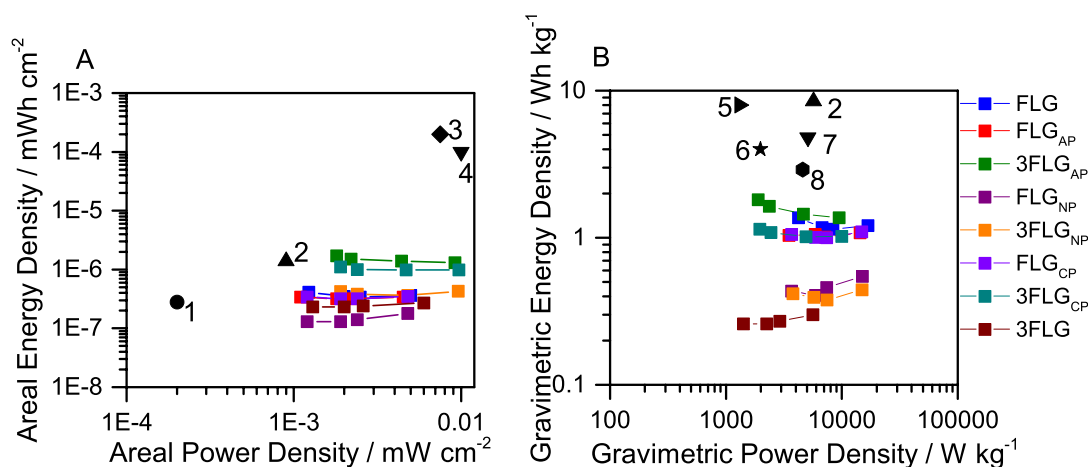


Figure 5.26: Ragone plots for FLG systems shown in colour. Power and energy density calculated at 6.25, 10.0, 12.5, 25.0, and 50.0 $\mu\text{F cm}^{-2}$. Literature examples of CVD graphene (1), reduced graphene oxide multilayer film (2),²⁴ graphene quantum dot micro-supercapacitor (3)⁷⁴, layer by layer graphene supercapacitors (4),⁷ holey graphene (5),⁵¹ activated reduced graphene oxide (6),⁷⁵ pillared graphene paper (7),⁷⁶ and reduced graphene oxide hydrogel (8)⁷⁷ also shown.

5.4 Conclusion

The capacitance of the FLG before and after reaction with aryldiazonium salts has been studied in detail. The modification of FLG with an AP or CP film did not decrease the total capacitance, however the presence of an NP film caused a slight decrease in capacitance, possibly due to the blocking nature of the film compared to the other film types. Upon stacking the modified sheets, a 7 hour, 20 mM aryldiazonium salt reaction was sufficient to completely prevent restacking of the FLG, and therefore maximise the available surface area for double layer formation. The FLG_{NP} and FLG_{CP} systems showed very good cycle stability over 20,000 charge discharge cycles with almost no decrease in capacitance, however the FLG_{AP} one- and three-sheet systems suffered some cyclic degradation caused by a loss in the pseudocapacitive behaviour. Ragone plots were constructed, and this highlighted the excellent power density of the modified FLG stacks. The FLG_{CP} system looks the most promising for building stacks of FLG: although the gravimetric capacitance and energy density of the FLG_{CP} and 3FLG_{CP} are slightly less than the related FLG_{AP} systems, the cycle stability is much better, with the capacitance, energy density and power density all being maintained after 20,000 charge discharge cycles.

5.5 References

1. Raccichini, R.; Varzi, A.; Passerini, S.; Scrosati, B., The role of graphene for electrochemical energy storage. *Nat. Mater.* **2015**, *14*, 271-279.
2. Lv, B.; Zheng, C.; Xu, L.; Zhou, X.; Cao, H.; Liu, Z., Porous graphene-like materials prepared from hollow carbonaceous microspheres for supercapacitors. *ChemNanoMat* **2015**, *1*, 422-429.
3. Shao, Y.; El-Kady, M. F.; Lin, C.-W.; Zhu, G.; Marsh, K. L.; Hwang, J. Y.; Zhang, Q.; Li, Y.; Wang, H.; Kaner, R. B., 3D freeze-casting of cellular graphene films for ultrahigh-power-density supercapacitors. *Adv. Mater.* **2016**, *28*, 6719-6726.
4. Wang, L. J.; El-Kady, M. F.; Dubin, S.; Hwang, J. Y.; Shao, Y.; Marsh, K.; McVerry, B.; Kowal, M. D.; Mousavi, M. F.; Kaner, R. B., Flash converted graphene for ultra-high power supercapacitors. *Adv. Energy Mater.* **2015**, *5*, 1500786.
5. Yadav, S.; Kaur, I., Low temperature processed graphene thin film transparent electrodes for supercapacitor applications. *RSC Adv.* **2016**, *6*, 78702-78713.
6. Lin, Z.; Taberna, P.-L.; Simon, P., Graphene-based supercapacitors using eutectic ionic liquid mixture electrolyte. *Electrochim. Acta* **2016**, *206*, 446-451.
7. Zang, X.; Li, P.; Chen, Q.; Wang, K.; Wei, J.; Wu, D.; Zhu, H., Evaluation of layer-by-layer graphene structures as supercapacitor electrode materials. *J. Appl. Phys.* **2014**, *115*.
8. Robat Sarpoushi, M.; Reza Borhani, M.; Nasibi, M.; Eghdami, B.; Kazerooni, H., Graphene nanosheets as electrode materials for supercapacitors in alkaline and salt electrolytes. *Mater. Sci. Semicond. Process.* **2015**, *31*, 195-199.
9. Qiu, Y.; Chen, Y., Capacitance performance of sub-2 nm graphene nanochannels in aqueous electrolyte. *J. Phys. Chem. C* **2015**, *119*, 23813-23819.
10. Galhena, D. T. L.; Bayer, B. C.; Hofmann, S.; Amaratunga, G. A. J., Understanding capacitance variation in sub-nanometer pores by *in situ* tuning of interlayer constrictions. *ACS Nano* **2016**, *10*, 747-754.
11. Ahn, E.; Lee, T.; Gu, M.; Park, M.; Min, S. H.; Kim, B.-S., Layer-by-layer assembly for graphene-based multilayer nanocomposites: The field manual. *Chem. Mater.* **2017**, *29*, 69-79.
12. Lee, T.; Min, S. H.; Gu, M.; Jung, Y. K.; Lee, W.; Lee, J. U.; Seong, D. G.; Kim, B.-S., Layer-by-layer assembly for graphene-based multilayer nanocomposites: Synthesis and applications. *Chem. Mater.* **2015**, *27*, 3785-3796.
13. Ji, H.; Zhao, X.; Qiao, Z.; Jung, J.; Zhu, Y.; Lu, Y.; Zhang, L. L.; MacDonald, A. H.; Ruoff, R. S., Capacitance of carbon-based electrical double-layer capacitors. *Nat. Commun.* **2014**, *5*.
14. Ke, Q.; Wang, J., Graphene-based materials for supercapacitor electrodes—a review. *J. Materiomics* **2016**, *2*, 37-54.
15. Wang, G.; Sun, X.; Lu, F.; Sun, H.; Yu, M.; Jiang, W.; Liu, C.; Lian, J., Flexible pillared graphene-paper electrodes for high-performance electrochemical supercapacitors. *Small* **2012**, *8*, 452-459.

16. Qiu, L.; Yang, X.; Gou, X.; Yang, W.; Ma, Z. F.; Wallace, G. G.; Li, D., Dispersing carbon nanotubes with graphene oxide in water and synergistic effects between graphene derivatives. *Chem. Eur. J.* **2010**, *16*, 10653-10658.
17. Si, Y.; Samulski, E. T., Exfoliated graphene separated by platinum nanoparticles. *Chem. Mater.* **2008**, *20*, 6792-6797.
18. Mousavi-Khoshdel, S. M.; Targholi, E., Exploring the effect of functionalization of graphene on the quantum capacitance by first principle study. *Carbon* **2015**, *89*, 148-160.
19. Pope, M. A.; Aksay, I. A., Four-fold increase in the intrinsic capacitance of graphene through functionalization and lattice disorder. *J. Phys. Chem. C* **2015**, *119*, 20369-20378.
20. Zhong, C.; Deng, Y.; Hu, W.; Qiao, J.; Zhang, L.; Zhang, J., A review of electrolyte materials and compositions for electrochemical supercapacitors. *Chem. Soc. Rev.* **2015**, *44*, 7484-7539.
21. Cuesta, A.; Kleinert, M.; Kolb, D. M., The adsorption of sulfate and phosphate on Au (111) and Au (100) electrodes: An in situ stm study. *Phys. Chem. Chem. Phys.* **2000**, *2*, 5684-5690.
22. Sharma, P.; Mišković, Z., Capacitance of graphene in aqueous electrolytes: The effects of dielectric saturation of water and finite size of ions. *Physical Review B* **2014**, *90*, 125415.
23. Stoller, M. D.; Ruoff, R. S., Best practice methods for determining an electrode material's performance for ultracapacitors. *Energy & Environmental Science* **2010**, *3*, 1294-1301.
24. Yoo, J. J.; Balakrishnan, K.; Huang, J.; Meunier, V.; Sumpter, B. G.; Srivastava, A.; Conway, M.; Mohana Reddy, A. L.; Yu, J.; Vajtai, R.; Ajayan, P. M., Ultrathin planar graphene supercapacitors. *Nano Lett.* **2011**, *11*, 1423-1427.
25. Luo, J.; Zhong, W.; Zou, Y.; Xiong, C.; Yang, W., Metal-organic coordination polymer to prepare density controllable and high nitrogen-doped content carbon/graphene for high performance supercapacitors. *ACS Appl. Mater. Interfaces* **2017**, *9*, 317-326.
26. Lin, Z.; Liu, Y.; Yao, Y.; Hildreth, O. J.; Li, Z.; Moon, K.; Wong, C.P., Superior capacitance of functionalized graphene. *J. Phys. Chem. C* **2011**, *115*, 7120-7125.
27. Wan, C.; Jiao, Y.; Li, J., Flexible, highly conductive, and free-standing reduced graphene oxide/polypyrrole/cellulose hybrid papers for supercapacitor electrodes. *J. Mater. Chem. A* **2017**, *5*, 3819-3831.
28. Ma, L.; Zheng, M.; Liu, S.; Li, Q.; You, Y.; Wang, F.; Ma, L.; Shen, W., Synchronous exfoliation and assembly of graphene on 3D Ni(OH)₂ for supercapacitors. *Chem. Commun.* **2016**, *52*, 13373-13376.
29. Yu, J.; Wu, J.; Wang, H.; Zhou, A.; Huang, C.; Bai, H.; Li, L., Metallic fabrics as the current collector for high-performance graphene-based flexible solid-state supercapacitor. *ACS Appl. Mater. Interfaces* **2016**.
30. Stoller, M. D.; Magnuson, C. W.; Zhu, Y.; Murali, S.; Suk, J. W.; Piner, R.; Ruoff, R. S., Interfacial capacitance of single layer graphene. *Energy & Environmental Science* **2011**, *4*, 4685-4689.

31. Zhang, D.; Zhang, X.; Chen, Y.; Yu, P.; Wang, C.; Ma, Y., Enhanced capacitance and rate capability of graphene/polypyrrole composite as electrode material for supercapacitors. *J. Power Sources* **2011**, *196*, 5990-5996.
32. Macdonald, D. D., Reflections on the history of electrochemical impedance spectroscopy. *Electrochim. Acta* **2006**, *51*, 1376-1388.
33. Benck, J. D.; Pinaud, B. A.; Gorlin, Y.; Jaramillo, T. F., Substrate selection for fundamental studies of electrocatalysts and photoelectrodes: Inert potential windows in acidic, neutral, and basic electrolyte. *PLoS One* **2014**, *9*, e107942.
34. Magdić, K.; Kvastek, K.; Horvat-Radošević, V., Impedance approach to activity of hydrogen evolution reaction on spatially heterogeneous GC electrode surfaces: Metal free vs. Ru catalysed case. *Electrochim. Acta* **2015**, *167*, 455-469.
35. Brooksby, P. A.; Farquhar, A. K.; Dykstra, H. M.; Waterland, M. R.; Downard, A. J., Quantum capacitance of aryldiazonium modified large area few-layer graphene electrodes. *J. Phys. Chem. C* **2015**, *119*, 25778-25785.
36. Nisancioglu, K.; Newman, J., Separation of double-layer charging and faradaic processes at electrodes. *J. Electrochem. Soc.* **2012**, *159*, E59-E61.
37. Newman, J., Frequency dispersion in capacity measurements at a disk electrode. *J. Electrochem. Soc.* **1970**, *117*, 198-203.
38. Zhong, J.-H.; Liu, J.-Y.; Li, Q.; Li, M.-G.; Zeng, Z.-C.; Hu, S.; Wu, D.-Y.; Cai, W.; Ren, B., Interfacial capacitance of graphene: Correlated differential capacitance and *in situ* electrochemical raman spectroscopy study. *Electrochim. Acta* **2013**, *110*, 754-761.
39. Randin, J.-P.; Yeager, E., Differential capacitance study on the basal plane of stress-annealed pyrolytic graphite. *J. Electroanal. Chem. Interfacial Electrochem.* **1972**, *36*, 257-276.
40. Gerischer, H.; McIntyre, R.; Scherson, D.; Storck, W., Density of the electronic states of graphite: Derivation from differential capacitance measurements. *J. Phys. Chem.* **1987**, *91*, 1930-1935.
41. Xia, J.; Chen, F.; Li, J.; Tao, N., Measurement of the quantum capacitance of graphene. *Nat. Nano* **2009**, *4*.
42. Zhan, C.; Jiang, D.E., Contribution of dielectric screening to the total capacitance of few-layer graphene electrodes. *J. Phys. Chem. Lett.* **2016**, *7*, 789-794.
43. Zhan, C.; Neal, J.; Wu, J.; Jiang, D.E., Quantum effects on the capacitance of graphene-based electrodes. *J. Phys. Chem. C* **2015**, *119*, 22297-22303.
44. Orazem, M. E.; Tribollet, B., *Electrochemical impedance spectroscopy*. John Wiley & Sons: 2011; Vol. 48.
45. Taberna, P.; Simon, P.; Fauvarque, J.-F., Electrochemical characteristics and impedance spectroscopy studies of carbon-carbon supercapacitors. *J. Electrochem. Soc.* **2003**, *150*, A292-A300.
46. Ates, M., Review study of electrochemical impedance spectroscopy and equivalent electrical circuits of conducting polymers on carbon surfaces. *Prog. Org. Coat.* **2011**, *71*, 1-10.

47. Barsoukov, E.; Kim, J. H.; Kim, J. H.; Yoon, C. O.; Lee, H., Effect of low-temperature conditions on passive layer growth on Li intercalation materials *in situ* impedance study. *J. Electrochem. Soc.* **1998**, *145*, 2711-2717.
48. Luo, J.; Ma, Q.; Gu, H.; Zheng, Y.; Liu, X., Three-dimensional graphene-polyaniline hybrid hollow spheres by layer-by-layer assembly for application in supercapacitor. *Electrochim. Acta* **2015**, *173*, 184-192.
49. Wu, M.; Li, Y.; Yao, B.; Chen, J.; Li, C.; Shi, G., A high-performance current collector-free flexible in-plane micro-supercapacitor based on a highly conductive reduced graphene oxide film. *J. Mater. Chem. A* **2016**, *4*, 16213-16218.
50. Bi, H.; Lin, T.; Xu, F.; Tang, Y.; Liu, Z.; Huang, F., New graphene form of nanoporous monolith for excellent energy storage. *Nano Lett.* **2016**, *16*, 349-354.
51. Walsh, E. D.; Han, X.; Lacey, S. D.; Kim, J.-W.; Connell, J. W.; Hu, L.; Lin, Y., Dry-processed, binder-free holey graphene electrodes for supercapacitors with ultrahigh areal loadings. *ACS Appl. Mater. Interfaces* **2016**, *8*, 29478-29485.
52. Casero, E.; Parra-Alfambra, A.; Petit-Domínguez, M.; Pariente, F.; Lorenzo, E.; Alonso, C., Differentiation between graphene oxide and reduced graphene by electrochemical impedance spectroscopy (EIS). *Electrochem. Commun.* **2012**, *20*, 63-66.
53. Pech, D.; Brunet, M.; Durou, H.; Huang, P.; Mochalin, V.; Gogotsi, Y.; Taberna, P.-L.; Simon, P., Ultrahigh-power micrometre-sized supercapacitors based on onion-like carbon. *Nat. Nano* **2010**, *5*, 651-654.
54. Saraf, M.; Natarajan, K.; Mobin, S., Microwave assisted fabrication of a nanostructured reduced graphene oxide (rGO)/Fe₂O₃ composite as a promising next generation energy storage material. *RSC Adv.* **2017**, *7*, 309-317.
55. Holzapfel, M.; Martinent, A.; Alloin, F.; Le Gorrec, B.; Yazami, R.; Montella, C., First lithiation and charge/discharge cycles of graphite materials, investigated by electrochemical impedance spectroscopy. *J. Electroanal. Chem.* **2003**, *546*, 41-50.
56. Abouzari, M. S.; Berkemeier, F.; Schmitz, G.; Wilmer, D., On the physical interpretation of constant phase elements. *Solid State Ionics* **2009**, *180*, 922-927.
57. Ceccato, M.; Nielsen, L. T.; Iruthayaraj, J.; Hinge, M.; Pedersen, S. U.; Daasbjerg, K., Nitrophenyl groups in diazonium-generated multilayer films: Which are electrochemically responsive? *Langmuir* **2010**, *26*, 10812-10821.
58. Brooksby, P. A.; Downard, A. J., Electrochemical and atomic force microscopy study of carbon surface modification via diazonium reduction in aqueous and acetonitrile solutions. *Langmuir* **2004**, *20*, 5038-5045.
59. Marcus, Y., Ionic radii in aqueous solutions. *Chem. Rev.* **1988**, *88*, 1475-1498.
60. Liu, Y.-C.; McCreery, R. L., Reactions of organic monolayers on carbon surfaces observed with unenhanced raman spectroscopy. *J. Am. Chem. Soc.* **1995**, *117*, 11254-11259.
61. Sheng, K.; Sun, Y.; Li, C.; Yuan, W.; Shi, G., Ultrahigh-rate supercapacitors based on electrochemically reduced graphene oxide for ac line-filtering. *Scientific reports* **2012**, *2*, 247.

62. Zhou, Q.; Zhang, M.; Chen, J.; Hong, J.-D.; Shi, G., Nitrogen-doped holey graphene film-based ultrafast electrochemical capacitors. *ACS Appl. Mater. Interfaces* **2016**, *8*, 20741-20747.
63. Kirubasankar, B.; Murugadoss, V.; Angaiah, S., Hydrothermal assisted in situ growth of cove onto graphene nanosheets as a nanohybrid positive electrode for asymmetric supercapacitors. *RSC Adv.* **2017**, *7*, 5853-5862.
64. Xie, B.; Yang, C.; Zhang, Z.; Zou, P.; Lin, Z.; Shi, G.; Yang, Q.; Kang, F.; Wong, C.-P., Shape-tailorable graphene-based ultra-high-rate supercapacitor for wearable electronics. *ACS Nano* **2015**, *9*, 5636-5645.
65. Alazmi, A.; El Tall, O.; Rasul, S.; Hedhili, M. N.; Patole, S. P.; Costa, P. M. F. J., A process to enhance the specific surface area and capacitance of hydrothermally reduced graphene oxide. *Nanoscale* **2016**, *8*, 17782-17787.
66. Kumar, R.; Singh, R. K.; Savu, R.; Dubey, P. K.; Kumar, P.; Moshkalev, S. A., Microwave-assisted synthesis of void-induced graphene-wrapped nickel oxide hybrids for supercapacitor applications. *RSC Adv.* **2016**, *6*, 26612-26620.
67. Yilmaz, G.; Lu, X.; Ho, G. W., Cross-linker mediated formation of sulfur-functionalized V₂O₅/graphene aerogels and their enhanced pseudocapacitive performance. *Nanoscale* **2017**, *9*, 802-811.
68. Liu, C.; Yu, Z.; Neff, D.; Zhamu, A.; Jang, B. Z., Graphene-based supercapacitor with an ultrahigh energy density. *Nano Lett.* **2010**, *10*, 4863-4868.
69. Frackowiak, E.; Beguin, F., Carbon materials for the electrochemical storage of energy in capacitors. *Carbon* **2001**, *39*, 937-950.
70. Frackowiak, E.; Metenier, K.; Bertagna, V.; Beguin, F., Supercapacitor electrodes from multiwalled carbon nanotubes. *Appl. Phys. Lett.* **2000**, *77*, 2421-2423.
71. Xu, B.; Yue, S.; Sui, Z.; Zhang, X.; Hou, S.; Cao, G.; Yang, Y., What is the choice for supercapacitors: Graphene or graphene oxide? *Energ. Environ. Sci* **2011**, *4*, 2826-2830.
72. El-Kady, M. F.; Ihns, M.; Li, M.; Hwang, J. Y.; Mousavi, M. F.; Chaney, L.; Lech, A. T.; Kaner, R. B., Engineering three-dimensional hybrid supercapacitors and microsupercapacitors for high-performance integrated energy storage. *Proc. Natl. Acad. Sci. U.S.A.* **2015**, *112*, 4233-4238.
73. Zhu, Y.; Murali, S.; Cai, W.; Li, X.; Suk, J. W.; Potts, J. R.; Ruoff, R. S., Graphene and graphene oxide: Synthesis, properties, and applications. *Adv. Mater.* **2010**, *22*, 3906-3924.
74. Liu, W. W.; Feng, Y. Q.; Yan, X. B.; Chen, J. T.; Xue, Q. J., Superior micro-supercapacitors based on graphene quantum dots. *Adv. Funct. Mater.* **2013**, *23*, 4111-4122.
75. Chang, H.-W.; Lu, Y.-R.; Chen, J.-L.; Chen, C.-L.; Chen, J.-M.; Tsai, Y.-C.; Chou, W. C.; Dong, C.-L., Electrochemically activated reduced graphene oxide used as solid-state symmetric supercapacitor: An X-ray absorption spectroscopic investigation. *J. Phys. Chem. C* **2016**.
76. Gogotsi, Y.; Simon, P., True performance metrics in electrochemical energy storage. *Science* **2011**, *334*, 917-918.

77. Pham, V. H.; Dickerson, J. H., Reduced graphene oxide hydrogels deposited in nickel foam for supercapacitor applications: Toward high volumetric capacitance. *J. Phys. Chem. C* **2016**, *120*, 5353-5360.

6 Electrochemical Deposition of Gold Nanoparticles and Cobalt-Nickel Hydroxide Thin Films onto FLG

6.1 Introduction

6.1.1 Gold Nanoparticle Deposition on Graphene

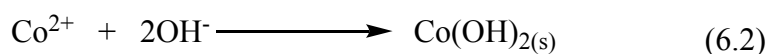
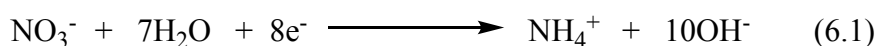
Graphene aggregation can also be inhibited using metal nanoparticle spacers.¹ In this thesis work, gold nanoparticles were used as a model system to establish whether metal nanoparticles are able to completely prevent aggregation of FLG sheets during the LBL assembly protocol, similar to the molecular spacers used in Chapter 5. Gold nanoparticles were deposited electrochemically, as this allows nanoparticle height and density to be tightly controlled.² Electrochemical deposition of gold nanoparticles is typically carried out in aqueous conditions, however this deposition process results in uncontrolled nanoparticle deposition onto FLG grown through CVD when the FLG is supported by copper. In water, the reduction potential of the Cu/Cu²⁺ couple (0.34 V vs. SHE) is less positive than the reduction potential of the Au/[AuCl₄]⁻ couple (1.002 V vs. SHE),³ hence the copper foil can reduce the gold salt, which can initiate nanoparticle nucleation, and cause dissolution of the copper foil. This means the electrochemical deposition process is difficult to control as the spontaneous and electrochemical processes will occur simultaneously.

Recently, Navarro et al.⁴ demonstrated that the spontaneous deposition of gold nanoparticles on graphene/Cu could be inhibited by applying a negative potential to the graphene/Cu working electrode prior to adding the metal salt precursor to the electrolyte solution. A simpler approach to controlling electrochemical deposition onto graphene/Cu working electrode is using non-aqueous conditions as the reduction potential of the gold salt is more negative in organic solvents due to differences in solvation energy. For example, in 1,2-dichloroethane, the calculated reduction potential of the Au/[AuCl₄]⁻ couple is -1.14 V vs. SHE,⁵ so the reduction of the gold salt by the copper foil and subsequent nanoparticle nucleation will become thermodynamically non-spontaneous, allowing better control over deposition. In this chapter, the electrochemical deposition of gold nanoparticles in the organic solvent N,N-dimethylformamide (DMF) will be used to controllably deposit gold nanoparticles onto copper supported FLG. DMF was chosen as an appropriate solvent as it is often used

in electrochemistry and can readily dissolve the tetraoctylammonium tetrachloroaurate ((TOA)[AuCl₄]) salt.

6.1.2 Cobalt-Nickel Hydroxide Deposition on Graphene

Metal hydroxides can also be deposited onto graphene surfaces. As explained in Chapter 1, Section 1.4, cobalt and nickel hydroxide nanomaterials are commonly used to increase the total capacitance of carbon electrodes through pseudocapacitance. Cobalt and nickel hydroxide nanomaterials can be electrochemically deposited onto carbon substrates. The carbon electrode is immersed in an aqueous solution of Co(NO₃)₂ or Ni(NO₃)₂ (or a mixture of both), and a negative potential applied. Application of a negative potential causes reduction of nitrate ions, resulting in the generation of hydroxide ions. The local increase in pH associated with hydroxide ion generation causes the precipitation of cobalt and nickel hydroxide at the electrode surface. This is shown in Equations 6.1 and 6.2 for cobalt hydroxide deposition (the same process is expected for nickel hydroxide deposition).



Jun et al.⁶ electrochemically deposited cobalt hydroxide flakes onto a 3D graphene foam. The resulting structures were vertically aligned, with a thickness of 20 to 40 nm. A maximum gravimetric capacitance of 1030 F g⁻¹ was achieved at 9 A g⁻¹, a significant increase compared with the graphene foam. Li et al.⁷ deposited nickel hydroxide nanoflakes onto a graphene/nickel foam electrode. Similar to cobalt hydroxide, the nickel hydroxide flakes were vertically aligned with the carbon surface, and the capacitance increased to ~ 2000 F g⁻¹ at 3 A g⁻¹, with a 64 % capacitance retention after 500 charge discharge cycles. Fisher et al.⁸ prepared a hybrid system with both cobalt and nickel hydroxide flakes on a graphene petal foam, and this method will be explored further in this thesis work. Literature reports have shown that binary metal hydroxide nanoparticles have superior electrochemical performance compared with the individual metal hydroxides.⁹ In Fisher's work, cobalt-nickel hydroxide/graphene foam surfaces were prepared via electrochemical deposition, where the graphene foam electrode was immersed in a Co(NO₃)₂:Ni(NO₃)₂ solution and a negative potential applied. Earlier work by Xu et al.¹⁰ demonstrated that a 1:3 ratio of cobalt to nickel in the electrolyte solution was best for pseudocapacitance applications, as the addition of cobalt

hydroxide effectively boosts the conductivity and stability of the system, but also decreases the overall specific capacitance meaning excess cobalt hydroxide may have a negative effect on the total capacitance. Analogous to the individual metal hydroxides, the binary metal hydroxide structure was described as individual platelets or flakes, vertically aligned with the surface. A very high areal capacitance of 15.3 F cm^{-2} was achieved at 5 mA cm^{-2} , which is higher than graphene foam composites with other pseudocapacitive metal hydroxides that give areal capacitances between 0.2 to 3.3 F cm^{-2} (calculated based on the geometric working electrode area).⁶⁻⁷

6.2 Experimental Methods

All experimental methods are outlined in Chapter 2. The gold nanoparticle and cobalt-nickel hydroxide film deposition procedures are given in Section 2.4.4 and 2.4.5, respectively. All gold depositions were in 0.36 mM (TOA)[AuCl₄] and 0.1 M tetrabutylammonium perchlorate (TBAClO₄) in DMF. All cobalt-nickel hydroxide depositions were in a solution of 0.03 M Co(NO₃)₂·6H₂O and 0.1 M Ni(NO₃)₂·6H₂O in water. Assembly of the modified electrodes for capacitance studies is described in Section 2.5.2 and 2.5.3 for the gold and metal hydroxide samples respectively. All characterisation methods are given in Section 2.6. Calculated capacitance values for the metal hydroxide deposition are given in Appendix C, Sections C.3 and C.4, and calculated power and energy densities are given in Appendix D, Sections D.3 and D.4.

6.3 Results and Discussion

6.3.1 FLG Decorated with Gold Nanoparticles

6.3.1.1 Inhibition of Spontaneous Nanoparticle Deposition

Figure 6.1 shows AFM images of copper-supported FLG before and after a 5 minute immersion in the DMF deposition solution (0.1 M TBAClO₄ and 0.36 mM (TOA)[AuCl₄]) in the absence of an applied potential. The FLG was subsequently transferred to a silicon wafer for imaging. There are no new features on the FLG after immersion in the DMF gold salt solution, which strongly suggests the use of an organic solvent prevents spontaneous nucleation of gold nanoparticles. As a comparison, immersion in an equivalent aqueous deposition solution for only 1 minute showed substantial gold nanoparticle deposition, with nanoparticles ranging from 5 - 10 nm in height.³ In Figure 6.1, numerous small circular features ($\sim 1 \text{ nm}$ in height), along with wrinkles and folds, can be seen both before and after immersion, and it is assumed these

arise from the etching and transfer process (see Chapter 3, Section 3.3.1.3). These AFM images therefore support that spontaneous nucleation of gold is inhibited in DMF.

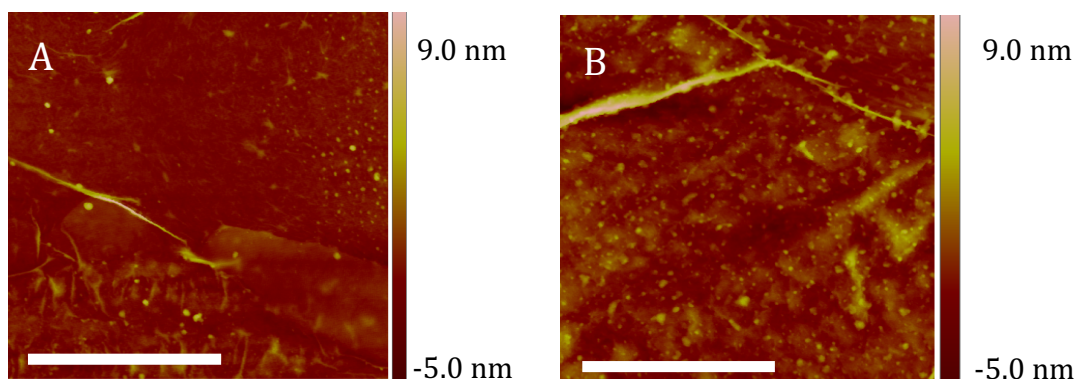


Figure 6.1: AFM images of FLG transferred to a Si wafer before (A) and after (B) a 5 minute immersion on the Cu foil in the DMF gold deposition solution, with no applied potential. Scale bar = 500 nm.

6.3.1.2 Electrodeposition of Gold Nanoparticles

CVs between -0.4 and -1.1 V with a FLG/Cu working electrode were collected to establish the appropriate potential for the electrochemical deposition of gold nanoparticles from DMF. Figure 6.2 shows the resulting CV (blue), with a large $[\text{AuCl}_4]^-$ reduction peak at -0.7 V caused by reduction to Au(0) at the surface of the FLG/Cu.¹¹

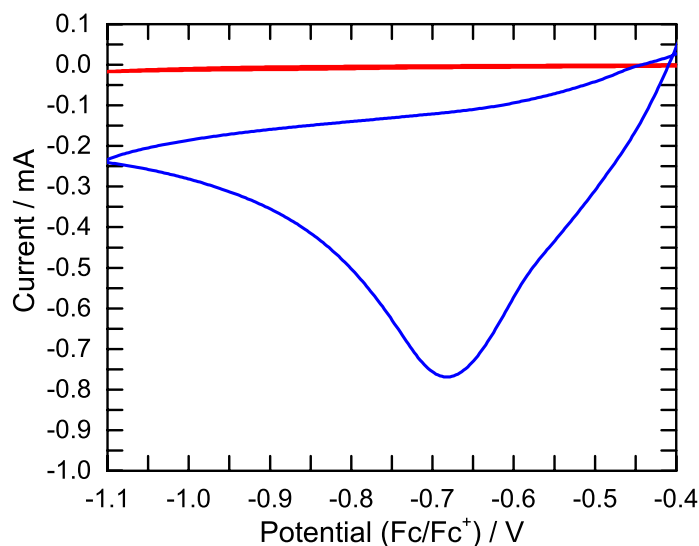
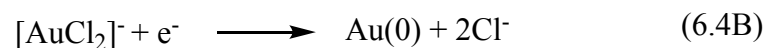


Figure 6.2: CV of FLG/Cu in DMF with: (blue) 0.36 mM (TOA)[AuCl₄] and 0.1 M TBAClO₄ or (red) 0.1 M TBAClO₄. Scan rate = 100 mV s⁻¹.

The $[\text{AuCl}_4]^-$ reduction can be via a one step, three electron reduction process (Equation 6.3), or a two step process, with a two electron and a subsequent one electron step (Equations 6.4A and B). The one step process is commonly seen in aqueous

conditions,¹¹⁻¹² whereas the two step process has been reported in ionic liquids¹³ and dimethyl sulfoxide (DMSO).¹⁴



Only one reduction peak is seen in Figure 6.2 at -0.68 V, therefore it is likely the reduction in DMF is via the one step, three electron process. Although a small shoulder can be seen at -0.51 V, this is not assigned to the first reduction step of the two step mechanism, as the first peak should be twice the height of the second as two electrons are involved in the first reduction step. It should be noted that in literature reports that utilise DMSO as the solvent, the first reduction peak is at -0.3 V, which is outside the potential window studied in this work. The experiment was therefore repeated with a GC working electrode, scanning from 0.9 to -1.1 V (Figure 6.3). GC was used as the working electrode instead of FLG/Cu, because applied potentials more positive than -0.4 V resulted in oxidation of the copper, which complicated the resulting CV, and caused copper dissolution. Only one reduction peak can be seen at -0.55 V (Figure 6.3) with this wider potential window, strongly suggesting that the reduction of $[\text{AuCl}_4]^-$ in DMF is through the one step, three electron process.

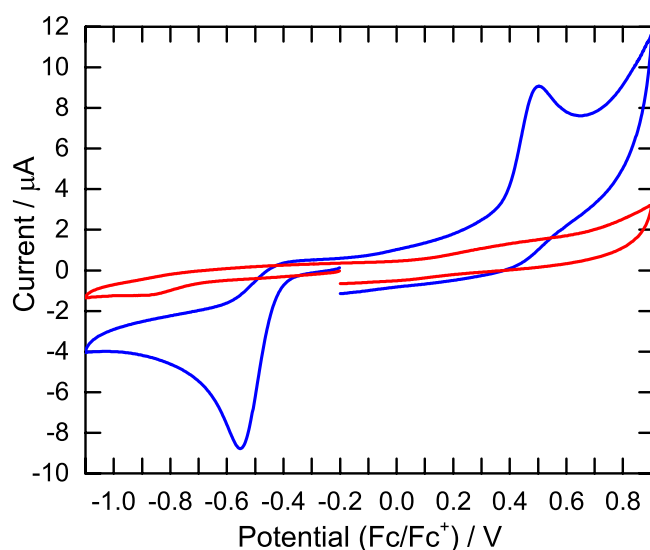


Figure 6.3: CV of GC in DMF with: (blue) 0.36 mM (TOA) $[\text{AuCl}_4]$ and 0.1 M TBAClO₄ or (red) 0.1 M TBAClO₄. Scan rate = 100 mV s⁻¹.

Based on the reduction potential of the peak seen in Figure 6.2, three potentials (-0.4 , -0.6 and -0.8 V vs. Fc/Fc^+) were selected for gold nanoparticle deposition on FLG/Cu

using a constant applied potential for selected times. Chronoamperometric transients were collected during each deposition process, with Figure 6.4 showing representative transients for a 1 minute deposition at -0.6 and -0.8 V. An initial nucleation phase, where the current rapidly increases, followed by an extended growth phase can be clearly seen. The nanoparticle deposition mechanism will be discussed further later in this chapter.

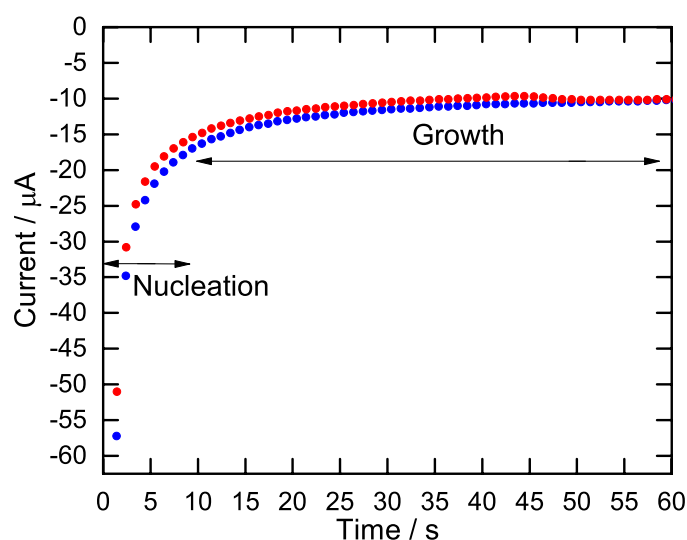


Figure 6.4: Chronoamperometric transients of FLG/Cu in the gold deposition solution at -0.6 (blue) and -0.8 V (red) for 1 minute.

Figure 6.5 shows representative AFM images of FLG_{Au} for five different deposition conditions. Nanoparticles can clearly be seen on the FLG_{Au} , which are much higher than the transfer residue features seen in Figure 6.1. The nanoparticle distribution across the surface is assumed to be influenced by variations in reactivity, for example edge and basal plane regions may exhibit different reactivity towards nanoparticle nucleation, as would folds and grain boundaries. The large, white areas are assumed to be caused by water trapped between FLG_{Au} and the silicon wafer during transfer.¹⁵⁻¹⁶

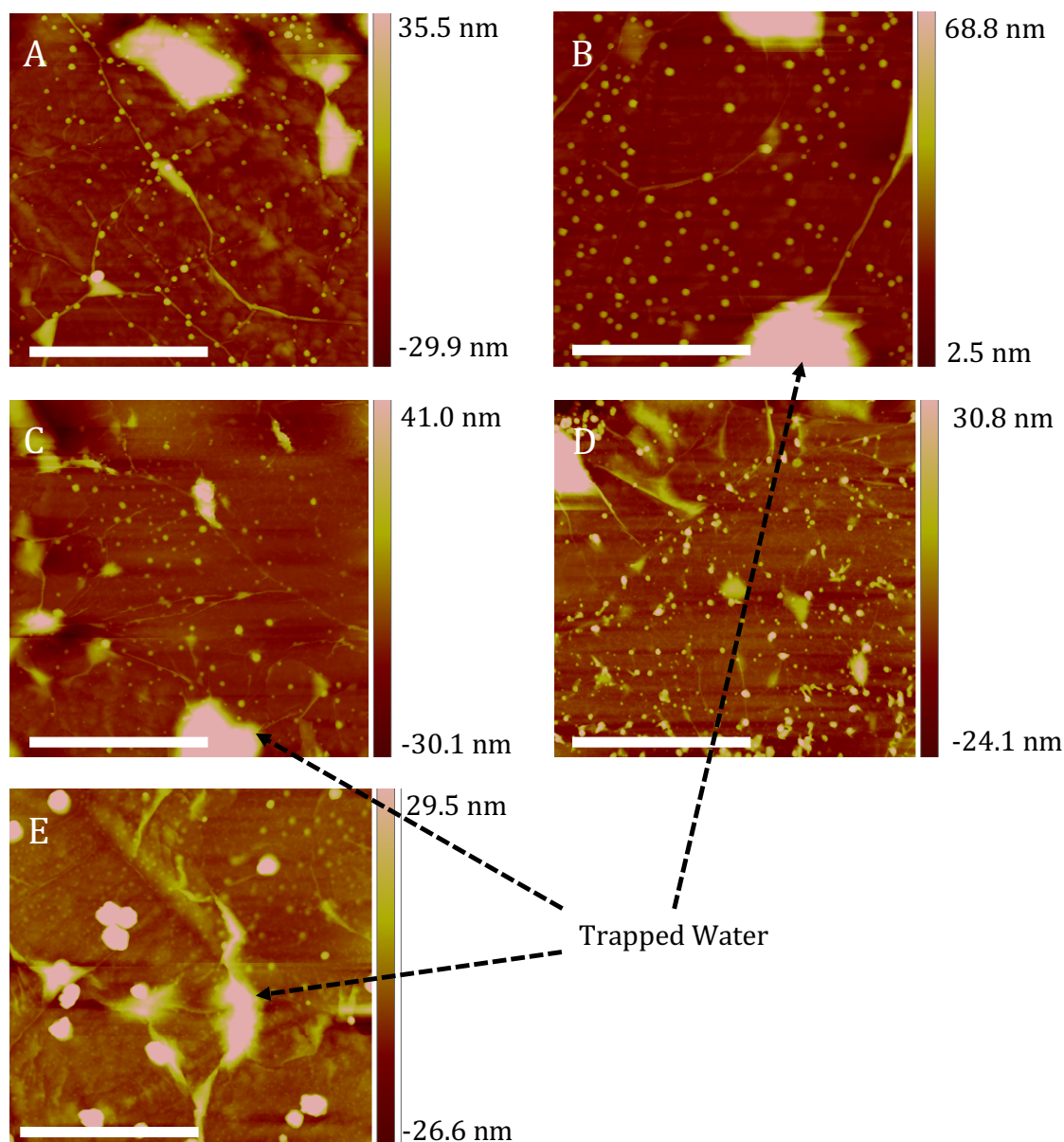


Figure 6.5: AFM images of FLG_{Au} transferred to a silicon wafer after electrodepositon of gold nanoparticles on FLG/Cu for: (A) 5 minutes at -0.4 V; (B) 10 minutes at -0.4 V; (C) 5 minutes at -0.6 V; (D) 10 minutes at -0.6 V; (E) 10 minutes at -0.8 V. Scale bar = $1.25 \mu\text{m}$.

The height and density of the nanoparticles can be calculated from the AFM images. Height rather than diameter was measured, as the diameter of nanoparticles less than 50 nm across cannot be accurately determined with the tip used in this AFM setup. Figure 6.6 shows the dependence of nanoparticle density and height on both deposition time and applied potential. The relationship between density or height, and applied potential or deposition time is similar to literature reports for gold nanoparticle deposition on carbon nanotubes and HOPG,¹⁷⁻¹⁹ and suggests a kinetically controlled, instantaneous nucleation step and diffusion controlled growth phase.⁵

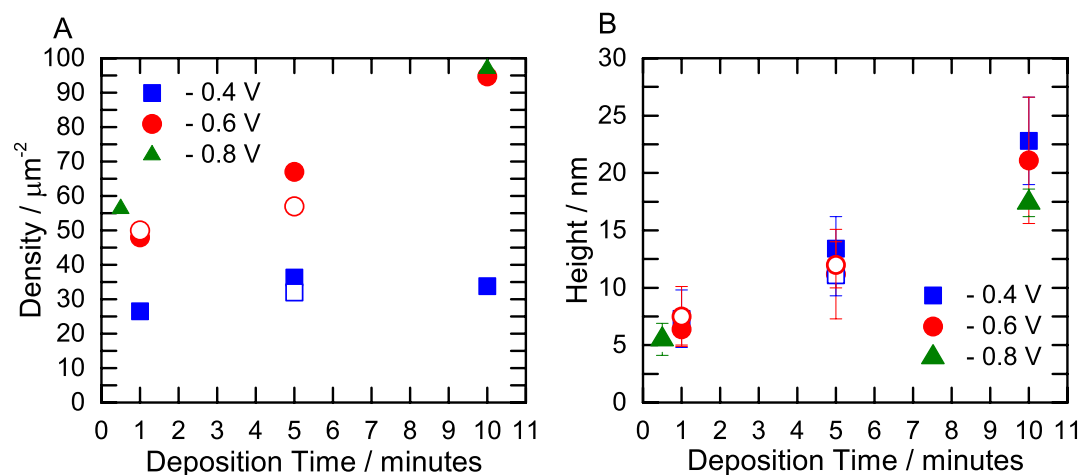


Figure 6.6: Dependence of (A) particle density, and (B) particle height on deposition time and applied potential. Error bars show the standard deviation of particle height over a $1 \mu\text{m} \times 1 \mu\text{m}$ area. Hollow and solid symbols of the same colour show results of duplicate experiments under the same conditions.

As expected for deposition by this mechanism, the density of the nanoparticles increased with more negative applied potentials, as a result of the higher reduction rate at the more negative potential.^{5, 17, 19-20} The slight increase in density with increasing deposition time, indicates that a small amount of nucleation continues throughout the growth phase. The sample prepared at -0.8 V did not show the same increase in nanoparticle density, which is assumed to be a consequence of the particle aggregation that can be seen in Figure 6.5E and in SEM images (Figure 6.7), which makes it difficult to accurately establish the nucleation density. Hence the measured value is assumed to be underestimated.

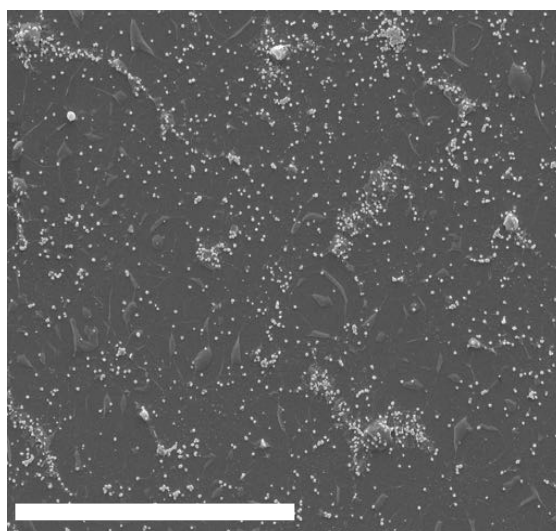


Figure 6.7: SEM image of FLG_{Au} transferred to a silicon wafer after a 10 minute electrodeposition of gold nanoparticles at -0.8 V on FLG/Cu . Scale bar = $5 \mu\text{m}$.

After the nucleation step, there is a diffusion controlled growth phase, evidenced by the increase in nanoparticle height at longer deposition times. Nanoparticle height is expected to be independent of deposition potential, however a slight decrease in height at more negative potentials can be seen, assumed to be caused by the increase in particle density resulting in a lower flux of $[\text{AuCl}_4]^-$ to each particle and therefore a slower growth rate.¹⁹ Differences in diffusion gradients at each nanoparticle surface is also thought to cause the broadening size distribution at longer reaction times, evidenced by the increase in error bar size (Figure 6.6B).¹⁷

Figure 6.8 shows the relationship between nanoparticle height and density. The area enclosed by the solid lines illustrates the accessible nanoparticle morphologies using this protocol, and it is reasonable to assume that any combination within this area can be achieved by selecting the appropriate conditions.

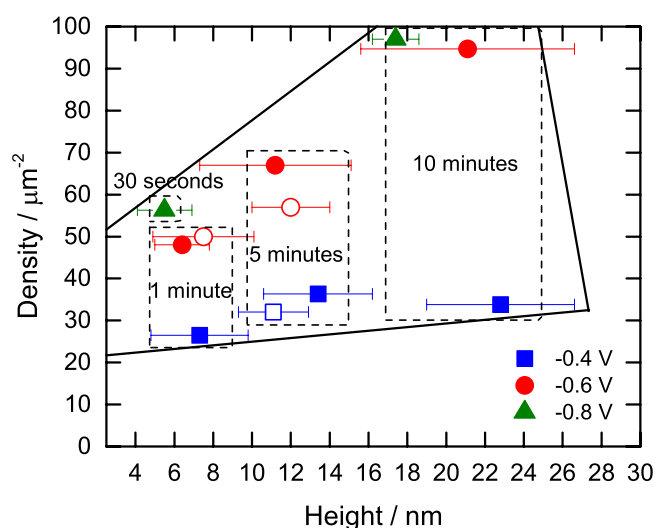


Figure 6.8: Relationship between nanoparticle density and particle height at different applied potentials and deposition times. Hollow and solid symbols of the same colour show results of duplicate experiments under the same conditions.

6.3.1.3 Growth in the Absence of an Applied Potential

It was noted that once nucleation was initiated by an applied potential, growth of the nanoparticles could continue in the absence of an applied potential. Figure 6.9 shows an AFM image of FLG that had a potential of -0.6 V applied for 1 minute in the DMF deposition solution, and then the FLG/Cu was left immersed in the solution for a further 9 minutes with no applied potential. The FLG_{Au} was transferred to a silicon substrate for imaging. The calculated nanoparticle density was close to the density of the sample prepared from a 1 minute deposition at -0.6 V ($51 \mu\text{m}^{-2}$), suggesting nucleation only

occurred when the potential was applied. However, the nanoparticle height was approximately 15.3 nm, which is much higher than the -0.6 V, 1 minute sample, and closer to the -0.6 V, 10 minute sample. This result indicates that nanoparticle growth does not require an applied potential, and that the growth rates in both the presence and absence of a potential are similar, implying growth is diffusion controlled. There must be a reducing agent present for growth to continue without an applied potential. It is proposed that the DMF solvent can reduce the $[\text{AuCl}_4]^-$, as literature reports have suggested that gold and silver nanoparticles can be prepared via reduction of the corresponding metal salt by DMF at elevated temperatures.²¹ The results therefore suggest that the spontaneous nucleation of gold nanoparticles on FLG/Cu is prohibited in DMF (Figure 6.1) but once nucleation has occurred, the DMF is able to reduce $[\text{AuCl}_4]^-$ at the nanoparticle surface leading to continued growth. This could be confirmed by changing to a different solvent based gold solution that would not reduce the gold salt, however the major consequence for this work is that the sample must be removed from the deposition solution to ensure the nanoparticle height and density was controlled, therefore this was not investigated further.

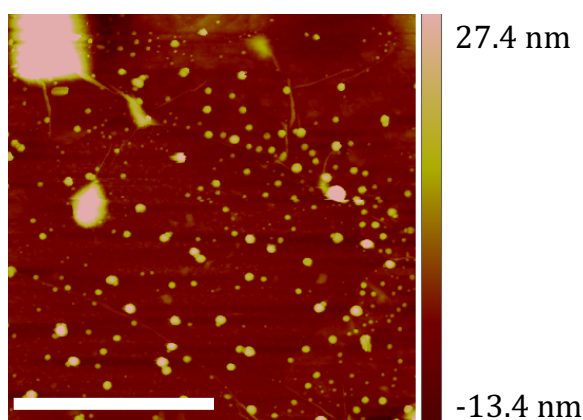


Figure 6.9: AFM image of FLG_{Au} transferred to a silicon wafer after deposition of gold nanoparticles on FLG/Cu for 1 minute at -0.6 V, followed by immersion in the same deposition solution for a further 9 minutes. Scale bar = $1.25 \mu\text{m}$.

6.3.1.4 Doping by Gold Nanoparticles

Figure 6.10 shows the Raman spectra of FLG before (blue) and after (red) a 5 minute gold nanoparticle deposition at -0.6 V. The D/G band intensity ratio has increased from 0.51 ± 0.09 to 0.71 ± 0.30 after modification, additionally, after deposition, a D' -band appears at 1625 cm^{-1} (indicated by an asterisk). This latter band is also a defect activated band.²² The increase in intensity of the D- and D' -bands supports the successful

modification of FLG, as the defects are likely created by chemical interactions between the gold nanoparticles and FLG.

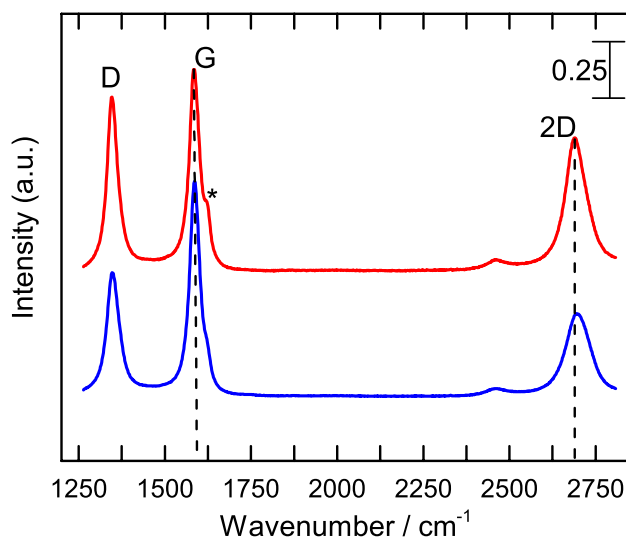


Figure 6.10: Raman spectra of FLG transferred to a silicon wafer before (blue) and after deposition of gold nanoparticles for 5 minutes at -0.6 V on FLG/Cu (red). Spectra normalised to give a G-band intensity of 1. Spectra offset for clarity.

As explained in Chapter 3, Section 3.3.2.1, Raman spectroscopy can be used to detect doping via shifts in the G- and 2D-band positions. Figure 6.11 shows the position of the G- and 2D-bands for FLG with gold nanoparticles deposited at different time and potential combinations. The average G-band position shifts to a higher wavenumber after a 1 minute deposition for both applied potentials (-0.4 and -0.6 V vs. Fc/Fc^+), and the 2D-band shifts to a lower wavenumber, indicating n-doping, especially for the samples prepared at -0.6 V. As the amount of gold on the surface increases with longer deposition times, the shift in the position of both bands reduces, with the 10 minute sample having almost the same peak position as the blank, suggesting a reduction in the n-doping character of the surface. This agrees with work by Ruoff et al.²² who studied the effect of gold nanoparticle coverage on doping, and reported that graphene decorated with gold nanoparticles was n-doped. As the amount of gold increased, the surface became increasingly less n-doped, until the sample became p-doped when the graphene was covered by a thin film of gold. They ascribed this behaviour to differences in the interfacial interactions between graphene and the nanoparticles, and graphene and a thin gold film. Although the average values reported here trend in the same manner, the standard deviation on each value is high, likely due to variations across the FLG surface, so it is not possible to establish with certainty the significance of any 2D- or G-band shifts.

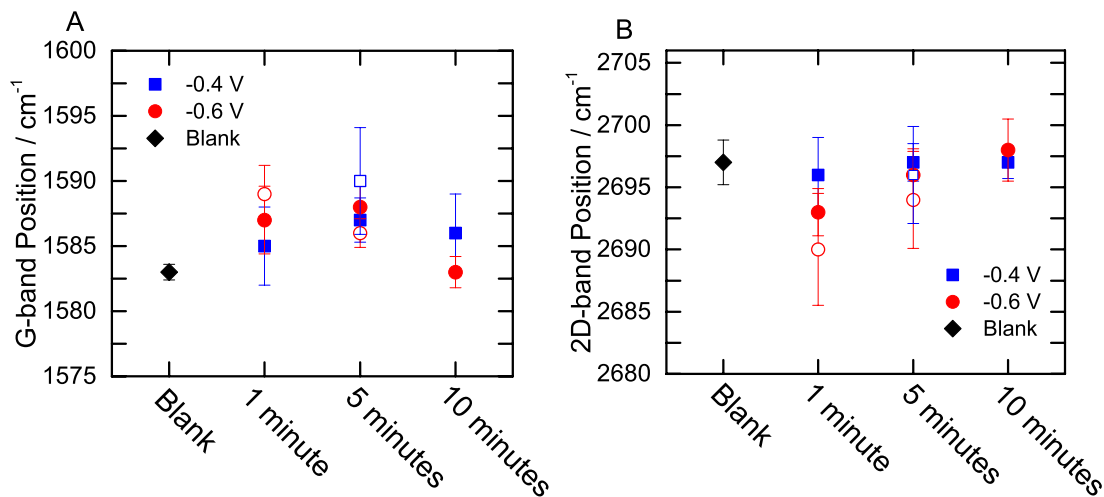


Figure 6.11: Shift in G-band (A) and 2D-band (B) position for FLG decorated with gold nanoparticles. Hollow and solid symbols of the same colour show results of duplicate experiments under the same conditions.

6.3.1.5 Capacitance of Gold Nanoparticle Modified FLG

As explained in Section 6.1.1, gold nanoparticles were used as a model system to establish whether the nanoparticles could effectively prevent aggregation of the FLG sheets upon stacking. EIS was used to determine the increase in capacitance from a single sheet of FLG with gold nanoparticles (FLG_{Au}) to a three-sheet stack of FLG with gold nanoparticles ($3FLG_{Au}$). Figure 6.12A shows the CV response of a one sheet sample of FLG_{Au} before and after EIS. Like the aryldiazonium modified samples, no redox events can be seen within the potential window studied, hence Equation 6.5 was used to calculate capacitance. Additionally, no changes can be seen after the EIS measurement, indicating good stability.

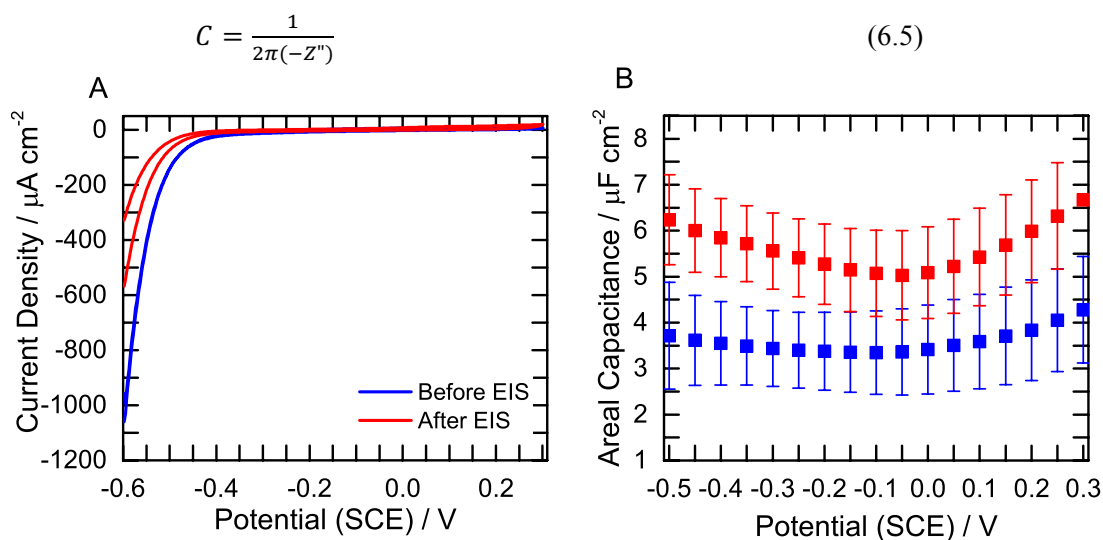


Figure 6.12: (A) CV in 1 M $HClO_4$ before and after EIS for FLG_{Au} . Scan rate = 200 mV s^{-1} . (B) Average areal capacitance of FLG on Au/epoxy derived from EIS at 115 Hz in 1 M $HClO_4$ before (blue) and after (red) gold deposition at -0.6 V for 10 minutes on FLG/Cu.

Figure 6.12B gives the capacitance versus potential plot for FLG after a 10 minute deposition at -0.6 V. The capacitance of an unmodified FLG from the same batch of FLG is included for comparison. The capacitance has increased after modification with gold nanoparticles, which may be a result of an increase in the carrier concentration caused by doping of FLG_{Au} by the gold nanoparticles. The total FLG surface area exposed to the electrolyte solution decreases due to the presence of nanoparticles on the surface. The decrease is approximately 10% (calculated based on the expected height and density of nanoparticles from Figure 6.6), which may mean the areal capacitance shown in Figure 6.12B is underestimated as the calculation is based on the geometric working electrode area. Nevertheless, the important result is that the areal capacitance has not diminished after gold nanoparticle deposition.

The modified FLG_{Au} was then stacked using the LBL protocol described in Chapter 2, Section 0. Initially, FLG_{Au} prepared via a 10 minute deposition at -0.6 V was considered (Figure 6.13A) From a one- to three-sheet system, the capacitance only increased by 1.2 \times , suggesting poor separation of the FLG sheets. This is surprising because the height of the nanoparticles (~ 22 nm) is greater than the radius of the electrolyte ions and greater than the thickness of the films used in Chapter 5. However, as shown by the AFM images (Figure 6.5) there are numerous regions on the FLG surface where there are no nanoparticles, therefore the stacked FLG sheets could make contact in these areas, and reduce the accessible surface area and hence the total electrical double layer capacitance. To investigate this possibility, nanoparticle density was increased by increasing the applied potential to -0.8 V (Figure 6.13B). The capacitance increased by 2.0 \times after stacking, suggesting the higher nanoparticle density gives better sheet separation (the deposition time was not changed, so the nanoparticle height is approximately the same), although still not the 3 \times separation achieved using the films grafted in Chapter 5. This was the highest particle density achieved using the experimental protocol developed, as at this potential the particles began to aggregate so density could not easily be increased further. Therefore, although the gold nanoparticles prevent some aggregation of the sheets, the grafted phenyl films were more successful.

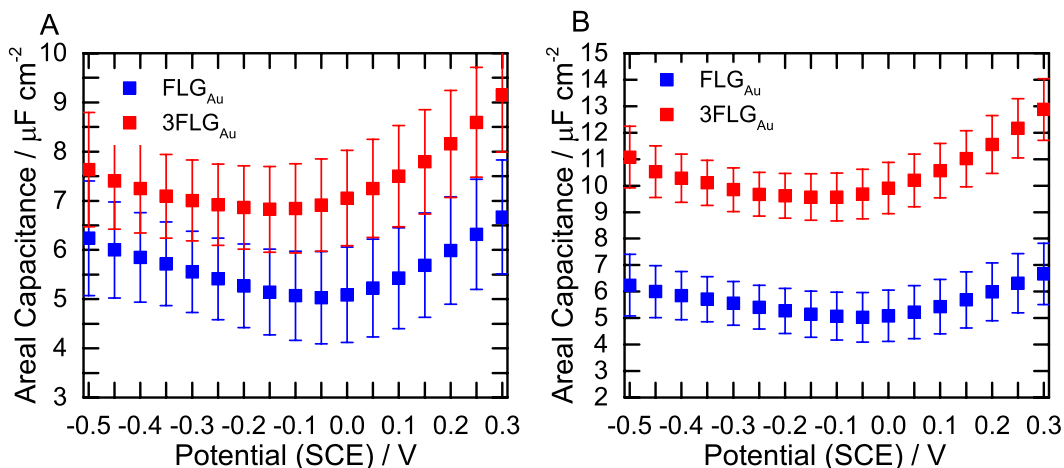


Figure 6.13: Average areal capacitance of FLG_{Au} (blue) and 3FLG_{Au} (red) derived from EIS at 115 Hz in 1 M HClO_4 , after: (A) 10 minute deposition at -0.6 V and (B) 10 minute deposition at -0.8 V.

6.3.2 Cobalt-Nickel Hydroxide Deposition on FLG

6.3.2.1 Deposition on FLG/Cu

Cobalt-nickel hydroxide thin films were deposited on the FLG surface to increase the total capacitance of the system. As explained in Section 6.1.2, vertically aligned cobalt-nickel hydroxide platelets have been successfully deposited onto porous graphene foams, from a cobalt nitrate and nickel nitrate aqueous solution.⁶⁻⁸ Unlike the gold nanoparticle deposition, the reduction potential of the nitrate ion is more negative than the Cu/Cu^{2+} redox couple in aqueous solution, so this procedure could be carried out in an aqueous electrolyte without the added complication of spontaneous nucleation on the FLG/Cu electrode.²³ The deposition was initially tested using HOPG as the working electrode by applying a potential of -1.0 V (vs. SCE) for 1 minute in a 0.1 M $\text{Ni}(\text{NO}_3)_2$ and 0.03 M $\text{Co}(\text{NO}_3)_2$ solution to confirm successful deposition of metal hydroxide particles using these parameters. The method was then repeated using a FLG/Cu coupon as the working electrode to give $\text{FLG}_{\text{Co/Ni}}$, which was transferred to a Au/epoxy surface for analysis. AFM images of both HOPG and FLG surfaces are given in Figure 6.14.

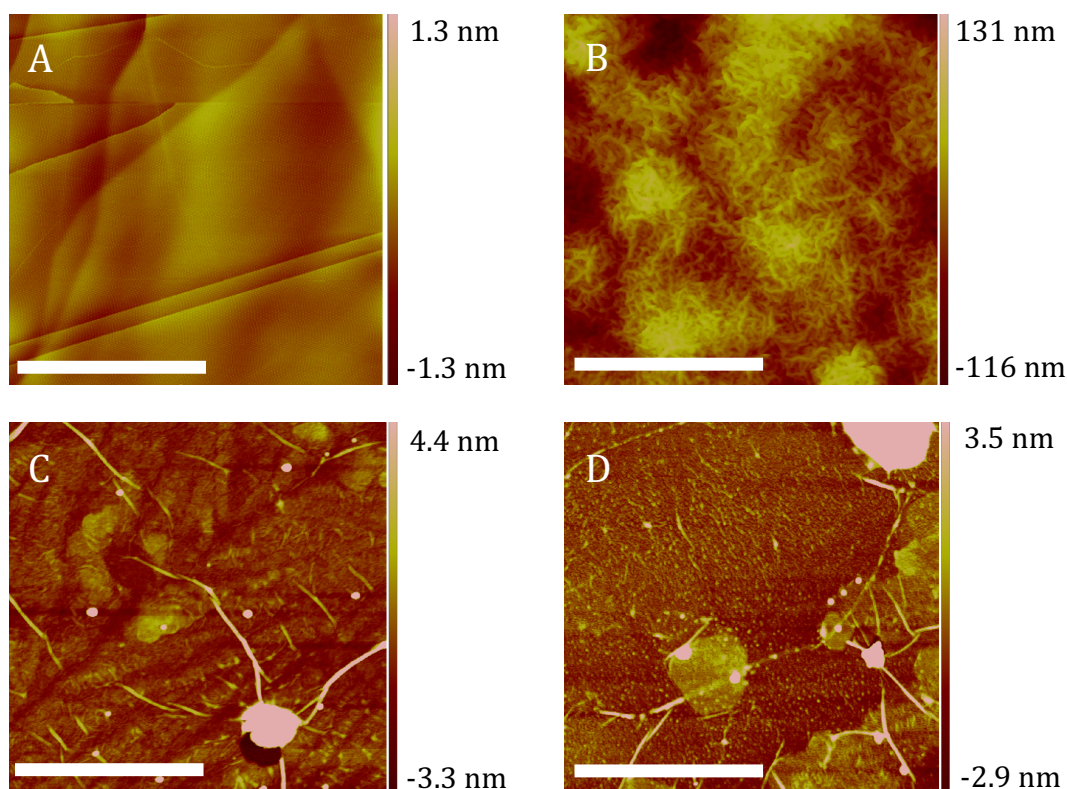


Figure 6.14: AFM images of a 1 minute Co-Ni hydroxide deposition at -1.0 V: (A) before and (B) after deposition on HOPG; (C) before and (D) after deposition on FLG/Cu. FLG transferred to Au/epoxy substrate for imaging. Scale bar = 1.25 μm .

On HOPG there is substantial film growth with whisker like structures approximately 100 nm in length covering the entire surface. No individual nanoparticles or platelets can be seen in the AFM images. Conversely, on the FLG surface there is little difference before and after deposition. A number of small protrusions (~ 1 nm high) can be seen both before and after deposition that cannot be differentiated from the circular features that are assumed to result from the etching and transfer process.

A CV of HOPG in 1 M KOH after cobalt-nickel hydroxide deposition is given in Figure 6.15 (blue). KOH is used as the electrolyte for these studies as the redox processes responsible for pseudocapacitance require hydroxide ions. The CV shows the expected redox peaks for the binary metal hydroxide that are the same shape and at the same potential as those reported for binary metal hydroxide deposition on graphene foam.⁸ The peaks correspond to the redox equations given in Equations 6.6, 6.7, and 6.8.



HOPG was also decorated with the individual metal hydroxides (Co(OH)_2 or Ni(OH)_2) for comparison and the resulting CVs are given in Figure 6.15 (red and green). The binary metal hydroxide shows peaks intermediate between the individual metal hydroxide redox peaks, which is indicative of a mixed Co-Ni composite material.²⁴

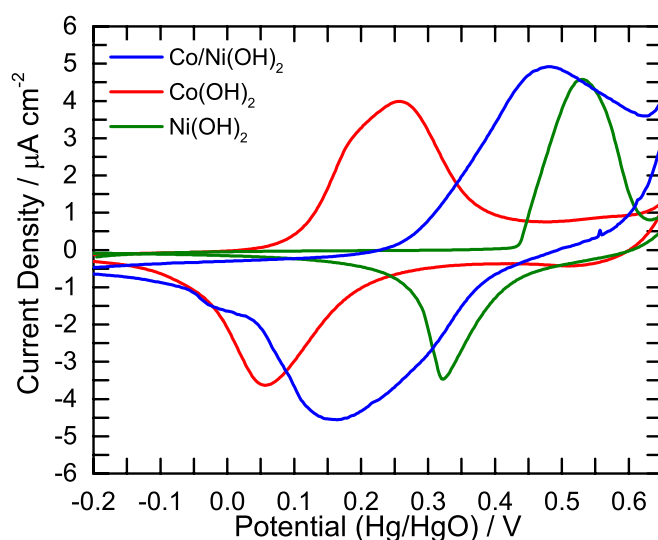


Figure 6.15: CVs of HOPG in 1 M KOH after a 1 minute Co-Ni hydroxide deposition at -1.0 V: (blue) cobalt and nickel hydroxide; (red) cobalt hydroxide only; (green) nickel hydroxide only. Scan rate = 20 mV s^{-1} .

CVs of $\text{FLG}_{\text{Co/Ni}}$ in 1 M KOH are given in Figure 6.16 (red and green). A CV for an unmodified FLG surface (blue) is included for comparison. The red CV shows the expected redox peaks for the binary metal hydroxide, similar to those seen on HOPG and reported by Fisher et al.⁸ Upon repeating the experiment, this response was seen only 20% of the time, with the remaining 80% of samples giving the green CV, which is the same as the unmodified FLG indicating that for most FLG samples, no detectable cobalt-nickel hydroxide resides at the surface. The copper etching step prior to the transfer of $\text{FLG}_{\text{Co/Ni}}$ was thought to cause this. The ammonium persulfate used to etch the copper foil is a powerful oxidising agent, and so it is reasonable to assume that it can oxidise the cobalt and nickel hydroxide deposits as well as the copper foil, removing most, if not all the metal hydroxide from the majority of the FLG samples studied, meaning experimental reproducibility is poor. This also explains the lack of any features in the AFM images compared with HOPG, which does not undergo an etching

step. Gold metal is less likely to be oxidised by ammonium persulfate, so this was not an issue for the gold nanoparticle deposition work described earlier.²³ For this reason, the experimental protocol was rearranged so that the FLG was removed from the copper and transferred to a Au/epoxy substrate prior to metal hydroxide deposition, and so the working electrode for deposition was FLG on Au/epoxy (see Chapter 2, Section 2.4.5).

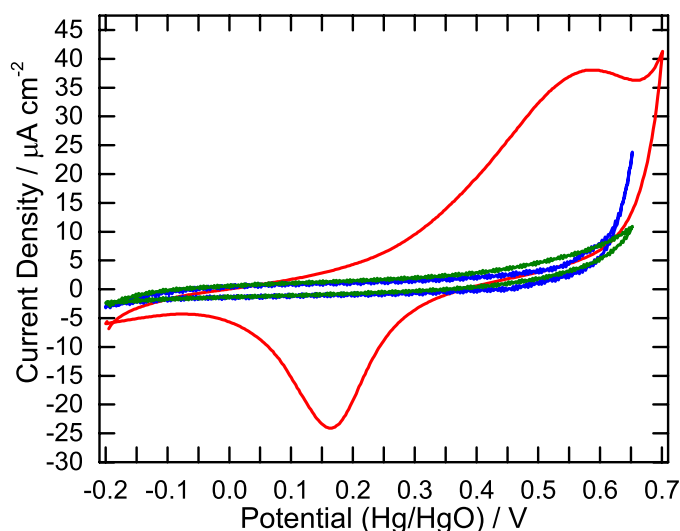


Figure 6.16: CV in 1 M KOH of FLG before (blue) and after (red/green) a 1 minute Co-Ni hydroxide deposition at -1.0 V. Scan rate = 20 mV s^{-1} .

6.3.2.2 Deposition on FLG on a Au/Epoxy Substrate

The cobalt-nickel hydroxide films were deposited onto FLG on Au/epoxy at -1.0 V for 30 seconds, 1 minute, and 2 minutes, and the surfaces were imaged using AFM and SEM. The AFM images in Figure 6.17 for the 30 second and 1 minute samples show a dense covering of whisker-like features similar to those seen on HOPG. For the 2 minute sample, large cracks appeared in the cobalt-nickel hydroxide film, which made AFM imaging difficult as the surface was very rough. This is assumed to be a consequence of an increase in the amount of cobalt-nickel hydroxide at the surface.

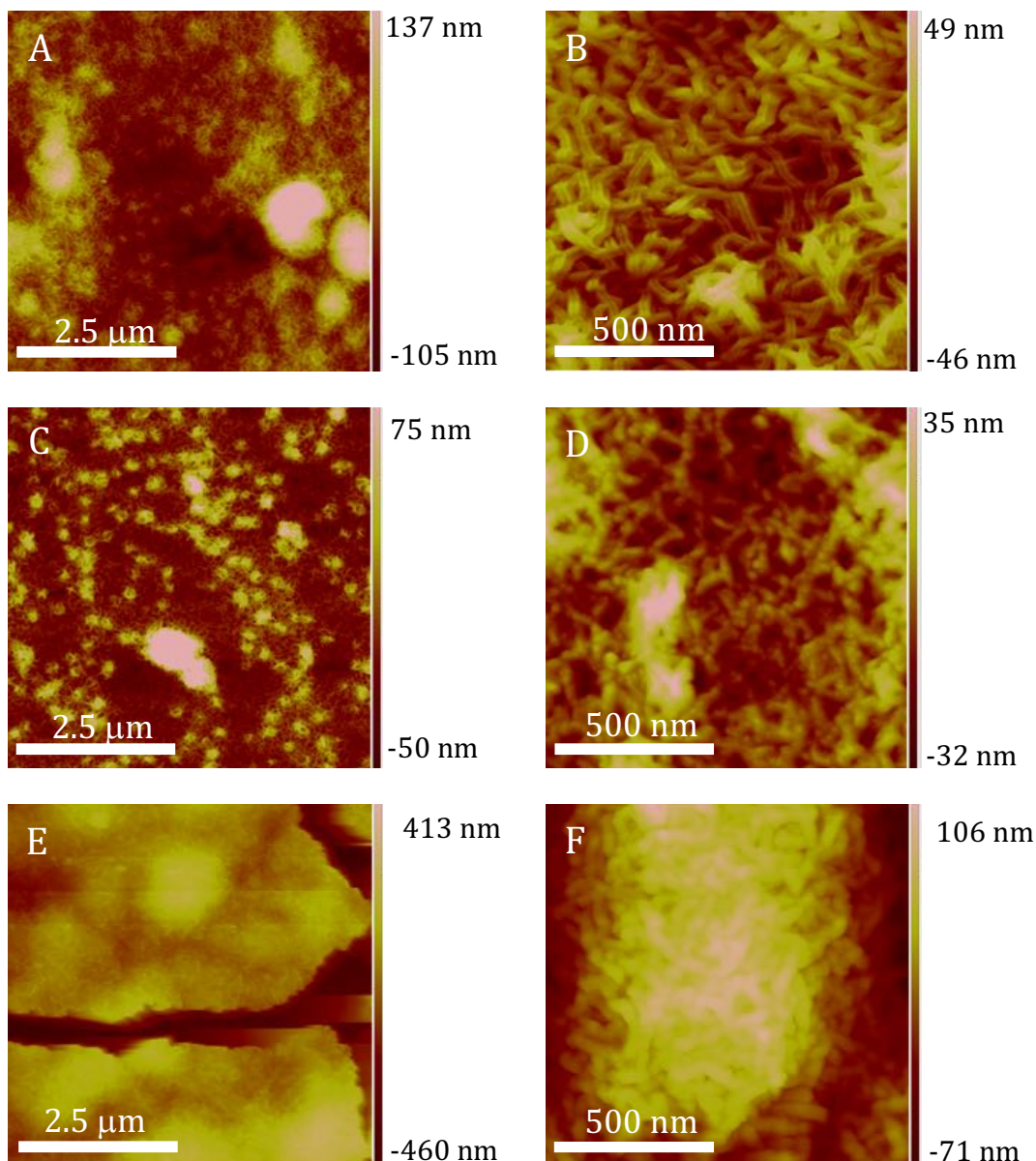


Figure 6.17: AFM images after Co-Ni hydroxide deposition at -1.0 V on FLG transferred to Au/epoxy for: (A) and (B) 30 seconds; (C) and (D) 1 minute; (E) and (F) 2 minutes.

The structure of the film can be more clearly seen in the SEM image in Figure 6.18, which shows the same dense coverage of whisker-like structures seen in the AFM images. This result is dissimilar to that reported by Fisher et al.⁸ for cobalt-nickel hydroxide deposition on a graphene foam, as in that work, individual, vertically aligned flakes were obtained. Individual nanoparticles were not seen for any of the samples analysed here. Furthermore, spherical nanoparticles, like those seen for gold nanoparticle deposition were not observed. As a result, the cobalt-nickel hydroxide films may be better able to separate the FLG sheets than the gold nanoparticles, as there are no regions where the FLG sheets can make contact. Energy dispersive X-ray

spectroscopy (EDS) coupled to the SEM imaging showed that the ratio of Co:Ni:O at the surface was approximately 2:3:5.

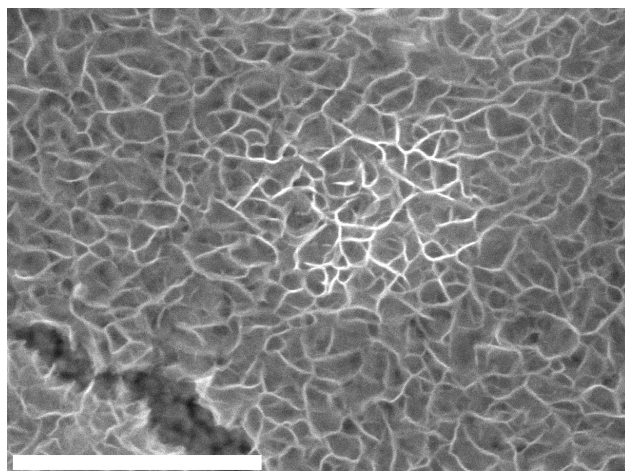


Figure 6.18: SEM image after cobalt-nickel hydroxide deposition on FLG transferred to a Au/epoxy surface at -1.0 V for 1 minute. Scale bar = 500 nm.

XPS was also used to characterise the cobalt-nickel hydroxide film and Tables 6.1 and 6.2 summarise the survey spectra and narrow scan data respectively, for FLG and $\text{FLG}_{\text{Co/Ni}}$ after a 1 minute deposition. Both samples contain carbon, as expected due to the underlying FLG surface. The oxygen content increased from 4.6% for FLG to 36.4% for $\text{FLG}_{\text{Co/Ni}}$ due to the additional oxygen provided by the metal hydroxide thin film. $\text{FLG}_{\text{Co/Ni}}$ has a nickel and cobalt content of 4.7% and 4.3% respectively, indicating that these metals now reside at the surface. The nickel to cobalt ratio of approximately 1:1 is different from the ratio obtained from EDS and inductively coupled mass spectrometry (ICPMS, see Table 6.5) The reason for this discrepancy will be considered later. The nitrogen detected on the FLG is assumed to be due to adventitious contamination.

Table 6.1: Atomic % values derived from XPS survey spectra for FLG, and $\text{FLG}_{\text{Co/Ni}}$ on a gold substrate.

| Sample | Survey Spectra Atomic % | | | | | |
|-----------------------------|-------------------------|----------|--------|------|--------|--------|
| | Carbon | Nitrogen | Oxygen | Gold | Nickel | Cobalt |
| FLG | 93.4 | 1.02 | 4.6 | 0.98 | 0 | 0 |
| $\text{FLG}_{\text{Co/Ni}}$ | 53.9 | 0 | 36.4 | 0.67 | 4.7 | 4.3 |

Table 6.2: Narrow scan data for O 1s, Co 2p and Ni 2p peaks of FLG, and FLG_{Co/Ni} on a gold substrate.

| Narrow scan data | | | | | | |
|----------------------|---------------------|----------|----------------------|----------|----------------------|----------|
| | O 1s | | Ni 2p _{3/2} | | Co 2p _{3/2} | |
| Sample | Binding energy / eV | Atomic % | Binding energy / eV | Atomic % | Binding energy / eV | Atomic % |
| FLG | 531.1 | 20.1 | | | | |
| | 531.9 | 49.3 | | | | |
| | 532.9 | 17.2 | | | | |
| | 533.5 | 10.6 | | | | |
| | 534.5 | 2.8 | | | | |
| FLG _{Co/Ni} | | | 854.2 | 16.0 | | |
| | 529.8 | 23.9 | 855.5 | 32.3 | 780.2 | 62.8 |
| | 531.1 | 59.1 | 857.1 | 12.5 | 782.5 | 11.8 |
| | 532.3 | 12.9 | 859.9 | 13.1 | 785.7 | 24.0 |
| | 533.3 | 4.1 | 861.6 | 16.9 | 790.2 | 1.5 |
| | | | 864.5 | 9.2 | | |

Figure 6.19 gives the O 1s, Ni 2p, and Co 2p narrow scans for FLG_{Co/Ni}, with peaks fitted according to literature reports²⁵. The O 1s narrow scan shows a broad peak at 531.1 eV, which is assigned to the hydroxide group of the nickel and cobalt hydroxides.²⁵⁻²⁶ The Co 2p and Ni 2p narrow scans show a 2p_{1/2} and 2p_{3/2} component that result from spin orbit coupling. The associated shake-up satellites are also seen in both narrow scans.^{8, 26} Shake-up satellites result from photoelectronic processes that leave the ion in an excited state, which makes the kinetic energy of the emitted photoelectron lower, therefore increasing the binding energy. These features are commonly seen for Co(II) and Ni(II) compounds. The 2p_{1/2} and 2p_{3/2} components qualitatively contain the same information, therefore only the 2p_{3/2} peak was fitted, as is common practice in literature reports.²⁶ The binding energies of the fitted components agree with literature reports for nickel and cobalt hydroxide.^{6, 25-29} Moreover, in the Co 2p narrow scan, a broad satellite at 785.7 eV has only been reported for Co(II) compounds (i.e. Co(OH)₂), and in the Ni 2p scan, a separation of 17.6 eV for the 2p_{1/2} and 2p_{3/2} peaks is characteristic of Ni(OH)₂ formation.²⁶⁻²⁷ Hence, the XPS data suggests that the film seen in the AFM and SEM images is comprised of both nickel and cobalt hydroxide, with the metals in the 2+ oxidation state.

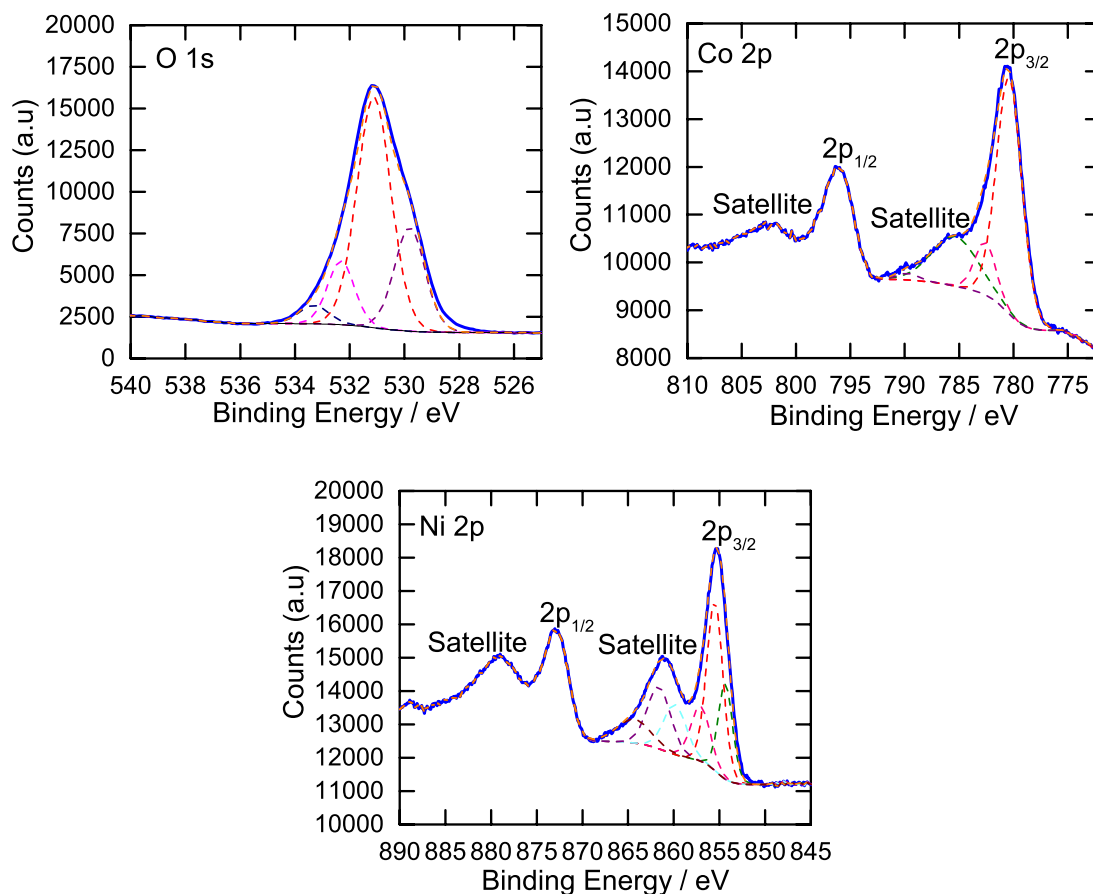


Figure 6.19: XPS narrow scans of FLG_{Co/Ni} after Co-Ni hydroxide deposition on FLG on a Au substrate at -1.0 V for 1 minute. Left to right: O 1s narrow scan and Co 2p narrow scan; bottom: Ni 2p narrow scan.

6.3.2.3 CV and CD of FLG after Cobalt-Nickel Hydroxide Deposition

The capacitance of the FLG surfaces after cobalt-nickel hydroxide deposition was determined by CV and CD. Figure 6.20A shows the CV response in 1 M KOH at 20 mV s^{-1} for FLG_{Co/Ni} after a 30 second, 1 minute, and 2 minute deposition. A bare FLG surface is included for comparison. The FLG_{Co/Ni} surfaces all show large, chemically reversible redox peaks that most likely result from the reactions given in Equations 6.6, 6.7, and 6.8.²⁷ The area enclosed by the CV increases with deposition time, resulting in an increase in the capacitance, suggesting an increase in the amount of metal hydroxide at the surface with longer deposition times. Figure 6.20B gives CVs at increasing scan rate for FLG_{Co/Ni} after a 1 minute deposition. The peak separation increases, and the oxidation and reduction peaks broaden with increasing scan rate. This is characteristic of quasi-reversible electrochemistry, suggesting slow electron transfer kinetics through the metal hydroxide film, presumably a result of the low conductivity of the deposited metal hydroxides.³⁰⁻³¹ The oxidation and reduction peak separation at 20 mV s^{-1} also

increases with increasing deposition time, consistent with a larger amount of metal hydroxide at the surface, as electron transfer would be slower through a thicker metal hydroxide film. The areal capacitance derived from the area enclosed by the CV at 20 mV s^{-1} for each sample is given in Table 6.3.

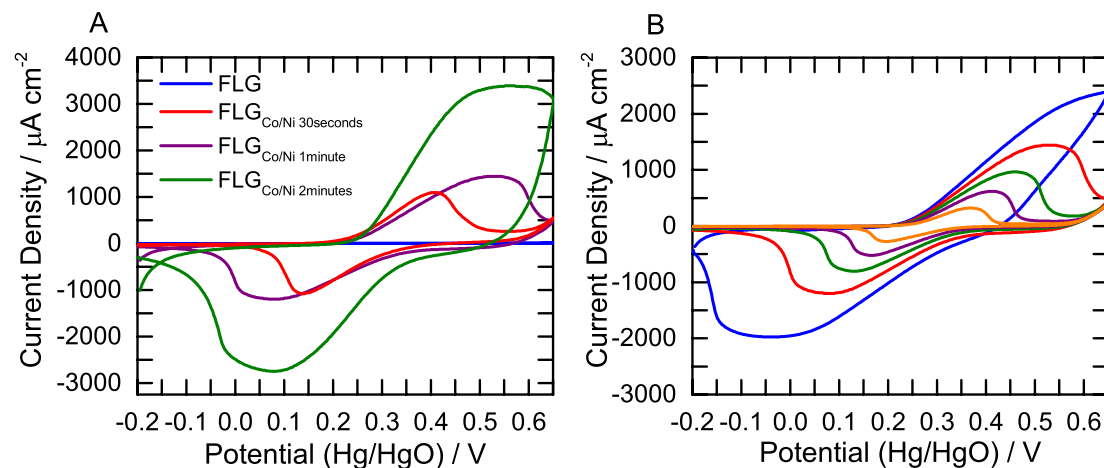


Figure 6.20: CV in 1 M KOH of $\text{FLG}_{\text{Co/Ni}}$ after Co-Ni hydroxide deposition at -1.0 V on FLG on a Au/epoxy substrate: (A) CV at 20 mV s^{-1} before and after 30 second, 1 minute, and 2 minute depositions; (B) CV at 50 (blue), 20 (red), 10 (green) 5 (purple), and 2 mV s^{-1} (orange) after a 1 minute deposition.

Figure 6.21A shows the CD response of the three systems at 1.6 mA cm^{-2} . The CD plots are typical of pseudocapacitive materials with distinctly different regions: from ~ 0.65 to 0.2 V where there is a fast discharge rate and electrical double layer capacitance only, and from ~ 0.2 to 0 V , where the discharge rate is much slower, due to the pseudocapacitance of the metal hydroxides.³²⁻³³ The potential window of each region aligns with the position of the redox peaks in Figure 6.20. Similar to the CV results, the discharge time increases with increasing deposition time, signifying an increase in the total capacitance. Figure 6.21B shows the variation in the CD plot at selected current densities for $\text{FLG}_{\text{Co/Ni}}$ after a 1 minute deposition, and Figure 6.21C shows the corresponding rate capability for all three samples. The capacitance drops at the highest current density for all samples, indicating the system could not operate as efficiently at fast charge and discharge rates. This is most significant for the 2 minute sample, presumably due to the increase in the total amount of metal hydroxide at the surface. A reduced rate capability is commonly seen for metal hydroxide materials, and is associated with restriction of the penetration and diffusion of electrolyte ions within the metal hydroxide film, required for the redox reactions in Equations 6.6, 6.7, and 6.8, and the low electrical conductivity of metal hydroxides.^{27, 34}

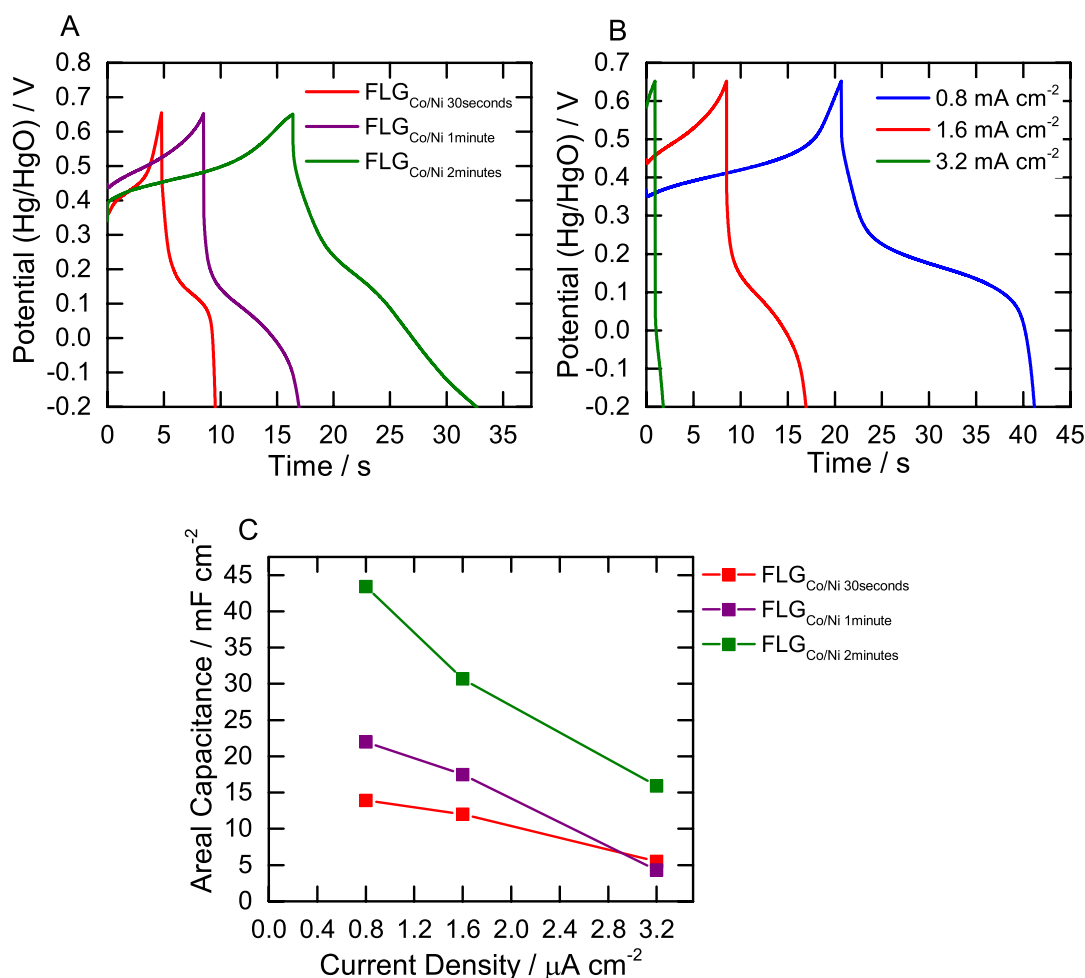


Figure 6.21: (A) CD at 1.6 mA cm⁻² in 1 M KOH of FLG_{Co/Ni} after a 30 second, 1 minute, and 2 minute deposition at -1.0 V on FLG on a Au/epoxy substrate; (B) CD at different current densities for a FLG_{Co/Ni} after a 1 minute deposition at -1.0 V; (C) change in areal capacitance with applied current density.

The areal capacitance at 20 mV s⁻¹ and 1.6 mA cm⁻² for each sample is given in Table 6.3, with the FLG capacitance included for comparison. At a current density of 1.6 mA cm⁻² the discharge time for the unmodified FLG was too fast to accurately measure, hence the capacitance at 0.1 mA cm⁻², is given as this was the highest current density at which it was possible to measure the discharge time. To calculate the areal capacitance, the geometric area of the working electrode was used, as this is approach is common in literature reports.^{8, 35-37} However, for surfaces with metal hydroxide coatings, gravimetric or volumetric capacitance is often used to give a more accurate representation for the capacitance of the system that accounts for the additional mass or volume of the metal hydroxide, thus the gravimetric capacitance of these systems will be discussed later in this chapter. Nonetheless, the areal capacitance was used to compare the different samples prepared in this thesis work. The areal capacitance after metal hydroxide deposition is significantly higher than for the unmodified FLG, with

the 2 minute sample giving an almost 1000× increase in capacitance. The total capacitance increases with deposition time, presumably due to an increase in the amount of active material at the surface. Coulombic efficiency was ~100% for all samples, showing good reversibility for charge storage (see Chapter 5, Equation 5.1 for details).³⁸

Table 6.3: Areal capacitance values derived from CV at 20 mV s⁻¹ and CD at 1.6 mA cm⁻² (0.1 mA cm⁻² for blank) in 1 M KOH before and after Co-Ni hydroxide deposition on FLG on a Au/epoxy substrate. *n*=2 for all samples.

| Sample | CV Capacitance / mF cm ⁻² | CD Capacitance / mF cm ⁻² |
|--------------------------------|---|---|
| FLG | 1.5 ± 0.1 × 10 ⁻² | 3.3 ± 0.4 × 10 ⁻² |
| FLG _{Co/Ni} 30seconds | 14.3 ± 2.9 | 12.0 ± 1.5 |
| FLG _{Co/Ni} 1minute | 21.5 ± 1.2 | 17.5 ± 1.6 |
| FLG _{Co/Ni} 2minutes | 50.2 ± 2.0 | 30.7 ± 2.0 |

Figure 6.22 shows CV plots taken before and after all electrochemistry measurements (15 CD cycles at three current densities and EIS). The 30 second and 1 minute samples showed very good electrochemical stability, while the 2 minute sample showed a significant decrease in the area enclosed by the CV and hence a decrease in capacitance after electrochemistry. Therefore, the more stable 1 minute sample was selected for further testing and FLG_{Co/Ni} will refer to a sample prepared via a 1 minute deposition from this point onwards.

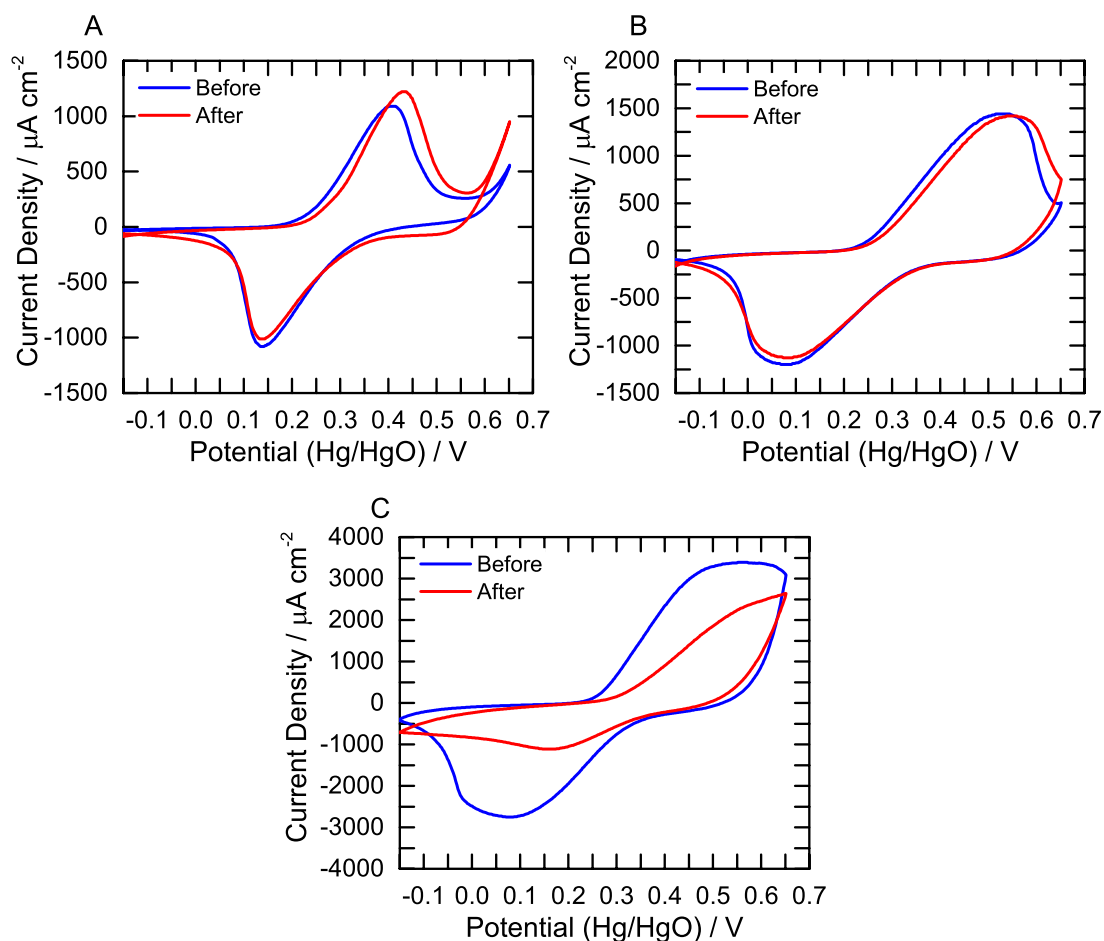


Figure 6.22: CV at 20 mV s^{-1} before and after all electrochemical measurements (15 CD cycles at each current density and EIS) of $\text{FLG}_{\text{Co/Ni}}$ in 1 M KOH: (A) 30 second deposition; (B) 1 minute deposition; (C) 2 minute deposition.

6.3.2.4 EIS of $\text{FLG}_{\text{Co/Ni}}$

EIS was used to interrogate the $\text{FLG}_{\text{Co/Ni}}$ surface. The Nyquist and Bode phase angle plots for FLG and $\text{FLG}_{\text{Co/Ni}}$ at 0.1 V in 1 M KOH are given in Figure 6.23. Unlike the surfaces studied in Chapter 5 and the FLG_{Au} samples, Equation 6.5 cannot be used to calculate the differential capacitance for the $\text{FLG}_{\text{Co/Ni}}$ surface, as Faradaic processes are operative. Clear differences can be seen between the FLG and $\text{FLG}_{\text{Co/Ni}}$ Nyquist plots. Similar to the FLG surfaces studied in Chapter 5, the unmodified FLG shows a short Warburg diffusion region, after which the plot becomes almost vertical with respect to the imaginary axis, where the FLG is behaving as a purely capacitive material.³⁹⁻⁴¹ The almost vertical line suggests the capacitive behaviour is not diffusion limited. On the other hand, the $\text{FLG}_{\text{Co/Ni}}$ sample shows a partial semicircle in the high frequency region that is a result of the charge transfer resistance, caused by redox processes occurring at the surface of the cobalt-nickel hydroxide nanoparticles.⁴² The greater the diameter of the semicircle, the higher the charge transfer resistance.⁴³ This is then followed by a short Warburg region and an almost vertical, low frequency tail.

The low frequency portion of the plot has a lower slope than for FLG, suggesting a higher ion diffusion resistance, as expected for ion diffusion within the cobalt-nickel hydroxide film.⁴³⁻⁴⁶

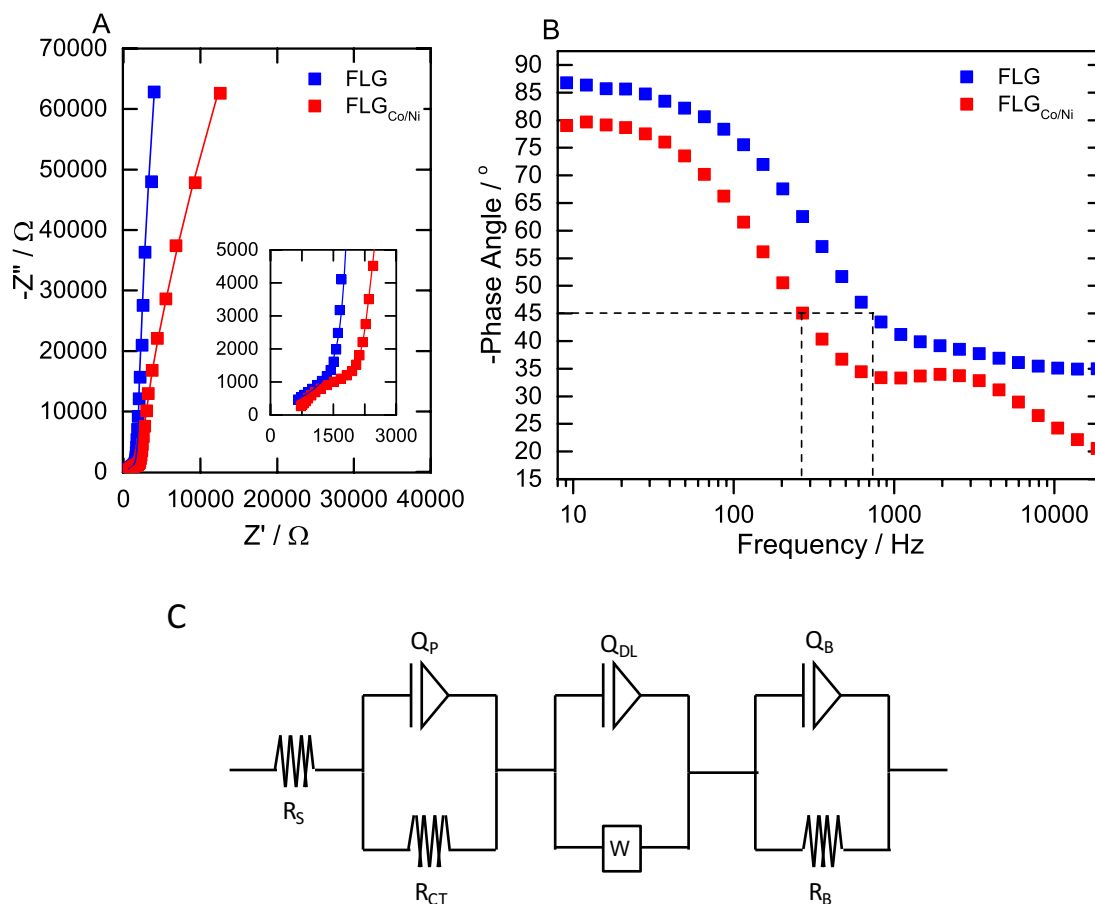


Figure 6.23: EIS data for FLG and FLG_{Co/Ni} at 0.1 V in 1 M KOH: (A) Nyquist plot with fits and (B) Bode phase angle plot. (C) EEC used to fit data.

Electrical equivalent circuits (EEC) were used to fit the EIS data. For FLG, the EEC used in Chapter 5, Section 5.3.1.3 was able to accurately fit the data, however for FLG_{Co/Ni}, additional circuit components that accounted for the pseudocapacitive metal hydroxide film were required, as shown in Figure 6.23C. All calculated values can be found in Appendix E, Section E.2. As expected, an additional charge transfer resistance (R_{CT}) was measured for FLG_{Co/Ni} ($27.9 \text{ k}\Omega \text{ cm}^{-2}$) indicating an increase in the resistance of the system due to the redox processes occurring.⁴² The R_s value does not change after metal hydroxide deposition because the electrolyte concentration has not changed.⁴³ Finally, the Warburg impedance has increased slightly after modification from $2.9 \mu\text{S cm}^{-2}$ to $9.5 \mu\text{S cm}^{-2}$ for FLG_{Co/Ni}, suggesting the film impedes ion diffusion.^{38, 45} The Bode phase angle plot shows two time constants for FLG_{Co/Ni} with the additional constant expected to be a result of the charge transfer processes occurring

at the surface. Additionally, the frequency at which the system moves from resistive to capacitive behaviour decreases for $FLG_{Co/Ni}$ compared to FLG confirming the presence of the film impedes ion movement.³⁹ To summarise, the cobalt-nickel hydroxide film is able to increase the areal capacitance of the system, however the addition of the cobalt-nickel hydroxide film may hinder ion diffusion, which could negatively impact the speed at which the device can operate and hence the power density.⁴⁷

6.3.2.5 Deposition on FLG_{CP} on a Au/Epoxy Substrate

The cobalt-nickel hydroxide deposition was also carried out on FLG_{CP} on a Au/epoxy substrate, giving $FLG_{CP+Co/Ni}$, to establish whether the presence of the grafted carboxyphenyl film influences metal hydroxide deposition, and also to determine if the film is beneficial in building stacks of $FLG_{Co/Ni}$. The CBD modification was carried out using the free-floating protocol, so that the CP film was sandwiched between the epoxy resin and the FLG. The resulting CV and CD plots are given in Figure 6.24. Both the CV and CD response shows similar shapes to those seen in Figure 6.20 and Figure 6.21, confirming the successful deposition of the metal hydroxide nanoparticles. The area enclosed by the CV and the CD discharge time has decreased for $FLG_{CP+Co/Ni}$ compared with the $FLG_{Co/Ni}$ surface, suggesting a decrease in the total capacitance of the system, possibly due to a decrease in the amount of metal hydroxide at the electrode surface. Table 6.4 gives the calculated capacitance at 20 mV s^{-1} and 1.6 mA cm^{-2} for each system. From these values, the capacitance has approximately halved when cobalt-nickel hydroxide is deposited onto a FLG_{CP} surface, which may mean the presence of the CP film prevents cobalt-nickel hydroxide deposition on one side of the FLG (the CP film is only on one side of the FLG, therefore blocks film growth on this side).

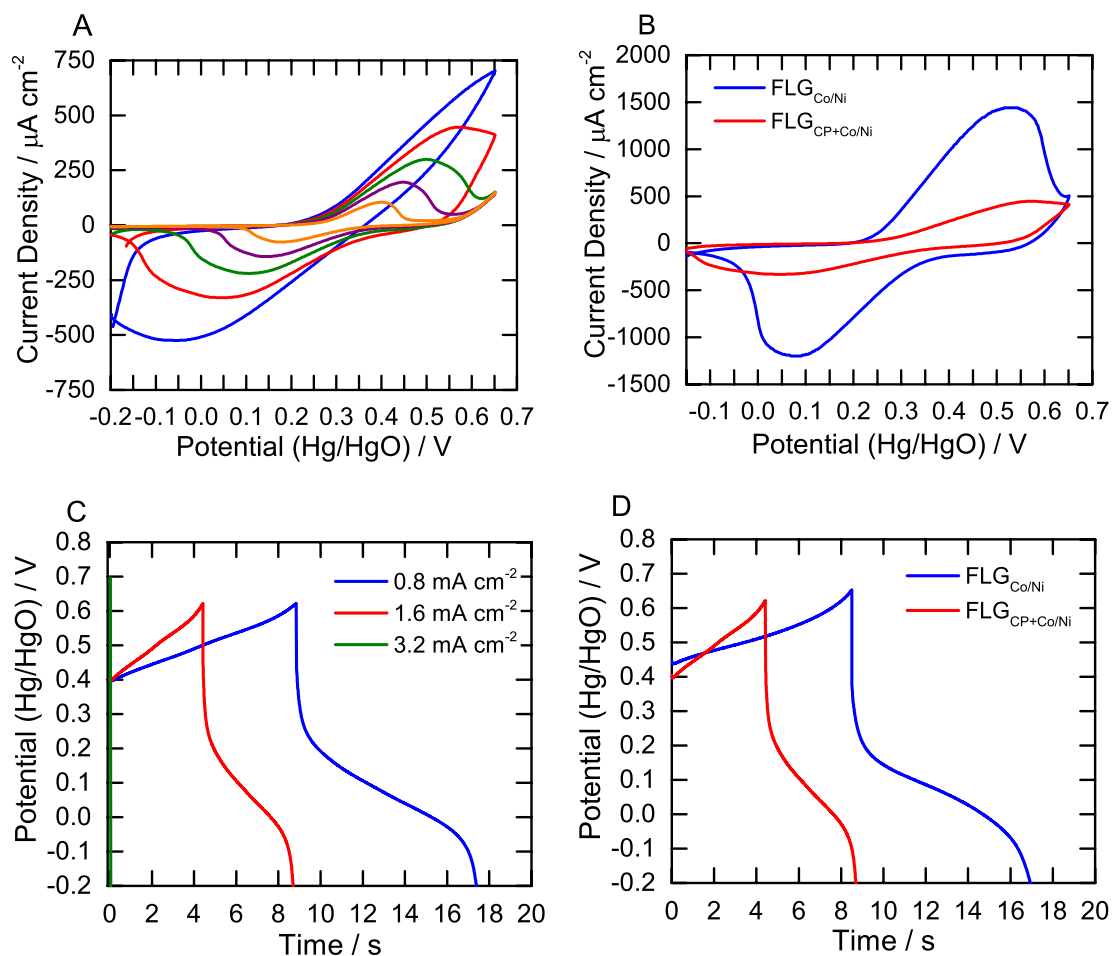


Figure 6.24: CV and CD in 1 M KOH of FLG_{CP+Co/Ni}: (A) CV at 50 (blue), 20 (red), 10 (green), 5 (purple), and 2 mV s⁻¹ (orange) after 1 minute deposition on FLG on a Au/epoxy substrate; (B) CV at 20 mV s⁻¹, FLG_{Co/Ni} shown for comparison; (C) CD at selected scan rates; (D) CD at 1.6 mA cm⁻², FLG_{Co/Ni} shown for comparison.

Table 6.4: Capacitance values derived from CV at 20 mV s⁻¹ and CD at 1.6 mA cm⁻² (0.1 mA cm⁻² for blank), for 1 M KOH after deposition with cobalt-nickel hydroxide nanoparticles onto FLG or FLG_{CP}. $n=2$ for all samples.

| Sample | CV Capacitance / mF cm ⁻² | CD Capacitance / mF cm ⁻² |
|-------------------------|--------------------------------------|--------------------------------------|
| FLG | $1.5 \pm 0.1 \times 10^{-2}$ | $3.3 \pm 0.4 \times 10^{-2}$ |
| FLG _{CP+Co/Ni} | 9.5 ± 0.2 | 7.9 ± 0.6 |
| FLG _{Co/Ni} | 21.5 ± 1.2 | 22.0 ± 2.6 |

To establish whether the presence of the film inhibited metal hydroxide deposition AFM images were collected for the FLG_{CP+Co/Ni} surface after deposition. For the FLG_{CP} modification, the modified FLG is collected in the sandwiched orientation, so the imaged surface is that with no CP film (Figure 6.25B). The deposition was also repeated on a FLG_{NP} surface, which can be more easily collected in the exposed orientation from the on-copper modification protocol, so that the imaged surface is that with the grafted film (Figure 6.25C).

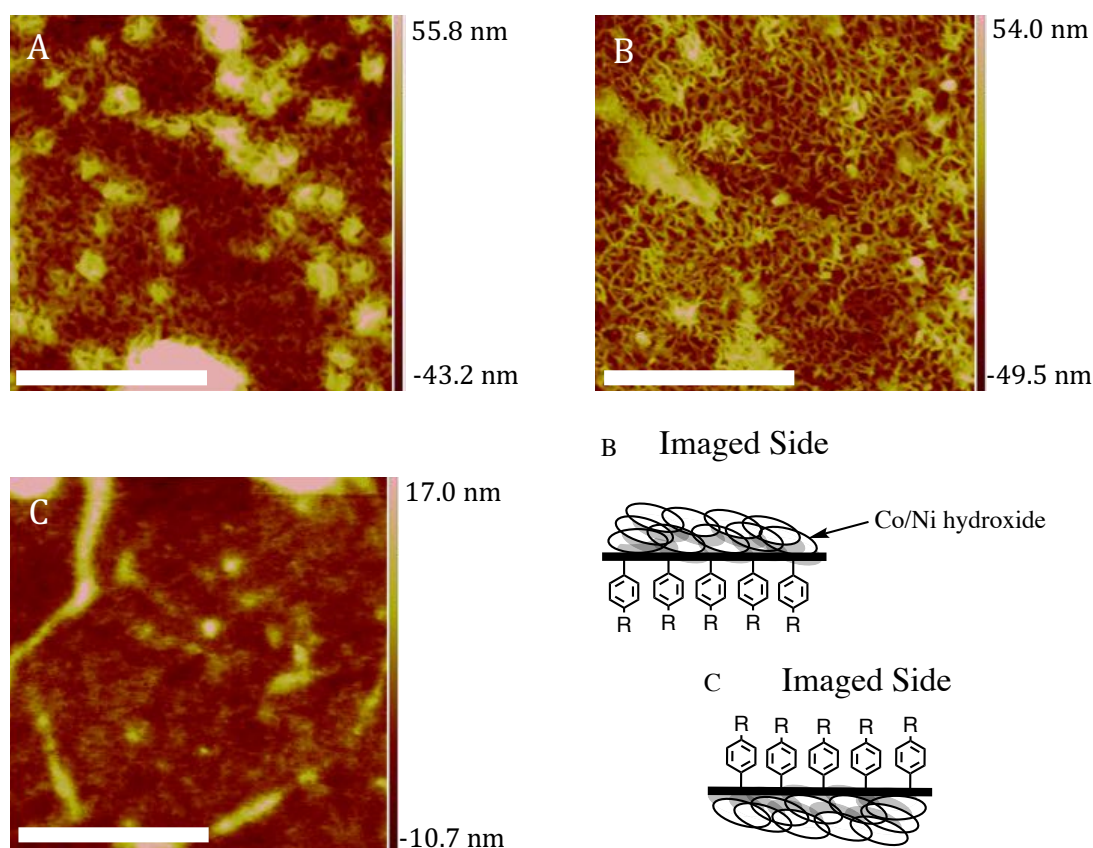


Figure 6.25: AFM images after a 1 minute cobalt-nickel deposition at -1.0 V: (A) $\text{FLG}_{\text{Co/Ni}}$; (B) $\text{FLG}_{\text{CP+Co/Ni}}$ with the metal hydroxide film exposed; (C) $\text{FLG}_{\text{Co/Ni+NP}}$ with the film exposed. Scale bar = $1.25 \mu\text{m}$.

Comparison of Figure 6.25A and B shows the metal hydroxide film deposits on the unmodified side of the FLG surface. In contrast, Figure 6.25C shows that on the modified side of the FLG, cobalt-nickel hydroxide deposition is inhibited, as no whisker-like structures can be seen in this image. These results support the CV and CD results: no metal hydroxide film deposits on the aryldiazonium modified FLG surface and hence for the $\text{FLG}_{\text{CP+Co/Ni}}$ sample, the cobalt-nickel hydroxide deposits onto one side of the FLG only and so the pseudocapacitance is approximately half that at $\text{FLG}_{\text{Co/Ni}}$.

The chronoamperometric transients for metal hydroxide deposition on FLG and FLG_{CP} are given in Figure 6.26. The plots show a similar shape to literature reports,⁴⁸ and indicate no significant difference in the charge passed for deposition on FLG_{CP} compared to FLG. This suggests the film does not influence the nitrate reduction step and therefore hydroxide ion production, hence this is not the origin of the decreased amount of metal hydroxide on the aryldiazonium modified FLG surfaces. An alternative explanation for the reduction in the amount of cobalt-nickel hydroxide on

the aryldiazonium modified FLG is the film blocks access of the cobalt and nickel ions to the FLG surface, which are also essential for metal hydroxide formation. However, in Chapter 5 the grafted films did not hinder ion transport to the surface for electrical double layer formation, so this is unlikely to be the reason for the reduction in metal hydroxide at FLG_{CP}. Hence, both hydroxide and metal ions are likely to be present at the surface even with a grafted phenyl film, therefore the film must physically block the formed metal hydroxides from adhering to the FLG surface with the grafted phenyl film.

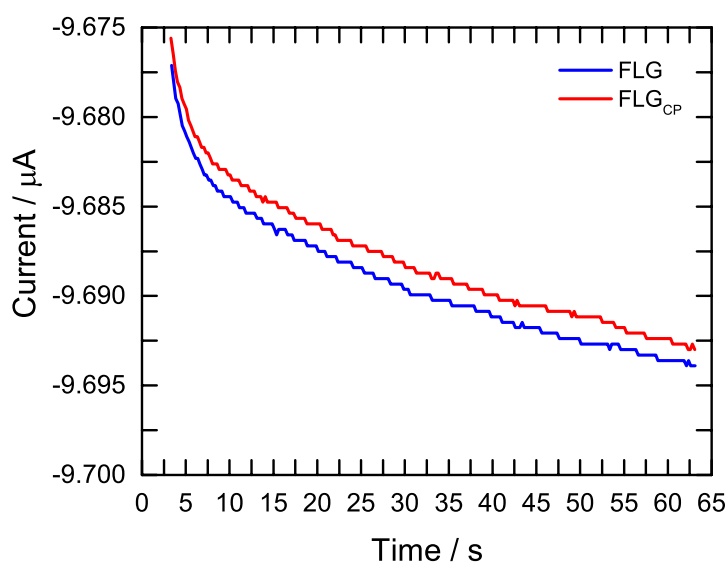


Figure 6.26: Chronoamperometric transients for a 1 minute Co-Ni deposition at -1.0V on FLG and FLG_{CP}.

This result was further supported by ICPMS analysis. ICPMS was used to measure the total mass of cobalt and nickel at the FLG and FLG_{CP} surface. For these measurements, the FLG_{Co/Ni} and FLG_{CP+Co/Ni} samples were soaked overnight in dilute nitric acid to etch the cobalt and nickel from the surface. Table 6.5 summarises the mass of cobalt and nickel hydroxide at the two different surface types, for the defined geometric area. The total metal hydroxide mass has approximately halved for FLG_{CP+Co/Ni} compared to FLG_{Co/Ni}, supporting the hypothesis that the grafted film blocks deposition on the aryldiazonium modified side of the FLG. The cobalt and nickel are in an approximately 2:3 ratio at the surface, the same ratio as that obtained via EDS. ICPMS measures the cobalt and nickel content from the entire surface and is therefore assumed to give the best indication of the overall cobalt to nickel ratio, compared with XPS and EDS, which sample at a spot on the surface that is smaller than the total geometric area.

Table 6.5: Total mass of cobalt and nickel hydroxide for $\text{FLG}_{\text{Co/Ni}}$ and $\text{FLG}_{\text{CP+Co/Ni}}$ after a 1 minute cobalt-nickel hydroxide deposition at -1.0 V on FLG on a Au/epoxy substrate derived from ICPMS analysis.

| Sample | Mass $\text{Co}(\text{OH})_2 / \text{mg cm}^{-2}$ | Mass $\text{Ni}(\text{OH})_2 / \text{mg cm}^{-2}$ | Total Mass / mg cm^{-2} |
|--------------------------------|---|---|----------------------------------|
| $\text{FLG}_{\text{Co/Ni}}$ | 0.19 | 0.28 | 0.47 |
| $\text{FLG}_{\text{CP+Co/Ni}}$ | 0.09 | 0.17 | 0.27 |

6.3.2.6 Capacitance of Three-Sheet Stacks

The $\text{FLG}_{\text{Co/Ni}}$ and $\text{FLG}_{\text{CP+Co/Ni}}$ were stacked using the LBL protocol described in Chapter 2, Section 2.5.3. This protocol is illustrated in Figure 6.27. For $\text{FLG}_{\text{CP+Co/Ni}}$ samples, each FLG sheet in the stack had a CP film on the underside. The resulting electrodes were characterised by CV and CD testing. Note that all FLG sheets are in contact with the Au surface during the deposition and subsequent electrochemical measurements.

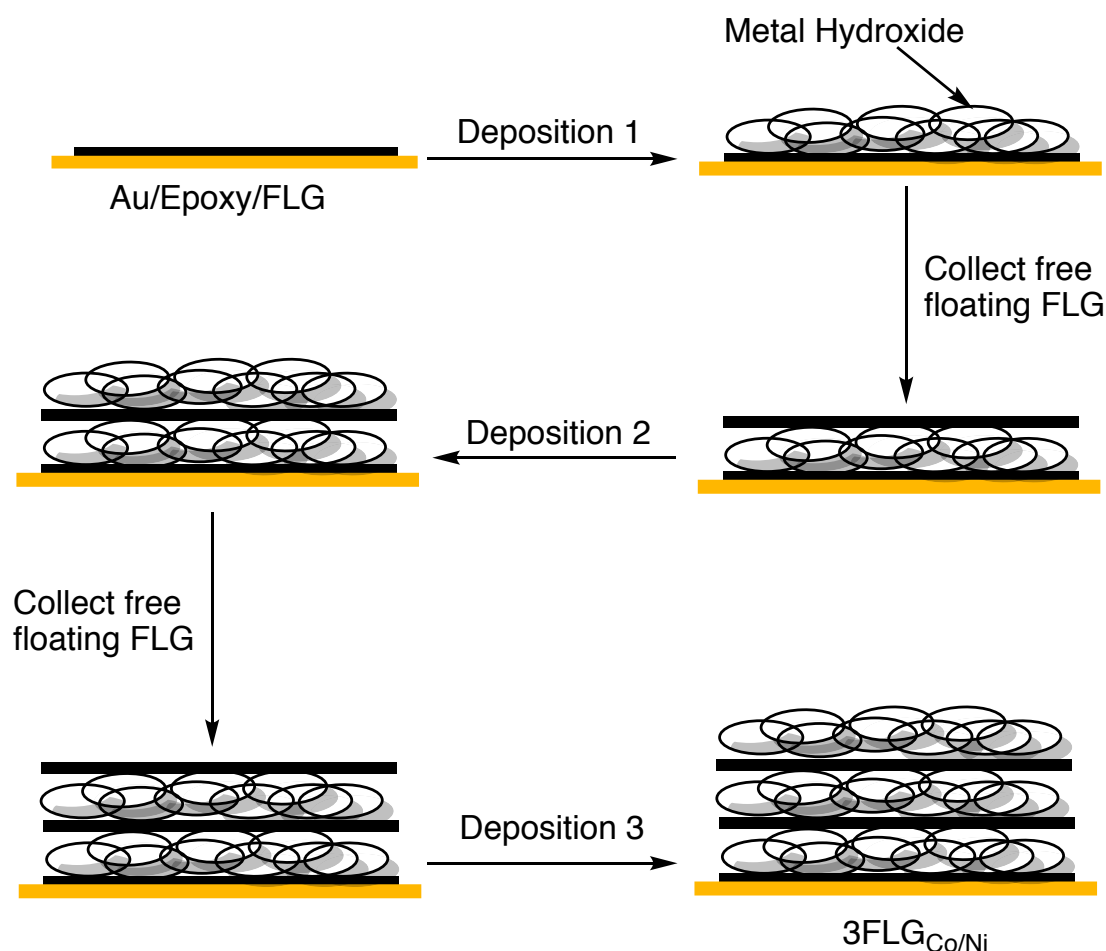


Figure 6.27: LBL deposition protocol to prepare $3\text{FLG}_{\text{Co/Ni}}$ (and $3\text{FLG}_{\text{CP+Co/Ni}}$ if a FLG_{CP} sheet is used rather than FLG). The metal hydroxide has only been drawn on one side of the FLG sheets for clarity.

Figure 6.28 shows the CV response of $3\text{FLG}_{\text{Co/Ni}}$ and $3\text{FLG}_{\text{CP+Co/Ni}}$ in 1 M KOH at selected scan rates. As expected, the CVs show redox peaks associated with the cobalt

and nickel hydroxide redox reactions given in Equations 6.6, 6.7, and 6.8. By comparing the one- and three-sheet systems, there is an obvious increase in the area enclosed by the CV, indicating the total capacitance has increased upon stacking.

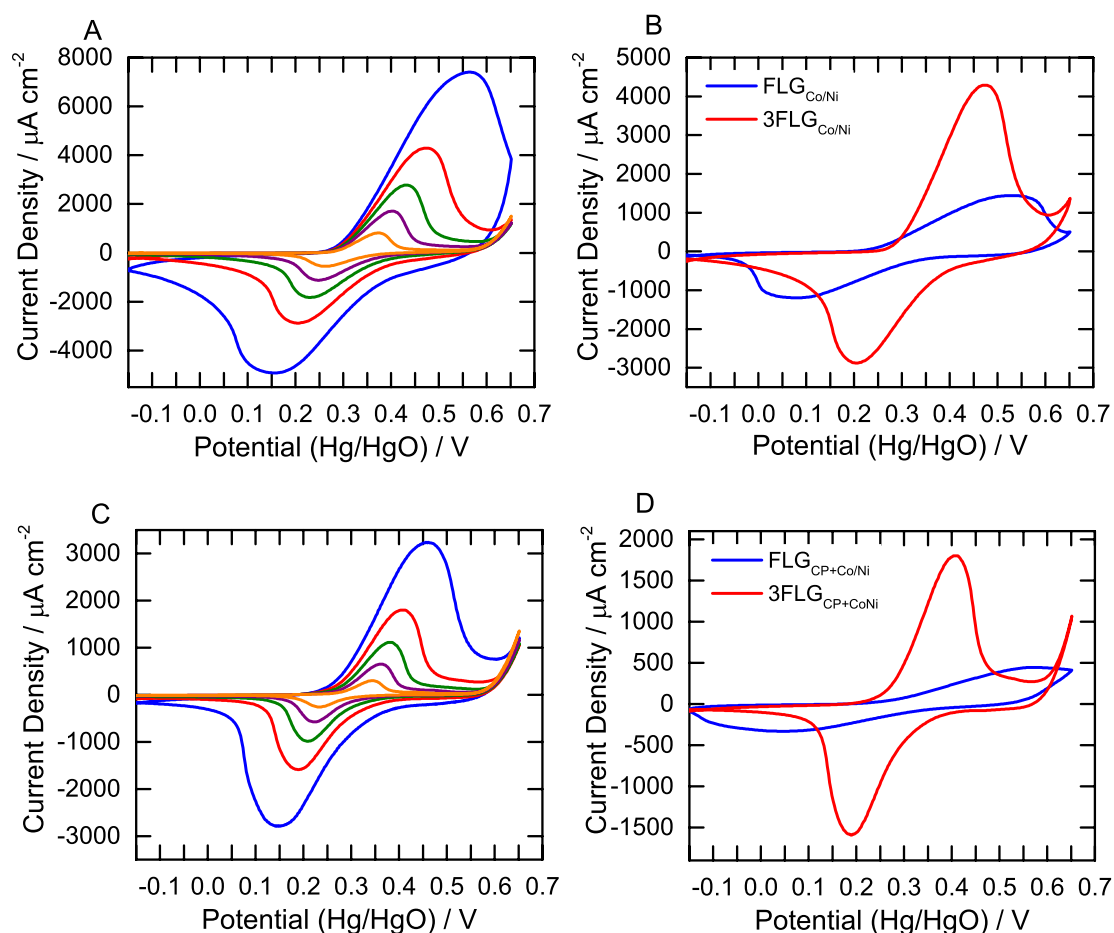


Figure 6.28: CV in 1 M KOH of three-sheet stacks of $\text{FLG}_{\text{Co/Ni}}$ and $\text{FLG}_{\text{CP+Co/Ni}}$: (A) $3\text{FLG}_{\text{Co/Ni}}$ at 50 (blue), 20 (red), 10 (green), 5 (purple), and 2 mV s^{-1} (orange); (B) $\text{FLG}_{\text{Co/Ni}}$ and $3\text{FLG}_{\text{Co/Ni}}$ at 20 mV s^{-1} ; (C) $3\text{FLG}_{\text{CP+Co/Ni}}$ at 50 (blue), 20 (red), 10 (green), 5 (purple), and 2 mV s^{-1} (orange); (D) $\text{FLG}_{\text{CP+Co/Ni}}$ and $3\text{FLG}_{\text{CP+Co/Ni}}$ at 20 mV s^{-1} .

An interesting difference between the one- and three-sheet stacks is the position of the oxidation and reduction peaks. In the three-sheet systems, both with and without the CP film, the peak separation has decreased as the oxidation and reduction peaks have shifted to less positive and less negative potentials respectively. Earlier, the increase in peak separation with increasing deposition time (and scan rate) was proposed to be caused by slower electron transport kinetics through the metal hydroxide film.²⁷ Hence, the reduced peak separation for the three-sheet stacks could be caused by improved electron transfer into the metal hydroxide film. For the three-sheet stacks, the cobalt-nickel hydroxide film is sandwiched between sheets of FLG, and so electrons can be transferred into the metal hydroxide film from both sides, likely giving improved electron transport kinetics, which would result in a decrease in the oxidation and

reduction peak separation. The $3\text{FLG}_{\text{CP}+\text{Co}/\text{Ni}}$ oxidation and reduction peak separation is decreased slightly compared to the $3\text{FLG}_{\text{Co}/\text{Ni}}$, which is presumably a result of the smaller amount of metal hydroxide between the FLG sheets for FLG_{CP} , as the metal hydroxide only deposits on one side of the FLG_{CP} sheet. The assumed electron transport pathways are illustrated in Figure 6.29.

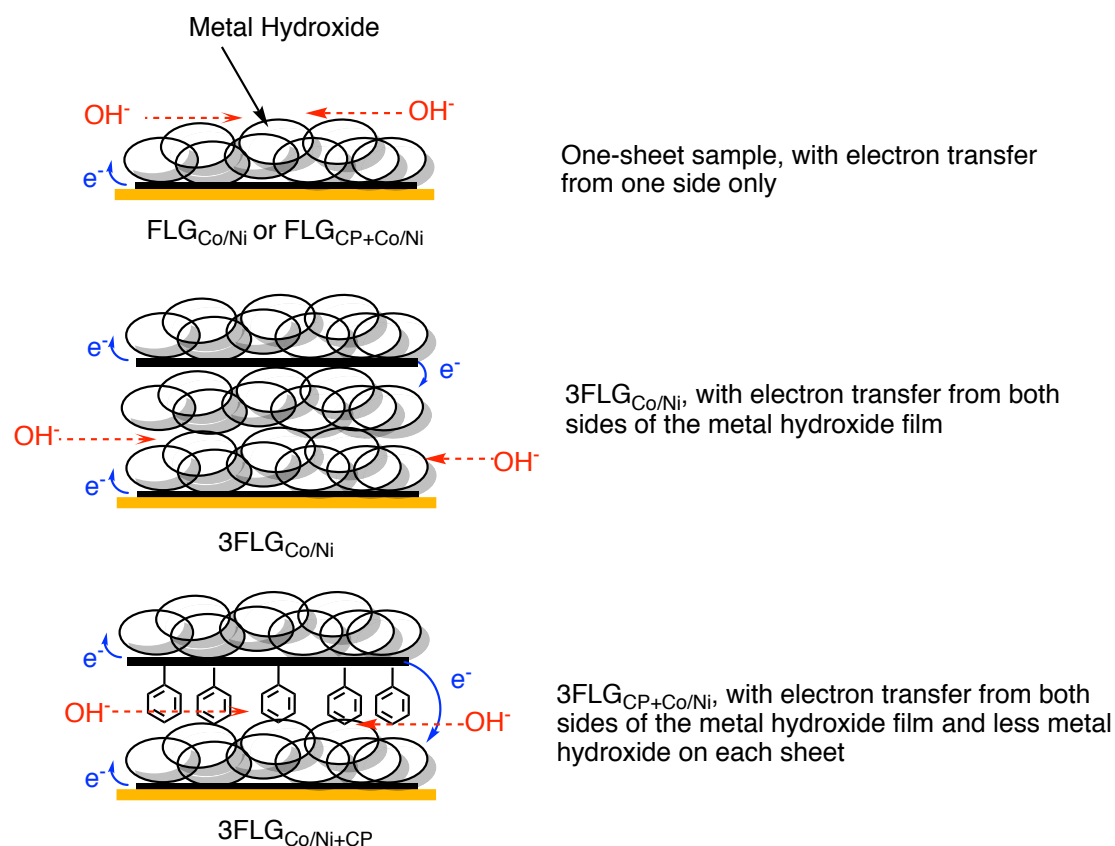


Figure 6.29: Possible electron transport pathways for one- and three-sheet stacks of FLG after cobalt-nickel hydroxide deposition. The metal hydroxide has only been shown on one side of the initial FLG sheet for clarity.

Figure 6.30 shows the CD profiles for the $3\text{FLG}_{\text{Co}/\text{Ni}}$ and $3\text{FLG}_{\text{CP}+\text{Co}/\text{Ni}}$ surfaces. As before, the plots show different regions that correspond to the redox processes seen in the CVs. Figure 6.30C shows the calculated areal capacitance at different current densities. All surfaces show a decrease in capacitance at higher current densities. The rate capability is similar between the one- and three-sheet systems, indicating the stacking process does not decrease the rate at which the system can be charged and discharged.

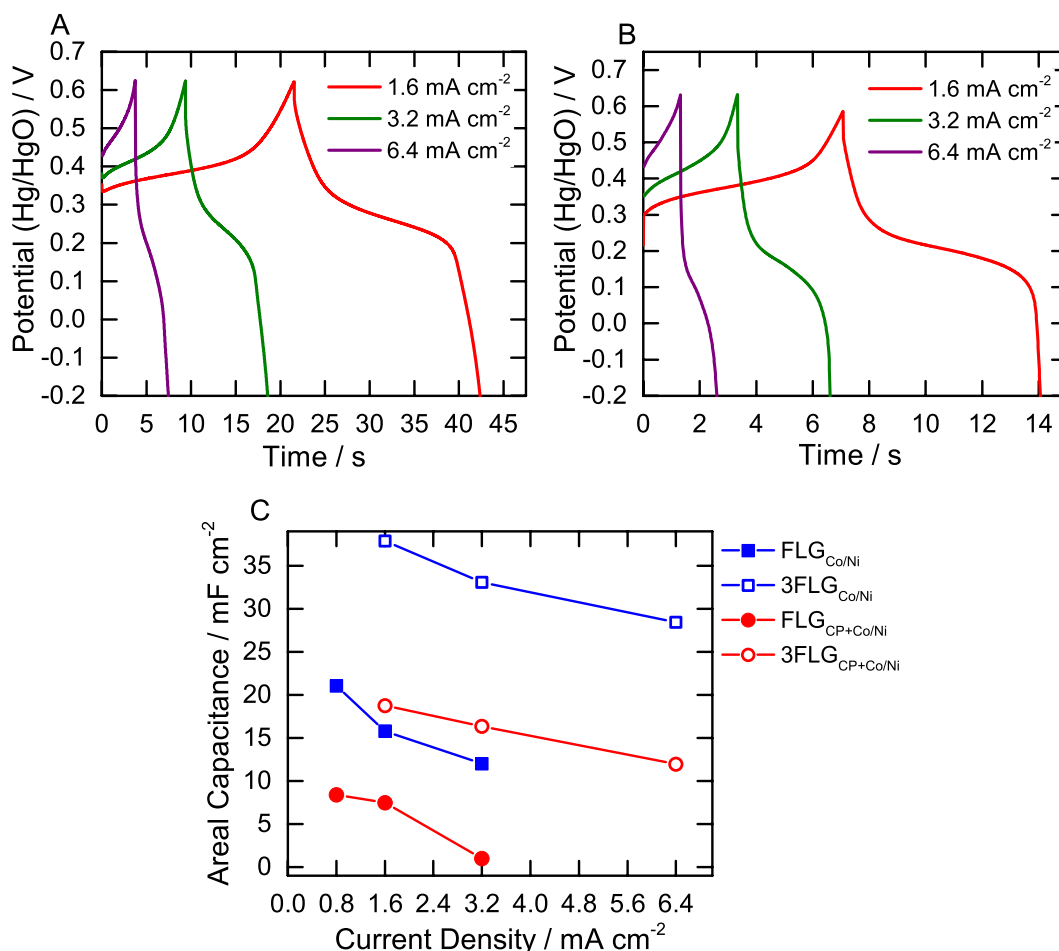


Figure 6.30: CD at selected current densities in 1 M KOH: (A) 3FLG_{Co/Ni} and (B) 3FLG_{CP+Co/Ni}. (C) Calculated areal capacitance at different current densities for the one- and three-sheet systems.

The areal capacitance was calculated from both the CV and CD results, and the values are tabulated in Table 6.6. As expected, the capacitance, as calculated from both CV and CD results, has increased with stacking. From the CD results, the capacitance has increased by approximately 2.0× for FLG_{Co/Ni} and 2.2× for FLG_{CP+Co/Ni}, indicating a 3× increase in capacitance is not accomplished for either three-sheet system. ICPMS was used to calculate the increase in the amount of cobalt-nickel hydroxide after the stacking protocol, to establish whether the less than 3× increase in capacitance could be attributed to a less than 3× increase in the amount of cobalt-nickel hydroxide present in the stacked samples. The measured cobalt hydroxide and nickel hydroxide masses are given in Table 6.6. For all systems, the total amount of cobalt-nickel hydroxide in the three-sheet stack samples is approximately 2× that in the one-sheet samples. Since the total capacitance increases approximately 2× after the LBL protocol, it is clear that the less than 3× increase upon stacking is associated with the amount of pseudocapacitive material rather than the incomplete separation of the FLG sheets. The increase in

capacitance is 2× in the presence and absence of the CP film, suggesting the presence of the film does not influence this behaviour.

Table 6.6: Capacitance calculated from CVs at 20 mV s⁻¹ and CD at 1.6 mA cm⁻² for FLG_{Co/Ni}, FLG_{CP+Co/Ni}, 3FLG_{Co/Ni}, and 3FLG_{CP+Co/Ni}, and mass of cobalt and nickel hydroxide for each system determined by ICPMS.

| Sample | CV Capacitance / mF cm ⁻² | CD Capacitance / mF cm ⁻² | Mass Co(OH) ₂ / mg cm ⁻² | Mass Ni(OH) ₂ / mg cm ⁻² | Total Mass / mg cm ⁻² |
|--------------------------|--------------------------------------|--------------------------------------|--|--|----------------------------------|
| FLG _{CP+Co/Ni} | 9.5 ± 0.2 | 7.9 ± 0.6 | 0.09 ± 0.01 | 0.17 ± 0.01 | 0.26 ± 0.01 |
| 3FLG _{CP+Co/Ni} | 20.3 ± 5.0 | 18.8 ± 4.4 | 0.17 ± 0.03 | 0.30 ± 0.06 | 0.47 ± 0.07 |
| <i>Increase</i> | <i>2.1 × ± 0.3</i> | <i>2.4 × ± 0.2</i> | <i>1.9 × ± 0.3</i> | <i>1.8 × ± 0.3</i> | <i>1.8 × ± 0.2</i> |
| FLG _{Co/Ni} | 21.5 ± 1.2 | 17.5 ± 1.6 | 0.19 ± 0.04 | 0.28 ± 0.04 | 0.47 ± 0.06 |
| 3FLG _{Co/Ni} | 35.8 ± 5.5 | 36.9 ± 3.9 | 0.45 ± 0.05 | 0.57 ± 0.05 | 1.02 ± 0.07 |
| <i>Increase</i> | <i>1.7 × ± 0.2</i> | <i>2.1 × ± 0.2</i> | <i>2.4 × ± 0.3</i> | <i>2.0 × ± 0.2</i> | <i>2.2 × ± 0.2</i> |

6.3.3 Summary of Metal Hydroxide Capacitance

The deposition of a metal hydroxide film onto FLG increases the areal capacitance of the system due to the additional pseudocapacitive material at the surface. The LBL deposition protocol can further increase the areal capacitance by increasing the amount of pseudocapacitive cobalt-nickel hydroxide at the surface.

As explained earlier, gravimetric capacitance is often a more useful way to express the capacitance of the system, especially when comparing results with literature reports. The gravimetric capacitance for each sample can be calculated using the mass of cobalt-nickel hydroxide measured through ICPMS, and is given in Table 6.7. The gravimetric capacitance is much lower than literature reports for cobalt hydroxide, nickel hydroxide, and the binary metal hydroxide on graphene materials (1000-2000 F g⁻¹)^{6, 8} and shows no increase compared with the unmodified FLG. It is assumed that the low gravimetric capacitance is primarily a result of electroinactive regions within cobalt-nickel hydroxide film. The CV at 20 mV s⁻¹ was used to calculate the electrochemically accessible amount of metal hydroxide at the surface, by calculating the charge associated with the reduction peak (Q). The charge can then be converted into a surface concentration (Γ) in mol cm⁻² based on Equation 6.9, where the number of electrons (n) is 1, and A is the working electrode area.

$$\Gamma = \frac{Q}{nFA} \quad (6.9)$$

It was not possible to distinguish between the individual metal hydroxide components using the reduction peak, however the molecular weights of cobalt and nickel hydroxide are approximately the same (92.95 and 92.71 g mol⁻¹ respectively), therefore the

combined mass of cobalt and nickel hydroxide can be calculated. Further, the cobalt to nickel ratio at the surface is approximately 2:3, as shown by ICPMS and EDS results, so the electrochemically accessible mass of the individual metal hydroxide components can be estimated. If CVs are used to calculate the electrochemically accessible mass of metal hydroxide at the surface (Table 6.7) then it is clear that only a small portion of the cobalt-nickel hydroxide film is electrochemically accessible, explaining why the gravimetric capacitance is low. The electrochemically inaccessible regions are likely a result of reduced electron transport through the cobalt-nickel hydroxide film. It is possible that this is a consequence of using planar FLG electrodes as the carbon substrate. When porous carbon foams are used as the carbon electrode higher gravimetric capacitances are obtained,^{6, 8, 49} possibly because these can provide a better template for metal hydroxide deposition where the metal hydroxide deposits as individual, vertically aligned flakes, rather than depositing as a film on the FLG surface, resulting in better pathways for electron transport.

Table 6.7: Areal and gravimetric capacitances (calculated using mass derived from ICPMS) for FLG and FLG_{CP} after cobalt-nickel hydroxide deposition, for one- and three-sheet systems (unmodified FLG shown for comparison). Mass of cobalt-nickel hydroxide determined using the area under the CV reduction peak at 20 mV s⁻¹ and from ICPMS analysis also shown.

| Sample | $C_A / \text{mF cm}^{-2}$ | $C_G / \text{F g}^{-1}$ | Mass Co(OH) ₂ (CV) / mg cm ⁻² | Mass Ni(OH) ₂ (CV) / mg cm ⁻² | Total Mass (CV) / mg cm ⁻² | Total Mass (ICPMS) / mg cm ⁻² |
|--------------------------|------------------------------|-------------------------|--|--|---|--|
| FLG | $1.3 \pm 0.1 \times 10^{-2}$ | 42.8 ± 8.0 | - | - | - | - |
| FLG _{CP+Co/Ni} | 7.9 ± 0.6 | 31.1 ± 8.0 | 0.004 | 0.003 | 0.007 ± 0.001 | 0.26 ± 0.01 |
| 3FLG _{CP+Co/Ni} | 18.8 ± 4.4 | 39.9 ± 9.1 | 0.009 | 0.006 | 0.015 ± 0.004 | 0.47 ± 0.07 |
| FLG _{Co/Ni} | 17.5 ± 1.6 | 37.2 ± 3.7 | 0.010 | 0.007 | 0.017 ± 0.005 | 0.47 ± 0.06 |
| 3FLG _{Co/Ni} | 36.9 ± 3.9 | 37.1 ± 3.7 | 0.017 | 0.012 | 0.029 ± 0.005 | 1.02 ± 0.07 |

The areal and gravimetric capacitances were used to calculate the energy and power density, and the resulting Ragone plots are given in Figure 6.31. The Ragone plots show three points for each sample, each corresponding to a different current density. As expected, the areal energy and power density increase after deposition, due to the increase in the areal capacitance resulting from the pseudocapacitive film. Furthermore, the three-sheet samples show a higher areal energy density than their one-sheet counterpart. On the other hand, due to the electroinactive regions of the cobalt-nickel hydroxide film that increase the mass but do not contribute to the total capacitance, the gravimetric energy density is low compared to literature reports for the deposition of

metal oxide or hydroxide materials onto porous graphene, however is comparable with some commercial amorphous carbon based supercapacitors.⁵⁰

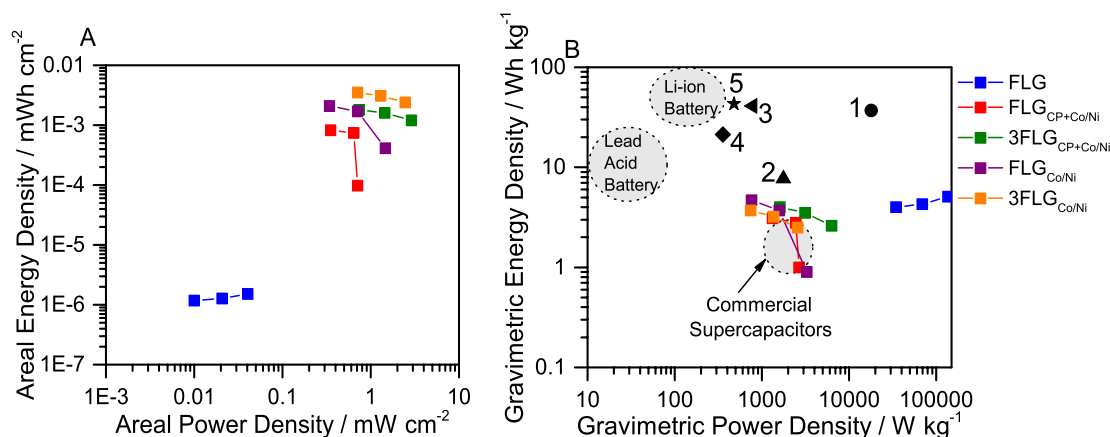


Figure 6.31: (A) Areal Ragone plot and (B) gravimetric Ragone plot for FLG, FLG_{Co/Ni}, 3FLG_{Co/Ni}, FLG_{CP+Co/Ni}, and 3FLG_{CP+Co/Ni}. Literature examples of 3D multilayered graphene foam with Co(OH)₂ flakes (1),⁶ reduced graphene oxide with ruthenium nanoparticles (2),⁴⁶ 3D graphene/nickel scaffold with MnO₂ nanoflowers (3),⁴² Ni-Fe layered double hydroxide/graphene aerogel (4),⁹ graphene aerogel with V₂O₅ particles (5)⁴³, and commercial lead acid batteries, Li-ion batteries, and carbon-based supercapacitors also shown.⁵⁰

The deposition and LBL stacking protocol need to be further developed to make devices with improved energy density. The deposition parameters (time, electrolyte concentration, and applied potential) should be altered so that only a very thin film of metal hydroxide is deposited on the surface. Decreasing the loading of the metal hydroxide on the surface will presumably improve the performance due to better electron transport.

6.4 Conclusion

FLG was modified with gold nanoparticles and metal hydroxide thin films through electrochemical deposition. The use of the organic solvent DMF for gold deposition, prevented the spontaneous nucleation of gold nanoparticles, and allowed the deposition to be carried out while the graphene was still supported by the copper foil. The size and density of the gold nanoparticles was easily controlled through varying the applied potential and deposition time: in this work particles with heights ranging from 5-25 nm were deposited with densities from 25-95 μm^{-2} . The ability of the deposited nanoparticles to prevent restacking of the FLG sheets was investigated using EIS. Unlike the molecular spacers used in Chapter 5, the gold nanoparticles were unable to fully separate the FLG sheets upon stacking.

The electrochemical deposition of cobalt-nickel hydroxide films resulted in a dense mat of whisker-like structures comprised of cobalt hydroxide and nickel hydroxide in a 2:3 ratio on the surface. The metal hydroxide film increased the total areal capacitance of the FLG system through redox reactions that provided additional pseudocapacitance. The presence of a CP film on one side of the FLG inhibited deposition on that side, presumably due to film preventing cobalt-nickel hydroxide adhesion to the FLG surface. The total areal capacitance could be increased further using a LBL protocol, with a 2× increase from a one- to three-sheet system for both $FLG_{Co/Ni}$ and $FLG_{CP+Co/Ni}$. The less than 3× increase was attributed to the less than 3× increase in the total mass of cobalt-nickel hydroxide at the FLG surface. Unfortunately, the gravimetric capacitance of the one- and three-sheet systems was lower than anticipated. It is assumed this is a result the film being too thick and therefore some regions of the metal hydroxide film are electrochemically inaccessible as these regions will increase the total mass of the electrode but do not add any additional capacitance, and so the gravimetric capacitance is reduced.

6.5 References

1. Ke, Q.; Wang, J., Graphene-based materials for supercapacitor electrodes—a review. *J. Materiomics* **2016**, *2*, 37-54.
2. Tian, Y.; Liu, H.; Zhao, G.; Tatsuma, T., Shape-controlled electrodeposition of gold nanostructures. *J. Phys. Chem. B* **2006**, *110*, 23478-23481.
3. Toth, P. S.; Velický, M.; Ramasse, Q. M.; Kepaptsoglou, D. M.; Dryfe, R. A. W., Symmetric and asymmetric decoration of graphene: Bimetal-graphene sandwiches. *Adv. Funct. Mater.* **2015**, *25*, 2899-2909.
4. Bosch-Navarro, C.; Rourke, J. P.; Wilson, N. R., Controlled electrochemical and electroless deposition of noble metal nanoparticles on graphene. *RSC Adv.* **2016**, *6*, 73790-73796.
5. Grunder, Y.; Ho, H. L. T.; Mosselmans, J. F. W.; Schroeder, S. L. M.; Dryfe, R. A. W., Inhibited and enhanced nucleation of gold nanoparticles at the water|1,2-dichloroethane interface. *Phys. Chem. Chem. Phys.* **2011**, *13*, 15681-15689.
6. Patil, U. M.; Nam, M. S.; Sohn, J. S.; Kulkarni, S. B.; Shin, R.; Kang, S.; Lee, S.; Kim, J. H.; Jun, S. C., Controlled electrochemical growth of Co(OH)₂ flakes on 3D multilayered graphene foam for high performance supercapacitors. *J. Mater. Chem. DA* **2014**, *2*, 19075-19083.
7. Wang, L.; Li, X.; Guo, T.; Yan, X.; Tay, B. K., Three-dimensional Ni(OH)₂ nanoflakes/graphene/nickel foam electrode with high rate capability for supercapacitor applications. *Int. J. Hydrogen Energy* **2014**, *39*, 7876-7884.
8. Xiong, G.; He, P.; Wang, D.; Zhang, Q.; Chen, T.; Fisher, T. S., Hierarchical Ni-Co hydroxide petals on mechanically robust graphene petal foam for high-energy asymmetric supercapacitors. *Adv. Funct. Mater.* **2016**, *26*, 5460-5470.
9. Gao, X.; Lv, H.; Li, Z.; Xu, Q.; Liu, H.; Wang, Y.; Xia, Y., Low-cost and high-performance of a vertically grown 3D Ni-Fe layered double hydroxide/graphene aerogel supercapacitor electrode material. *RSC Adv.* **2016**, *6*, 107278-107285.
10. Wang, Y.-M.; Zhang, X.; Guo, C.-Y.; Zhao, Y.-Q.; Xu, C.-L.; Li, H.-L., Controllable synthesis of 3D NiCo oxides with different morphologies for high-capacity supercapacitors. *J. Mater. Chem. A* **2013**, *1*, 13290-13300.
11. Komsiyiska, L.; Staikov, G., Electrocrystallization of Au nanoparticles on glassy carbon from HClO₄ solution containing [AuCl₄]⁻. *Electrochim. Acta* **2008**, *54*, 168-172.
12. Holt, K. B.; Sabin, G.; Compton, R. G.; Foord, J. S.; Marken, F., Reduction of tetrachloroaurate(iii) at boron-doped diamond electrodes: Gold deposition versus gold colloid formation. *Electroanal.* **2002**, *14*, 797-803.
13. Aldous, L.; Silvester, D. S.; Villagran, C.; Pitner, W. R.; Compton, R. G.; Cristina Lagunas, M.; Hardacre, C., Electrochemical studies of gold and chloride in ionic liquids. *New J. Chem.* **2006**, *30*, 1576-1583.
14. Monzon, L. M. A.; Byrne, F.; Coey, J. M. D., Gold electrodeposition in organic media. *J. Electroanal. Chem.* **2011**, *657*, 54-60.
15. Lee, M. J.; Choi, J. S.; Kim, J. S.; Byun, I. S.; Lee, D. H.; Ryu, S.; Lee, C.; Park, B. H., Characteristics and effects of diffused water between graphene and a SiO₂ substrate. *Nano Res.* **2012**, *5*, 710-717.

16. Bom, N. M.; Soares, G. V.; de Oliveira Junior, M. H.; Lopes, J. M. J.; Riechert, H.; Radtke, C., Water incorporation in graphene transferred onto SiO₂/Si investigated by isotopic labeling. *J. Phys. Chem. C* **2016**, *120*, 201-206.
17. Penner, R. M., Mesoscopic metal particles and wires by electrodeposition. *J. Phys. Chem. B* **2002**, *106*, 3339-3353.
18. Day, T. M.; Unwin, P. R.; Macpherson, J. V., Factors controlling the electrodeposition of metal nanoparticles on pristine single walled carbon nanotubes. *Nano Lett.* **2007**, *7*, 51-57.
19. Zhang, H.; Xu, J.-J.; Chen, H.-Y., Shape-controlled gold nanoarchitectures: Synthesis, superhydrophobicity, and electrocatalytic properties. *J. Phys. Chem. C* **2008**, *112*, 13886-13892.
20. Huang, L.; Lee, E.-S.; Kim, K.-B., Electrodeposition of monodisperse copper nanoparticles on highly oriented pyrolytic graphite electrode with modulation potential method. *Colloids Surf., A* **2005**, *262*, 125-131.
21. Pastoriza-Santos, I.; Liz-Marzán, L. M., Formation and stabilization of silver nanoparticles through reduction by N,N-dimethylformamide. *Langmuir* **1999**, *15*, 948-951.
22. Wu, Y.; Jiang, W.; Ren, Y.; Cai, W.; Lee, W. H.; Li, H.; Piner, R. D.; Pope, C. W.; Hao, Y.; Ji, H.; Kang, J.; Ruoff, R. S., Tuning the doping type and level of graphene with different gold configurations. *Small* **2012**, *8*, 3129-3136.
23. Haynes, W. M.; Lide, D. R.; Bruno, T. J., *Handbook of chemistry and physics*. CRC Press: 2012; Vol. 93rd Edition.
24. Cheng, Y.; Zhang, H.; Varanasi, C. V.; Liu, J., Improving the performance of cobalt-nickel hydroxide-based self-supporting electrodes for supercapacitors using accumulative approaches. *Energy & Environmental Science* **2013**, *6*, 3314-3321.
25. Biesinger, M. C.; Payne, B. P.; Grosvenor, A. P.; Lau, L. W.; Gerson, A. R.; Smart, R. S. C., Resolving surface chemical states in XPS analysis of first row transition metals, oxides and hydroxides: Cr, Mn, Fe, Co and Ni. *Appl. Surf. Sci.* **2011**, *257*, 2717-2730.
26. Yang, J.; Liu, H.; Martens, W. N.; Frost, R. L., Synthesis and characterization of cobalt hydroxide, cobalt oxyhydroxide, and cobalt oxide nanodiscs. *J. Phys. Chem. C* **2009**, *114*, 111-119.
27. Li, H.; Yu, M.; Wang, F.; Liu, P.; Liang, Y.; Xiao, J.; Wang, C.; Tong, Y.; Yang, G., Amorphous nickel hydroxide nanospheres with ultrahigh capacitance and energy density as electrochemical pseudocapacitor materials. *Nat. Commun.* **2013**, *4*, 1894.
28. Grosvenor, A. P.; Biesinger, M. C.; Smart, R. S. C.; McIntyre, N. S., New interpretations of XPS spectra of nickel metal and oxides. *Surf. Sci.* **2006**, *600*, 1771-1779.
29. Casella, I. G.; Guascito, M. R.; Sannazzaro, M. G., Voltammetric and XPS investigations of nickel hydroxide electrochemically dispersed on gold surface electrodes. *J. Electroanal. Chem.* **1999**, *462*, 202-210.

30. Bond, A. M., *Broadening electrochemical horizons: Principles and illustration of voltammetric and related techniques*. Oxford University Press on Demand: 2002.
31. Bard, A. J.; Faulkner, L. R.; Leddy, J.; Zoski, C. G., *Electrochemical methods: Fundamentals and applications*. Wiley New York: 1980; Vol. 2.
32. Gupta, V.; Gupta, S.; Miura, N., Potentiostatically deposited nanostructured $\text{Co}_x\text{Ni}_{1-x}$ layered double hydroxides as electrode materials for redox-supercapacitors. *J. Power Sources* **2008**, *175*, 680-685.
33. Kong, L.-B.; Lang, J.-W.; Liu, M.; Luo, Y.-C.; Kang, L., Facile approach to prepare loose-packed cobalt hydroxide nano-flakes materials for electrochemical capacitors. *J. Power Sources* **2009**, *194*, 1194-1201.
34. Zhang, J.; Liu, F.; Cheng, J.; Zhang, X., Binary nickel–cobalt oxides electrode materials for high-performance supercapacitors: Influence of its composition and porous nature. *ACS Appl. Mater. Interfaces* **2015**, *7*, 17630-17640.
35. Wan, C.; Jiao, Y.; Li, J., Flexible, highly conductive, and free-standing reduced graphene oxide/polypyrrole/cellulose hybrid papers for supercapacitor electrodes. *J. Mater. Chem. A* **2017**, *5*, 3819-3831.
36. Ma, L.; Zheng, M.; Liu, S.; Li, Q.; You, Y.; Wang, F.; Ma, L.; Shen, W., Synchronous exfoliation and assembly of graphene on 3D $\text{Ni}(\text{OH})_2$ for supercapacitors. *Chem. Commun.* **2016**, *52*, 13373-13376.
37. Yu, J.; Wu, J.; Wang, H.; Zhou, A.; Huang, C.; Bai, H.; Li, L., Metallic fabrics as the current collector for high-performance graphene-based flexible solid-state supercapacitor. *ACS Appl. Mater. Interfaces* **2016**.
38. Zhang, D.; Zhang, X.; Chen, Y.; Yu, P.; Wang, C.; Ma, Y., Enhanced capacitance and rate capability of graphene/polypyrrole composite as electrode material for supercapacitors. *J. Power Sources* **2011**, *196*, 5990-5996.
39. Shao, Y.; El-Kady, M. F.; Lin, C.-W.; Zhu, G.; Marsh, K. L.; Hwang, J. Y.; Zhang, Q.; Li, Y.; Wang, H.; Kaner, R. B., 3D freeze-casting of cellular graphene films for ultrahigh-power-density supercapacitors. *Adv. Mater.* **2016**, *28*, 6719-6726.
40. Liu, W.; Li, J.; Feng, K.; Sy, A.; Liu, Y.; Lim, L.; Lui, G.; Tjandra, R.; Rasenthiram, L.; Chiu, G.; Yu, A., Advanced Li-ion hybrid supercapacitors based on 3D graphene–foam composites. *ACS Appl. Mater. Interfaces* **2016**.
41. Narayanan, R.; Yamada, H.; Karakaya, M.; Podila, R.; Rao, A. M.; Bandaru, P. R., Modulation of the electrostatic and quantum capacitances of few layered graphenes through plasma processing. *Nano Lett.* **2015**, *15*, 3067-3072.
42. Wu, L.; Hao, L.; Pang, B.; Wang, G.; Zhang, Y.; Li, X., MnO_2 nanoflowers and polyaniline nanoribbons grown on hybrid graphene/Ni 3D scaffolds by *in situ* electrochemical techniques for high-performance asymmetric supercapacitors. *J. Mater. Chem. A* **2017**, *5*, 4629-4637.
43. Yilmaz, G.; Lu, X.; Ho, G. W., Cross-linker mediated formation of sulfur-functionalized V_2O_5 /graphene aerogels and their enhanced pseudocapacitive performance. *Nanoscale* **2017**, *9*, 802-811.

44. Wang, B.; Park, J.; Wang, C.; Ahn, H.; Wang, G., Mn₃O₄ nanoparticles embedded into graphene nanosheets: Preparation, characterization, and electrochemical properties for supercapacitors. *Electrochim. Acta* **2010**, *55*, 6812-6817.
45. Liu, L.; Su, L.; Lang, J.; Hu, B.; Xu, S.; Yan, X., Controllable synthesis of Mn₃O₄ nanodots@nitrogen-doped graphene and its application for high energy density supercapacitors. *J. Mater. Chem. A* **2017**, *5*, 5523-5531.
46. Hassan, H. K.; Atta, N. F.; Hamed, M. M.; Galal, A.; Jacob, T., Ruthenium nanoparticles-modified reduced graphene prepared by a green method for high-performance supercapacitor application in neutral electrolyte. *RSC Adv.* **2017**, *7*, 11286-11296.
47. Taberna, P.; Simon, P.; Fauvarque, J.-F., Electrochemical characteristics and impedance spectroscopy studies of carbon-carbon supercapacitors. *J. Electrochem. Soc.* **2003**, *150*, A292-A300.
48. Nguyen, T.; Carmezim, M. J.; Montemor, M. F., Current transient and *in situ* AFM studies of initial growth stages of electrochemically deposited nickel cobalt hydroxide nanosheet films. *Phys. Chem. Chem. Phys.* **2016**, *18*, 12368-12374.
49. Wang, X.; Liu, J.; Wang, Y.; Zhao, C.; Zheng, W., Ni(OH)₂ nanoflakes electrodeposited on Ni foam-supported vertically oriented graphene nanosheets for application in asymmetric supercapacitors. *Mater. Res. Bull.* **2014**, *52*, 89-95.
50. Romero, J.; Rodriguez-San-Miguel, D.; Ribera, A.; Mas-Balleste, R.; Otero, T. F.; Manet, I.; Licio, F.; Abellan, G.; Zamora, F.; Coronado, E., Metal-functionalized covalent organic frameworks as precursors of supercapacitive porous N-doped graphene. *J. Mater. Chem. A* **2017**, *5*, 4343-4351.

7 Overall Conclusion and Future Work

7.1 Conclusion

The overall goal of this thesis work was to prepare FLG via CVD, and modify the sheets so that upon layer-by-layer (LBL) assembly aggregation was prevented and the full surface area of each sheet was accessible to electrolyte ions, allowing optimal electrical double layer formation at each interface. Initially, FLG, on a copper foil support, was prepared via CVD, and two separate protocols were developed to give 3-4 and 6-7 layer graphene, that was polycrystalline with hexagonal domains interconnected by defective grain boundary regions. The FLG was removed from the copper foil support to allow transfer to different substrates either before or after modification using a polymer free and aqueous based process, that prevented the undesirable contamination of FLG with polymeric residues.

Aqueous aryldiazonium chemistry was used to graft a molecular layer to FLG using either a free floating, or on copper protocol. FLG was modified using five aryldiazonium salts: NBD, NABD, IBD, CBD, and MBD, with the NBD modification studied in detail, highlighting the applicability of this protocol to a wide range of functional groups. Covalent bonding was confirmed through Raman spectroscopy, with an increase in the D/G band intensity ratio after modification resulting from the conversion of sp^2 -carbon atoms to sp^3 -hybridisation. IR spectroscopy of the FLG_{NP} further confirmed the presence of the grafted film, and showed evidence for azo linkages. Additionally, the importance of washing the FLG_{NP} with methanol after the reaction was realised, as this removed a substantial amount of physisorbed material from the surface. XPS analysis of FLG_{NP} and FLG_{IP} confirmed the presence of azo linkages indicating the modification must take place via either the direct attack of the diazonium functionality or through a diazoate intermediate. Moreover, the ratio of nitro to azo nitrogen in FLG_{NP} confirmed a second reaction mechanism was occurring simultaneously, resulting in carbon-carbon bond formation. Electrochemistry of the FLG_{NP} was carried out in either a sandwiched or exposed orientation and in the sandwiched orientation two NP reduction peaks were sometimes seen, a behaviour that has not been reported previously for NP films on carbon substrates. It was proposed that the two reduction peaks resulted from limitations in proton diffusion within the film, with areas of decreased proton availability giving the peak at a more negative

potential. Furthermore, electrochemical surface concentration measurements were shown to depend on film orientation: in the exposed orientation, the surface concentration plateaued at approximately 0.5 nmol cm^{-2} , while in the sandwiched orientation the surface concentration increased linearly with reaction time. It was postulated that in the sandwiched orientation all of the film was electrochemically accessible, as electron transfer from both working electrodes (HOPG/PPF and FLG) is possible, whereas in the exposed orientation electron transfer is from one working electrode (FLG) only, therefore part of the film becomes electrochemically inaccessible above a certain film thickness.

FLG was also modified via a Diels-Alder reaction with an aryne. Anthranilic acids, after conversion of the primary amine to a diazonium group, can thermally decompose to give a highly reactive aryne, which can undergo a cycloaddition with FLG. This reaction was confirmed via Raman spectroscopy, with an increase in the D/G band intensity ratio after reaction with two anthranilic acids: NAA or ME. IR spectroscopy confirmed the successful generation of the aryne, as no amine or carboxylic acid peaks were observed for FLG_{NAA} or FLG_{ME} . Further, XPS results for FLG_{ME} showed no evidence of azo nitrogen, suggesting the observed reactivity is not due to the reaction of the generated diazonium moiety with the FLG. It is therefore likely that the aryne reacts with the FLG via a two-point binding mode (either a [2+2] or [4+2] cycloaddition), however confirmation of this binding mode requires further exploration. Additional investigation of this reaction with collaborators will involve using surface enhanced Raman spectroscopy on modified graphene and other graphitic carbon surfaces to confirm the reaction mechanism. The reaction was expected to provide monolayer coverage, which was studied using electrochemistry and AFM imaging after the reaction on FLG and PPF. Electrochemistry of FLG_{NAA} gave a limiting surface concentration, in both the exposed and sandwiched orientation, consistent with monolayer formation. Successful modification of PPF using NAA indicated this reaction is applicable to both basal plane and edge plane carbon materials, and AFM scratch testing of modified PPF confirmed the reaction was limited to a monolayer. In addition, electrochemistry of the modified PPF surfaces showed a limiting surface concentration of $0.55 \text{ nmol cm}^{-2}$, consistent with dense monolayer formation.

The final method used for molecular functionalisation of the FLG surface was the addition of a primary amine. The primary amine was expected to react with FLG via either a Michael-type addition activated by oxygen containing functionalities on the FLG surface, or through partial intercalation of the amine. Further work is required to distinguish between these two proposed reaction mechanisms. Two amines were trialled for this reaction, namely NPEA and AAQ. Raman and IR spectroscopy results gave no clear evidence for FLG modification, however both modifiers were detected using electrochemistry. The reaction protocol was repeated using physisorption analogues, which demonstrated that the surface concentration obtained via the amine reaction was not solely a result of physisorption.

The aryldiazonium modification route was selected for subsequent capacitance studies. The aryldiazonium reaction allowed covalent functionalisation of the FLG sheets in aqueous conditions. Regarding the development of environmentally conscious energy storage technologies, it is desirable that the reaction utilises environmentally benign solvents such as water. Furthermore, the aryldiazonium reaction gave a wide range of accessible surface concentrations, so it was possible to tune the reaction conditions to give multilayer films with varying thickness. Finally, a large array of functionalised aryldiazonium salts can be prepared by simple synthetic strategies (beyond those studied in this thesis work), which may be beneficial for future applications. The Diels-Alder reaction also gave a covalently bound film, with very good control over film thickness. However, the modification protocol was more complex and utilised organic solvents, thus this reaction was not pursued for the target application. Nevertheless, the ability to limit grafting to a monolayer could be highly beneficial for other applications that were not explored in this thesis work. The amine addition reaction was considered the least useful for the target application. This was due to the lack of evidence for covalently bonded groups, which may decrease the stability of the system, the uncertainty surrounding the modification mechanism, and the use of organic solvents making it less useful in environmentally conscious applications such as energy storage. Thus, for capacitance studies, the aryldiazonium reaction was investigated.

Following the aryldiazonium modification, the capacitance of FLG was studied. Compared with as prepared FLG, the FLG_{AP} and FLG_{CP} surfaces showed no loss of capacitance, however the NP film decreased the capacitance of the FLG, possibly due

to less space at the surface for electrical double layer formation. The modified sheets were assembled into three-sheet stacks via a LBL protocol and a NP surface concentration of $0.21 \pm 0.02 \text{ nmol cm}^{-2}$, corresponding to a film height between 0.6 and 0.7 nm, was sufficient to completely prevent aggregation of the modified FLG sheets during assembly and cycling, and allowed the full surface area of each modified FLG sheet to be accessed by electrolyte ions. This was true for all three film types on FLG. Cycle stability testing of the one- and three-sheet stacks demonstrated the FLG_{CP} and FLG_{NP} surfaces showed the best stability, as the FLG_{AP} surfaces suffered some capacitance degradation due to loss of pseudocapacitance. The gravimetric Ragone plots demonstrated that all the systems studied had a very high power density indicating good ion accessibility and transport, therefore a fast charge discharge capability, however the energy density was low.

The FLG was also decorated using gold nanoparticles and metal hydroxide thin films through electrochemical deposition. Initially, gold nanoparticles were used as a model system to establish if nanoparticles could also prevent aggregation of the sheets during LBL assembly. The deposition of gold nanoparticles onto FLG/Cu was carried out in non-aqueous conditions, as this allowed good control of the deposition process, due to inhibition of the reduction of the gold salt by the copper foil, preventing spontaneous nucleation of nanoparticles. AFM and SEM imaging confirmed the successful deposition of nanoparticles, unevenly distributed across the FLG surface. The size and density of the nanoparticles was efficiently controlled by altering the applied potential or deposition time, with nanoparticle heights ranging from 5-25 nm and densities from 25-95 μm . The FLG sheets, after decoration with gold nanoparticles, were assembled using the LBL protocol. The gold nanoparticles were unable to completely prevent aggregation of the FLG sheets upon stacking, indicating that the phenyl film grafted from the aryldiazonium reaction was a better option for preventing aggregation during assembly of supercapacitor electrodes from FLG.

To increase the energy density of the electrodes, cobalt-nickel hydroxide films were deposited on the surface, as these possessed their own pseudocapacitance. Cobalt-nickel hydroxide thin films were successfully deposited from an aqueous solution onto the FLG after transfer to a Au/epoxy surface. AFM and SEM images confirmed the

deposition of a mat of whisker-like structures on the surface, and XPS results indicated these were comprised of cobalt hydroxide and nickel hydroxide with the metal in the 2+ oxidation state. Repetition of this protocol on a FLG_{CP} surface illustrated that the grafted film blocked deposition of a metal hydroxide layer on one side of the FLG sheet. The cobalt-nickel hydroxide film increased the total capacitance of the system, however some regions of the film were electrochemically inaccessible, presumably due to limitations in electron transport through the film, which resulted in a low gravimetric capacitance and therefore a low gravimetric energy density.

The development of graphene-based supercapacitor electrodes is a highly active research field. This thesis work has established a convenient approach for the modification of graphene and subsequent LBL assembly, providing complete separation of graphene sheets, and therefore efficient double layer formation. Although some literature reports have utilised spacers to prevent aggregation (for example metal nanoparticles and carbon nanotubes), highly-controlled protocols for stacking of graphene functionalised with molecular spacers, like that developed here, are limited.⁴ Furthermore, verifying that the spacers provide complete sheet separation is often overlooked, with reports suggesting spacers provide an increase in the capacitance by preventing agglomeration, but do not provide experimental evidence for complete separation, like that presented in Chapter 5 of this work.⁴⁻⁶ The covalent bonding between the spacers and the FLG ensures the outstanding stability of the electrodes, with no aggregation of the sheets or decrease in capacitance even after 20,000 galvanostatic charge discharge cycles. Finally, although the energy density of the electrodes is lower than literature reports for other graphene materials, especially compared with pseudocapacitive materials,⁷⁻¹² the power density and therefore the speed at which the electrodes can operate is high. Moreover, the time constant calculated via electrochemical impedance spectroscopy is low compared with other porous carbons,¹¹ even after stacking. This suggests the electrodes can operate at high speeds, which is beneficial in real-world devices. Maintaining the high power density and stability obtained in this thesis work, while increasing the total capacitance and energy density will be highly beneficial in developing supercapacitor electrodes from graphene.

7.2 Future Work

In this thesis, the Diels-Alder reaction of an aryne with graphene and PPF was studied. The reaction mechanism is expected to result in a two-point binding mode, either through a [4+2] or a [2+2] mechanism. Future work will involve further investigations of this binding mode. This will initially involve using surface enhanced Raman spectroscopy to confirm the binding mode. After confirmation of the binding mode, advantages of this binding mode could be investigated, including increased stability and additional

Throughout this thesis work the quantum capacitance of the graphene was noted as a limitation to the total double layer capacitance. Literature reports emerging in the past 12 months have evaluated the importance of quantum capacitance for FLG electrodes.¹⁻³ Density functional theory calculations have suggested that for single layer systems the quantum capacitance is the limiting component to the capacitance. As quantum capacitance is dependent on the density of states it should scale with layer number, however beyond four layers calculations have shown that the total capacitance of the system does not increase with layer number, and instead becomes static. This implies an additional component to the capacitance of the system, which is suggested to be related to dielectric screening of the electrolyte by the additional graphene layers. The systems studied in this thesis work were all FLG, with a minimum of three layers, which indicates that this additional dielectric capacitance will play a role in the total capacitance of the electrode. However, as this has only recently been suggested, it was not considered during this thesis work. Future work will look to understand the contribution of this fourth capacitance component to the total capacitance of the system, which may provide better models to accurately fit the data and predict the impact of modification on the capacitance of FLG electrodes. Furthermore, as this component is related to the electrolyte it is reasonable to assume the choice of electrolyte will impact the total capacitance of the system, while for single layer systems, where the quantum capacitance is the limiting component, the choice of electrolyte should not significantly influence the total capacitance. Therefore, for FLG, variation of the electrolyte may result in systems with improved capacitance and this should be investigated as an option to increase the total capacitance.

Large surface area electrodes were prepared during this thesis work, through the prevention of aggregation using molecular spacers. These electrodes were investigated in terms of capacitance, with an increase in the surface area giving an increase in the electrical double layer capacitance of the electrode. This is only one possible application of these materials. Large surface area graphene electrodes would show promise in several fields, for example as catalytic supports, in gas sorption, in biosensing, and as electrode materials for Li-ion batteries. Hence, future work could involve investigation of any of these potential applications.

In this thesis work pseudocapacitive metal hydroxide thin films were deposited on the FLG surface to increase the total capacitance of the system. Unfortunately, the gravimetric capacitance of the resulting electrodes was lower than expected, hence the deposition procedure needs to be improved to ensure the full mass of metal hydroxide is electrochemically accessible, allowing improved gravimetric capacitances. It is likely that depositing individual platelets of cobalt-nickel hydroxide will result in improved electron transport, and therefore the deposition parameters must be tuned (for example deposition time or electrolyte concentration) to decrease the amount of metal hydroxide on the surface and provide such structures. In future work, the deposition protocol will be modified to increase the gravimetric capacitance of the FLG surfaces. Once the deposition procedure is optimised the sheets can be assembled using the LBL protocol developed in this thesis work. It may be beneficial to have the cobalt-nickel hydroxide sandwiched between two FLG sheets (Figure 7.1), as this will allow electron transfer into the metal hydroxide film from both sides, which would increase the amount of electrochemically accessible material at the surface, therefore this configuration will be investigated further. After finalising an appropriate deposition protocol, the modified FLG surfaces should be tested for cycle stability. Metal hydroxide pseudocapacitors suffer from cyclability issues, hence it is critical to ensure that depositing the cobalt-nickel hydroxide on the graphene has improved the stability of the pseudocapacitive system.

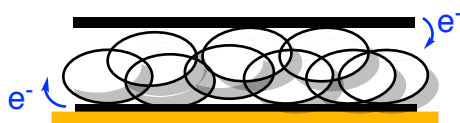


Figure 7.1: Metal hydroxide film sandwiched between two sheets of FLG to allow electron transfer from both sides of the film.

In this thesis work metal hydroxide nanoparticles were deposited on the FLG surfaces to increase the total capacitance of the system through additional pseudocapacitance reactions. Metal hydroxides are not the only option for increasing pseudocapacitance. Redox active molecular species, such as anthraquinone derivatives or conducting polymers, could be grafted to the graphene sheets prior to stacking. These groups could impart additional pseudocapacitance to the systems, and act as the spacer molecules. Hence, future work could involve using molecular redox species to increase capacitance.

7.3 References

1. Ahn, E.; Lee, T.; Gu, M.; Park, M.; Min, S. H.; Kim, B.-S., Layer-by-layer assembly for graphene-based multilayer nanocomposites: The field manual. *Chem. Mater.* **2017**, *29*, 69-79.
2. Si, Y.; Samulski, E. T., Exfoliated graphene separated by platinum nanoparticles. *Chem. Mater.* **2008**, *20*, 6792-6797.
3. Liu, Z.-A.; Tao, Y.; Song, X.-Z.; Bao, M.; Tan, Z., A three dimensional n-doped graphene/CNTs/AC hybrid material for high-performance supercapacitors. *RSC Adv.* **2017**, *7*, 6664-6670.
4. Kirubasankar, B.; Murugadoss, V.; Angaiah, S., Hydrothermal assisted *in situ* growth of CoSe onto graphene nanosheets as a nanohybrid positive electrode for asymmetric supercapacitors. *RSC Adv.* **2017**, *7*, 5853-5862.
5. Hassan, H. K.; Atta, N. F.; Hamed, M. M.; Galal, A.; Jacob, T., Ruthenium nanoparticles-modified reduced graphene prepared by a green method for high-performance supercapacitor application in neutral electrolyte. *RSC Adv.* **2017**, *7*, 11286-11296.
6. Yue, S.; Tong, H.; Lu, L.; Tang, W.; Bai, W.; Jin, F.; Han, Q.; He, J.; Liu, J.; Zhang, X., Hierarchical NiCo₂O₄ nanosheets/nitrogen doped graphene/carbon nanotube film with ultrahigh capacitance and long cycle stability as a flexible binder-free electrode for supercapacitors. *J. Mater. Chem. A* **2017**, *5*, 689-698.
7. Luo, J.; Zhong, W.; Zou, Y.; Xiong, C.; Yang, W., Metal-organic coordination polymer to prepare density controllable and high nitrogen-doped content carbon/graphene for high performance supercapacitors. *ACS Appl. Mater. Interfaces* **2017**, *9*, 317-326.
8. Shao, Y.; El-Kady, M. F.; Lin, C.-W.; Zhu, G.; Marsh, K. L.; Hwang, J. Y.; Zhang, Q.; Li, Y.; Wang, H.; Kaner, R. B., 3D freeze-casting of cellular graphene films for ultrahigh-power-density supercapacitors. *Adv. Mater.* **2016**, *28*, 6719-6726.
9. El-Kady, M. F.; Ihns, M.; Li, M.; Hwang, J. Y.; Mousavi, M. F.; Chaney, L.; Lech, A. T.; Kaner, R. B., Engineering three-dimensional hybrid supercapacitors and microsupercapacitors for high-performance integrated energy storage. *Proc. Natl. Acad. Sci. U.S.A.* **2015**, *112*, 4233-4238.
10. Zhan, C.; Jiang, D.-E., Contribution of dielectric screening to the total capacitance of few-layer graphene electrodes. *J. Phys. Chem. Lett.* **2016**, *7*, 789-794.
11. Ma, K.; Wang, X.; Cui, Y.; Lin, F.; Deng, C.; Shi, H., Understanding the graphene-based electric double layer from dielectric perspective: A density functional study. *Chem. Phys. Lett.* **2017**, *677*, 137-142.
12. Zhan, C.; Lian, C.; Zhang, Y.; Thompson, M. W.; Xie, Y.; Wu, J.; Kent, P. R.; Cummings, P. T.; Jiang, D. e.; Wesolowski, D. J., Computational insights into materials and interfaces for capacitive energy storage. *Advanced Science* **2017**.

Appendices

Appendix A: Explanations of Experimental Techniques

A.1 Raman and IR spectroscopy

Raman and IR spectroscopy measure vibrational transitions in the molecules. In IR spectroscopy, a sample is irradiated with an IR beam. The molecule absorbs IR radiation of energy corresponding to a vibrational transition, typically labelled as a bend or stretch motion of the bonds. The difference in energy between the residual and the incident beam corresponds to the energy of the vibrational transition. Vibrational transitions must involve a change in dipole moment to be IR active. As such, vibrations in completely symmetrical bonds are forbidden. The origin of the Raman spectrum is different from IR.¹ This means vibrations that are inactive in the IR spectrum may be active in the Raman spectrum. In Raman spectroscopy, the sample is irradiated with an intense laser beam, typically in the UV/visible region, (532 nm in this work) and the scattered light that is perpendicular to the incident beam is measured. The scattered light can be split into two categories: namely Raleigh scattering and Raman scattering.¹ When a sample is irradiated with light, it transitions to an excited state due to the distortion of the chemical bond (vibration). This results in an induced dipole moment. This is a virtual state, as it is not a quantum mechanical stationary state. The excited state returns to a vibrational level in the ground state by emitting a photon.² Photons that result from the molecule returning to the original vibrational level have the same frequency as the incident beam, giving bands with typically strong intensity. This is Rayleigh scattering. Photons that are emitted from returning to a vibrational level one vibrational quantum level higher (stokes) or lower (anti-stokes) than the original level are known as Raman scattering. These three types of transition along with the transition measured in IR spectroscopy are illustrated in Figure A.1. In both, the difference between the final and initial vibrational states is measured in units of wavenumber (cm^{-1}). Stokes transitions are typically stronger than anti-stokes, due to the increased population of molecules at the $v=0$ level compared to the $v=1$ level, so it is common to show only stokes transitions in a Raman spectrum.

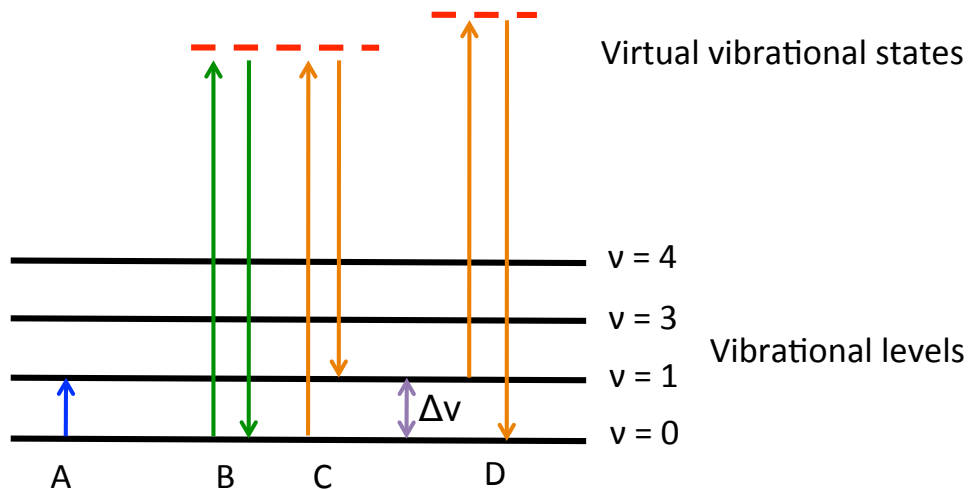


Figure A.1: Diagram illustrating the differences in IR and Raman transitions. (A) IR transition, (B) Rayleigh Scattering, (C) Stokes Raman Scattering, and (D) anti-Stokes Raman Scattering.

A.2 Hall Effect Measurements

Edwin H. Hall first described the Hall effect in 1879. It is defined as the generation of an electromotive force in a sample when a current is applied and the sample is exposed to a perpendicular magnetic field. This can cause a transverse voltage across the sample known as the Hall voltage, also represented as a current deflection.³ The Hall voltage can be used to calculate the carrier concentration and mobility.

The Van der Pauw method was used to determine the sheet resistance. This is one of the most widely used and effective methods for calculating the resistance of thin films and overcomes the geometry dependence of resistivity measurements.⁴ The Van der Pauw method relies on a four-point probe measurement; in this work gold contacts are attached to the four corners of the FLG sample (Figure A.2).

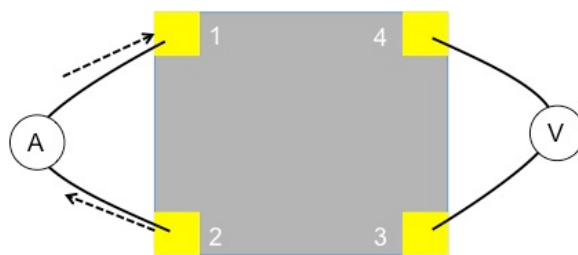


Figure A.2: Four-point probe contact configuration, with current measured across points one and two, and voltage across points three and four

A current is applied across two points positioned next to each other (1 and 2), and then the voltage across the other two points is recorded (3 and 4). The Van der Pauw equation is given in Equation A.1.

$$e^{(-\pi R_A/R_{SH})} + e^{(-\pi R_B/R_{SH})} = 1 \tag{A.1}$$

where, R_{SH} is the sheet resistance and

$$R_A = \frac{R_{21} + R_{12} + R_{43} + R_{34}}{4} \quad (\text{A.2})$$

and

$$R_B = \frac{R_{23} + R_{32} + R_{14} + R_{41}}{4} \quad (\text{A.3})$$

For example, R_{43} is the resistance calculated using Ohms law ($R = V/I$) from the voltage across points 3 and 4, when a current is applied across points 2 and 1, as illustrated in Figure A.2. This calculation only uses voltages recorded in the absence of an applied magnetic field. It must be solved numerically.⁵

To measure the Hall voltage the same set up is required, but a magnetic field is applied, as illustrated in Figure A.3.

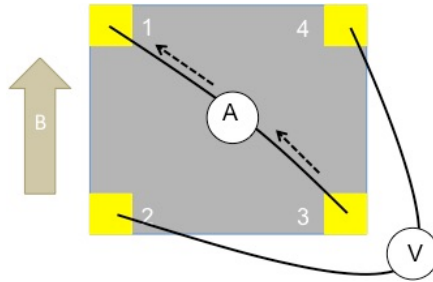


Figure A.3: Four-point probe measurement set up to calculate the Hall voltage, where B is a magnetic field applied perpendicular to the direction of the current

To measure the Hall voltage, the current is applied across opposing contacts (1 and 3), and the voltage is recorded across the other opposing contacts (2 and 4) with a positive magnetic field direction to give V_{24P} and then in a negative magnetic field direction to give V_{24N} . This is repeated to give eight separate voltages V_{24P} , V_{42P} , V_{13P} , V_{31P} , and their respective negative magnetic field voltages. The Hall voltage is then given by Equation A.4:⁶

$$V_H = \frac{|V_C| + |V_D| + |V_E| + |V_F|}{8} \quad (\text{A.4})$$

where

$$V_C = V_{24P} - V_{24N} \quad (\text{A.5})$$

$$V_D = V_{42P} - V_{42N} \quad (\text{A.6})$$

$$V_E = V_{13P} - V_{13N} \quad (\text{A.7})$$

$$V_F = V_{31P} - V_{31N} \quad (\text{A.8})$$

When the sum shown in Equation A.9 is positive p-doping is indicated, whereas a negative result represents n-doping.

$$V_C + V_D + V_E + V_F \quad (\text{A.9})$$

The Hall voltage can then be used to calculate the sheet carrier concentration (n_s) (Equation A.10):

$$n_s = \frac{IB}{q|V_H|} \quad (\text{A.10})$$

where I is the applied current, B is the magnetic field strength, and q is the elementary charge. Mobility is calculated based on the sheet resistance and the Hall voltage (Equation A.11):

$$\mu = \frac{|V_H|}{R_{SH}IB} \quad (\text{A.11})$$

Appendix B: NP Surface Concentration Data

B.1 Calculating Surface Concentration from IR

Surface concentration was calculated using the Beer-Lambert Law (Equation B.1).

$$Abs = \varepsilon cl \quad (B.1)$$

If the modified FLG sheet is modelled as a rectangular prism, where the film height corresponds to both the z-axis and the pathlength (Figure B.1).

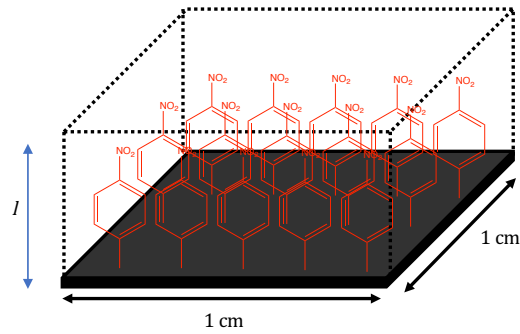


Figure B.1: Modified FLG surface with pathlength shown.

The concentration is:

$$c = \frac{mol}{cm^2 l} \quad (B.2)$$

therefore

$$Abs = \varepsilon \times \frac{mol}{cm^2 l} \times l \quad (B.3)$$

$$Abs = \varepsilon \times \frac{mol}{cm^2} \quad (B.4)$$

hence, pathlength (l) is not required to calculate surface concentration in $mol\ cm^{-2}$.

B.2 IR surface concentration values

Table B.1: Surface concentration values of FLG_{NP} calculated using IR spectroscopy based on area under 1344 cm⁻¹ peak.

| Modification time / hours | Surface concentration / nmol cm ⁻² |
|------------------------------|--|
| 2 | 6.1 |
| 6 | 4.1 |
| 8 | 8.8 |
| 16 | 21.7 |
| 16 | 7.4 |
| 17 | 16.5 |
| 17 | 21.7 |
| 17 | 14.3 |
| 20 | 11.6 |
| 23 | 9.1 |
| 24 | 6.6 |
| 27 | 29.7 |
| 41 | 15.7 |
| 44 | 21.2 |
| 50 | 16.2 |
| 66 | 38.2 |
| 66 | 20.9 |

B.3 Electrochemistry Surface Concentration Values

Table B.2: Surface concentrations calculated from electrochemistry for FLG_{NP} after reaction with 20 mM NBD.

| Modification time/ hours | Substrate | Orientation | Surface Concentration / nmol cm ⁻² | Number of NP reduction peaks |
|--------------------------|-----------|-------------|---|------------------------------|
| 2 | HOPG | Sandwiched | 0.41 | 2 |
| 7 | PPF | Sandwiched | 0.19 | 1 |
| 8 | PPF | Sandwiched | 0.22 | 1 |
| 16 | PPF | Sandwiched | 0.41 | 1 |
| 16 | PPF | Sandwiched | 0.51 | 1 |
| 17 | HOPG | Sandwiched | 0.21 | 1 |
| 17 | HOPG | Sandwiched | 0.28 | 1 |
| 23 | PPF | Sandwiched | 0.61 | 1 |
| 25 | PPF | Sandwiched | 0.29 | 1 |
| 27 | HOPG | Sandwiched | 0.62 | 2 |
| 41 | HOPG | Sandwiched | 0.93 | 1 |
| 41 | HOPG | Sandwiched | 0.93 | 1 |
| 41 | PPF | Sandwiched | 1.08 | 1 |
| 44 | HOPG | Sandwiched | 1.12 | 2 |
| 64 | FLG | Sandwiched | 1.71 | 1 |
| 66 | HOPG | Sandwiched | 1.45 | 1 |
| 66 | PPF | Sandwiched | 1.77 | 2 |
| 69 | HOPG | Sandwiched | 2.01 | 1 |
| 69 | HOPG | Sandwiched | 2.01 | 2 |
| 69.5 | HOPG | Sandwiched | 1.74 | 1 |
| 70 | FLG | Sandwiched | 1.32 | 1 |
| 1 | HOPG | Exposed | 0.12 | 1 |
| 6 | HOPG | Exposed | 0.36 | 1 |
| 17.5 | HOPG | Exposed | 0.56 | 1 |
| 20 | HOPG | Exposed | 0.83 | 1 |
| 20 | HOPG | Exposed | 0.40 | 1 |
| 27 | HOPG | Exposed | 0.62 | 1 |
| 41 | HOPG | Exposed | 0.52 | 1 |
| 69 | HOPG | Exposed | 0.24 | 1 |
| 69.5 | HOPG | Exposed | 0.57 | 1 |

Table B.3: Surface concentration values calculated from electrochemistry for FLG_{NAA}.

| Modification time / hours | Surface concentration / nmol cm ⁻² |
|---------------------------|---|
| 0.5 | 0.35 |
| 1 | 0.25 |
| 2 | 0.61 |
| 2 | 0.59 |
| 4 | 0.71 |
| 4 | 0.45 |
| 6 | 0.80 |
| 6 | 0.60 |
| 6 | 0.52 |

Appendix C: Calculated Capacitance

C.1 Areal Capacitance from CV for Aryldiazonium Modified FLG

Table C.1: Areal capacitance derived from CV for FLG before and after aryldiazonium salt reaction (7 hour, 20 mM).

| Sample | C_A 200mV s ⁻¹ / μF cm ⁻² | C_A 100mV s ⁻¹ / μF cm ⁻² | C_A 50mV s ⁻¹ / μF cm ⁻² | C_A 20mV s ⁻¹ / μF cm ⁻² | C_A 5mV s ⁻¹ / μF cm ⁻² | C_A 2mV s ⁻¹ / μF cm ⁻² |
|--------------------|---|---|--|--|---|---|
| FLG | 9.6 | 8.2 | 10.0 | 20.3 | 58.4 | 96.8 |
| FLG | 10.2 | 9.1 | 13.0 | 26.0 | 82.3 | 139.7 |
| 3FLG | 5.6 | 5.8 | 7.1 | 9.7 | 17.0 | 25.8 |
| FLG _{NP} | 4.7 | 3.2 | 2.9 | 3.1 | 4.0 | 4.9 |
| FLG _{NP} | 3.2 | 2.6 | 2.9 | 3.5 | 5.5 | 7.1 |
| 3FLG _{NP} | 11.7 | 10.2 | 12.0 | 14.5 | 21.5 | 27.8 |
| 3FLG _{NP} | 25.5 | 16.9 | 19.1 | 22.9 | 35.1 | 58.8 |
| FLG _{AP} | 7.0 | 8.1 | 10.0 | 17.0 | 43.3 | 81.5 |
| FLG _{AP} | 8.4 | 11.0 | 9.8 | 12.9 | 28.5 | 58.3 |
| 3FLG _{AP} | 64.8 | 70.7 | 83.8 | 104.1 | 118.2 | 122.9 |
| 3FLG _{AP} | 54.5 | 54.9 | 59.9 | 68.1 | 85.4 | 103.9 |
| FLG _{CP} | 3.5 | 2.8 | 3.1 | 3.6 | 5.0 | 6.8 |
| FLG _{CP} | 8.6 | 8.3 | 9.7 | 12.5 | 20.5 | 29.2 |
| 3FLG _{CP} | 30.2 | 25.1 | 27.6 | 27.9 | 49.2 | 70.4 |
| 3FLG _{CP} | 31.4 | 26.6 | 29.8 | 34.9 | 47.3 | 59.0 |

Table C.2: Areal capacitance derived from CV for FLG before and after aryldiazonium salt reaction (7 hour, 20 mM), after 20,000 charge discharge cycles at 10 μA cm⁻².

| Sample | C_A 200mV s ⁻¹ / μF cm ⁻² | C_A 100mV s ⁻¹ / μF cm ⁻² | C_A 50mV s ⁻¹ / μF cm ⁻² | C_A 20mV s ⁻¹ / μF cm ⁻² | C_A 5mV s ⁻¹ / μF cm ⁻² | C_A 2mV s ⁻¹ / μF cm ⁻² |
|--------------------|---|---|--|--|---|---|
| FLG | 10.1 | 9.1 | 11.2 | 21.2 | 60.7 | 96.5 |
| FLG | 10.2 | 9.9 | 6.8 | 9.3 | 51.2 | 81.1 |
| 3FLG | 6.2 | 6.6 | 9.0 | 13.4 | 23.9 | 32.8 |
| FLG _{NP} | 8.1 | 7.1 | 6.4 | 6.4 | 10.0 | 14.5 |
| FLG _{NP} | 6.8 | 5.1 | 4.0 | 3.8 | 4.5 | 5.7 |
| 3FLG _{NP} | 19.5 | 17.7 | 18.3 | 19.4 | 23.1 | 31.4 |
| 3FLG _{NP} | 22.6 | 19.3 | 18.6 | 19.1 | 23.5 | 28.8 |
| FLG _{AP} | 5.8 | 5.5 | 7.4 | 13.3 | 35.5 | 55.5 |
| FLG _{AP} | 5.6 | 4.9 | 5.6 | 9.8 | 26.5 | 50.7 |
| 3FLG _{AP} | 20.6 | 20.2 | 24.1 | 33.3 | 65.5 | 99.5 |
| 3FLG _{AP} | 15.2 | 15 | 19.2 | 33.2 | 70.2 | 117.9 |
| FLG _{CP} | 4.0 | 3.1 | 3.1 | 3.5 | 8.4 | 17.7 |
| FLG _{CP} | 7.3 | 6.9 | 8.2 | 11.5 | 19.8 | 28.2 |
| 3FLG _{CP} | 43.4 | 34.7 | 36.6 | 43.6 | 79.9 | 121 |
| 3FLG _{CP} | 28.1 | 26.7 | 31.4 | 40.8 | 61.2 | 83.2 |

C.2 Areal and Gravimetric Capacitance from CD for Aryldiazonium

Modified FLG

Table C.3: Areal capacitance derived from CD for FLG before and after aryldiazonium salt reaction (7 hour, 20 mM).

| Sample | C_A 6.25 $\mu\text{A cm}^{-2}$ / $\mu\text{F cm}^{-2}$ | C_A 10.0 $\mu\text{A cm}^{-2}$ / $\mu\text{F cm}^{-22}$ | C_A 12.5 $\mu\text{A cm}^{-2}$ / $\mu\text{F cm}^{-2}$ | C_A 25.0 $\mu\text{A cm}^{-2}$ / $\mu\text{F cm}^{-2}$ | C_A 50.0 $\mu\text{A cm}^{-2}$ / $\mu\text{F cm}^{-2}$ |
|--------------------|--|---|--|--|--|
| FLG | 12.9 | 12.8 | 12.7 | 14.3 | - |
| FLG | 23.8 | 18.3 | 17.8 | 18.0 | - |
| 3FLG | 10.4 | 10.3 | 10.8 | 12.0 | - |
| FLG _{NP} | 6.2 | 6.6 | 7.0 | 8.4 | - |
| FLG _{NP} | 5.8 | 6.1 | 6.3 | 8.4 | - |
| 3FLG _{NP} | - | 21.0 | 18.9 | 16.9 | 19.0 |
| 3FLG _{NP} | - | 17.1 | 17.0 | 17.6 | 21.5 |
| FLG _{AP} | 13.6 | 12.8 | 13.3 | 14.3 | - |
| FLG _{AP} | 20.3 | 19.0 | 18.4 | 19.7 | - |
| 3FLG _{AP} | - | 108.0 | 96.5 | 86.3 | 80.8 |
| 3FLG _{AP} | - | 63.3 | 57.7 | 50.5 | 51.2 |
| FLG _{CP} | 8.7 | 9.1 | 9.5 | 11.5 | - |
| FLG _{CP} | 23.2 | 21.5 | 21.0 | 22.0 | - |
| 3FLG _{CP} | - | 63.0 | 59.0 | 54.6 | 55.1 |
| 3FLG _{CP} | - | 41.5 | 40.2 | 38.2 | 38.3 |

Table C.4: Areal capacitance derived from CD for FLG before and after aryldiazonium salt reaction (7 hour, 20 mM) after 20,000 charge discharge cycles at 10 $\mu\text{A cm}^{-2}$.

| Sample | C_A 6.25 $\mu\text{A cm}^{-2}$ / $\mu\text{F cm}^{-2}$ | C_A 10.0 $\mu\text{A cm}^{-2}$ / $\mu\text{F cm}^{-22}$ | C_A 12.5 $\mu\text{A cm}^{-2}$ / $\mu\text{F cm}^{-2}$ | C_A 25.0 $\mu\text{A cm}^{-2}$ / $\mu\text{F cm}^{-2}$ | C_A 50.0 $\mu\text{A cm}^{-2}$ / $\mu\text{F cm}^{-2}$ |
|--------------------|--|---|--|--|--|
| FLG | 14.0 | 13.5 | 13.0 | 13.6 | - |
| FLG | 19.6 | 16.8 | 16.6 | 16.7 | - |
| 3FLG | 10.3 | 9.8 | 10.1 | 11.4 | - |
| FLG _{NP} | 10.6 | 9.8 | 9.8 | 9.6 | - |
| FLG _{NP} | 11.2 | 11.0 | 11.4 | 12.8 | - |
| 3FLG _{NP} | - | 26.3 | 26.2 | 24.6 | 25.2 |
| 3FLG _{NP} | - | 34.8 | 34.3 | 32.0 | 34.0 |
| FLG _{AP} | 10.4 | 10.3 | 10.4 | 12.4 | - |
| FLG _{AP} | 13.8 | 13.3 | 13.4 | 14.8 | - |
| 3FLG _{AP} | - | 37.0 | 35.5 | 36.2 | 38.1 |
| 3FLG _{AP} | - | 51.5 | 47.7 | 44.4 | 44.7 |
| FLG _{CP} | 8.7 | 9.1 | 9.5 | 11.5 | - |
| FLG _{CP} | 20.5 | 19.5 | 19.1 | 20.7 | - |
| 3FLG _{CP} | - | 58.8 | 57.0 | 53.0 | 53.0 |
| 3FLG _{CP} | - | 62.6 | 58.4 | 52.2 | 51.0 |

Table C.5: Gravimetric capacitance derived from CD for FLG before and after aryldiazonium salt reaction (7 hour, 20 mM).

| Sample | Total Mass / μg | C_G | C_G | C_G | C_G | C_G |
|--------------------|----------------------------|--|--|--|--|--|
| | | 6.25 μA $\text{cm}^{-2} / \text{F g}^{-1}$ | 10.0 μA $\text{cm}^{-2} / \text{F g}^{-1}$ | 12.5 μA $\text{cm}^{-2} / \text{F g}^{-1}$ | 25.0 μA $\text{cm}^{-2} / \text{F g}^{-1}$ | 50.0 μA $\text{cm}^{-2} / \text{F g}^{-1}$ |
| FLG | 0.026 | 43.5 | 43.2 | 42.8 | 48.2 | - |
| FLG | 0.019 | 80.2 | 61.7 | 60.1 | 60.7 | - |
| 3FLG | 0.089 | 11.7 | 11.6 | 12.1 | 13.5 | - |
| FLG _{NP} | 0.023 | 20.5 | 19.2 | 21.7 | 25.8 | - |
| FLG _{NP} | 0.019 | 18.0 | 18.8 | 19.6 | 26.0 | - |
| 3FLG _{NP} | 0.060 | - | 21.7 | 19.6 | 17.5 | 19.7 |
| 3FLG _{NP} | 0.075 | - | 17.7 | 17.6 | 18.2 | 22.2 |
| FLG _{AP} | 0.020 | 43.1 | 40.5 | 42.1 | 45.2 | - |
| FLG _{AP} | 0.015 | 60.1 | 64.3 | 58.2 | 62.4 | - |
| 3FLG _{AP} | 0.042 | - | 113.9 | 101.8 | 91.1 | 85.4 |
| 3FLG _{AP} | 0.057 | - | 66.8 | 60.9 | 53.3 | 51.2 |
| FLG _{CP} | 0.028 | 27.0 | 28.3 | 29.5 | 35.7 | - |
| FLG _{CP} | 0.013 | 72.0 | 66.8 | 65.2 | 68.3 | - |
| 3FLG _{CP} | 0.047 | - | 65.2 | 61.1 | 56.5 | 57 |
| 3FLG _{CP} | 0.060 | - | 54.1 | 51.4 | 48.0 | 48.3 |

Table C.6: Gravimetric capacitance derived from CD for FLG before and after aryldiazonium salt reaction (7 hour, 20 mM) after 20,000 charge discharge cycles at 10 $\mu\text{A cm}^{-2}$.

| Sample | Total Mass / μg | C_G | C_G | C_G | C_G | C_G |
|--------------------|----------------------------|--|--|--|--|--|
| | | 6.25 μA $\text{cm}^{-2} / \text{F g}^{-1}$ | 10.0 μA $\text{cm}^{-2} / \text{F g}^{-1}$ | 12.5 μA $\text{cm}^{-2} / \text{F g}^{-1}$ | 25.0 μA $\text{cm}^{-2} / \text{F g}^{-1}$ | 50.0 μA $\text{cm}^{-2} / \text{F g}^{-1}$ |
| FLG | 0.026 | 47.2 | 45.5 | 43.8 | 45.9 | - |
| FLG | 0.019 | 66.1 | 56.6 | 56.0 | 56.3 | - |
| 3FLG | 0.089 | 11.6 | 11.0 | 11.4 | 12.8 | - |
| FLG _{NP} | 0.023 | 32.9 | 30.4 | 30.4 | 29.8 | - |
| FLG _{NP} | 0.019 | 34.8 | 34.1 | 35.4 | 39.7 | - |
| 3FLG _{NP} | 0.060 | - | 27.1 | 27.1 | 25.4 | 26.0 |
| 3FLG _{NP} | 0.075 | - | 36.0 | 35.5 | 33.1 | 35.2 |
| FLG _{AP} | 0.020 | 32.9 | 32.6 | 32.9 | 39.3 | - |
| FLG _{AP} | 0.015 | 43.7 | 42.1 | 42.4 | 46.9 | - |
| 3FLG _{AP} | 0.042 | - | 48.5 | 41.0 | 38.6 | 38.9 |
| 3FLG _{AP} | 0.057 | - | 54.3 | 50.3 | 46.8 | 47.2 |
| FLG _{CP} | 0.028 | 27.0 | 28.3 | 29.5 | 35.7 | - |
| FLG _{CP} | 0.013 | 62.7 | 60.6 | 59.3 | 64.3 | - |
| 3FLG _{CP} | 0.047 | - | 60.8 | 59.0 | 54.9 | 54.9 |
| 3FLG _{CP} | 0.060 | - | 64.8 | 60.5 | 54.0 | 52.8 |

C.3 Areal Capacitance from CV for Cobalt-Nickel Hydroxide Modified FLG

Table C.7: Areal capacitance for FLG on Au/epoxy after cobalt-nickel hydroxide deposition derived from CV.

| Sample | C_A 50mV s ⁻¹ / mF cm ⁻² | C_A 20mV s ⁻¹ / mF cm ⁻² | C_A 10mV s ⁻¹ / mF cm ⁻² | C_A 5mV s ⁻¹ / mF cm ⁻² | C_A 2mV s ⁻¹ / mF cm ⁻² |
|------------------------------------|--|--|--|---|---|
| FLG | 15.6×10^{-3} | 18.2×10^{-3} | 24.7×10^{-3} | 36.8×10^{-3} | 49.1×10^{-3} |
| FLG | 15.7×10^{-3} | 16.0×10^{-3} | 20.7×10^{-3} | 29.4×10^{-3} | 38.5×10^{-3} |
| FLG _{Co/Ni} 1 minute | 12.2 | 20.3 | 21.3 | 22.1 | 22.8 |
| FLG _{Co/Ni} 1 minute | 11.4 | 22.8 | 25.9 | 24.4 | 24.0 |
| FLG _{Co/Ni} 2 minutes | 11.1 | 28.0 | 54.2 | 60.1 | 64.2 |
| FLG _{Co/Ni} 2 minutes | 25.7 | 50.1 | 55.6 | 55.5 | 55.8 |
| FLG _{Co/Ni} 30 seconds | 12.5 | 17.2 | 17.8 | 18.0 | 18.1 |
| FLG _{Co/Ni} 30 seconds | 9.7 | 11.4 | 12.6 | 14.5 | 13.9 |

Table C.8: Areal capacitance for FLG on Au/epoxy with and without CP film after 1 minute cobalt-nickel hydroxide deposition derived from CV, one- and three-sheet stacks.

| Sample | C_A 50mV s ⁻¹ / mF cm ⁻² | C_A 20mV s ⁻¹ / mF cm ⁻² | C_A 10mV s ⁻¹ / mF cm ⁻² | C_A 5mV s ⁻¹ / mF cm ⁻² | C_A 2mV s ⁻¹ / mF cm ⁻² |
|---------------------------|--|--|--|---|---|
| FLG | 15.6×10^{-3} | 18.2×10^{-3} | 24.7×10^{-3} | 36.8×10^{-3} | 49.1×10^{-3} |
| FLG | 15.7×10^{-3} | 16.0×10^{-3} | 20.7×10^{-3} | 29.4×10^{-3} | 38.5×10^{-3} |
| FLG _{Co/Ni} | 12.2 | 20.3 | 21.3 | 22.1 | 22.8 |
| FLG _{Co/Ni} | 11.4 | 22.8 | 25.9 | 24.4 | 24.0 |
| FLG _{CP+Co/Ni} | 4.1 | 9.3 | 11.2 | 11.7 | 12.0 |
| FLG _{CP+Co/Ni} | 6.3 | 9.4 | 10.0 | 10.6 | 11.1 |
| 3FLG _{Co/No} | 26.3 | 30.2 | 32.1 | 33.6 | 34.7 |
| 3FLG _{Co/Ni} | 36.6 | 41.3 | 43.0 | 44.1 | 44.6 |
| 3 FLG _{CP+Co/Ni} | 14.4 | 15.3 | 15.6 | 15.9 | 16.9 |
| 3 FLG _{CP+Co/Ni} | 23.4 | 25.2 | 26.2 | 27.0 | 27.9 |

C.3 Areal and Gravimetric Capacitance from CD for Cobalt-Nickel Hydroxide Modified FLG

Table C.9: Areal capacitance for FLG on Au/epoxy after cobalt-nickel hydroxide deposition for different times, derived from CD.

| Sample | C_A 0.8 mA cm ⁻² / mF cm ⁻² | C_A 1.6 mA cm ⁻² / mF cm ⁻² | C_A 3.2 mA cm ⁻² / mF cm ⁻² |
|------------------------------------|---|---|---|
| FLG | 8.3×10^{-3} | 10.1×10^{-3} | 12.6×10^{-3} |
| FLG | 15.3×10^{-3} | 15.3×10^{-3} | 17.6×10^{-3} |
| FLG _{Co/Ni} 1 minute | 19.1 | 15.9 | 3.4 |
| FLG _{Co/Ni} 1 minute | 24.7 | 19.1 | 5.1 |
| FLG _{Co/Ni} 2 minutes | 40.2 | 31.4 | 14.2 |
| FLG _{Co/Ni} 2 minutes | 43.3 | 30.7 | 15.9 |
| FLG _{Co/Ni} 30 seconds | 15.8 | 13.5 | 2.8 |
| FLG _{Co/Ni} 30 seconds | 11.9 | 10.5 | 8.2 |

Table C.10: Areal capacitance for FLG on Au/epoxy with and without CP film after 1 minute cobalt-nickel hydroxide deposition derived from CD, one- and three-sheet stacks.

| Sample | C_A 0.8 mA cm ⁻² / mF cm ⁻² | C_A 1.6 mA cm ⁻² / mF cm ⁻² | C_A 3.2 mA cm ⁻² / mF cm ⁻² | C_A 6.4 mA cm ⁻² / mF cm ⁻² |
|---------------------------|---|---|---|---|
| FLG | 8.3×10^{-3} | 10.1×10^{-3} | 12.6×10^{-3} | - |
| FLG | 15.3×10^{-3} | 15.3×10^{-3} | 17.6×10^{-3} | - |
| FLG _{Co/Ni} | 19.1 | 15.9 | 3.4 | - |
| FLG _{Co/Ni} | 24.7 | 19.1 | 5.1 | - |
| FLG _{CP+Co/Ni} | 8.4 | 7.5 | 1.0 | - |
| FLG _{CP+Co/Ni} | 8.2 | 7.4 | 1.5 | - |
| 3FLG _{Co/No} | - | 33.4 | 28.5 | 20.9 |
| 3FLG _{Co/Ni} | - | 40.7 | 36.1 | 29.1 |
| 3 FLG _{CP+Co/Ni} | - | 14.4 | 13.0 | 10.3 |
| 3 FLG _{CP+Co/Ni} | - | 23.1 | 19.8 | 13.6 |

Table C.11: Gravimetric capacitance for FLG on Au/epoxy with and without CP film after 1 minute cobalt-nickel hydroxide deposition derived from CD, one- and three-sheet stacks.

| Sample | Total Mass / mg | C_G 0.8 mA cm ⁻² / F g ⁻¹ | C_G 1.6 mA cm ⁻² / F g ⁻¹ | C_G 3.2 mA cm ⁻² / F g ⁻¹ | C_G 6.4 mA cm ⁻² / F g ⁻¹ |
|--------------------------|-----------------------|---|---|---|---|
| FLG | 0.29×10^{-3} | 28.0 | 34.1 | 42.5 | - |
| FLG | 0.29×10^{-3} | 51.6 | 51.6 | 59.3 | - |
| FLG _{Co/Ni} | 0.47 | 40.6 | 33.8 | 7.3 | - |
| FLG _{Co/Ni} | 0.47 | 52.5 | 40.6 | 10.9 | - |
| FLG _{CP+Co/Ni} | 0.27 | 31.1 | 27.7 | 3.4 | - |
| FLG _{CP+Co/Ni} | 0.27 | 31.0 | 27.6 | 3.6 | - |
| 3FLG _{Co/No} | 1.00 | - | 33.4 | 28.5 | 20.9 |
| 3FLG _{Co/Ni} | 1.00 | - | 40.7 | 36.1 | 29.1 |
| 3FLG _{CP+Co/Ni} | 0.47 | - | 30.6 | 27.7 | 21.9 |
| 3FLG _{CP+Co/Ni} | 0.47 | - | 49.1 | 42.1 | 28.9 |

Appendix D: Calculated Power and Energy Density

D.1 Areal Power and Energy Density for Aryldiazonium Modified FLG

Table D.1: Areal energy density for aryldiazonium modified FLG one- and three-sheet samples (7 hour, 20 mM reaction).

| Sample | $E_A \times 10^{-6}$ | $E_A \times 10^{-6}$ | $E_A \times 10^{-6}$ | $E_A \times 10^{-6}$ | $E_A \times 10^{-6}$ |
|--------------------|--|--|--|--|--|
| | $6.25 \mu\text{A cm}^{-2}$ / mWh cm^{-2} | $10.0 \mu\text{A cm}^{-2}$ / mWh cm^{-2} | $12.5 \mu\text{A cm}^{-2}$ / mWh cm^{-2} | $25.0 \mu\text{A cm}^{-2}$ mWh cm^{-2} | $50.0 \mu\text{A cm}^{-2}$ / mWh cm^{-2} |
| FLG | 0.29 | 0.28 | 0.28 | 0.32 | - |
| FLG | 0.52 | 0.41 | 0.40 | 0.40 | - |
| 3FLG | 0.23 | 0.29 | 0.24 | 0.26 | - |
| FLG _{NP} | 0.13 | 0.14 | 0.15 | 0.18 | - |
| FLG _{NP} | 0.12 | 0.13 | 0.13 | 0.18 | - |
| 3FLG _{NP} | - | 0.44 | 0.40 | 0.36 | 0.40 |
| 3FLG _{NP} | - | 0.36 | 0.36 | 0.37 | 0.45 |
| FLG _{AP} | 0.27 | 0.26 | 0.27 | 0.29 | - |
| FLG _{AP} | 0.41 | 0.38 | 0.37 | 0.39 | - |
| 3FLG _{AP} | - | 2.16 | 1.94 | 1.73 | 1.62 |
| 3FLG _{AP} | - | 1.27 | 1.16 | 1.01 | 1.03 |
| FLG _{CP} | 0.18 | 0.19 | 0.20 | 0.24 | - |
| FLG _{CP} | 0.49 | 0.45 | 0.44 | 0.46 | - |
| 3FLG _{CP} | - | 1.33 | 1.24 | 1.15 | 1.16 |
| 3FLG _{CP} | - | 0.88 | 0.85 | 0.81 | 0.81 |

Table D.2: Areal power density for aryldiazonium modified FLG one- and three-sheet samples (7 hour, 20 mM reaction).

| Sample | $P_A \times 10^{-3}$ | $P_A \times 10^{-3}$ | $P_A \times 10^{-3}$ | $P_A \times 10^{-3}$ | $P_A \times 10^{-3}$ |
|--------------------|---|---|---|---|---|
| | $6.25 \mu\text{A cm}^{-2}$ / mW cm^{-2} | $10.0 \mu\text{A cm}^{-2}$ / mW cm^{-2} | $12.5 \mu\text{A cm}^{-2}$ / mW cm^{-2} | $25.0 \mu\text{A cm}^{-2}$ mW cm^{-2} | $50.0 \mu\text{A cm}^{-2}$ / mW cm^{-2} |
| FLG | 1.25 | 2.00 | 2.48 | 4.97 | - |
| FLG | 1.26 | 2.00 | 2.49 | 4.96 | - |
| 3FLG | 1.26 | 2.00 | 2.00 | 5.00 | - |
| FLG _{NP} | 1.17 | 1.92 | 2.42 | 4.78 | - |
| FLG _{NP} | 1.19 | 1.90 | 2.39 | 4.84 | - |
| 3FLG _{NP} | - | 1.90 | 2.39 | 4.91 | 9.51 |
| 3FLG _{NP} | - | 1.91 | 2.39 | 4.75 | 9.51 |
| FLG _{AP} | 1.14 | 1.81 | 2.28 | 4.65 | - |
| FLG _{AP} | 1.14 | 1.80 | 2.24 | 4.42 | - |
| 3FLG _{AP} | - | 1.80 | 2.25 | 4.41 | 8.81 |
| 3FLG _{AP} | - | 1.81 | 2.25 | 4.44 | 9.68 |
| FLG _{CP} | 1.18 | 1.91 | 2.39 | 4.83 | - |
| FLG _{CP} | 1.19 | 1.90 | 2.38 | 4.75 | - |
| 3FLG _{CP} | - | 1.90 | 2.33 | 4.66 | 9.70 |
| 3FLG _{CP} | - | 1.90 | 2.38 | 4.83 | 9.64 |

D.2 Gravimetric Power and Energy Density for Aryldiazonium Modified FLG

Table D.3: Gravimetric energy density for aryldiazonium modified FLG one- and three-sheet samples (7 hour, 20 mM reaction).

| Sample | E_G 6.25 $\mu\text{A cm}^{-2}$ / Wh kg ⁻¹ | E_G 10.0 $\mu\text{A cm}^{-2}$ / Wh kg ⁻¹ | E_G 12.5 $\mu\text{A cm}^{-2}$ / Wh kg ⁻¹ | E_G 25.0 $\mu\text{A cm}^{-2}$ / Wh kg ⁻¹ | E_G 50.0 $\mu\text{A cm}^{-2}$ / Wh kg ⁻¹ |
|--------------------|--|--|--|--|--|
| FLG | 0.97 | 0.96 | 0.95 | 1.07 | - |
| FLG | 1.78 | 1.37 | 1.33 | 1.35 | - |
| 3FLG | 0.26 | 0.26 | 0.27 | 0.3 | - |
| FLG _{NP} | 0.43 | 0.41 | 0.46 | 0.54 | - |
| FLG _{NP} | 0.38 | 0.40 | 0.41 | 0.56 | - |
| 3FLG _{NP} | - | 0.46 | 0.41 | 0.37 | 0.42 |
| 3FLG _{NP} | - | 0.37 | 0.37 | 0.38 | 0.47 |
| FLG _{AP} | 0.86 | 0.81 | 0.84 | 0.91 | - |
| FLG _{AP} | 1.21 | 1.29 | 1.17 | 1.25 | - |
| 3FLG _{AP} | - | 2.28 | 2.04 | 1.83 | 1.71 |
| 3FLG _{AP} | - | 1.33 | 1.22 | 1.07 | 1.03 |
| FLG _{CP} | 0.57 | 0.59 | 0.62 | 0.75 | - |
| FLG _{CP} | 1.52 | 1.41 | 1.38 | 1.44 | - |
| 3FLG _{CP} | - | 1.38 | 1.29 | 1.19 | 1.20 |
| 3FLG _{CP} | - | 0.91 | 0.88 | 0.83 | 0.84 |

Table D.4: Gravimetric power density for aryldiazonium modified FLG one- and three-sheet samples (7 hour, 20 mM reaction).

| Sample | P_G 6.25 $\mu\text{A cm}^{-2}$ / W kg ⁻¹ | P_G 10.0 $\mu\text{A cm}^{-2}$ / W kg ⁻¹ | P_G 12.5 $\mu\text{A cm}^{-2}$ / W kg ⁻¹ | P_G 25.0 $\mu\text{A cm}^{-2}$ / W kg ⁻¹ | P_G 50.0 $\mu\text{A cm}^{-2}$ / W kg ⁻¹ |
|--------------------|---|---|---|---|---|
| FLG | 4228 | 6763 | 8351 | 16765 | - |
| FLG | 4243 | 6744 | 8407 | 16733 | - |
| 3FLG | 1413 | 2252 | 2915 | 5625 | - |
| FLG _{NP} | 3878 | 5575 | 7491 | 14990 | - |
| FLG _{NP} | 3681 | 5910 | 7386 | 14991 | - |
| 3FLG _{NP} | - | 1959 | 2476 | 5079 | 9856 |
| 3FLG _{NP} | - | 1973 | 2469 | 4908 | 9815 |
| FLG _{AP} | 3609 | 5712 | 7202 | 14700 | - |
| FLG _{AP} | 3384 | 6092 | 7098 | 13991 | - |
| 3FLG _{AP} | - | 1902 | 2369 | 4658 | 9314 |
| 3FLG _{AP} | - | 1904 | 2374 | 4681 | 9677 |
| FLG _{CP} | 3653 | 5945 | 7428 | 14999 | - |
| FLG _{CP} | 3694 | 5893 | 7378 | 14756 | - |
| 3FLG _{CP} | - | 1967 | 2417 | 4817 | 10034 |
| 3FLG _{CP} | - | 1963 | 2467 | 4989 | 9972 |

D.3 Areal Energy and Power Density for Cobalt-Nickel Hydroxide Decorated FLG

Table D.5: Areal energy density for cobalt-nickel hydroxide decorated FLG on Au/epoxy one- and three-sheet samples, with and without a CP film.

| Sample | $E_A \times 10^{-3}$ 0.8 mA cm ⁻² / mWh cm ⁻² | $E_A \times 10^{-3}$ 1.6 mA cm ⁻² / mWh cm ⁻² | $E_A \times 10^{-3}$ 3.2 mA cm ⁻² / mWh cm ⁻² | $E_A \times 10^{-3}$ 6.4 mA cm ⁻² / mWh cm ⁻² |
|--------------------------|---|---|---|---|
| FLG | 0.83 x 10 ⁻³ | 1.01 x 10 ⁻³ | 1.26 x 10 ⁻³ | - |
| FLG | 1.54 x 10 ⁻³ | 1.54 x 10 ⁻³ | 1.77 x 10 ⁻³ | - |
| FLG _{Co/Ni} | 1.83 | 1.52 | 3.25 | - |
| FLG _{Co/Ni} | 2.36 | 1.83 | 4.88 | - |
| FLG _{CP+Co/Ni} | 0.82 | 0.74 | 0.10 | - |
| FLG _{CP+Co/Ni} | 0.82 | 0.73 | 0.10 | - |
| 3FLG _{Co/No} | - | 3.20 | 2.73 | 2.00 |
| 3FLG _{Co/Ni} | - | 3.89 | 3.45 | 2.78 |
| 3FLG _{CP+Co/Ni} | - | 1.41 | 1.27 | 1.01 |
| 3FLG _{CP+Co/Ni} | - | 2.26 | 1.94 | 1.33 |

Table D.6: Areal power density for cobalt-nickel hydroxide decorated FLG on Au/epoxy one- and three-sheet samples, with and without a CP film.

| Sample | P_A 0.8 mA cm ⁻² / mW cm ⁻² | P_A 1.6 mA cm ⁻² / mW cm ⁻² | P_A 3.2 mA cm ⁻² / mW cm ⁻² | P_A 6.4 mA cm ⁻² / mW cm ⁻² |
|--------------------------|---|---|---|---|
| FLG | 0.01 | 0.02 | 0.04 | - |
| FLG | 0.01 | 0.02 | 0.04 | - |
| FLG _{Co/Ni} | 0.33 | 0.68 | 1.17 | - |
| FLG _{Co/Ni} | 0.35 | 0.73 | 1.76 | - |
| FLG _{CP+Co/Ni} | 0.35 | 0.65 | 0.71 | - |
| FLG _{CP+Co/Ni} | 0.34 | 0.64 | 0.73 | - |
| 3FLG _{Co/No} | - | 0.72 | 1.22 | 2.40 |
| 3FLG _{Co/Ni} | - | 0.70 | 1.38 | 2.51 |
| 3FLG _{CP+Co/Ni} | - | 0.73 | 1.39 | 2.79 |
| 3FLG _{CP+Co/Ni} | - | 0.75 | 1.49 | 2.99 |

D.4 Gravimetric Energy and Power Density for Cobalt-Nickel Hydroxide Decorated FLG

Table D.7: Gravimetric energy density for cobalt-nickel hydroxide decorated FLG on Au/epoxy one- and three-sheet samples, with and without a CP film.

| Sample | E_A 0.8 mA cm ⁻² / Wh kg ⁻¹ | E_A 1.6 mA cm ⁻² / Wh kg ⁻¹ | E_A 3.2 mA cm ⁻² / Wh kg ⁻¹ | E_A 6.4 mA cm ⁻² / Wh kg ⁻¹ |
|--------------------------|---|---|---|---|
| FLG | 2.81 | 3.41 | 4.27 | - |
| FLG | 5.18 | 5.18 | 5.96 | - |
| FLG _{Co/Ni} | 4.07 | 3.39 | 0.73 | - |
| FLG _{Co/Ni} | 5.27 | 4.08 | 1.09 | - |
| FLG _{CP+Co/Ni} | 3.12 | 2.79 | 0.37 | - |
| FLG _{CP+Co/Ni} | 3.11 | 2.77 | 0.39 | - |
| 3FLG _{Co/No} | - | 3.35 | 2.86 | 2.09 |
| 3FLG _{Co/Ni} | - | 4.08 | 3.62 | 2.92 |
| 3FLG _{CP+Co/Ni} | - | 3.07 | 2.77 | 2.19 |
| 3FLG _{CP+Co/Ni} | - | 4.93 | 4.23 | 2.90 |

Table D.8: Gravimetric power density for cobalt-nickel hydroxide decorated FLG on Au/epoxy one- and three-sheet samples, with and without a CP film.

| Sample | P_A 0.8 mA cm ⁻² / W kg ⁻¹ | P_A 1.6 mA cm ⁻² / W kg ⁻¹ | P_A 3.2 mA cm ⁻² / W kg ⁻¹ | P_A 6.4 mA cm ⁻² / W kg ⁻¹ |
|--------------------------|--|--|--|--|
| FLG | 36128 | 72410 | 139607 | - |
| FLG | 33299 | 66598 | 134067 | - |
| FLG _{Co/Ni} | 734 | 1527 | 2613 | - |
| FLG _{Co/Ni} | 791 | 1631 | 3919 | - |
| FLG _{CP+Co/Ni} | 1322 | 2447 | 2675 | - |
| FLG _{CP+Co/Ni} | 1320 | 2440 | 2700 | - |
| 3FLG _{Co/No} | - | 754 | 1286 | 2516 |
| 3FLG _{Co/Ni} | - | 735 | 1449 | 2628 |
| 3FLG _{CP+Co/Ni} | - | 1581 | 3027 | 6089 |
| 3FLG _{CP+Co/Ni} | - | 1628 | 3238 | 6533 |

Appendix E: Results from EIS Fitting

E.1 Aryldiazonium Modified FLG

Table E.1: Values calculated using electrical equivalent circuit fitting for EIS data collected at 0.1 V in 1 M HClO₄ for one- and three-sheet stacks of FLG and aryldiazonium modified FLG.

| Value | FLG | FLG _{AP} | FLG _{NP} | FLG _{CP} | 3FLG _{AP} | 3FLG _{CP} |
|---------------------------------------|------|-------------------|-------------------|-------------------|--------------------|--------------------|
| R _s / Ω | 6.8 | 27.4 | 22.4 | 9.1 | 6.3 | 9.3 |
| Q _L / μS cm ⁻² | - | 2.9 | 12.3 | 0.2 | 9.0 | 0.12 |
| n _L | - | 0.97 | 0.98 | 1.1 | 1.1 | 0.8 |
| R _L / kΩ cm ⁻² | - | 12.2 | 36.7 | 18.7 | 40.0 | 60.0 |
| Q _{DL} / μS cm ⁻² | 0.87 | 4.6 | 1.5 | 6.2 | 17.4 | 9.2 |
| n _{DL} | 0.96 | 0.92 | 1.0 | 0.95 | 0.98 | 0.96 |
| W / μS cm ⁻² | 5.6 | 1.7 | 3.1 | 1.2 | 1.2 | 15.0 |
| Q _B / μS cm ⁻² | 42.6 | 278.6 | 44.5 | 72.8 | 224 | 78.9 |
| n _B | 0.4 | 0.1 | 0.2 | 0.5 | 0.6 | 0.6 |
| R _B / kΩ cm ⁻² | 13.5 | 96.4 | 49.9 | 28.6 | 11.6 | 9.5 |

E.2 Cobalt Nickel Hydroxide Decorated FLG

Table E.2: Values calculated using electrical equivalent circuit fitting for EIS data collected at 0.1 V in 1 M KOH for one- and three-sheet stacks of FLG and cobalt nickel hydroxide decorated FLG.

| Value | FLG | FLG _{CoNi} |
|---------------------------------------|-------|---------------------|
| R _s / Ω | 185.2 | 180.2 |
| Q _P / μS cm ⁻² | - | 3.7 |
| n _L | - | 0.98 |
| R _{CT} / kΩ cm ⁻² | - | 27.9 |
| Q _{DL} / μS cm ⁻² | 4.8 | 5.9 |
| n _{DL} | 0.98 | 0.96 |
| W / μS cm ⁻² | 2.9 | 9.5 |
| Q _B / μS cm ⁻² | 47.3 | 1.0 |
| n _B | 0.5 | 0.6 |
| R _B / kΩ cm ⁻² | 13.1 | 6.1 |

References

1. Ferraro, J. R.; Nakamoto, K.; Brown, C. W., *Introductory Raman Spectroscopy*. Academic Press: San Diego, 2003.
2. Pelletier, M. J.; Pelletier, C. C., Spectroscopic Theory for Chemical Imaging. In *Raman, Infrared, and Near-Infrared Chemical Imaging*, Ozaki, Y.; Sasic, S., Eds. Wiley: Hoboken, New Jersey, 2010.
3. Popvic, R. S., *Hall Effect Devices, Second Edition*. Taylor & Francis: 2003.
4. Ramadan, A. A.; Gould, R. D.; Ashour, A., On the Van der Pauw method of resistivity measurements. *Thin Solid Films* **1994**, *239*, 272-275.
5. Thurber, W. R. The Hall Effect. <https://www.nist.gov/pml/engineering-physics-division/hall-effect> (accessed 22/09/2016).
6. Thurber, W. R. Resistivity and Hall Measurements. <https://www.nist.gov/pml/engineering-physics-division/hall-effect> (accessed 22/09/16).